

*X-RAY AND ELECTRON MICROANALYSES
OF A MARTIAN BRECCIA AND
COMET 81P/WILD 2 SAMPLES*

Jane Linda MacArthur

Department of Physics and Astronomy

University of Leicester

Thesis submitted for the degree of Doctor of Philosophy

at the University of Leicester

November 2018

X-RAY AND ELECTRON MICROANALYSES OF A MARTIAN BRECCIA AND COMET 81P/WILD 2 SAMPLES

Jane Linda MacArthur

ABSTRACT

X-ray spectroscopy and electron microscopy have been used to study a martian breccia meteorite and grains from Comet 81P/Wild 2 retrieved by NASA's *Stardust* mission.

Martian meteorite Northwest Africa (NWA) 8114 (paired with NWA 7034) allows examination of the thermal history of a regolith near an impact crater on Mars. Transmission electron microscopy (TEM) reveals that some pyroxene clasts are porous and have partially re-crystallised, forming magnetite and a K-bearing feldspathic glassy material with relict pyroxene. Fe-K X-ray absorption spectroscopy (XAS) shows the pyroxene to be oxidised, with up to 25% $\text{Fe}^{3+}/\Sigma\text{Fe}$. A partially re-crystallised augite clast gave a ^{40}Ar - ^{39}Ar maximum age of 1.13 Ga to 1.25 Ga, inferred to correspond to the impact heating event causing pyroxene breakdown, being held above 700 °C for at least seven days in an oxidising regolith environment. A Fourier cooling model indicates that a regolith of at least five metres depth would provide these temperatures. Low temperature hydrous alteration formed goethite, identified with X-ray diffraction (XRD), XAS and Fourier transform infrared spectroscopy (FTIR).

Fe-K XAS and XRD identified magnetite and olivine in terminal grains 1 and 2 respectively of *Stardust* track #187 and provisionally iron sulphide, magnetite and pyroxene in tracks #188, #189 and #190. Magnetite provides evidence for aqueous alteration on a cometary parent body. The same preparation techniques with carbonaceous chondrites yielded the identification of two magnetite and three olivine particles, suggesting dense magnetite is preferentially preserved during capture.

TEM analysis of *Stardust* terminal grains identifies chondrule-like fragments with pyroxenes, olivines and feldspars, and iron sulphides that were originally pyrrhotite, but have lost volatile sulphur due to heating during the capture process.

The combination of XRD, FTIR and Fe-K XAS are a powerful non-destructive method for mineralogical identification on a micron scale for small planetary samples.

ACKNOWLEDGEMENTS

I thank my supervisors John, Mike and Steve for the opportunity to work with these specialised techniques and samples. I thank the *Diamond Light Source* for five beamtime allocations and the beamline I-18 staff and MIRIAM beamline B-22 staff for their help in data acquisition. Thanks to Ray and Katie at the University of Manchester for their help with the ^{40}Ar - ^{39}Ar analyses.

I thank Leon, John, Graeme, Steve, Laura, Graham, Vinay, Rob, Colin, Lin, Tom, Dan and Mike for assistance with CT, SEM, EPMA, TEM, and synchrotron operation, analysis, and sample preparation. Thanks to Beth, Susanne and Natasha for the SEM and EPMA data. Thanks to Roger Hewins for many helpful conversations and a review of my paper about the martian breccia, and also to two anonymous reviewers that helped to improve the manuscript. Thanks to K. Friedman and M. Morgan for the thesis template.

Thanks to STFC for the *Diamond Light Source* synchrotron summer school and workshops as well as the PhD studentship that funded my studies. Thanks to NASA's *JSC* for the *Stardust* comet samples. Thanks to the Royal Astronomical Society, Meteoritical Society, Royal Microscopical Society and the Volcanic and Magmatic Studies Group for funding to attend conferences. Thanks to the Space Research Centre for funding and Europlanet for funding EPEC week.

The journey started at a shuttle launch in 2011; fond memories of FoTT where it all began. The path full of fabulous people at BIS, UKSEDS, RAS, LJMU, Alpbach, UCL, OeWF, SpaceUp, ESA and NASA Socials, #MeetESO and countless talks, conferences and space events. Thanks to Wolf, Oz and David for the amazing field school and training opportunities. Many thanks to AL for being my roommate in five countries, ST, CB, TC for all the coffee, JA, MR, MG, SD, JP for support, training and friendship, and KD, TN, LA, AM, JB, GN, GE, KAG for long distance support, friendship and inspiration.

Finally, the biggest thanks to my parents, sister and Torsten Henkel.

CONTENTS

ABSTRACT	I
ACKNOWLEDGEMENTS	II
CONTENTS	III
LIST OF TABLES	VII
LIST OF FIGURES	VIII
LIST OF ABBREVIATIONS AND ACRONYMS	XII
1 PLANETARY MATERIALS	1
1.1 PLANETARY SAMPLE COLLECTION.....	2
1.1.1 <i>Meteorites, dust and rocks from space</i>	2
1.1.2 <i>Samples returned by space missions</i>	6
1.2 MARTIAN METEORITES	7
1.3 WHY STUDY COMETS?	12
1.3.1 <i>Features of comets</i>	13
1.3.2 <i>Comets visited by missions</i>	14
1.3.3 <i>Relationships between carbonaceous chondrites and comets</i>	19
2 TECHNIQUES	20
2.1 OPTICAL AND REFLECTED LIGHT MICROSCOPY	21
2.2 ELECTRON MICROSCOPY.....	21
2.2.1 <i>Scanning electron microscope (SEM)</i>	22
2.2.2 <i>Electron Probe Microanalysis (EPMA)</i>	24
2.2.3 <i>Focused ion beam (FIB)</i>	27
2.2.4 <i>Scanning Transmission Electron Microscopy (STEM)</i>	28
2.2.5 <i>Energy dispersive X-ray (EDX) quantitative analysis</i>	30
2.2.6 <i>Experimental calibration of K-factors for STEM-EDX</i>	32
2.3 SYNCHROTRON RADIATION	36
2.3.1 <i>The Diamond Light Source synchrotron and beamlines</i>	37
2.3.2 <i>X-ray Fluorescence (XRF)</i>	40
2.3.3 <i>X-ray Absorption Spectroscopy (XAS)</i>	41
2.3.4 <i>Transmission X-ray Diffraction (XRD)</i>	45
2.3.5 <i>Fourier Transform Infrared Spectroscopy (FTIR)</i>	46
2.4 CT SCANNING.....	50
2.5 ⁴⁰ AR- ³⁹ AR DATING.....	51

3 THERMAL HISTORY OF MARTIAN REGOLITH BRECCIA NORTHWEST AFRICA 8114	55
3.1 INTRODUCTION	55
3.2 METHODS AND SAMPLES	61
3.2.1 SEM-EDX, EPMA and CT Scanning	61
3.2.2 FIB-SEM and TEM-STEM-EDX.....	62
3.2.3 Synchrotron techniques at the Diamond Light Source	62
3.2.4 ⁴⁰ Ar- ³⁹ Ar dating	63
3.3 RESULTS.....	65
3.3.1 Breccia and Clast Textures	65
3.3.2 Mineral Compositions.....	70
3.3.3 TEM Investigations of Pyroxene Texture.....	74
3.3.4 Iron Oxidation State.....	76
3.3.5 Mineral Identification by XRD.....	80
3.3.6 FTIR Search for Evidence of Hydration	83
3.3.7 ⁴⁰ Ar- ³⁹ Ar dating	83
3.4 DISCUSSION.....	86
3.4.1 Five Distinct Events in the Martian Breccia's Formation.....	87
3.4.2 Formation of Regolith Ejecta Blankets	97
3.4.3 Thermal Structure of the Martian Breccia Parental Regolith and Simple Cooling Model.....	97
3.5 CONCLUSIONS	101
4 SYNCHROTRON ANALYSES OF COMET WILD 2 AND ANALOGUE CHONDRITES.....	103
4.1 INTRODUCTION.....	104
4.1.1 Comet 81P/Wild 2	104
4.1.2 The Stardust mission	105
4.1.3 The Stardust Spacecraft	106
4.1.4 The Stardust Samples	107
4.1.5 Stardust science: affinities with carbonaceous chondrites	111
4.1.6 Selection of CV3 and CR2 chondrites as analogues.....	115
4.2 METHODS	117
4.2.1 Sample preparation.....	117
4.2.2 Techniques	118
4.3 RESULTS.....	119

4.3.1	<i>Characterisation of carbonaceous chondrites</i>	119
4.3.2	<i>Characterisation of Stardust terminal grains</i>	120
4.3.3	<i>Characterisation of carbonaceous chondrite terminal grains</i>	129
4.3.4	<i>Unit cell fit for magnetite and olivine terminal grains</i>	133
4.3.5	<i>Summary of results</i>	135
4.4	DISCUSSION	137
4.4.1	<i>Classifications of CR2 and CV3 carbonaceous chondrites</i>	137
4.4.2	<i>Mineralogy of Stardust and carbonaceous chondrite terminal grains</i>	137
4.4.3	<i>Formation of magnetite</i>	138
4.4.4	<i>Complementary Raman studies</i>	143
4.4.5	<i>Formation in the early solar system</i>	143
4.4.6	<i>Best carbonaceous chondrite match for comet Wild 2</i>	146
4.5	CONCLUSIONS	147
5	STEM-EDX ANALYSES OF COMET WILD 2	148
5.1	INTRODUCTION	149
5.2	SAMPLES AND METHODS	150
5.2.1	<i>Track #77, terminal grain 1 (Tg1)</i>	151
5.2.2	<i>Track #81, terminal grains 1 and 2</i>	152
5.2.3	<i>Track #108, terminal grain 20</i>	154
5.2.4	<i>Track #153, terminal grain 2</i>	155
5.3	RESULTS	156
5.3.1	<i>Terminal grain 1 from Track #77</i>	156
5.3.2	<i>Terminal grain 1 from Track #81</i>	158
5.3.3	<i>Terminal grain 2 from Track #81</i>	161
5.3.4	<i>Terminal grain 20 from Track #108</i>	163
5.3.5	<i>Terminal grain 2 from Track #153</i>	164
5.3.6	<i>Comparisons of mineralogy with previous results</i>	165
5.4	DISCUSSION	168
5.4.1	<i>Chondrule-like fragments</i>	168
5.4.2	<i>Fe-Ni metal and sulphides</i>	169
5.4.3	<i>Limitations and future investigations</i>	170
6	CONCLUSIONS	171
6.1	THERMAL HISTORY OF MARTIAN METEORITES	171
6.2	MAGNETITE AND SILICATES IDENTIFIED IN COMET WILD 2	172
6.3	ADVANCEMENT IN SAMPLE ANALYSIS CAPABILITIES	173

6.4 THE FUTURE FOR PLANETARY MATERIALS.....	174
6.4.1 <i>New meteorites</i>	175
6.4.2 <i>Interplanetary dust particles (IDPs)</i>	176
6.4.3 <i>Stardust samples</i>	176
6.4.4 <i>Sample return missions</i>	177
6.4.5 <i>Asteroid and comet missions</i>	182
APPENDIX A: PUBLICATIONS LIST	184
BIBLIOGRAPHY	188

LIST OF TABLES

TABLE 2.1. EPMA CRYSTAL SPECTROMETERS SPECIFICATIONS.....	26
TABLE 2.2. EPMA AND STEM-EDX DATA FOR REFERENCE MATERIALS..	34
TABLE 2.3. COMPARISON OF K-FACTORS FOR MAJOR ELEMENTS.....	35
TABLE 3.1. DIFFERENT CLASSIFICATIONS OF CLASTS WITHIN THE MARTIAN BRECCIAS	59
TABLE 3.2: SEM-EDX AND EPMA COMPOSITIONS OF CLASTS IN NWA 8114 .	73
TABLE 3.3: REPRESENTATIVE TEM-EDX COMPOSITIONS OF THE PYROXENES	75
TABLE 3.4: PRE-EDGE CENTROID AND FE-K EDGE ENERGIES.	79
TABLE 3.5: XRD ANALYSES FOR MAGNETITE AND GOETHITE FOUND IN NWA 8114..	82
TABLE 3.6. ^{40}Ar - ^{39}Ar ANALYTICAL DATA FOR NWA 8114 CLASTS..	86
TABLE 4.1. THE RANGE OF COUNTS FOR EACH XRF MAP SHOWN IN FIG. 4.33.	132
TABLE 4.2. FE-K XAS ANALYSES OF <i>STARDUST</i> CR2 AND CV3 GRAINS.	135
TABLE 4.3. XRD ANALYSES FROM <i>STARDUST</i> TRACKS, CR2 AND CV3 GRAINS.....	136
TABLE 5.1. NORMALISED STEM-EDX DATA FOR OLIVINES AND PYROXENES.	157
TABLE 5.2. NORMALISED STEM-EDX DATA FOR PYROXENES AND FELDSPARS	159

LIST OF FIGURES

FIG. 1.1. METEORITE COMPOSITIONAL CLASSIFICATION CHART	3
FIG. 1.2. CHONDRULES IN ORDINARY AND CARBONACEOUS CHONDRITES.	5
FIG. 1.3. IMAGES OF SHERGOTTY, NAKHLA AND CHASSIGNY.....	8
FIG. 1.4. THE NUCLEUS OF COMET HALLEY FROM THE GIOTTO SPACECRAFT	15
FIG. 1.5. IMAGES OF COMET TEMPEL 1 FROM DEEP IMPACT AND STARDUST-NEXT.	16
FIG. 1.6. COMET HARTLEY 2 IMAGED BY NASA'S EPOXI MISSION.....	17
FIG. 1.7. IMAGES FROM ROSETTA OF COMET 67P/CHURYUMOV-GERASIMENKO.....	18
FIG. 2.1. OLYMPUS DP70 OPTICAL MICROSCOPE.....	21
FIG. 2.2. SCHEMATICS OF AN SEM AND TEM.....	21
FIG. 2.3. SEM-EDX SPECTRUM FROM THE OXFORD INSTRUMENTS INCA PROGRAMME ..	23
FIG. 2.4. SCHEMATIC OF THE SAMPLE, CRYSTAL DETECTOR IN EPMA-WDS	25
FIG. 2.5. FIB-SEM MILLING PROCEDURE.	27
FIG. 2.6. SCHEMATIC AND IMAGE OF TEM.	29
FIG. 2.7. OVERVIEW OF THE <i>DIAMOND LIGHT SOURCE</i> SYNCHROTRON.	36
FIG. 2.8. SCHEMATIC OF BEAMLINE I-18.	37
FIG. 2.9. AERIAL VIEW OF THE I-18 SAMPLE STAGE CONFIGURATION.....	38
FIG. 2.10. SCHEMATIC OF THE FTIR BEAMLINE B-22 AND EXPERIMENT HUTCH.	39
FIG. 2.11. XAS DETECTOR SETUP FOR TRANSMISSION AND FLUORESCENCE.....	41
FIG. 2.12. EXAMPLE XAS SPECTRUM.....	42
FIG. 2.13. FE-K XANES FOR NATURAL OLIVINE $Fe_{0.85}$ AND FAYALITE.....	43
FIG. 2.14. $Fe^{3+}/\Sigma Fe$ CALIBRATION FROM FE-K XANES $1s \rightarrow 3d$ CENTROID ENERGIES.	43
FIG. 2.15. FTIR: THREE VIBRATIONAL MODES OF WATER VAPOUR	47
FIG. 2.16. MICHELSON INTERFEROMETER FOR FTIR	47
FIG. 2.17. FTIR: VARIATION OF DISPERSION AS A FUNCTION OF WAVENUMBER.	49
FIG. 2.18. CT-SCAN CONFIGURATION OF SAMPLE AND DETECTOR.....	51
FIG. 2.19. AR ISOTOPES WITH THEIR NATURAL ABUNDANCES.	51

FIG. 2.20. THERMO SCIENTIFIC ARGUS VI MASS SPECTROMETER.	53
FIG. 3.1. MAIN MASS AND CT IMAGES OF NWA 8114.....	56
FIG. 3.2. BSE IMAGE AND MLA MAP OF SECTION A OF NWA 8114	65
FIG. 3.3. EDS X-RAY ELEMENT MAP OF SECTION C.....	66
FIG. 3.4. CLASTS FROM POLISHED SECTIONS OF NWA 8114.	67
FIG. 3.5. BSE IMAGE AND XRF MAP OF AN EXSOLUTION PYROXENE CLAST.....	68
FIG. 3.6. BSE IMAGES OF THE RELICT PIGEONITE CLAST WITH VEINS.	68
FIG. 3.7. BSE, EDS AND XRF MAPS OF A RELICT PYROXENE WITH GOETHITE	69
FIG. 3.8. PYROXENE QUADRILATERAL FOR CLASTS IN NWA 8114.....	70
FIG. 3.9. MINERAL COMPOSITIONS OF FELDSPARS IN NWA 8114.....	71
FIG. 3.10. BSE IMAGE OF THE AUGITE CLAST 3 ANALYSED WITH ⁴⁰ AR- ³⁹ AR.....	72
FIG. 3.11. STEM BF IMAGE OF FIB1 AND FIB7 FROM RELICT PYROXENE CLASTS.....	74
FIG. 3.12. BF STEM IMAGES SHOWING OXIDISED RELICT PIGEONITE.....	76
FIG. 3.13. FE-K XAS MAPS FOR OXIDISED PYROXENE CLASTS IN NWA 8114.....	77
FIG. 3.14. PRE-EDGE CENTROID VS. FE-K EDGE ENERGIES FOR NWA 8114.	78
FIG. 3.15. XRD D-SPACING PEAKS FOR CLASTS IN NWA 8114.....	80
FIG. 3.16. FTIR REFLECTANCE ABSORPTION FOR CLASTS IN NWA 8114.....	83
FIG. 3.17. ⁴⁰ AR- ³⁹ AR LASER AGE DETERMINATIONS OF CLASTS FROM NWA 8114	85
FIG. 3.18. REPORTED AGES FOR PAIRS OF NWA 8114.....	93
FIG. 3.19: SIMPLE COOLING MODEL FOR MARTIAN REGOLITH.	100
FIG. 4.1 IMAGE OF THE NUCLEUS OF COMET WILD 2 FROM THE <i>STARDUST</i> SPACECRAFT .	104
FIG. 4.2. ASTEROID ANNEFRANK AND THE NUCLEUS OF COMET TEMPEL 1.....	106
FIG. 4.3. ARTIST’S CONCEPT OF THE <i>STARDUST</i> SPACECRAFT AT COMET WILD 2.	107
FIG. 4.4. AEROGEL CELL	107
FIG. 4.5. <i>STARDUST</i> COMETARY TRAY 2.	108
FIG. 4.6 EXTRACTED AEROGEL KEYSTONE	109
FIG. 4.7. DISTRIBUTION OF AEROGEL TRACKS IN THE COMETARY TRAY	110

FIG. 4.8. EXAMPLES OF TYPE A, B AND C <i>STARDUST</i> TRACKS (HÖRZ ET AL., 2006).....	110
FIG. 4.9. GEMS IN A CP-IDP AND GEMS-LIKE MATERIAL IN A <i>STARDUST</i> TRACK.	114
FIG. 4.10. NWA 10256 CR2 SLICE.....	117
FIG. 4.11. KENT LIGHT-GAS GUN AND SCHEMATIC	117
FIG. 4.12. IMAGES OF A CV3 (NWA 4502) AND A CR2 (NWA 10256) METEORITE.....	119
FIG. 4.13. HISTOGRAM SHOWING OLIVINE COMPOSITIONS IN CR2 AND <i>STARDUST</i>	120
FIG. 4.14. TRACK #187: A TYPE B TRACK, WITH THREE TERMINAL GRAINS	120
FIG. 4.15. XRF MAP OF THE ~5 μM FIRST TERMINAL GRAIN (TG1) IN #187.	121
FIG. 4.16. FE-K XAS OF <i>STARDUST</i> , CV3 AND CR2 GRAINS (MAGNETITE).....	121
FIG. 4.17. XRD ANALYSES OF <i>STARDUST</i> , CV3 AND CR2 GRAINS (MAGNETITE).....	122
FIG. 4.18. XRF MAP OF THE ~5 μM SECOND TERMINAL GRAIN (TG2) IN #187.	122
FIG. 4.19. FE-K XAS OF <i>STARDUST</i> , CV3 AND CR2 TERMINAL GRAINS.....	123
FIG. 4.20. XRD ANALYSES OF <i>STARDUST</i> , CV3 AND CR2 GRAINS (OLIVINE).....	124
FIG. 4.21. XRF MAP OF THE ~5 μM THIRD TERMINAL GRAIN IN #187.....	124
FIG. 4.22. FE-K XANES OF <i>STARDUST</i> TERMINAL GRAINS	125
FIG. 4.23. XRD ANALYSES OF <i>STARDUST</i> TERMINAL GRAINS.	125
FIG. 4.24. TRACK #188 IS TYPE B WITH ONE STYLUS AND ONE TERMINAL GRAIN (TG)...	126
FIG. 4.25. XRF MAP OF THE ~5 μM TERMINAL GRAIN (TG) IN #188.	126
FIG. 4.26. TRACK #189 IS TYPE B WITH THREE TERMINAL GRAINS (TG1, TG2, TG3).....	127
FIG. 4.27. XRF MAP OF THE ~7 μM FIRST TERMINAL GRAIN (TG1) IN #189.	127
FIG. 4.28. XRF MAP OF THE ~6 μM THIRD TERMINAL GRAIN (TG3) IN #189.	128
FIG. 4.29. TRACK #190 IS TYPE B WITH ONE TERMINAL GRAIN (TG).....	128
FIG. 4.30. XRF MAP OF THE ~7 μM TERMINAL GRAIN (TG) IN #190.....	129
FIG. 4.31. CR2 CARBONACEOUS CHONDRITE IMPACT TRACK IN AEROGEL.....	129
FIG. 4.32. MICROSCOPE IMAGES FOR CV3 AND CR2 IMPACT TRACKS IN AEROGEL.....	131
FIG. 4.33. XRF MAPS OF THE CARBONACEOUS CHONDRITE TERMINAL GRAINS	132
FIG. 4.34. OLIVINE UNIT CELL DIMENSIONS FOR CV3, CR2 AND <i>STARDUST</i> GRAINS.....	134

FIG. 5.1. A ~1 MM FERROMAGNESIAN CHONDRULE.....	149
FIG. 5.2. TEM GRID 2009-20-77-1-6 WITH FIVE SLICES.....	151
FIG. 5.3. TRACK #81, TYPE B, WITH TWO TERMINAL GRAINS.....	152
FIG. 5.4. IMAGES OF SLICES 13-18 (2092-7-81-1-4) AND SLICE 22 (2092-7-81-1-7).	152
FIG. 5.5. IMAGE OF FOUR SLICES OF TERMINAL GRAIN 2 (2092-7-81-2-5).	153
FIG. 5.6. IMAGES OF TRACK #108, TYPE B, CONTAINING 30 TERMINAL GRAINS.....	154
FIG. 5.7. IMAGES OF FOUR SLICES (2081-1-108-20-1), ONE SLICE (2081-1-108-20-3). ...	154
FIG. 5.8. TRACK #153, NINE SLICES (2035-3-153-2-7), 7 SLICES (2035-3-153-2-8).	155
FIG. 5.9. DF AND BF IMAGES (2009-20-77-1-6).	156
FIG. 5.10. BF IMAGE AND EDX MAP WITH OLIVINE FO_{70-73} (2009-20-77-1-12).	157
FIG. 5.11. (A) BF AND DF IMAGES AND STEM-EDX OF SLICE 16 (2092-7-81-1-4).	158
FIG. 5.12. BF IMAGE OF SLICE 17 (2092-7-81-1-4).....	159
FIG. 5.13. (A) GATAN AND STEM-EDX DF IMAGES OF SLICE 18 (2092-7-81-1-4).	160
FIG. 5.14. BF IMAGES AND STEM-EDX MAPS OF SLICE 22 (2092-7-81-1-7).....	160
FIG. 5.15. BF AND DF IMAGES OF THE FOUR SLICES A-D (2092-7-81-2-5).....	161
FIG. 5.16. SLICE B (2092-7-81-2-5) WITH FE METAL-SULPHIDE SPHERE.....	162
FIG. 5.17. BF IMAGE AND EDX MAP OF THE GRAIN (2081-1-108-20-1).....	163
FIG. 5.18. GATAN AND DF IMAGES OF THE SLICE FROM GRID 3 (2081-1-108-20-3)..	163
FIG. 5.19. BF IMAGE OF SLICE 4 AND DF IMAGE OF SLICE 1 (2035-3-153-2-7).....	164
FIG. 5.20. BF IMAGE AND STEM-EDX OF SLICE 1 (2035-3-153-2-8).	164
FIG. 5.21. PYROXENE QUADRILATERAL AND OLIVINE LINE PLOT FOR <i>STARDUST</i>	165
FIG. 5.22. STEM-EDX FELDSPAR TERNARY OF <i>STARDUST</i> GRAINS.....	166
FIG. 5.23. STEM-EDX FE-NI-S TERNARY OF <i>STARDUST</i> GRAINS.	167
FIG. 6.1. THE I-14 NANOPROBE BEAMLINE AT <i>DIAMOND LIGHT SOURCE</i>	174
FIG. 6.2. ASTEROID RYUGU FROM THE HAYABUSA 2 SPACECRAFT	178
FIG. 6.3. <i>CAESAR</i> MISSION CONCEPT	180
FIG. 6.4. ARTISTS'S CONCEPT OF THE <i>PSYCHE</i> SPACECRAFT AT THE METAL ASTEROID....	183

LIST OF ABBREVIATIONS AND ACRONYMS

^{40}Ar - ^{39}Ar	Argon dating
AU	Astronomical Unit (distance from Sun to Earth)
BF	Bright Field
BSE	Back Scattered Electrons
CC	Carbonaceous Chondrites
DF	Dark Field
EDX	Energy Dispersive X-ray
EPMA	Electron Probe Micro-Analysis
ESA	European Space Agency
EXAFS	Extended X-ray Absorption Fine Structure
FIB	Focused Ion Beam
FTIR	Fourier Transform Infrared Spectrometry
GEMS	Glass Embedded Metal and Sulphides
GIS	Gas Injection System
IDP	Interplanetary Dust Particle
JAXA	Japan Aerospace Exploration Agency
JFC	Jupiter Family Comet
NASA	National Aeronautics and Space Administration
NWA	Northwest Africa
OC	Ordinary Chondrites
RF	Radiofrequency
SDD	Silicon Drift Detector
SEM	Scanning Electron Microscope
SNC	Martian meteorites (shergottites, nakhlites and chassignites)
STEM	Scanning Transmission Electron Microscope
TEM	Transmission Electron Microscope
UL	University of Leicester
WD	Working Distance
WDS	Wavelength Dispersive Spectrometry
XAS	X-ray Absorption Spectroscopy
XAFS	X-ray Absorption Fine Structure
XANES	X-ray Absorption Near-Edge Structure
XRD	X-ray Diffraction
XRF	X-ray Fluorescence

1 PLANETARY MATERIALS

This thesis investigates and constrains the formation conditions of planetary materials using electron microscopy and X-ray spectroscopy. By studying the first regolith breccia meteorite from Mars and *Stardust* comet grains, the aim is to improve our knowledge of the formation and evolution of these Solar System bodies.

The introductory first chapter reviews the current collection of planetary materials and provides the context to the investigation of the martian regolith breccia (Chapter 3) and the investigation of comet samples (Chapters 4 and 5). Meteorite groups and asteroids are discussed in order to understand the selection and study of carbonaceous chondrites as the closest analogues to *Stardust* samples in Chapter 4.

Chapter 2 documents the full range of techniques employed in this research; scanning electron microscopy (SEM) and scanning transmission electron microscopy (STEM), both with energy dispersive X-ray spectroscopy (EDX), electron probe microanalysis (EPMA), focused ion beam (FIB), X-ray absorption spectroscopy (XAS), X-ray fluorescence (XRF), X-ray diffraction (XRD), Fourier transform infrared spectroscopy (FTIR) and micro-computed tomography (CT) scan. ^{40}Ar - ^{39}Ar dating has been carried out in collaboration with the University of Manchester.

Chapter 3 describes the results from using the above techniques on the regolith breccia from Mars, investigating the mineral compositions and iron oxidation states and looking for alteration textures, as well as determining the identity of hydrated iron oxide phases from their crystal structure. The results have been used to construct a

simple thermal model, constraining conditions at the impact site on Mars where the breccia was deposited.

Chapter 4 identifies minerals in comet terminal grains in tracks in four aerogel keystones returned by NASA's *Stardust* mission from comet Wild 2. The affinities between carbonaceous chondrites and comets are investigated by comparing the *Stardust* terminal grains with carbonaceous chondrite CR2 and CV3 samples, shot into aerogel by a light gas-gun by collaborators at the University of Kent and made into keystones at the University of Berkeley in a process analogous to the capture of *Stardust* comet grains.

Chapter 5 presents results of STEM-EDX analysis of microtome slices of *Stardust* terminal grains and compares them with the mineralogy of *Stardust* grains from other studies.

Chapter 6 summarises the results of the thesis, places the contributions made in context, and suggests future lines of further investigation, including techniques that are being proposed and developed for laboratory analysis on Earth, sample return missions that are currently in progress, and other planned and proposed space missions..

1.1 Planetary sample collection

Earth's inventory of extra-terrestrial planetary materials consists of meteorites, dust and rocks from space that land on Earth, and specimens from sample return missions. This section sets out the different meteorite classification groups, petrologic types and background; martian meteorites are discussed separately in section 1.2.

1.1.1 Meteorites, dust and rocks from space

Over 50,000 meteorites have been classified (LPI, 2018) and the vast majority are thought to have originated from the asteroid belt between Mars and Jupiter, between ~1.8 A.U. and ~5.2 A.U. This belt has a mass of $\sim 3.7 \times 10^{21}$ kg, equivalent to ~5% of the mass of the Moon and is thought to represent left-over building blocks from the formation of the Solar System (Shearer et al., 1998). The low mass distribution, together with the variation in compositional and abundance distributions, is thought to be caused by the growth of Jupiter and resonances with Jupiter's orbital period as

Jupiter’s gravity and orbital resonances caused too much perturbation for the small asteroids to accrete into fewer larger objects or a single body (Shearer et al., 1998).

The meteorite collection has been sorted into groups that share similar compositional characteristics, and are thus thought to come from the same parent body (Fig. 1.1). Each group has features in common that are different to the features of other groups. They are thought to record at least 40 unique parent bodies. This is a relatively small number considering the asteroid belt contains more than 200 asteroids larger than 100 km in diameter (NASA, 2018) and 1.2 ± 0.5 million asteroids with diameters greater than 1 km (Tedesco & Desert, 2002).

1.1.1.1 Classification of meteorites

All chondrites and some achondrites are stony meteorites. Chondrites contain chondrules (Fig. 1.2), which are fast-cooled ferromagnesian silicate melt droplets <1 mm in size, thought to have formed in flash-heating events in the solar nebula (Brearley & Jones, 1998).

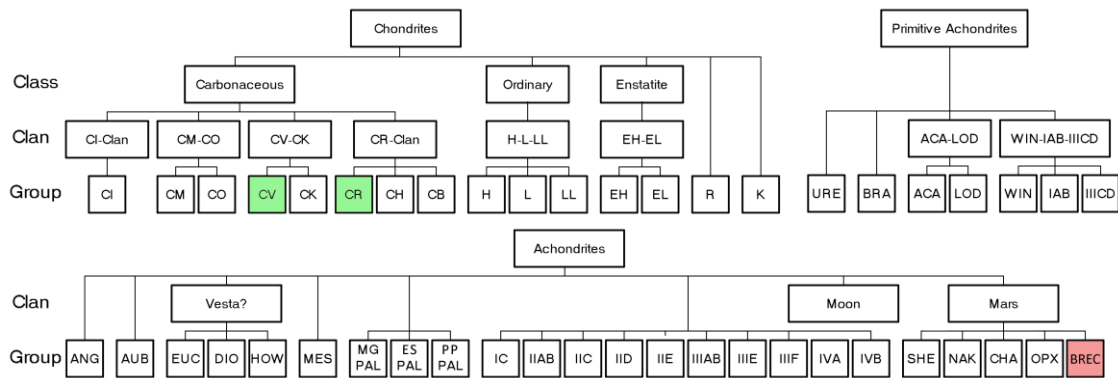


Fig. 1.1. Meteorite compositional classification chart highlighting the martian regolith breccia studied (red, Chapter 3) and the CV and CR carbonaceous chondrite groups (green) compared with *Stardust* comet grains in this thesis (Chapter 4). Based on Weisberg et al. (2006), modified from Tobias (1984) from Wikimedia Commons, 2012, CC-BY-SA-3.0. The abbreviations are explained in the text of this section.

Ordinary chondrites (OC) are the most common and include 50,985 of the 59,218 meteorites classified to date (LPI, 2018). The three types H, L and LL (Fig. 1.1) have respectively high total iron, low total iron, and low metallic Fe relative to total Fe (Brearley & Jones, 1998). Enstatite chondrites (EC) are divided into two types: EH have high iron and EL have low iron (Brearley & Jones, 1998), with the EH type being

more reduced and having ~3% Si in the Fe,Ni metal whereas the EL type have <1% Si in the metal (Weisberg et al., 2006).

Two thousand, two-hundred and ninety-six carbonaceous chondrites (CC) have been identified (LPI, 2018). These primitive rocks contain higher volatile contents than ordinary chondrites, and refractory objects such as calcium aluminium inclusions (CAIs) and amoeboid olivine aggregates (AOAs). The subgroups CI, CM, CO, CV, CK, CR, CH, and CB (Fig. 1.1) are named C for carbonaceous with the initial of the following representative meteorites: Ivuna, Mighei, Ornans, Vigarano, Karoonda, Renazzo, “High metal” and Bencubbin respectively. The subgroups have distinct oxygen isotopic and bulk compositional characteristics (Brearley & Jones, 1998).

Chondrule abundances in OC and EC are between 60% and 80%, whereas those in CCs range from 0% to 70%. Refractory inclusions are <1 vol% in OC and EC but can be as high as 13 vol% in CCs. An oxygen isotope plot of $\Delta^{17}\text{O}$ vs $\Delta^{18}\text{O}$ shows that most CC meteorites (except CI and CM) plot on the carbonaceous chondrite anhydrous minerals mixing line (CCAM), whereas the OCs plot above the terrestrial fractionation line (TFL). The different chondrite groups all show distinct iron contents and oxidation states on a plot of iron present as metal or sulphide vs iron within silicate and oxide phases (Urey-Craig diagram) (Brearley & Jones, 1998).

Chondrites are classified using petrologic types thought to reflect the degree of thermal and aqueous alteration. Type 3.0 chondrites are the most pristine unaltered primitive material, with a sliding scale up to 6, which indicates the material has been subjected to significant heat processing, resulting in poor definition of the individual chondrules and recrystallization of the matrix (Van Schmus & Wood, 1967). Type 7 refers to chondrites that are completely recrystallized, with the chondrules no longer distinguishable. Type 2.0 chondrites contain 2-16 weight% water and show signs of aqueous alteration. Type 1.0 chondrites are so intensely hydrated that the separate chondrules are no longer distinguishable (Huss et al., 2006; McSween, 1979). Only the CC show signs of hydrous alteration. Most CC have experienced little heat processing, with types CI, CM, CO, CV, CR, CH (Fig. 1.1) having no members \geq petrologic type 4. CI can contain up to 25% water, with CM, CR and CH also showing aqueous alteration. Nearly all CV and CO meteorites are type 3.

Achondrites do not contain chondrules as they have undergone melting and recrystallization indicative of igneous processes, differentiation and/or impact processing. Primitive stony achondrites have similar chemical compositions to chondrites and either they have experienced partial melting or they came from parent bodies where differentiation did not achieve isotopic equilibrium. Some rare stony achondrites are thought to have derived from larger bodies that underwent differentiation, such as Mars, Vesta (eucrites EUC, diogenites DIO howardites HOW) and the Moon, and from other, unidentified parent bodies of angrites (ANG) and aubrites (AUB) (Fig. 1.1). Achondrites also include rare stony-iron meteorites (115 pallasites PAL, 240 mesosiderites MES) and 1204 iron meteorites (types IC, IIAB, IIC, IID, IIE, IIIAB, IIIE, IIIF, IVA, IVB; Fig. 1.1) (LPI, 2018). These are from the core-mantle boundary and the cores of these larger differentiated bodies.

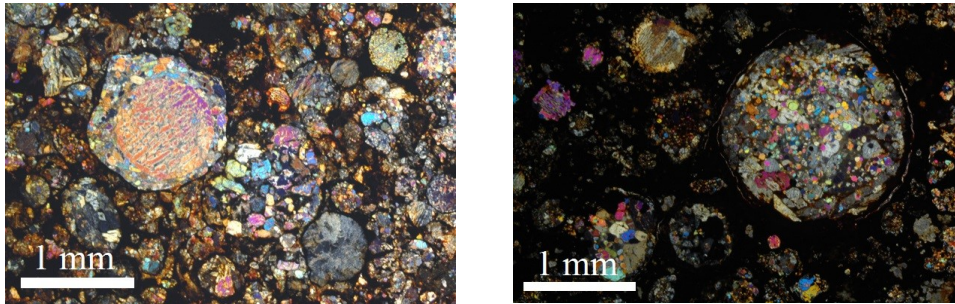


Fig. 1.2. Cross-polarised microscope images of chondrules in (1) ordinary chondrite DaG 405, type H3.5 and (2) carbonaceous chondrite NWA 5239, type CV3 (Images: P. Marmet).

1.1.1.2 Interstellar Dust Particles (IDPs)

Comets, asteroids and the interstellar medium are thought to be the main sources of interstellar dust particles (IDPs). IDPs can be collected in the stratosphere and laboratory techniques have been developed to deal with small samples (Brownlee, 1979). This makes them an important part of the inventory of extra-terrestrial materials for study as they are easier to obtain and do not require the expense and timescale of a sample return space mission. The deceleration of IDPs entering the upper stratosphere acts to concentrate the flux compared with near-Earth space, making it the best area for efficient collection, with 30 to 40 hours of sampling capturing ~10 IDPs greater than 10 μm in size (Rietmeijer, 1998). All IDPs collected in the stratosphere show signs of atmospheric entry heating, with loss of volatiles (Rietmeijer, 1998). However, as most IDPs are less than 100 μm and highly porous they slow down more gently than

micrometeorites and cosmic spherules, and are less intensely heated (Marty et al., 2013). IDPs are chondritic where the proportions of elements within them match the cosmic solar elemental abundance (the CI carbonaceous chondrite composition). They form two groups: chondritic porous IDPs (CP-IDPs) comprise 90% of chondritic IDPs, tend to be anhydrous, and are thought to come from comets, chondritic smooth IDPs (CS-IDPs) comprise 10% of chondritic IDPs, are dominated by hydrous minerals, and are thought to come from asteroids (Marty et al., 2013). Most non-chondritic IDPs are formed of silicates (Mg-rich olivine, pyroxenes) and iron and nickel sulphides. Chondritic and non-chondritic IDPs are commonly found adhered to each other, suggesting a relationship between them (Rietmeijer, 1998).

Chondritic IDPs represent protoplanets that were far enough from the Sun not to have been affected by heat in the inner disk, so that they did not evaporate and condense. Thus, they are thought to originate from the least altered carbon-rich icy bodies in the outer asteroid belt and comets (Rietmeijer, 1998). The *Stardust* missions to comet Wild 2 provided our first cometary samples to compare with CP-IDPs that will be discussed further in Chapters 4 and 5.

1.1.2 Samples returned by space missions

Sample return space missions have provided the opportunity to ground-truth, discover relationships between meteorites and their possible parent bodies, and to constrain theories from remote sensing observations. One of the biggest benefits of sample return missions is that the samples can be curated for many years after their return, allowing analyses to be carried out by instruments not yet conceived at the time of mission design (Westphal et al., 2017). A research group can easily spend over a year on the analysis of just one grain, and many techniques are non-destructive, so samples like *Stardust* comet grains will remain available for future generations (Westphal et al., 2017).

The first extra-terrestrial samples to be returned by space missions were the Apollo human lunar missions. These collected 2200 samples, weighing a total of 381 kg from six different landing locations, between 1969 and 1972 (NASA, 2018). The first robotic sample return missions collected 301 g, in three Russian *Luna* (16, 20 and 24) missions to the Moon in 1970, 1972 and 1976 (LPI Luna, 2018).

Three types of solar wind atom were collected by NASA's *Genesis* mission in 2004, the first to return material from beyond the orbit of the Moon. The proportion of ^{16}O in planetary materials varies and the *Genesis* mission provided the first measurements that show the Sun is highly enriched in ^{16}O compared with the Earth, Moon, Mars, and bulk meteorites (McKeegan et al., 2011). This demonstrates that planetary objects in the inner Solar System have been enriched in both $^{18}\text{O}/^{16}\text{O}$ and $^{17}\text{O}/^{16}\text{O}$ by non-mass-dependent fractionation processes (McKeegan et al., 2011).

NASA's *Stardust* mission to comet Wild 2 has provided ~ 300 μg cometary grains (Horz 2006) and ~ 12 pg size potential interstellar grains (Westphal et al), with the samples safely landing on Earth in 2006. Initial *Stardust* results identified high temperature minerals in the comet grains, and this suggested that material formed in the inner solar nebula had been transported to the outer solar system comet-forming regions, with implications for Solar System formation models (Brownlee et al., 2006). Section 1.3 provides more information on comets, and Chapters 4 and 5 document the comet Wild 2 grains analyses from the present study.

JAXA's *Hayabusa* spacecraft visited a silicaceous (S-type), space-weathered asteroid, 25143 Itokawa, and brought back ~ 1500 rocky particle grains in 2010 (Tsuchiyama et al., 2011). Most asteroids over 1 km in size are thought to be 'rubble piles', and this was the first mission to make close-up observations of the properties, such as high porosity, low density and being boulder-rich, providing a potential benchmark that may be common to many small asteroids (Fujiwara et al., 2006). The mission found that the Itokawa S-type asteroid composition was nearly identical to that of LL ordinary chondrite meteorites (Nakamura et al., 2011; Tsuchiyama et al., 2011).

Sample return missions that are currently in progress are described in Chapter 6.

1.2 Martian meteorites

The only known samples of Mars on Earth are martian meteorites. One hundred and seventeen distinct meteorites, ignoring pairs (Irving, 2018), thought to be from Mars have provided a vital new source of information that can be compared with orbital spacecraft and rover data to improve our understanding of martian climate and geological history. They include shergottites, nakhlites and chassignites (SNC) achondritic meteorites, which took their names from the observed falls of Shergotty

(India, 1865), Nakhla (Egypt, 1911) and Chassigny (France, 1815) (Fig. 1.3). These were initially classified alongside the howardite, eucrite and diogenite (HED) meteorites as they showed signs of igneous processing and were differentiated (Urey & Craig, 1953). The individual meteorites Shergotty and Zagami were considered to form a unique class, the shergottites, as they contained maskelynite and had similar mineralogy (Binns, 1967), after the original discovery of maskelynite, (formed from shocked plagioclase) in Shergotty by Gustav Tschermak (1872).

The SNC meteorites were found to have much younger crystallisation ages than the ~ 4.4 Gyr ages of the HED achondrites (Bogard, 1995). The shergottites are 175 Myr to 475 Myr old, and the nakhlites and chassignites are ~ 1.3 Gyr old (Nyquist et al., 2001). These younger ages suggest that the parent body must have been geologically active until much more recently than most asteroids in the asteroid belt.

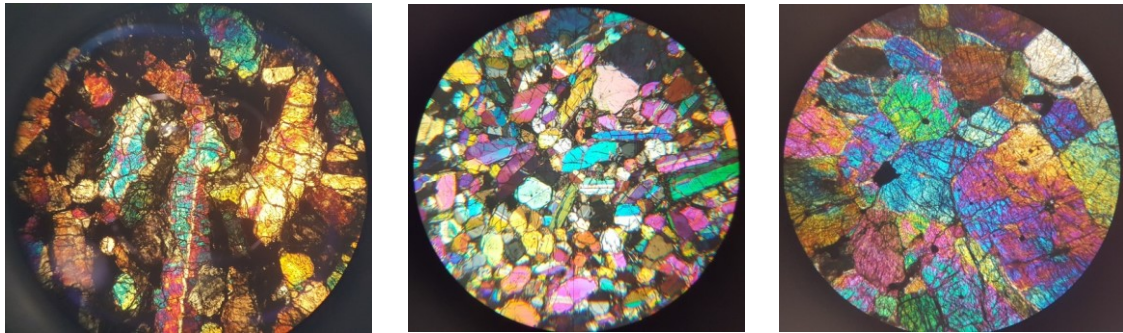


Fig. 1.3. Cross-polarised images of Shergotty, Nakhla and Chassigny, field of view diameter 4.0 mm.

The discovery of noble gas isotopic ratios within the Elephant Moraine shergottite meteorite (EETA79001) (Bogard & Johnson, 1983) that matched the those measured in the martian atmosphere by the Viking spacecraft (Nier & McElroy, 1977) was the first direct evidence that the SNC meteorites were from Mars. Nitrogen isotopes in EETA79001 also matched those measured by the Viking spacecraft (Becker & Pepin, 1984).

1.2.1.1 Shergottites

Of the 101 unique shergottites (ignoring pairs), 95 are basaltic shergottites, some of which form an olivine-phyric subgroup. The remaining 6 are lherzolitic shergottites (LPI, 2018; Irving, 2018).

Most of the basaltic shergottites are thought to have formed by the accumulation of crystals from a magma and are fine-grained cumulates, composed mainly of pyroxene

(augite and pigeonite) and shocked plagioclase (maskelynite), and they are very similar to terrestrial basaltic rocks (McSween & Stolper, 1980). Fractionation may account for the different types of shergottite seen (Smith et al., 1984).

The olivine-phyric subgroup are more Mg-rich than the other basaltic shergottites and have large olivine phenocrysts in a finer grained pyroxene groundmass. The subgroup are thought to be from olivine-saturated magmas, parental to the magmas that produced the basaltic shergottites (McCall et al., 2006).

The lherzolitic shergottites are cumulates containing small olivine and chromite crystals enclosed by larger orthopyroxene crystals (McSween, 1994). They contain less maskelynite than the basaltic shergottites (Bridges & Warren, 2006). Their coarse-grainsize indicates they have cooled slower than the basaltic shergottites (McCall et al., 2006).

The shergottites can alternatively be classified by their LREE (light rare earth element) geochemistry: shergottites that are slightly depleted in LREEs are mainly basaltic shergottites, whereas moderately depleted shergottites are mainly the lherzolitic shergottites, and the highly depleted shergottites are the olivine-phyric shergottites (Bridges & Warren, 2006). However, the classifications do not correspond perfectly; each geochemically depleted group includes members from each petrological group.

Tissint was the 5th witnessed fall of a Martian meteorite. It fell in Morocco on 18 July 2011. It provided a fresh olivine-phyric shergottite in which the in situ martian weathering should be distinguishable from terrestrial contamination. The glass of Tissint was LREE-enriched, which suggested that martian weathering had taken place, leaching elements from the regolith into the rock (Aoudjehane et al., 2012). However, the trace elements in the impact melts were shown to match those in the bulk rock, which suggests that the LREE enrichment was terrestrial (Barrat et al., 2014).

1.2.1.2 Nakhrites

The ten known nakhrites (LPI, 2018) are cumulate augite-rich pyroxenites with iron-rich olivine grains, plagioclase and alkali feldspar, enriched in LREE (McSween, 1985). Small amounts of alteration phases were originally identified in three nakhrites: iron-rich silicate rust, Ca-sulphate, Mg-sulphate and NaCl, though this represented less than 0.01 wt.% of each meteorite (Gooding et al., 1991). Veins containing

hydrothermal assemblages occur within many of the nakhlites, and are probably pre-terrestrial in origin as they are truncated by the fusion crusts. Radiometric dating of iddingsite in Lafayette veins yielded a formation date of ~670 Ma (Swindle et al., 2000), distinct from the ~1.3 Ga age of the nakhlites, suggesting a later alteration event (Nyquist et al., 2001). Similar traces of hydrous alteration phases were found in all SNC subgroups suggesting that oxidising aqueous conditions have existed on Mars during the radiometric ages of the meteorites ie 200 Ma to 1300 Ma (Gooding, 1992).

A trace element ion microprobe investigation into the sequence of salt crystallisation in three nakhlites indicated progressive evaporation of brine (Bridges & Grady, 2000). The Nakhla meteorite shows the point where less than 10% of the water remain, from the final products of the evaporating brine (clay minerals, Mn-rich siderite gypsum veins, anhydrite), whereas the Lafayette meteorite shows over 25% of the water remains (indicated by the presence of Ca-rich siderite, smectite and illite) (Bridges & Grady, 2000). This would have most likely occurred at temperatures of 25 °C to 150 °C, given the simple mineral assemblages present. Such brine activity is likely to have occurred intermittently over the last 1 Ga, because more continuous brine activity would have produced more silicate alteration than is seen (Bridges et al., 2001). It has been suggested that an impact shock event caused the fracturing in nakhlites, and melted the martian subsurface permafrost, creating a hydrothermal system that led to the melted brine fluid flowing upwards, from Lafayette at greatest depth towards Nakhla nearer the surface (Changela & Bridges, 2010). The variation in Mg# and Ca fractionation found in secondary phases in nine nakhlites is thought to be related to the distance of each nakhlite from the fluid source causing the alteration (Hicks et al., 2014). The secondary phases were identified as phyllosilicates, ferric saponite and Fe-serpentine (Hicks et al., 2014).

1.2.1.3 Chassignites

Three chassignites, Chassigny, NWA 2737, and NWA 8694 are known. All are dunite cumulates. Chassigny is composed of 91.6% olivine, crystallised from an iron-rich magma, indicated by igneous and metamorphic textures (Prinz et al., 1974; Mason et al., 1976). REE abundance patterns suggest that the magma was enriched in LREE (Boynton et al., 1976). A fast cooling rate of 28 °C/yr is indicated by olivine zoning profiles and pyroxene exsolution features (Monkawa et al., 2004).

1.2.1.4 Orthopyroxenite meteorite ALH 84001

ALH84001 is a coarse-grained cumulate orthopyroxenite martian meteorite, although it was formerly classified as a diogenite (Mittlefehldt, 1994). It is relatively homogeneous, which suggests it cooled more slowly than the shergottites, which often display complex zoning. An announcement of possible biogenic processes recorded in ALH84001 (McKay et al., 1996) resulted in a widespread increase in interest in martian meteorites, but the speculations are not considered adequately proved (Treiman, 2003).

1.2.1.5 Meteorite NWA 8159

Meteorite NWA 8159 is a martian augite basalt, composed primarily of augite pyroxene, plagioclase and maskelynite with small amounts of olivine, magnetite and orthopyroxene (Agee et al., 2014). Around half of the plagioclase has been converted to maskelynite glass due to shock, indicating that the peak shock pressures experienced were less than that experienced by the shergottites, which contain only the maskelynite phase. It is the second most magnetic martian meteorite, after NWA 7034.

1.2.1.6 Regolith breccias: NWA 7034 and pairs

Ejecta blankets around impact craters on Mars are gradually modified by heating, alteration and transport processes, leading to reprocessed rocks that have undergone multiple disruption and re-accumulation events (Melosh, 2011). Most impact ejecta do not travel more than two crater diameters from the source, with small impacts regularly overturning the top centimetre of surface material and less frequent larger impacts excavating and stirring up deeper lying material in a “gardening” process (Melosh, 2011). Therefore, the composition of ejecta regolith is thought to represent the composition of the local upper crust to surface. In the past, regolith on Mars accumulated at a much faster rate than today, because there was a greater flux of impact events (Golombek et al., 2006). The average surface impact velocity on Mars is 8.6 km s^{-1} , much lower than the average impact velocity on the Moon (16.2 km s^{-1} ; (Ivanov, 2001), so melting and vaporization should be less common on Mars than on the Moon.

Meteorite NWA 7034 and its pairs (NWA 7475, NWA 7533, NWA 7906, NWA 7907, NWA 8114, NWA 8171, NWA 10922, NWA 11220, NWA 11522 and Rabt Sbayta 003) are the first discovered regolith breccia meteorites from Mars. Lunar breccia meteorites are common, but higher escape velocities are needed for ejecta to escape

from Mars and the greater shock processes involved are more likely to disintegrate the breccia ejecta, which could explain the greater rarity of martian breccia meteorite finds on Earth.

The martian origin of meteorite NWA 8114 is confirmed by a trapped noble gas component similar to the modern martian atmosphere (Cartwright et al., 2014), together with oxygen isotope $\Delta^{17}\text{O}$ values that match and exceed those of other martian meteorites (Agee et al., 2013; Nemchin et al., 2014). The presence of meteoritic siderophiles (Ni, Ir) in the fine matrix have been taken to indicate a 5% component of carbonaceous chondrite material and provides evidence that this is a regolith (i.e., surface soil) breccia (Humayun, 2013). These meteorites provide the first opportunity to study regolith breccias from the surface or near-surface in the vicinity of an impact crater on Mars.

The paired stone, NWA 8114, classified at the University of Leicester, has been studied in detail for aspects of interest such as different clast types, any evidence for hydrothermal alteration, its thermal history and how brecciation occurred, as laid out in Chapter 3.

“These new Martian meteorite breccias are fiendishly complex rocks, and forthcoming investigations will surely reveal more surprises and conundrums. Detailed studies of the various types of breccia clast, including age dating and analysis of their geochemistry and petrology, could help to unravel the geological record of early Mars”, (McSween, 2013).

1.3 Why study comets?

Understanding how and where particles accreted to form the bodies in the Solar System, and the subsequent evolution of the system, is a key issue in the field of planetary science. Early ideas were that icy comets originate in the Kuiper Belt and Oort cloud in the outer Solar System under freezing low temperature conditions (Oort, 1950) and that unknown parent bodies of meteorites formed under high temperature conditions in the asteroid belt in the inner Solar System (Brearley & Jones, 1998).

However, *Stardust* comet grains contain refractory minerals formed at high temperature, including chondrule fragments and CAIs. Carbonaceous chondrites have a high volatile and water content. Thus, more complex mixing models are required to

explain these features and explain the origins of the Solar System. Determining the mineralogical compositions of these different and varied objects is one of the most important ways in which their formation can be constrained.

Chapter 4 analyses the mineralogy of cometary terminal grains captured by the *Stardust* mission and compares them with carbonaceous chondrites, using X-ray absorption spectroscopy and X-ray diffraction. Chapter 5 contains transmission electron microscopy investigations of a number of slices of seven different *Stardust* terminal grains. These investigations will add to previous studies of other particles, test the similarities to different types of carbonaceous chondrites and provide new information on the mineral composition of the comet and possible formation mechanisms.

1.3.1 Features of comets

Comets were observed in ancient times. Records of Halley's Comet date back to 240 BC and the first known picture of it appears in the Bayeux tapestry. However, it was not until 1705 that Edmond Halley calculated its 75 year period. Once comets were recognised to be astronomical objects, measurements were taken in order to observe their motion and orbits, but it was not until the middle of the 20th century that they were recognised as being ancient solar system objects.

Short period comets have orbits lasting less than 200 years with motion in the same direction as the planets, whereas long period comets have elliptical orbits in all directions that can be over a million years, and may extend hundreds of times further from the Sun than the orbits of the outer planets. Oort (1950) proposed a spherical cloud of objects from 50,000 AU extending out to 150,000 A.U. that explained the origin of long period comets, and became known as the Oort cloud. Short period comets were assumed to have been gravitationally altered by the planets, though the idea was not tested.

Kuiper (1951) estimated the mass of material in the protoplanetary disk and concluded that beyond Neptune there was a smooth distribution of material, insufficient to form a planet, that would have condensed to form billions of small icy bodies, like comets. This work suggested that comets must have condensed at low temperatures, ~10 K consistent with the Kuiper belt temperatures, and not in the asteroid belt as previously proposed (Oort, 1950). Gravitational perturbations from the planets would have ejected

the bulk of these icy bodies to form the Oort cloud, where stellar perturbations continued to alter their orbits to random inclinations, but the remainder form what we now know as the Kuiper belt.

Jupiter-family comets (JFCs) are thought to have originated in the scattered disk of the Kuiper belt and then moved inward, being scattered inward or outward by the nearest planet that has the strongest gravitational influence on it (Levison & Duncan, 1997). However, observational surveys suggest this source falls short of the number of comets required by theoretical models of the evolution from the Kuiper belt into Jupiter-family comets (Volk & Malhotra, 2008). This could indicate that other sources contribute to the Jupiter-family comets, that comets break up to form multiple fragments as they transition towards Jupiter, or that the current Jupiter-family comet population has fluctuated above the long term average (Volk & Malhotra, 2008). The lifetime of a Jupiter-family comet has been estimated using numerical orbital integrations of thousands of particles evolving from the Kuiper belt (Levison & Duncan, 1997). Comparing these simulations with observed JFCs suggests they are between 3000 and 30,000 years old, with 12,000 years as the most likely value, after which they are ejected from the Solar System, placed in the Oort cloud or collide with another body (Levison & Duncan, 1997).

The ‘dirty snowball’ model proposed that the nucleus of a comet was a conglomerate of ices such as water, methane, ammonia and carbon dioxide, combined with meteoritic materials (Whipple, 1950). Thus the observed acceleration of comet Encke was explained by the emission of vaporised volatile material in the opposite direction to its motion and the approximate mass loss was calculated (Whipple, 1950).

1.3.2 Comets visited by missions

1.3.2.1 Comet 1P/Halley

The first close-up images and measurements of comets were made by spacecraft when Halley’s Comet returned to the inner Solar System in 1986. The European Space Agency designed the *Giotto* mission, the Soviet Union launched *Vega 1* and *Vega 2*, and Japan sent the *Sakigake* and *Suisei* spacecraft. Collaboration and images from the *Vegas* that had a closest approach to the comet of ~8000 km, helped to allow *Giotto* to pass within 600 km of the nucleus safely.

Giotto images quickly confirmed that there was a solid nucleus at the heart of the comet (Fig. 1.4). Dust particle analysers on Giotto and Vega showed larger number of small particles ($<10^{-14}$ g) than expected, and that the particles are rich in C, H, O and N light elements, the first evidence of

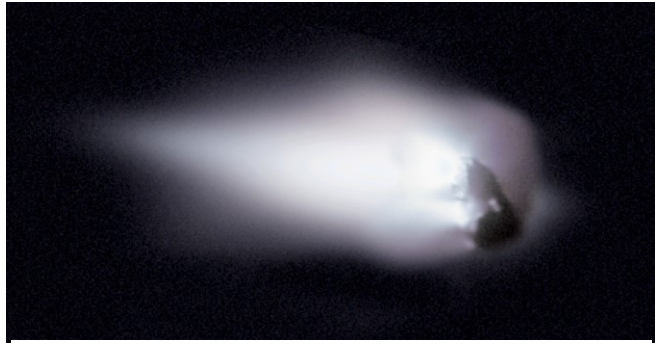


Fig. 1.4. The nucleus of comet Halley (~15km x 8km x 8 km) from the Giotto spacecraft as it passed within 600 km on 13 March 1986 (Image: ESA/MPAe Lindau).

organic material in comets (Kissel, Brownlee, et al., 1986; Kissel, Sagdeev, et al., 1986). Silicate-like grains and particles of mixed composition were also detected, showing that the comet nucleus was heterogeneous (Clark et al., 1987). These results confirmed the cometary material was the most primitive material encountered in the Solar System.

Infrared detectors on Vega 1 detected temperatures of over 300 K from an emissive centre a few kilometres in size, and also detected H₂O and CO₂ (Combes et al., 1986; Emerich et al., 1987). Giotto's ion mass spectrometer measured temperatures of ~340 K and outflow velocities of ~1 kms⁻¹, together with a large C⁺ abundance throughout the coma, but relatively low abundance of nitrogen (Balsiger et al., 1986).

1.3.2.2 Comet 19P/Borrelly

The Jupiter-family comet 19P/Borrelly has an orbital period of 6.85 years and is approximately 8 x 4 x 4 km in size. It was visited by NASA's *Deep Space 1* spacecraft in 2001 eight days after perihelion (~1.36 A.U.), returning the best images from a comet at that time. The spacecraft's closest approach was ~2170 km with a relative speed of 16.5 kms⁻¹ (Boice et al., 2000). Infrared spectra showed a dry surface with a temperature of ~345 K. No impact craters over 200 m in diameter were seen, indicating an active young surface (Boice et al., 2000). The main dust jet was found to be aligned with the rotation axis of the nucleus (Boice et al., 2000).

1.3.2.3 Comet 9P/Tempel 1

Jupiter-family comet 9P/Tempel 1, with an orbital period of 5.5 years, was the target for NASA's *Deep Impact* spacecraft. Built in two sections, the high speed 364 kg "smart" impactor excavated a crater in the comet nucleus on 4 July 2005, while the

flyby section took images and measurements from a safe distance with a closest approach of 500 km (Blume, 2005). Follow-up images were taken by the Stardust-NExT mission in 2011 (Fig. 1.5).

Around 10^4 tons of material was excavated, and showed signs of layering. More than half of the material consisted of water ice (A'Hearn & Combi, 2007). The comet's bulk density was estimated to be 400 kgm^{-3} , indicating that the nucleus is highly porous and the material strength is less than bulk ice (A'Hearn & Combi, 2007).

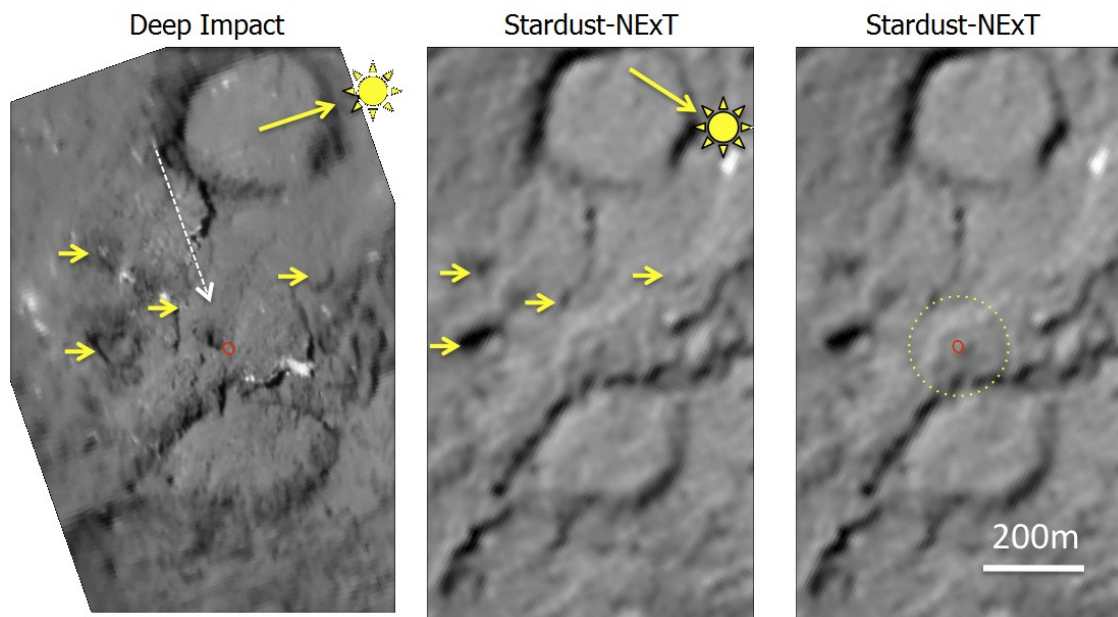


Fig. 1.5. Comparison of an image from the Deep Impact spacecraft of comet Tempel 1 immediately before the impact event (red oval) in 2005, with an image from the Stardust-NExT mission taken six years later from a distance of 178 km. Yellow arrows show the same features on the different images. (Image: NASA/JPL-Caltech/Cornell/Univ. of Maryland).

The Deep Impact spacecraft was repurposed with two further sub-missions that became known as the EPOXI (Extrasolar Planet Observation and Deep Impact Extended Investigation) mission.

1.3.2.4 Comet 103P/Hartley 2

Comet 103P/Hartley 2 is a small (< 1.6 km diameter) Jupiter-family comet with an orbital period of 6.46 years (Fig. 1.6). Remote sensing showed it to be hyperactive, releasing more gas at perihelion than comet Tempel 1, despite its radius being five times smaller (A'Hearn et al., 2011). On 4 November 2010, the EPOXI mission flew by the comet with a closest approach of 694 km and a speed of 12.3 kms^{-1} (A'Hearn et

al., 2011). Chunks of particles over a few cm in size were detected by the radar, all within 15 km of the large end of the nucleus, moving relatively slowly, with 20% moving at less than their local escape velocity (A'Hearn et al., 2011).



Fig. 1.6. Comet Hartley 2 imaged by NASA's EPOXI mission. The nucleus is ~2 km long and 0.4 km at the most narrow portion. (Image: NASA/JPL-Caltech/UMD).

1.3.2.5 Comet 81P/Wild 2

NASA's *Stardust* spacecraft collected cometary dust at a distance of 234 km from the nucleus of comet 81P/Wild 2 as well as interstellar

particles on the journey, and returned them to Earth on 15 January 2006 (Brownlee et al., 2006). *Stardust* grains are the first comet samples to be returned to Earth and offer the potential to ground-truth many theories offered from measurements from remote sensing telescopes (both in space and on Earth) and other spacecraft missions, such as Giotto and Rosetta. See Chapters 4 and 5 for detailed analysis of *Stardust* grains.

1.3.2.6 Comet 67P/Churyumov–Gerasimenko

ESA's Rosetta spacecraft launched in 2004 and, together with the Philae lander, arrived at comet 67P/Churyumov–Gerasimenko in August 2014 and studied it until the end of mission with Rosetta crashing onto the comet on 30th September 2016. On 12 November 2014, the Philae lander made two bounces, due to the failure of harpoons and thrusters, before making the first ever landing on a comet nucleus. It managed to deploy most of the instruments and return data for up to three days, but then had insufficient power to continue communicating. Philae was eventually located in a crack on its side, explaining why it was difficult for the solar panels to gain any power. However, by finding and imaging the lander on 2nd September 2015, the scientists now have the context to interpret data returned from the instruments.

Comet 67P did not have sufficient gravity to capture the Rosetta spacecraft, so a complex trajectory was constantly monitored and modified, which sometimes brought the spacecraft as close as 3 km to the surface. A mosaic of images by ESA (Fig. 1.7) shows a fraction of the enormous wealth of data gathered by this two year dedicated mission. Some of the key findings are summarised below, out of the hundreds of papers already published using data from this mission.

The discovery that comet 67P is a binary comet was unexpected, the smaller lobe measuring 2.6 x 2.3 x 1.8 km and the larger 4.1 x 3.3 x 1.8 km with a volume of $\sim 19 \text{ km}^3$ and a mass of $\sim 9980 \times 10^9 \text{ kg}$ (Taylor et al., 2017). It is thought to have formed from the gentle collision of two comets, each about 1 km each in size, about 4 billion years ago. Complex topography was imaged, of cliffs, canyons, boulders, bumps, inky pits, fine fractures, indicating a number of different geological processes taking place. Long term monitoring has shown that the shape of the comet influences seasons, moves dust, and helps explain variations in density and composition of the coma (Taylor et al., 2017).

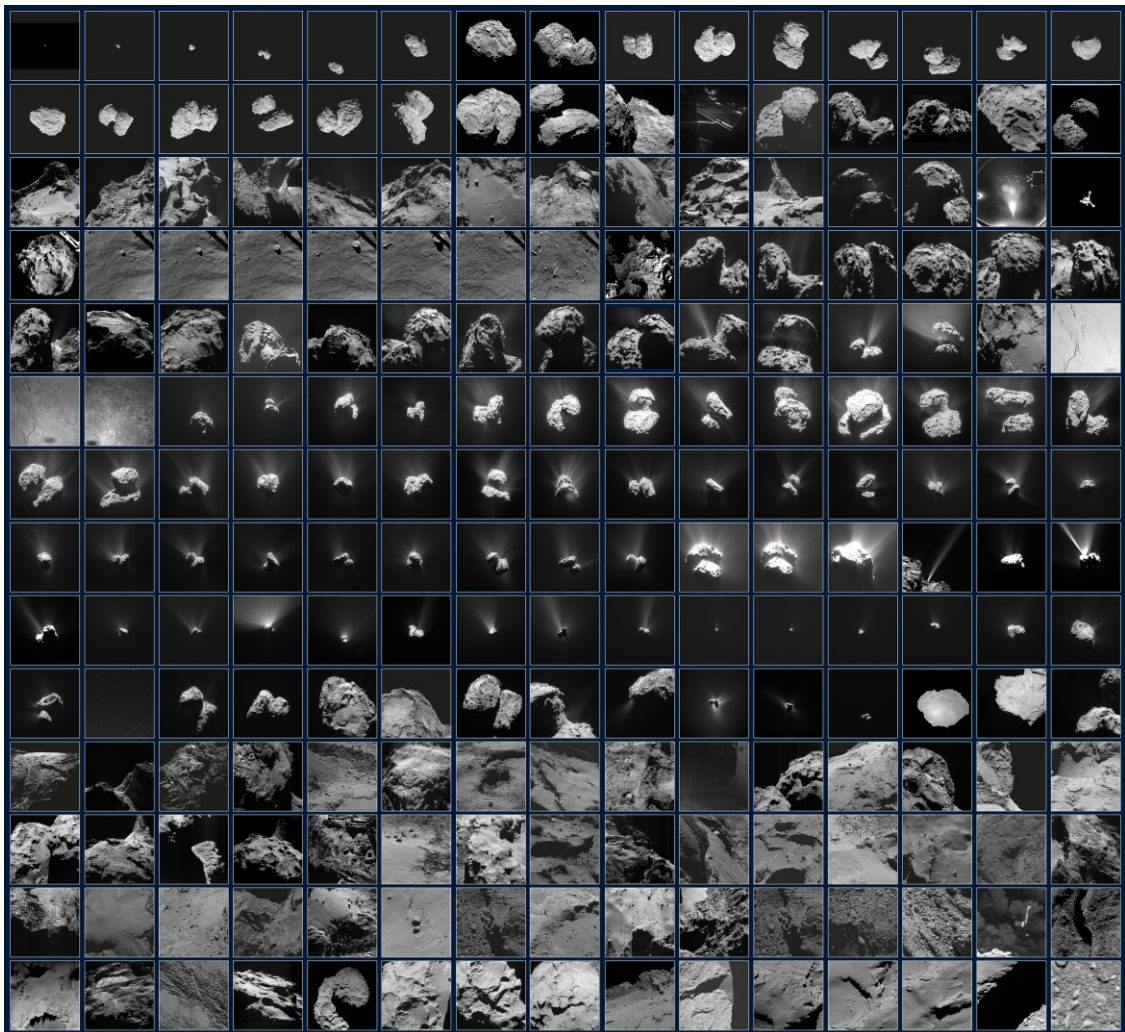


Fig. 1.7. 210 images from Rosetta of comet 67P/Churyumov-Gerasimenko between July 2014 and September 2016. ESA/Rosetta/NavCam CC BY-SA IGO 3.0; ESA/Rosetta/MPS for OSIRIS Team MPS/UPD/LAM/IAA/SSO/INTA/UPM/DASP/IDA; ESA/Rosetta/Philae/CIVA; ESA/Rosetta/Philae/ROLIS/DLR

Molecular oxygen was found throughout the nucleus, and it did not vary with heliocentric distance (Bieler et al., 2015). This indicates that the comet formed in a very cold region far from the sun, for primordial O₂ to be trapped into the nucleus during formation (Bieler et al., 2015). The water in comet 67P has a deuterium-hydrogen ratio of $(5.3 \pm 0.7) \times 10^{-4}$, which is ~ 3 times the terrestrial value (Altwegg et al., 2014), ruling out the delivery of Earth's ocean water from this particular comet, though this ratio might vary for different comets. Comet 67P has been found to contain more organic compounds than previously known in a comet, including ethanol, glycolaldehyde and glycine, an amino acid commonly found in proteins and phosphorus, a key component of DNA and cell membranes (Biver et al., 2015).

The Rosetta mission has confirmed that Jupiter-family comet 67P, like comet Wild 2, comprises both volatile ices from very cold formation regions and some minerals from the inner hot protoplanetary disk (Fulle et al., 2016).

Future possible and planned cometary missions are discussed in Chapter 6.

1.3.3 Relationships between carbonaceous chondrites and comets

Carbonaceous asteroids are the potential parent bodies of carbonaceous chondrites (CC), which are found today in the outer asteroid belt, within Jupiter's orbit. Distinct isotopic characteristics show different origins for CC parent bodies compared with ordinary chondrites (OC) parent bodies (Budde et al., 2016; Kruijjer et al., 2017). Desch et al. (2018) proposed that carbonaceous asteroids originally formed further out, beyond a pressure gap caused by Jupiter's core formation in the early protoplanetary disk, and were later perturbed inward to their present positions by Jupiter's outward migration (Desch et al., 2018). This model offers explanations for carbonaceous chondrites having a greater content of volatiles and carbonaceous aluminium inclusions (CAIs) than OC, and for OC, formed within Jupiter's orbit, being depleted in CAIs due to aerodynamic drag causing them to spiral into the Sun (Desch et al., 2018).

The greater volatile content of carbonaceous chondrites, together with initial results from the *Stardust* mission identifying chondrules fragments and CAI-like material, suggest similarities between carbonaceous chondritic material and comet Wild 2 explored further in Chapter 4.

2 TECHNIQUES

This chapter introduces the theory and details of the instruments that have been employed to study the planetary samples included in this thesis. Optical and electron microscopes at the University of Leicester and University of Nottingham have been used, together with electron probe microanalysis (EPMA) at the Open University. Synchrotron techniques including X-ray absorption spectroscopy (XAS), X-ray fluorescence (XRF), X-ray diffraction (XRD) and Fourier-transform infrared spectroscopy (FTIR) have been carried out using the I-18 and B-22 beamlines at the *Diamond Light Source*. ^{40}Ar - ^{39}Ar dating methods for small samples have been carried out in collaboration with colleagues at the University of Manchester.

All these techniques were used on the martian breccia (Chapter 3) to investigate different aspects of its mineralogy, determine the location of any hydrated phases and link these to ages in its evolution.

Synchrotron beam lines were used to study *Stardust* tracks and carbonaceous chondrite tracks in aerogel kestones (Chapter 4) in order to identify mineral phases and oxidation states from XRF, XAS and XRD by comparing with reference materials. The grains were too small for scanning electron microscopy.

A scanning electron microscope (SEM), scanning transmission electron microscope (STEM) and electron dispersive X-ray (EDX) spectroscopy were used to image and examine the mineralogy of slices of *Stardust* terminal grains (Chapter 5).

2.1 Optical and reflected light microscopy



Fig. 2.1. Olympus DP70 optical microscope.

An Olympus DP70 optical microscope (Fig. 2.1) was used to take images of NWA 8114 grains and *Stardust* grain tracks. It uses visible light and a range of lenses to provide different magnifications and has the option to either view directly or on a computer screen. The resolution of the optical microscope is limited by the wavelength of light, thus the best theoretical resolution with the shortest wavelength of visible light (~ 400 nm) is approximately $0.2 \mu\text{m}$ (Fellers & Davidson, 2014). This allows for magnification up to 1000 times.

Reflected light microscopy was also used, which shows contrasting regions of these samples from differences in reflectivity and topography from different phases and grain sizes. These images are particularly useful at the *Diamond Light Source* synchrotron in order to find specific locations for analysis.

2.2 Electron microscopy

This section describes the scanning electron microscope (SEM), electron probe microanalysis (EPMA), a focused ion beam scanning electron microscope (FIB-SEM) and transmission electron microscopy (TEM). EDX quantification theory for all of the above is then discussed.

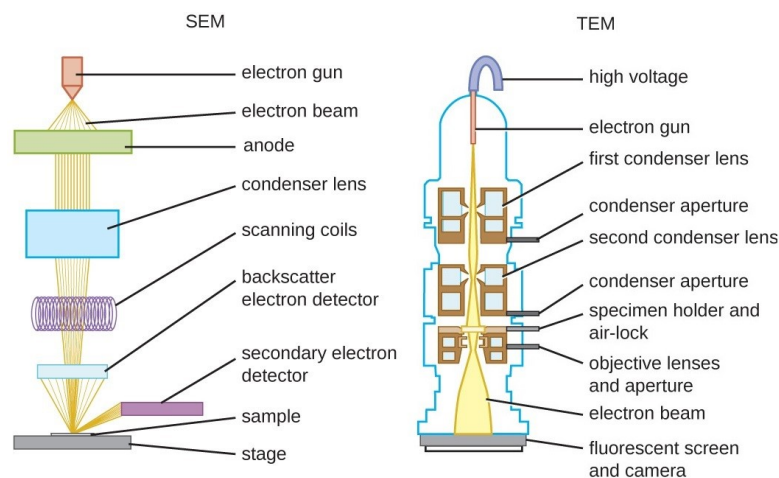


Fig. 2.2. Schematics showing the main features of a scanning electron microscope (SEM) and transmission electron microscope (TEM) (OpenStax, 2018).

In order to achieve superior resolution over optical microscopes, electron microscopy is used, as the wavelength of electrons is $\sim 10,000$ times shorter than visible light, allowing resolution to reach the order of 0.1 nm (Leng, 2010). Whereas optical microscopes use lenses to focus light, electron microscopes use electromagnets to focus electrons. The main features of an SEM and a TEM are shown in Fig. 2.2.

2.2.1 Scanning electron microscope (SEM)

A scanning electron microscope (SEM) optimised for imaging can achieve spatial resolution of less than 10 nm. Using an SEM is advantageous as sample preparation is straightforward, the time per analysis and time to change samples is short and the technique is non-destructive (Reed, 2005). The ways in which the electron beam can interact with the sample are described below.

In order to ionise an atom, the incoming electron must have minimum energy at least equal to the binding energy of the relevant shell of the target element, which varies approximately with the square of the atomic number of the emitting element via Moseley's Law. The energy necessary to excite a given X-ray line is always slightly greater than the corresponding characteristic X-ray emission line. Therefore, the accelerating voltage must be greater than this, to obtain reasonably intense X-ray emission and a range of 5 kV to 30 kV is suggested (Reed, 2005). However, higher voltages giving greater X-ray emission also limits the resolution obtainable.

A tungsten element in the electron gun is heated to ~ 2700 K, liberating electrons from the surface. A grid placed near the tip of the element limits the effective emitting area and a beam of ~ 50 μm diameter is produced. This is focused further, to ~ 2 nm in the highest performing SEMs, by a series of electromagnetic lenses, usually two condenser lenses and one objective lens. A lens produces a magnetic field by containing a copper wire that carries a current. The magnetic field is exposed to the electron beam at a specific gap in the iron shroud that otherwise contains the copper wire and magnetic field and this focuses the beam towards the centre. The condenser lens settings can be adjusted to alter the beam diameter, which is also known as the spot size.

The beam penetrates and interacts with the sample to a depth of approximately 1 μm , forming an interaction volume. The interaction volume increases with increasing beam

energy, and decreases as the average atomic number of the specimen increases. Low energy secondary electrons (SE) can be liberated from the outer orbitals of the atoms in the sample near the surface, and the detection of these produces an image showing topographic contrast. Higher energy back scattered electrons (BSE) are elastically scattered, with a larger proportion being scattered at high-angle from material with a higher atomic number (Z). Thus, greyscale BSE images range from white atomically heavier areas, to dark grey atomically lighter areas, allowing qualitative estimates of the composition to be made by observation. BSE are emitted from much larger depths than SE.

Quantitative energy-dispersive X-ray spectroscopy analysis (EDX) allows the proportions of each element in the sample to be measured. The EDX detector is a semiconductor, usually silicon or germanium, with fully occupied valence bands. The X-ray photons emitted from the sample cause ionization in the detector by raising electrons from the valence to the conduction band. These pulses are amplified giving output pulses proportional to the photon energy and averaged over a time interval (a few μs) to minimise noise. This process time is the ‘dead-time’, during which the system does not respond to further pulses from the detector. An EDX spectrum is produced as a plot of intensity (number of counts) against the X-ray energy, where the peaks are characteristic of a particular element (Fig. 2.3). All elements

with atomic number greater than 3 can be detected.

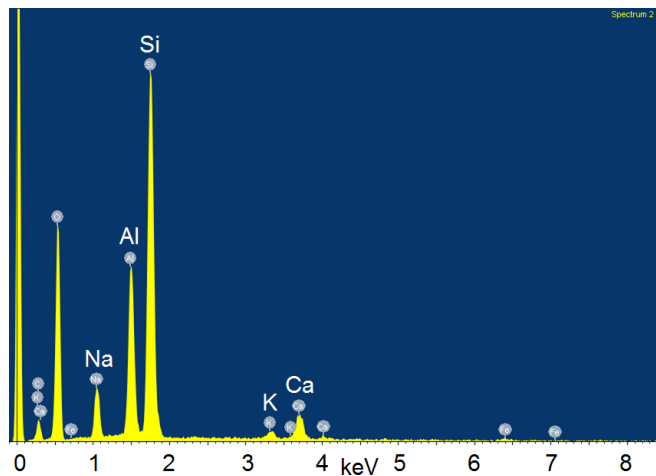


Fig. 2.3. Example spectrum with sodium, aluminium, silicon, potassium and calcium peaks, identified as feldspar $\text{Ab}_{63.9}\text{An}_{28.6}\text{Or}_{7.5}$.

Detection limits are typically 1000 ppm but can be reduced using long counting times (UCR, 2018). The overall analytical accuracy is usually $\pm 1\%$ accuracy for major elements. Accurate mass absorption coefficients are needed to correct for absorption effects (Friel, 2003). Further corrections are required for fluorescence and atomic number in the sample and continuum X-rays which are generated from inelastic

scattering of beam electrons (a major source of background and dead time). Further inaccuracies exist due to physical factors such as imperfectly polished surfaces, variation in carbon coating thickness, uncertainties in the composition of standards to which the SEM is calibrated etc.

A Philips XL30 (Hainsworth, 2014) environmental SEM and a Hitachi S-3600N environmental SEM (Wilson, 2014) with Oxford INCA 350 EDX spectroscopy system at the Advanced Microscopy Centre at the University of Leicester were used for characterisation work. A Sirion 200 Field Emission Gun Scanning Electron microscope (FEGSEM) and Princeton Gamma Technology Spirit EDX analysis system at the University of Leicester were used to initially survey the *Stardust* TEM grids (Chapter 5). This is capable of a resolution of 1.5 nm at 10 kV.

Samples examined were either polished thin sections on glass slides, or polished resin blocks, in order to minimise any topographic effects and reduce secondary excitation processes. Although the SEM is operated under vacuum with pressure below 10^{-4} mbar, the sample also needs to be earthed to reduce any possible charging effects. The samples were either given a thin coating of carbon, ~15 nm, or metallic tape or paint linked the edges of the sample to the metal base in the microscope chamber.

Back-scattered electron (BSE) images and EDX spectroscopy element data for point analyses were obtained using an accelerating voltage of 15 kV or 20 kV, giving current of ~70 μ A in order to produce a small spot size while keeping sufficient resolution. A working distance of 6 mm to 10 mm was used for imaging, and the minimum working distance of 10 mm was used for EDX, which is the closest the detector can be to the sample without physical obstruction. During this study EDX analysis times used were all over 50 seconds. The INCA system provides quantitative analysis of each EDX spectrum giving atomic%, weight% and compound%, combined with oxygen by stoichiometry and normalised to 100%, assuming the material to be anhydrous. Carbon was excluded as the samples were carbon coated.

2.2.2 Electron Probe Microanalysis (EPMA)

SEM-EDX was used extensively to survey the martian sample in chapter 3 as it is more convenient and faster. However, for greater accuracy for the quantitative analysis,

Electron Probe Microanalysis (EPMA) with Wavelength Dispersive Spectrometry (WDS) provides higher spectral resolution and lower detection limits.

The WDS has three crystal spectrometers enabling the measurement of elements from fluorine upwards in the periodic table. A diffraction crystal with lattice spacings (d -spacings) will scatter the incident X-rays from the sample and reflect a specific selected wavelength ($n\lambda$) towards the detector. The angle of incidence of the X-rays to the crystal (θ) determines the wavelength selected, using Bragg's Law:

$$n\lambda = 2d\sin\theta \quad 2.1$$

The wavelength selected corresponds to the X-ray quantum energy of the element being measured in the sample (Reed, 2005).

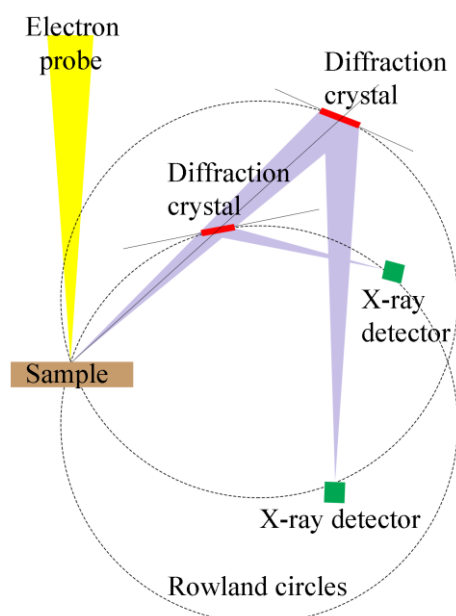


Fig. 2.4. Schematic of the electron probe microanalysis instrument with the positions of the crystals and X-ray detectors at particular angles in relation to the sample.

The sample, crystal and detector lie on a Rowland circle, this allows a constant Bragg angle to be obtained (Fig. 2.4). The crystal is moved in a straight line away from the sample and rotated to stay tangential to the Rowland circle. As it moves it can reflect a range of different selected wavelengths. The detector is also moved by a corresponding amount so that it receives the diffracted X-rays and stays on a Rowland circle relative to the sample and crystal. Angles of incidence from $\sim 13^\circ$ to $\sim 55^\circ$ allow a range of K-alpha -ray energies to be detected for different elements.

Moseley showed that a plot of atomic number Z versus the square root of the frequency of characteristic X-rays from the elements gives a straight line. Using the Bohr model, Moseley's empirical relationship is:

$$E = \frac{hc}{\lambda_{\kappa\alpha}} = h\nu_{\kappa\alpha} = 13.6 \text{ eV} (Z - 1)^2 \left[\frac{1}{1^2} - \frac{1}{2^2} \right] = \frac{3}{4} 13.6 (Z - 1)^2 \text{ eV} \quad 2.2$$

where E is energy (eV), h is Planck's constant (4.136×10^{-15} eVs), c is the speed of light (2.998×10^8 m s⁻¹), λ is the wavelength and $\nu_{\kappa\alpha}$ is the frequency of the K-alpha X-ray energy of the element.

The crystal spectrometers used for EPMA in this thesis utilised TAP, PET and LiF crystals, with their d -spacings, detectable wavelength and detectable element ranges given in Table 2.1. LTAP and LLiF spectrometers (large versions) were also used, that are designed to provide more counts by having a larger crystal area, in order to produce lower detection limits. It can be seen that the crystals overlap, e.g. Si ($Z=14$) can be measured by PET or by TAP. The Si $K\alpha$ line is reflected at 55.4° by PET and by 16.1° by TAP. The crystal giving the smaller Bragg angle (larger d -spacing) is usually preferable as it gives higher intensity, although poorer resolution (Reed, 2005). The final column of the table shows the elements of interest in order to accurately characterise the planetary materials examined in this thesis.

Table 2.1. EPMA crystal spectrometers with their lattice spacing, detectable wavelengths and corresponding elements (Reed, 2005).

Crystal	2d (Å)	Range of λ (Å)	Range of Z	Elements of interest
TAP Thallium acide phthalate	25.9	6.5 – 20.0	${}_9\text{F} - {}_{15}\text{P}$	F, Na, Mg, Al, Si
PET Pentaerythritol	8.742	2.2 – 7.1	${}_{14}\text{Si} - {}_{25}\text{Mn}$	P, S, Cl, K, Ca, Ti
LiF Lithium Fluoride	4.026	0.9 – 3.3	${}_{21}\text{Sc} - {}_{37}\text{Rb}$	Mn, Fe

EPMA data were obtained for different phases in three sections of the martian breccia studied in Chapter 3, using a Cameca SX100 at the Open University, a focused 1 μm beam, at an accelerating voltage of 20 kV and beam current of 20 nA. A JEOL 8600 S automated electron microprobe equipped with a wavelength-dispersive spectrometry (WDS) system at the University of Leicester was also used.

2.2.3 Focused ion beam (FIB)

An FEI Quanta 200 3D dual Focused Ion Beam (FIB-SEM) was used to prepare wafers from specific regions of interest in polished sections, for viewing in the transmission electron microscope (TEM). Wafers need to be less than 100 nm thick to be electron transparent, so that absorption and fluorescence effects are negligible and can be ignored.

The dual beam system has the ion beam column positioned at 52° with an electron beam perpendicular to the sample surface, allowing the same feature to be investigated with both beams simultaneously and to target the exact location desired for the TEM sample. The sample is raised to eucentric height and can be tilted for observations in either beam at different angles.

To overcome the binding energy of the material comprising the sample surface, a liquid metal ion source of gallium (Ga^+) is used by the ion beam. The target wafers were first capped with a ~ 150 nm thick protective Pt layer, to reduce Ga^+ contamination of the sample, following the methods of Changela and Bridges (2010). A FIB milling procedure (Hicks, 2015) used the Ga^+ ion beam to mill and extract wafers measuring $5 \times 15 \mu\text{m}$ at 30 kV, using currents from 5 nA to less than 100 pA (Fig. 2.5A,B). The FIB-SEM carbon gas injection system (GIS) was used to weld an *Omniprobe* W probe tip microneedle to the wafer, which was then cut free using the Si application (Fig. 2.5C). The carbon GIS was then used to weld the wafer to a TEM copper grid and then the Si application cut the needle tip free. The wafer was subsequently thinned to be less than 100 nm thick, using a current of 0.10 nA (Fig. 2.5D).

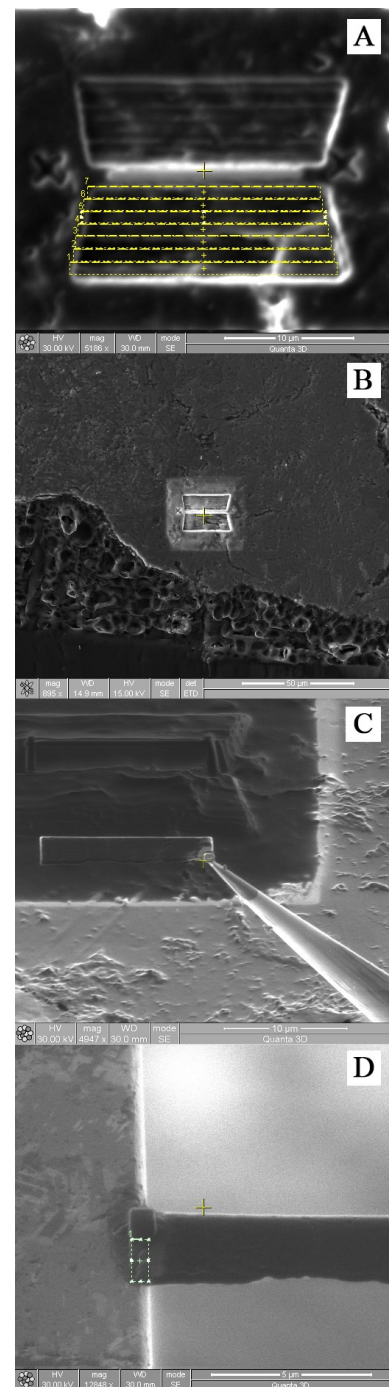


Fig. 2.5. (A) Milling the trench in strips in an NWA 8114 pyroxene grain. (B) Context image of wafer location. (C) Wafer being lifted out, on the Omniprobe tip. (D) Attaching the wafer to the copper grid.

2.2.4 Scanning Transmission Electron Microscopy (STEM)

The transmission electron microscope (TEM) allows spatial resolutions of less than 1 nm to be achieved due to the short wavelength of the electrons, comparable to the atomic scale. This enables the crystal lattice structure to be identified and understood.

The electron wavelength λ can be related to the accelerating voltage by using de Broglie's relationship between particle momentum, $p = m_0v$, with Planck's constant h : $\lambda = \frac{h}{p}$, the kinetic energy eV which is equal to the potential energy, the electron mass m_0 and velocity v , to give:

$$\lambda = \frac{h}{(2m_0eV)^{\frac{1}{2}}} \quad 2.3$$

However, at the energies involved, relativistic effects must be taken into account, which modifies equation 2.3 to:

$$\lambda = \frac{h}{\left(2m_0eV \left(1 + \frac{eV}{2m_0c^2}\right)\right)^{\frac{1}{2}}} \quad 2.4$$

Using equation 2.4 for an accelerating voltage of 200 kV, the electrons have a mass of 1.391 m_0 (where $m_0 = 9.109 \times 10^{-31}$ kg), velocity of 2.086×10^8 m s⁻¹ and relativistic wavelength of 0.00251 nm (Williams & Carter, 2009b). The electrons are liberated by the lanthanum hexaboride (LaB₆) thermionic source at the top of the TEM. LaB₆ has a melting point of 2210 °C and one of the highest electron emissivities known.

For static beam TEM imaging, the lenses and apertures are used to select a portion of electrons for viewing. The electrons pass through two condenser lenses and apertures and the sample. An objective lens and aperture then project the image onto the viewing screen at the bottom (Fig. 2.2). Electrons from the direct beam give bright-field (BF) images, showing heavier elements as darker areas (the inverse of an SEM image), whereas scattered-electrons result in dark field (DF) images. By changing the objective aperture or adjusting the beam tilt, BF or DF images can be obtained.

Scanning transmission electron microscope (STEM) imaging allows capture of BF and DF images simultaneously, and as imaging lenses are not used, chromatic aberration

does not occur in STEM images. However, the time taken to scan an image is much longer than static beam imaging.

STEM mode

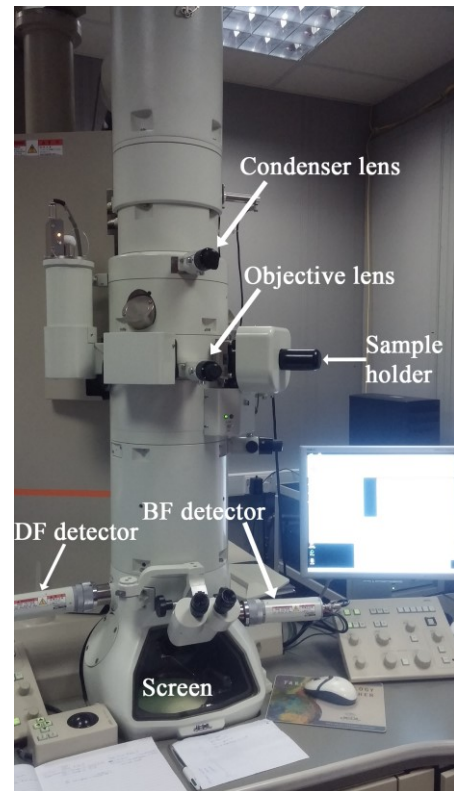
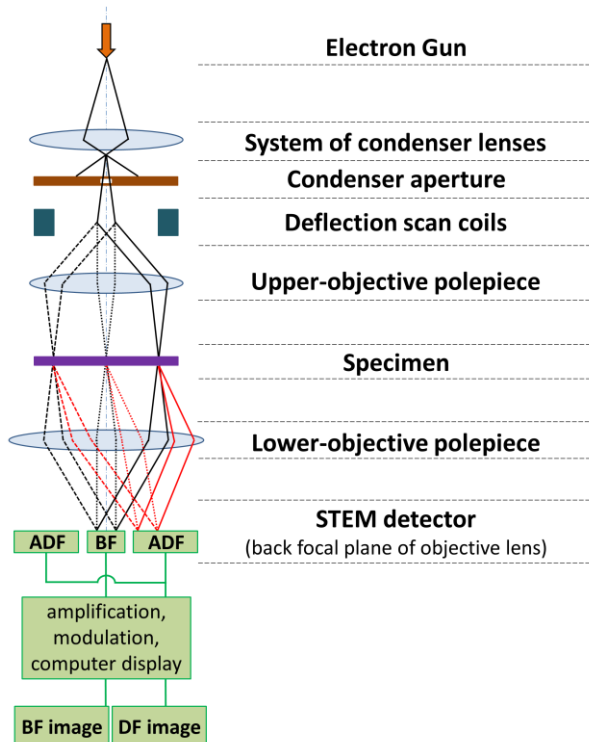


Fig. 2.6. (A) Schematic of scanning transmission electron microscope (STEM) imaging mode showing the deflection scan coils and the positioning of bright field (BF) and annular dark field (ADF) detectors (Tubus, 2017). (B) JEOL 2100 LaB6 TEM at the University of Leicester.

Two pairs of scan coils are used to control the beam and keep it parallel to the optic axis at all times (Fig. 2.6A). Simultaneously the coils are used to scan and build up the image on the cathode ray tube (CRT) computer display, thus requiring no lenses (Williams & Carter, 2009b).

Two detectors are inserted in a plane conjugate to the diffraction pattern, below the projector lens, above the screen. An annular DF detector (ADF) collects and amplifies the signal of the scattered electrons and allows a BF detector to sit in the middle, to collect the direct electron signal (Fig. 2.6).

The wafers extracted from NWA 8114 using the FIB (Chapter 3.2.2), and *Stardust* microtomed samples provided on TEM grids (Chapter 5), were analysed on a JEOL 2100 LaB6 transmission electron microscope (TEM) with scanning-TEM (STEM)

facilities and an Oxford Instruments system with AZtec energy dispersive X-ray (EDX) at the University of Leicester or at the University of Nottingham (Fig. 2.6B). All TEM, STEM and EDX work was carried out using an accelerating voltage of 200 kV and beam current of $\sim 110 \mu\text{A}$. Magnifications used were generally between $\times 20,000$ and $\times 150,000$.

The TEM was set up to ensure the beam is correctly aligned by adjusting the apertures and condenser lenses, and the sample is in focus at the eucentric height, following the steps described in Hicks (2015). Some EDX spectrums for Chapter 3 were taken by spreading the beam at the location of interest, though the majority and all EDX for Chapter 5 were taken in STEM mode. AZtec software supplied quantitative analysis of the atomic %, oxide % and weight % that was extracted to spreadsheet. For more details of EDX quantitative analysis see the next section.

2.2.5 Energy dispersive X-ray (EDX) quantitative analysis

The basis for quantitative X-ray analysis started with using a focused electron beam (Hillier & Baker, 1944). Castaing (1951) developed methodology for how to obtain quantitative data, when using a focused electron beam on a sample. The concentration C_i of an element i in the sample is assumed to be proportional to the intensity I_i of the characteristic X-rays for that element that emerge from the sample. As the intensity is very hard to measure, we instead measure the ratio I_i / I_j for a standard with known concentration C_j , where I_j is the intensity emerging from the standard.

$$\frac{C_i}{C_j} = K \cdot \frac{I_i}{I_j} \quad 2.5$$

Due to the absorption (A) and fluorescence (F) of X-rays within the specimen, and depending on its atomic number (Z), there will be some difference between the measured and generated X-ray intensities for both the sample and the standard. This is accounted for by a sensitivity factor (not a constant), K, which also varies according to the kV and the system used. This theory forms the basis of the essential procedures used in the EPMA (Williams & Carter, 2009a).

To measure a standard and then an unknown sample in a transmission electron microscope (TEM), the beam would have to be switched off and on in between the two

analyses. This would make accurate comparison impossible due to fluctuation in the probe current and variations from electron gun instabilities and drift. However, as characteristic intensities can be measured for more than one element simultaneously, there is no need for a standard (Cliff & Lorimer, 1975). Thus equation 2.5 can be rewritten for a sample containing elements A and B, with weight percent $C_A + C_B = 100\%$, as:

$$\frac{C_A}{C_B} = K_{AB} \cdot \frac{I_A}{I_B} \quad 2.6$$

For a sample with more than two phases, each can be calculated provided the relevant K-factors are known. By using an electron-transparent sample rather than a bulk specimen, absorption and fluorescence can be ignored, thus K_{AB} is only related to a correction for the atomic number, Z .

K-factors can be derived theoretically, or experimentally. For experimental determination, a standard should preferably be single phase and well characterised, thinned to electron transparency without undergoing chemical changes and should have no significant absorption or fluorescence. The thin foil should be stable under the beam and long count times should be used for good statistics. An experimental calibration of the K-factors is conducted in the next section.

The Oxford INCA 350 EDX system software controlling the SEM produces spectra in both graphical and numerical form, giving atomic weight %, compound weight % and oxide weight %, which can be output for each site into a spreadsheet. Data processing proved laborious and error prone given each site has a varying number of identified elements and a different number of spectra taken, and ratio calculations need to be manually input for each batch of SEM data.

Python programmes were written to aid data processing. One transforms the format of SEM raw at% data from different sample sites from INCA software so that the same element can be compared at different sites easily. A second programme was written to transform the TEM EDX output data from AZtec software similarly.

2.2.6 Experimental calibration of K-factors for STEM-EDX

A JEOL 2100 TEM with AZtec EDX system was used with an accelerating voltage of 200 kV and beam current of $\sim 110 \mu\text{A}$ for STEM bright field (BF) and dark field (DF) imaging as described in section 2.2.4. The density was set as 3.2 g cm^{-3} , suitable for silicate minerals, and the thickness as 80 nm, in line with the average thickness of ultramicrotomed sections assumed by Leroux et al. (2008). The typical errors for major elements (O, Si, Mg, Ca and Fe) are 2% and for minor elements (Cr and Mn) are 20%.

The following elements detected were ignored in the analyses, as they were most likely to be the result of analysing the aerogel material, the copper TEM grid or other materials used in the sample preparation process rather than the sample: Cu, Ga, Au, C, F.

K-factors are the sensitivity factors that account for the difference between measured and generated X-ray intensities due to an element's atomic number, which are discussed in detail in the previous section. K-factors are measured as ratios; for example, where the relative concentrations of element x and Si are proportional to the relative intensities I_x and I_{Si} respectively, the Cliff-Lorimer equation (2.6) is adapted to:

$$\frac{C_x}{C_{Si}} = \frac{K_x}{K_{Si}} \cdot \frac{I_x}{I_{Si}} \quad 2.7$$

Reference materials with known compositions were examined with STEM-EDX to ensure the settings used were appropriate. Electron probe microanalysis (EPMA) point measurements were previously recorded on focused ion beam (FIB) extractions of San Carlos olivine (Mg# 91), NWA 5790 olivine (Mg# 34), NWA 5790 pyroxene ($\text{En}_{34}\text{Fs}_{26}\text{Wo}_{40}$), and magnetite, (Table 2.2), where $\text{Mg\#} = 100 \text{ Mg} / (\text{Mg} + \text{Fe})$. EPMA data for the reference standards was provided by L. Hicks, obtained from a Cameca SX100 at the Open University in July 2011, using a $10 \mu\text{m}$ defocused beam, an accelerating voltage of 20 kV and beam current of 20 nA. Further details of this instrument are in section 2.2.2. These FIB wafers were examined with STEM-EDX and the results discussed in the next section.

STEM-EDX data were taken with the default AZtec settings using a thirty second count time and averaged for seven or eight data points taken at different locations on the

reference material. The atomic% for both STEM-EDX and EPMA data on the reference materials is shown in Table 2.2.

NWA 5790 Fe-rich olivine with Mg# 34 (EPMA) shows high Mg and low Fe atomic% for the STEM-EDX data, where the average of seven data points gives a Mg# of 40, using the default software Fe K-factor of 1.21 (first line, Table 2.2). The stoichiometry shown by the Si/O ratio as being 0.26 was reasonable for olivine $(\text{Mg,Fe})_2\text{SiO}_4$. This suggests a possible problem with the K-factors used for Mg and/or Fe.

Examining the San Carlos Mg-rich olivine with Mg# 91 (EPMA), the STEM-EDX measurement of Mg# 90 was a close match. This suggested that the default software Mg K-factor of 1.04 was calibrated correctly (Table 2.2).

The default Fe K-factor of 1.21 was compared with other work that used similar 200 keV settings, $K_{\text{Fe}} = 1.35$ (Williams & Carter, 2009a) and work that used similar calibration minerals, $K_{\text{Fe}} = 1.36$ (Changela, 2011). These indicated that it was too low (Table 2.3). Setting the Fe k-factor to 1.32 yielded the rest of the data (Table 2.2), which has reduced the difference between the EPMA and STEM-EDX data, and resulted in a Mg# of 38 for the NWA 5790 olivine average measurement. A single data point shown for NWA 5790 olivine, with Mg# 35 is now in good agreement with the EPMA data. The STEM-EDX atomic% varied by ± 0.8 at% for Fe over the seven data points so the heterogeneity of this sample and/or variation in its thickness may have contributed towards the differences recorded, especially as the EPMA data was a single point measurement. Setting the Fe k-factor any higher, resulted in the Fe at% in NWA 5790 pyroxene and magnetite becoming too high.

The chosen value of 1.32 is in good agreement with theoretical Fe k-factors that are calculated as 1.32 at 100 keV (Lorimer et al., 1977) and range from 1.28 to 1.61 at 120 keV (Wood et al., 1984).

Chapter 2: Techniques

Table 2.2. EPMA and STEM-EDX data normalised at% for reference materials. Data are either averaged (av) over 7 or 8 measurements or are single point (pt) measurements.

	Na	Mg	Al	Si	Ca	Ti	V	Cr	Mn	Fe	Ni	O	Mg#	Si/O	Wo%	Fs%	En%
Olivines																	
NWA 5790 TEM (av)*		10.8		15.0	0.2			0.1	0.4	16.1		57.5	40	0.26			
NWA 5790 TEM (av)		10.5		14.6	0.2			0.1	0.3	17.0		57.3	38	0.25			
NWA 5790 TEM (pt)		9.8		14.3	0.3			0.2	0.3	17.9		57.2	35	0.25			
NWA 5790 EPMA (pt)		9.5		14.3	0.3				0.4	18.5		57.1	34	0.25			
San Carlos TEM (av)		25.6		14.3				0.1		2.7	0.1	57.2	90	0.25			
San Carlos EPMA (3 pts)		25.6		14.5						2.6		57.2	91	0.25			
Pyroxene																	
NWA 5790 TEM (av)		6.2	0.6	19.9	7.3	0.1		0.1	0.1	5.4		60.2		0.33	39	29	33
NWA 5790 EPMA (pt)	0.3	6.6	0.4	19.8	7.8	0.1			0.2	5.0		60.0		0.33	40	26	34
Magnetite																	
Magnetite TEM (av)			2.3	0.9		3.3	0.3	1.3		38.7		53.2					
Magnetite EPMA (pt)			2.1			5.1	0.4	1.3		37.5		53.6					

*This data uses the default software Fe k-factor of 1.21. All other data uses the calibrated Fe k-factor of 1.32.

Table 2.3. Comparison of k-factors for major elements between AZtec default software settings and those determined experimentally for similar samples.

	AZtec software default	Calibrated values for this thesis	¹ Defaults	¹ Calibrated	² At 200 kV
Mg	1.04	1.04	1.81	1.25	1.81 ± 0.18
Fe	1.21	1.32	1.25	1.36	1.35 ± 0.16
Ca	0.97	0.97	1.05	1.10	1.05 ± 0.10
Al	1.03	1.03	1.25	1.00	1.25 ± 0.16
Si	1.00	1.00	1.00	1.00	1.00

¹ PhD thesis (Changela, 2011)

² Experimentally determined k-factors at 200 kV (Williams & Carter, 2009a)

2.3 Synchrotron radiation

This section introduces synchrotron radiation and describes the set-up of the beam lines used at the *Diamond Light Source* national synchrotron, established in 2002, in Oxfordshire, UK. Subsequent sections go into the detail of each synchrotron technique used in this thesis.

The maximum energies achievable by a cyclotron or betatron, using a ring of magnetic fields to accelerate particles and to keep them in a constant circle, are dependent on the maximum magnetic field strength. As the speeds of the particles become fast enough, their mass grows into the relativistic range and they become out of phase with the electric field, so the radio-frequency (RF) voltage cannot accelerate them further. The principle of phase stability, proposed independently by both McMillan (1945) and Veksler (1944), was vital for the development of synchrotrons. Taking into account the increased relativistic mass of the electrons at such high speeds, phase stability theory proposed the magnetic field and frequency adjustments needed in order to maintain the orbital period in a cyclotron. The first synchrotron acceleration to 8 MeV was carried out in 1946 by Goward and Barnes at Woolwich Arsenal, UK (Wilson, 1996). Over fifty synchrotrons are now used worldwide, with the *Diamond Light Source* being classified as medium energy, at 3 GeV.

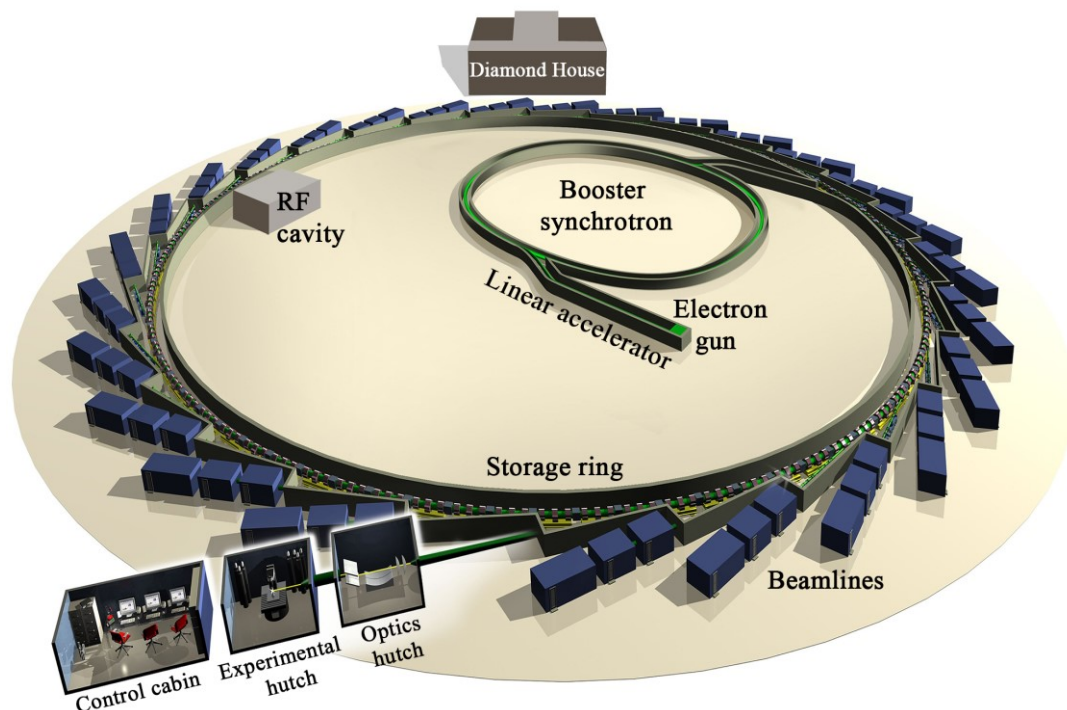


Fig. 2.7. Overview of the *Diamond Light Source* synchrotron (Diamond, 2018).

2.3.1 The *Diamond Light Source* synchrotron and beamlines

The Diamond Light Source is a 48 sided polygon of 560 m, kept under vacuum, with each of the 48 bending magnets deflecting the beam by 7.5° , totalling the full 360° closed loop (Fig. 2.7). 29 beamlines are currently operational although there is room for up to 40 beamlines to be fitted.

The electrons are generated from an electron gun that uses a high voltage cathode heated under vacuum, providing thermal energy to liberate electrons. These are first accelerated to 90 keV by anodes and then to 100 MeV by a linear accelerator (linac) using radiofrequency (RF) cavities. They then enter the Booster synchrotron, with 36 dipole bending magnets guiding the electrons around the bends. A radio frequency voltage accelerates the electrons up to 3 GeV at which point they are ready for the main storage ring, which they orbit in two millionths of a second (Diamond, 2018).

The synchrotron radiation is channelled into the optics hutch of a beamline from the storage ring, with the connection through the shield wall being known as the front end. This front end allows safe access into the optics hutch if required, protects the storage ring against beamline leaks and removes as much heat as possible, as well as monitoring the exact position of the beam. Each beamline has its own series of diffraction gratings and mirrors in its optics hutch to focus and filter the beam to the desired parameters for the technique employed, before it enters the experimental hutch, where the sample is mounted (Fig. 2.8). The scientists monitor the experiment from the control cabin, from where they can control the sample position, alignments and collect data from the detectors.

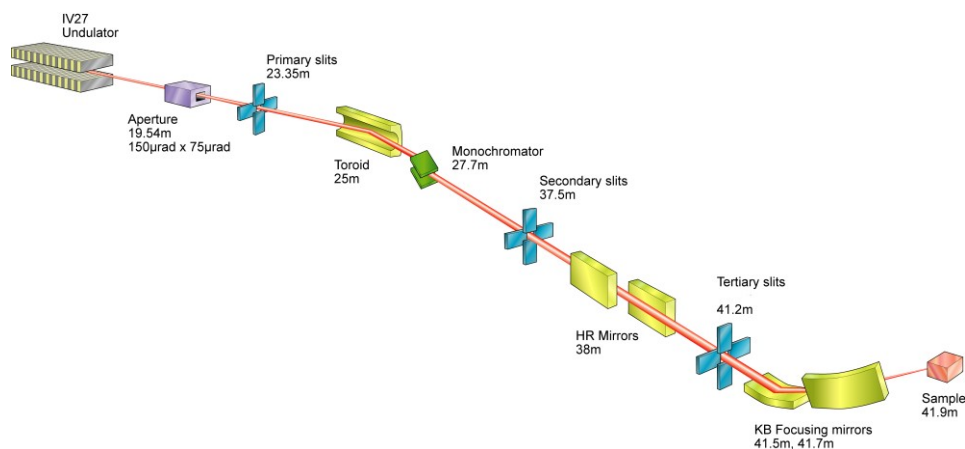


Fig. 2.8. Schematic of beamline I-18, showing the distances of the monochromators, slits and mirrors used in the optics hutch between the storage ring and the sample (Mosselmans et al., 2009).

2.3.1.1 Beamline I-18: microfocus spectroscopy

The Diamond Light Source synchrotron microfocus beamline I-18 has an energy range of 2.0 keV to 20.7 keV, and a minimum spot size resolution of $\sim 2 \times 2.5 \mu\text{m}$, together with tuneable monochromators capable of resolving 0.1 eV spectra energy increments (Mosselmans et al., 2009).

The I-18 beamline passes through a sequence of optics from the storage ring (Fig. 2.8). It goes through a cooled aperture and water-cooled slits to reduce heat load on the optics upstream and to define the incoming beam. A toroidal mirror brings the beam into parallel alignment in the vertical plane (Mosselmans et al., 2009). The liquid-nitrogen-cooled monochromator uses three pairs of crystals, Si(111) and Si(311), and operates on the principle of the Bragg equation (2.1) with an angular range of 80° (Evans, 2018). The desired energy is selected from the range achievable by varying the angle (Mosselmans et al., 2009). The secondary slits focus the beam in the horizontal plane and monitor the position of the beam. The horizontally reflecting (HR) mirrors remove higher harmonics from the X-ray beam and tertiary slits limit the horizontal beam size and remove vertical scatter (Fig. 2.8). The final pair of Kirkpatrick-Baez (KB) focusing mirrors use an adaptive system to control the shape, allowing the focal point to be adjusted over a range of 10 cm to allow for variation in sample positioning requirements (Mosselmans et al., 2009).

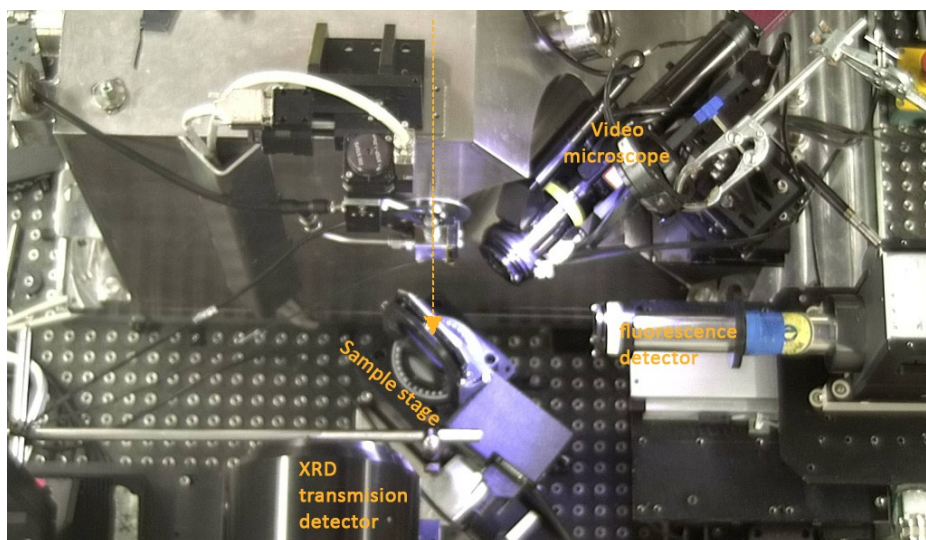


Fig. 2.9. Aerial view of the I-18 sample stage (centre) at 45° to the beamline direction from the end of the room (arrow), with the XRD transmission detector able to collect X-rays passing through the sample, and the fluorescence detector at 45° to the sample, to collect fluorescence X-rays. The video microscope is used to position the sample correctly.

The sample is placed in the holder so the transmission detector lies in the path of the beamline beyond the sample, and the fluorescence detector is at 90° to the beamline direction (Fig. 2.9). The sample stage can be rotated and moved in all three dimensions. The sample can be viewed using the video microscope, showing the position of the beam on the sample in order to find the region of interest for measurement.

The beamline can be used to make measurements of X-ray Fluorescence (XRF), X-ray Absorption Spectroscopy (XAS), and X-ray Diffraction (XRD), which are described in the following sections. I-18 has previously been used for similar work on *Stardust* comet grains and martian meteorites by Changela et al. (2012) and Hicks et al. (2014).

2.3.1.2 Beamline B-22: FTIR

The synchrotron offers up to 2 orders of magnitude more brightness in the mid-IR and up to 1000 times in the far-IR, compared to a classical blackbody source (Cinque et al., 2011).

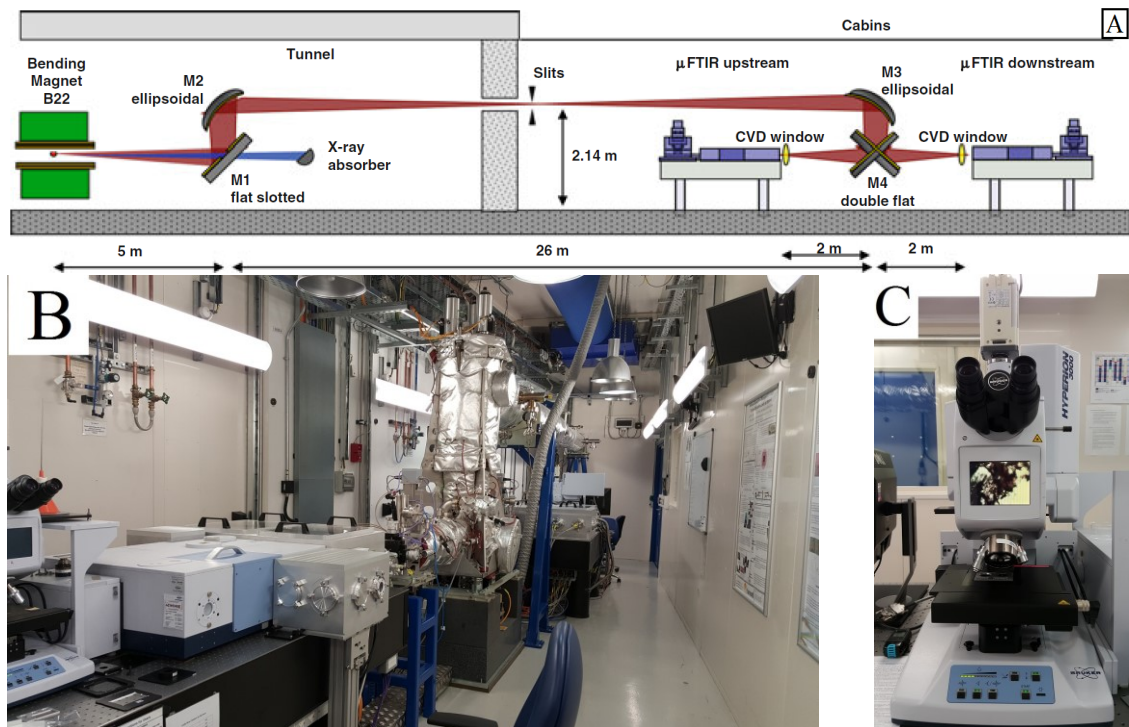


Fig. 2.10. (A) Schematic of the focusing optics and end stations for the FTIR beamline B-22, with synchrotron radiation originating at the left (Cinque et al., 2011). (B) Experiment hutch of the B-22 beamline and end stations. (C) The Hyperion 3000 optical microscope at the end station, used to identify locations for analysis.

The path of beamline B-22 from the storage ring first reaches a flat slotted mirror M1 that dumps the inner X-ray beam while reflecting the wider IR range beam. The beamline then passes via mirror M2 to mirror M3 and is then split by the double mirrors at M4 to two end stations Bruker Vertex 80 V under vacuum, with Hyperion 3000 microscopes (Fig. 2.10A-C) (Cinque et al., 2011).

2.3.1.3 Beamline sessions

In this thesis, data was collected at the microfocus beamline I-18 during three separate beamline sessions sp10328-1 (December 2014), sp13690-1 (July 2016), nt16688-1 (December 2016) and three XAS data points for NWA 8114 were collected by L. Hicks at sp19641-1 (January 2018). The FTIR beamline B-22 was used for one beamline session, sm12761-1 (December 2015).

2.3.2 X-ray Fluorescence (XRF)

XRF uses X-rays to excite a sample, and a detector to measure the fluorescent (secondary) X-ray emitted. Each element present in the sample produces characteristic fluorescent X-rays allowing it to be identified.

Using a beam between 8.5 and 10.0 keV, XRF measures elements from Ca ($Z=20$) to Zn ($Z=30$) producing elemental maps. The sample is usually placed at 45° to the beam and fluorescence detector, and the stage moves the sample in increments according to the resolution selected, usually 2 μm , 5 μm or 10 μm . The resulting elemental maps show which elements are present and have an associated X-ray fluorescence spectrum for each pixel. The maps are used to pinpoint the location of Fe in order to position the beam with ~ 2 μm accuracy for longer XAS measurements. The maps were analysed using *PyMca 4.4.1* software. The XRF data gives an indication of the presence or absence of elements, but the data are not calibrated so the 'counts' only give a very approximate measure of the relative quantities.

2.3.3 X-ray Absorption Spectroscopy (XAS)

X-ray absorption spectroscopy measures the X-ray absorption of a material at a specific energy level. Each element shows an absorption peak at a unique characteristic energy level, which is equal to the energy required for an electron to escape from the atom. This is known as the absorption edge, and is a K-edge where an electron escapes from the 1s orbital, an L-edge where an electron escapes from the n=2 shell, and an M edge for where an electron escapes from n=3 shell, etc. There is also a smaller peak at a slightly lower energy level known as the pre-edge centroid; this is the amount of energy needed to raise an electron from the 1s to the 3d orbital shell.

The oxidation state of Fe is studied by measuring the Fe-K edge, though the energy range of the beamline allows the K-edge of all elements from P (Z=15) to Mo (Z=42) to be examined.

The X-ray absorption coefficient μ gives the proportion of photons absorbed by the sample. In transmission mode, this is measured as the difference between the intensity of the incident (I_0) and transmitted (I_t) X-rays at each energy level (Fig. 2.11A).

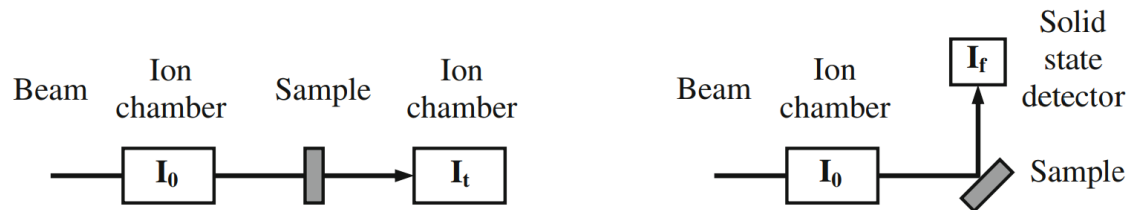


Fig. 2.11. X-ray absorption spectroscopy (XAS) detector setup for (A) transmission and (B) fluorescence (Schnohr & Ridgway, 2015). The latter arrangement can be seen in Fig. 2.9 though the XAS transmission detector is out of view, behind the XRD transmission detector.

Thus, the reduction in intensity I of an X-ray beam passing through a sample with thickness x (Calvin, 2013):

$$\mu(E) = -\frac{dI}{dx} \quad 2.8$$

Integrating this gives a result known as Bourguer's Law:

$$I_t = I_0 e^{-\mu x} \quad 2.9$$

which is equal to:

$$\mu x = \ln\left(\frac{I_0}{I_t}\right) \quad 2.10$$

In fluorescence mode, the sample is usually placed at 45° to the beam and detector (Fig. 2.11B). When the beam interacts with the sample, some photons are scattered both elastically and inelastically, and some are absorbed by the element of interest, causing a core hole in one of the lower energy shells either from an electron transition e.g. $1s \rightarrow 3d$ or by emission of the electron. This causes a fluorescent photon to be released in order to fill the core hole. Fluorescent photons are emitted in all directions randomly, so a much lower intensity I_f will reach the fluorescence detector compared with transmission mode. The absorption coefficient becomes:

$$\mu(E)x = -\ln\left[1 - \frac{I_f}{I_0}\right] \propto \frac{I_f}{I_0} \quad \text{For } I_f \ll I_0 \quad 2.11$$

The absorption coefficient, $\mu(E)$, is a smooth function over large ranges and proportional to the density d , atomic number Z , and inversely proportional to the X-ray energy E and mass m (Schnohr & Ridgway, 2015):

$$\mu(E) \sim \frac{dZ^4}{mE^3} \quad 2.12$$

However, due to scattering from neighbouring atoms, there are oscillations producing a larger edge (Fig. 2.12).

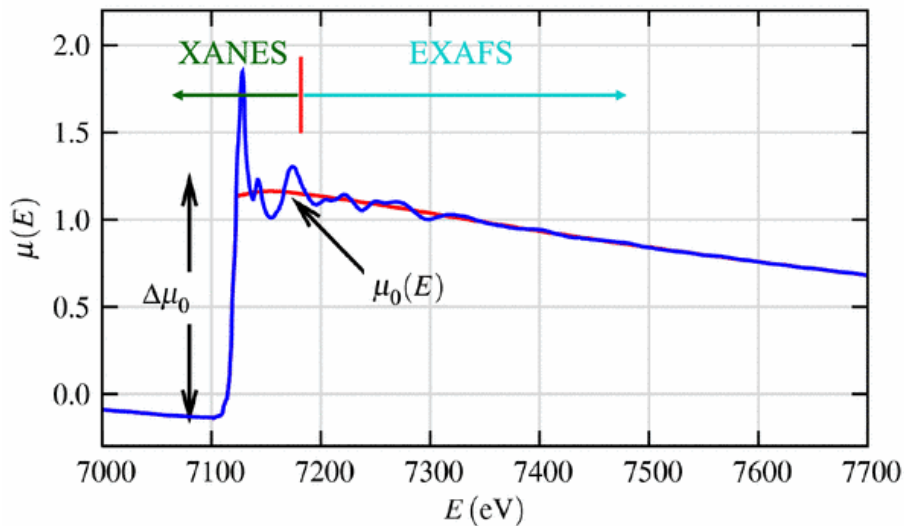


Fig. 2.12. The smooth modelled absorption coefficient μ_0 for an isolated atom compared to an experimentally measured absorption result with oscillations from scattering (TU Wien, 2018).

2.3.3.1 X-ray absorption near edge structure (XANES) for mineral identification

The shape of the XANES can help to identify minerals. Silicate minerals often contain non-equivalent cationic sites with similar coordination number. For example olivine, $(\text{Mg,Fe})_2\text{SiO}_4$, has an M1 and an M2 site, which can both be filled with iron, both with magnesium, or some combination of the two (Calas et al., 1986). Olivine has a characteristic narrow pointed high peak, also known as the ‘white line’, when the sites are unequal with a

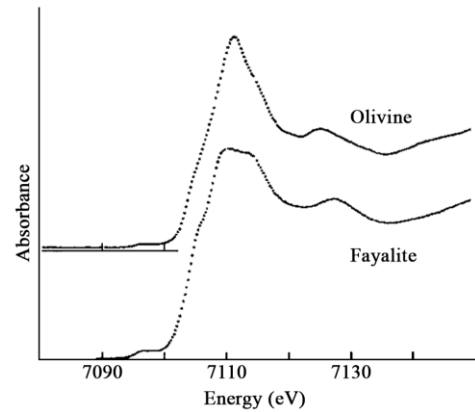


Fig. 2.13. Fe-K XANES for natural olivine Fo_{85} and fayalite (Calas et al., 1986).

combination of Mg and Fe in natural olivine Fo_{85} ($\text{Mg}_{1.7}\text{Fe}_{0.3}$) SiO_4 (Fig. 2.13). A broader, flatter edge maximum is seen for Fe-rich olivine, fayalite Fe_2SiO_4 , when M1 and M2 are both iron (Fig. 2.13; Calas et al., 1986). Pyroxene often shows a peak split into two when the iron content is low (Fig. 3.13G).

2.3.3.2 Fe-K XANES for oxidation state investigation

It is known that the energy level for the pre-edge centroid and absorption edge for Fe^{3+} is higher than for Fe^{2+} (Koningsberger & Prins, 1988). Previous work provides a calibration scale for Fe-silicates to determine $\text{Fe}^{3+}/\Sigma\text{Fe}$ (Fig. 2.14) (Hicks et al., 2014). This makes it possible to determine the proportion of oxidised iron present in the meteorite in specific locations, to determine if it is equally distributed or in specific clasts, grains or areas.

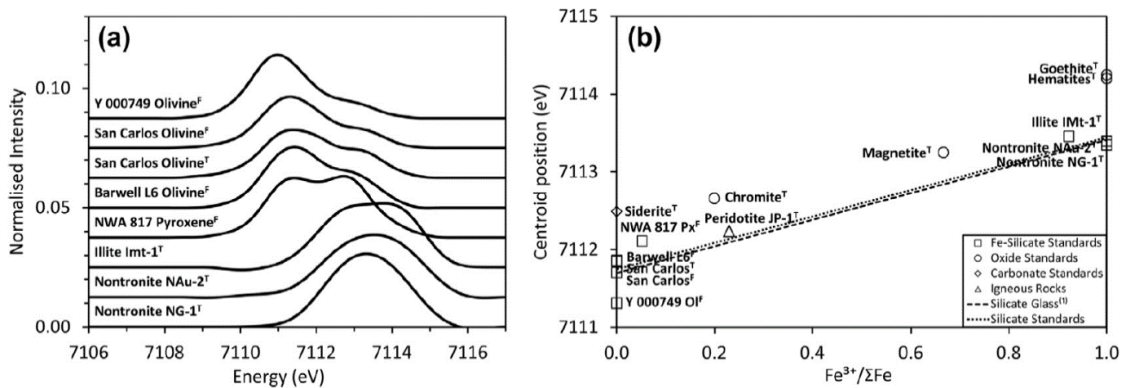


Fig. 2.14. Calibration for $\text{Fe}^{3+}/\Sigma\text{Fe}$ from Fe-K XANES 1s→3d centroid energies for five Fe-silicate standards and two nakhlite standards (Hicks et al., 2014).

2.3.3.3 Fe-K XANES operating conditions

Transmission mode was used for the powdered reference materials, and fluorescence mode was used for the planetary samples and a San Carlos olivine. An XRF map was produced to locate the region of interest before taking the XAS measurements.

The iron K-edge (Fe-K) XAS measurements were taken with a $2 \times 2.5 \mu\text{m}$ spot size. The spectra were taken over an energy range of 6900 eV to 7600 eV, with a high resolution of 0.1 eV over the known XANES region for iron 7090 eV to 7145 eV, to accurately capture the $1s \rightarrow 3d$ pre-edge centroid and absorption edge positions, and a lower resolution of 5 or 10 eV over the rest of the range. The 9 element Ge solid state high-rate fluorescence detector was used for these measurements.

The spectra were processed and normalised using *Athena 0.9.24* software (Ravel & Newville, 2005) and the absorption edge was estimated to be at half the normalised intensity. The $1s \rightarrow 3d$ pre-edge centroids were analysed by fitting and subtracting a baseline and calculating the intensity-weighted average energy position of the pre-edge centroid, using the methods of Hicks et al. (2014). The ratio of oxidised iron to total iron, $\text{Fe}^{3+}/\Sigma\text{Fe}$, has been calculated using the silicate calibration scale (Fig. 2.14) (Hicks et al., 2014). In addition to point measurements, Fe-K XANES maps were made to show the variation in iron oxidation state visually over the absorption edge energy range 6900 eV to 7300 eV, with the Fe-K XANES spectra for each pixel being normalised and analysed using *MANTiS 2.06* (Lerotic et al., 2014). A *Python* programme was written in order to extract the Fe-K XANES spectra for each pixel on the XANES maps, as the raw data was stored as 141 separate maps for each energy step level.

Fe-K XANES were measured during four separate beamtime sessions in December 2014, July 2016, December 2016 and January 2018. Due to minor drift in the monochromators over time, an energy calibration is required to compare data from different sessions. An estimation of the energy variation was calculated by measuring reference materials such as Fe-metal foil, powdered magnetite, hematite and San Carlos olivine at each beamtime, determining their Fe-K $1s \rightarrow 3d$ pre-edge centroid and absorption edge positions, and adjusting all the results to the peak positions observed during the most recent beamtime (Hicks et al., 2017).

2.3.4 Transmission X-ray Diffraction (XRD)

Different crystalline materials diffract an X-ray beam by different measurable amounts (angle θ), which allow the characteristic d -spacings to be calculated using Bragg's law (equation 2.1). These can be compared to reference databases e.g. ICDD (2014) to identify the exact elements or minerals in a sample, and its detailed structure.

Every crystalline structure has a unique unit cell, in which atoms are arranged in a pattern that repeats periodically in three dimensions in a crystal lattice. Miller Indices hkl are used to describe planes in a crystal lattice, perpendicular to the reciprocal lattice vectors. This is calculated as the inversion of where the plane intercepts the a , b , and c unit cell axes, with any fractions multiplied by a common factor to make hkl integers (Klein & Philpotts, 2012). For example, (032) describes a plane parallel to the a axis that intersects the b axis at 2, and the c axis at 3, so the inversions are $1/\infty$, $1/2$, $1/3$, multiplied by 6 giving (032). Diffraction of the X-ray beam occurs when it interacts with the atoms, so the characteristic d -spacings provide information on the size and shape of the unit cell, with dimensions a , b , c , and interaxial angles of α , β , and γ .

XRD is a powerful identification tool for mineralogy, as it can distinguish the unique characteristic peaks of the different iron oxides and hydroxides, whereas SEM can only identify a mineral as iron oxide, and EPMA and XANES provide an indication of how oxidised it is. Magnetite Fe_3O_4 and maghemite Fe_2O_3 have a cubic unit cell where the axial lengths $a = b = c$, and goethite $\text{FeO}(\text{OH})$ has an orthorhombic unit cell where the axial lengths $a \neq b \neq c$. Both systems have interaxial angles of $\alpha = \beta = \gamma = 90^\circ$.

For a cubic lattice:

$$d_{hkl} = \frac{a}{\sqrt{h^2 + k^2 + l^2}} \quad 2.13$$

For an orthorhombic lattice:

$$\frac{1}{d_{hkl}^2} = \frac{h^2}{a^2} + \frac{k^2}{b^2} + \frac{l^2}{c^2} \quad 2.14$$

The d -spacings measured are matched to the characteristic Miller indices, hkl planes, using the ICDD (2014). For a cubic lattice, equation 2.13 is used to calculate the unit cell dimension a . This can be done for each d -spacing that matches a characteristic plane, although all will give slightly different values for a . Using an IDL computer

programme (Hansford, 2015), calculations can be done the other way around to find the unit cell dimension a that best fits all of the measured hkl planes. A value of a is used to calculate the ideal d -spacing for an hkl plane, then the difference between the ideal d -spacing and measured d -spacing is calculated as a measure of error, and the programme iterates accordingly, refining the value of a until the 2σ measure of error is as small as possible. For an orthorhombic lattice, the IDL programme can calculate a , b and c using equation 2.14 if sufficient hkl planes were identified, though the errors are likely to be greater.

Transmission synchrotron XRD measurements were taken between 9 keV and 15 keV, with the majority at 11 keV and 13 keV, with a 2θ range of $\sim 4.3^\circ$ to $\sim 41.7^\circ$ detectable and an exposure time of 300 seconds. Using equations 2.1 and 2.2 this corresponds to d -spacings of ~ 1 Å up to ~ 9.1 Å. XRD measurements were taken on a LaB6 standard at each energy level in order to produce a calibration file for each energy level using *DAWN (Data Analysis Workbench) 2.1.0* software. All other measurements were processed using the calibration file and a rolling ball correction in *Dawn*.

XRD measurements were point measurements for the martian meteorite, but area measurements for the *Stardust* grains, as the grain sometimes moved within the data collection times due to some melting of the aerogel. The area measurement was explored in *Dawn* to locate the grain material, and the sub-area giving the most intense d -spacing peaks was extracted. The *Dawn* software then calculates the exact positions of these peaks using the Nelder Mead fitting algorithm, which is a numerical method used to find the maximum of a function for nonlinear problems where derivatives are not known (Nelder & Mead, 1965).

2.3.5 Fourier Transform Infrared Spectroscopy (FTIR)

Infrared (IR) radiation covers the wavelengths from 0.8 to 1000 μm , usually reported as wavenumbers in cm^{-1} units (the inverse of the wavelength). The mid-IR, between 4000 cm^{-1} and 400 cm^{-1} is used to characterise the vibrational and rotational-vibrational energy structure of molecules. Far-IR is used for lower energy rotational spectroscopy.

IR spectroscopy uses an IR beam to excite molecular vibrations in bonds with a dipole moment. The energy of these vibrations (wavenumbers) depends on the molecular composition, the nature of the atoms and bonds between them. A sample compound can

then be identified by matching its IR absorption spectrum to a characteristic spectrum from a database, treating the absorption spectrum as a unique fingerprint.

In order for a molecule to absorb IR, the incident frequency must match one of the natural frequencies of vibration of the sample molecule. The molecule is excited to a higher energy state as the polar bond (with dipole moment) is stretched, bent and compressed by absorbing the IR. The vibrational frequency of a bond is directly proportional to its bond strength and inversely proportional to the masses at the ends of bonds. Water has polar O-H bonds and has three vibrational modes (Fig. 2.15).

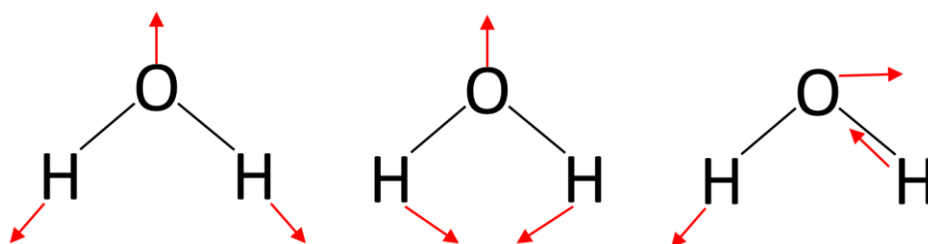


Fig. 2.15. Three vibrational modes of water vapour: (a) Symmetric stretch 3657 cm^{-1} (b) Symmetric bend 1595 cm^{-1} (c) Asymmetric stretch 3756 cm^{-1} (Zobov et al., 1996).

The stretching bands for liquid water occur at lower wavenumber, symmetric at 3200 cm^{-1} , asymmetric at 3530 cm^{-1} , and the bending band increases to 1645 cm^{-1} (Bonner & Curry, 1970).

Dispersive IR spectrometry only allows radiation of a single wavelength to be

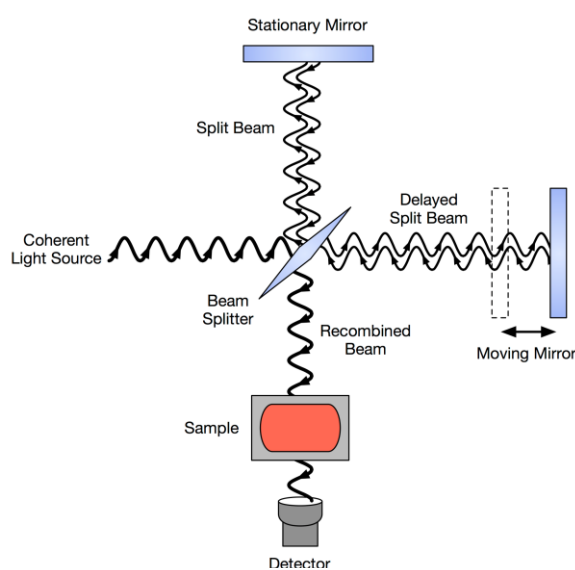


Fig. 2.16. Michelson interferometer for FTIR (Sanchox, 2011).

measured at one time by a detector. Fourier Transform Infrared Spectroscopy (FTIR) enables the whole IR spectrum to be measured at once, by modulating the frequency of the radiation to be low enough to be detectable over time. The use of a Michelson interferometer enables an IR signal of lower frequency to be produced, that a detector is capable of recording over time.

The interferometry approach splits the

source infrared radiation beam, part travelling to a fixed mirror, and part to a moving mirror (Fig. 2.16). The radiation is reflected from each mirror and recombined with a difference in path length, and some of it is redirected by the beam splitter to pass through the sample. As the moving mirror varies one of the path lengths, different wavelengths are in or out of phase, depending on the rate of the mirror movement and the wavelength of the radiation. The sample absorbs some of the radiation, and the detector records the remaining signal at sufficient speed relative to the moving mirror speed. The resulting interferogram recorded gives the intensity versus the path difference, which is the spectrum of the source minus the sample spectrum. Therefore, computer software processing uses a reference spectrum for the source to deconvolute the sample spectrum, and a Fast Fourier Transform is applied, to invert the path difference (resulting in cm^{-1}). This gives an absorption spectrum, showing absorbance at each wavenumber.

This method also allows for a much higher signal to noise ratio than that of dispersive IR spectrometers, making it much faster to collect comparable data. The resolution achievable is an inverse of the path difference, so the *Diamond Light Source* synchrotron can achieve a high spectral resolution of 0.07 cm^{-1} .

An FTIR spectrometer is used together with a microscope in order to be able to select a specific region for analysis with the microscope, and carry out point or area measurements to acquire infrared spectra. Synchrotron radiation is far brighter than other sources, so allows the beam size to be much smaller, less than $10 \mu\text{m}$ without a significant loss of photons.

Some IR light is absorbed, some is transmitted and some is reflected from the sample. This can be plotted either as transmittance, where absorption bands show as dips, or as absorbance, where the bands show as peaks.

$$\text{Transmittance}(T) = \frac{\text{radiant power transmitted by a sample}}{\text{radiant power incident on the sample}}$$

$$\text{Absorbance}(A) = \log_{10} \left(\frac{1}{T} \right)$$

2.3.5.1 Reflectance FTIR

FTIR can also be used on samples too thick to transmit, by measuring the specular reflectance, which is related to the refractive index n . If a material is non-absorbing, then n is constant as a function of wavenumber. If a material is absorbing, the refractive index (n) of an absorbing sample is related to the absorption. The variation of n as a function of wavenumber is shown in Fig. 2.17, where n has been derived from k , a synthesised Lorentzian representing a typical absorption band (Bassan et al., 2009).

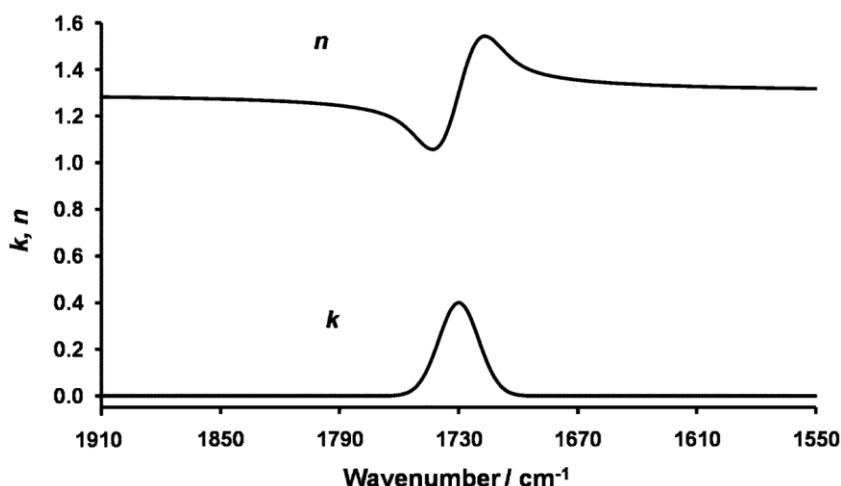


Fig. 2.17. Variation of refractive index n (dispersion) as a function of wavenumber, derived from a representative typical absorption band k (here a synthesised Lorentzian function) (Bassan et al., 2009).

A reflection spectrum is like a first-order differential for an individual absorption band, as, the refractive index is a minimum on the high wavenumber side of the band, and a maximum on the low wavenumber side. Therefore, the reflection spectrum needs to be converted to an absorption spectrum using Kramer's-Kronig transformation.

OPUS 7.0 software calculates the phase rotation angle $\phi(\nu)$ (a function of the wave number ν) of an optically thick sample from a measured reflectance spectrum $R(\nu) = r^2(\nu)$ (Bruker, 2011). Then the Fresnel equation is used to calculate the reflectivity of the air-sample interface:

$$\Gamma(\nu)e^{i\phi(\nu)} = \frac{[n(\nu) - 1]}{[n(\nu) + 1]} \quad 2.15$$

The real and imaginary parts of the refractive index $n = n + ik$ are linked by the Kramers-Kronig relationship and calculated as:

$$n(\nu) = \frac{[1 - R(\nu)]}{[1 + R(\nu) - 2R^{0.5}(\nu)\cos(\phi(\nu))]} \quad 2.16$$

$$\kappa(\nu) = \frac{2R^{0.5}(\nu)\sin(\phi(\nu))}{[1 + R(\nu) - 2R^{0.5}(\nu)\cos(\phi(\nu))]} \quad 2.17$$

Using the absorption index $\kappa(\nu)$ (the imaginary part of the refractive index), the absorptivity $A(\nu)$ of a layer with thickness d is:

$$A(\nu) = \log(e) 2\pi\nu d \kappa(\nu) \quad 2.18$$

The Kramer's-Kronig transformation has been applied to all reflectance spectrum data in this thesis, using the *OPUS 7.0* software (Bruker, 2011).

MIRIAM beamline B-22 (session sm12761-1, December 2015), was used to investigate which phases were hydrated in the martian meteorite NWA 8114 with reflectance FTIR for polished sections A, B, C and transmission FTIR for double polished section F (Cinque et al., 2011) (Sections 3.2.3.4 and 3.3.6).

B-22 has a spectral range of 10000 to 5 cm^{-1} and beam size of 3 μm to 15 μm at the sample, with achievable resolution of 0.07 cm^{-1} . Both point and map measurements were made using a 10 \times 10 μm or 15 \times 15 μm spot size and resolution of either 4 cm^{-1} (with 256 scans) or 8 cm^{-1} (with 128 scans), with a spectral range in the mid-IR of wavenumber 4000 cm^{-1} to 500 cm^{-1} (wavelength 2.5 μm to 20 μm). *OPUS 7.0* (Bruker, 2011) software was used to process the data and a Kramer's-Kronig transformation function within it was used to obtain absorbance values from reflectance data.

2.4 CT scanning

An X-ray micro computerised tomography (CT) scan passes X-rays through a rotating cylindrical sample to a detector (Fig. 2.18). The material absorbs some of the X-ray radiation, which varies according to the atomic number of the material it is made of, as well as the density and thickness. With geological samples and radiation sources up to 100 keV, the most important interaction for absorption is photoelectric absorption.

There must be air on each side of the sample so that every voxel is in view at every rotation position, in order for software to be able to reconstruct it. A separate projection is captured by the detector following each rotation, and these two dimensional slice

images are constructed into a three dimensional model. A small sample, far from the detector (Fig. 2.18, green), can be scanned at higher resolution than a larger sample that has to be positioned nearer the detector (Fig. 2.18, yellow).

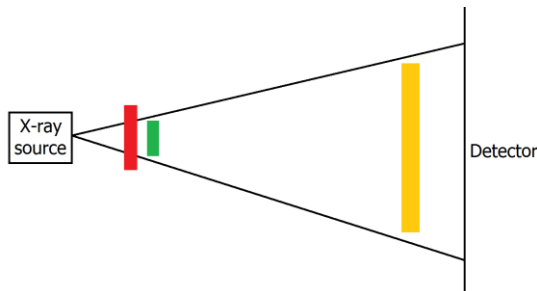


Fig. 2.18. A cylindrical sample rotates while X-rays from the source pass through it to a detector. The red sample is too close to the source to be reconstructed; the yellow sample would be scanned at lower resolution than the green sample, as it is larger and has to be closer to the detector.

An X-ray CT scan was taken of the remainder of the 1.9 g NWA 8114 main mass (after sections A-D were prepared, but before further material was consumed in preparing sections E-G) using a Nikon Metrology XT H 225 scanner at the University of Leicester at 160 kV. This provides a 3D image at high resolution of the internal structure and the composition of the bulk sample, processed using *VG Studio Max* (version 3) software (VG, 2017). The voxel size was $8 \times 8 \times 8 \mu\text{m}$.

2.5 ^{40}Ar - ^{39}Ar dating

This work was carried out with expert collaborators at the University of Manchester. I spent two days with them using a Thermo Scientific Argus VI mass spectrometer, designed to quantify Ar isotopes from small samples. Once the data was obtained, they processed the data presented in this thesis and discussed the results with us.

Potassium-40 (^{40}K) is a radioactive isotope with a very long half-life of 1.27×10^9 years (Emsley, 2011), making it suitable for dating rocks up to four billion years old. It comprises about 0.012% of the

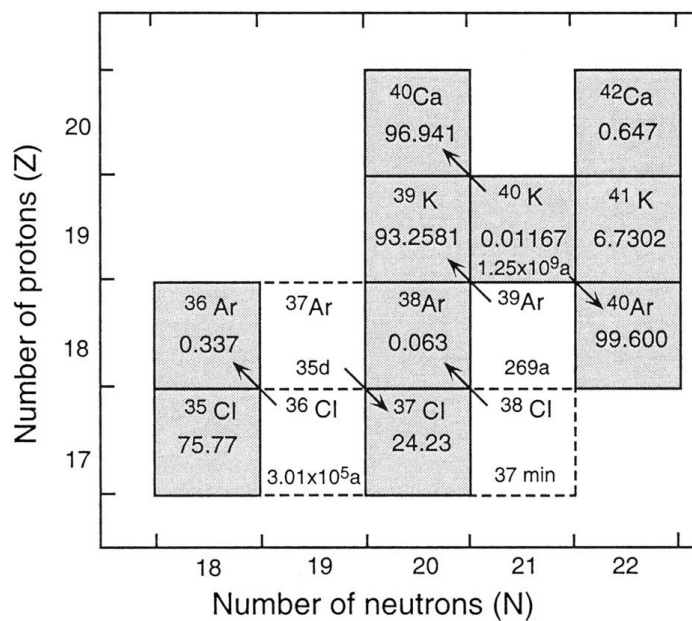


Fig. 2.19. The naturally occurring isotopes with their natural abundance at% (solid grey boxes) and each artificial radioactive isotope with its half life (dotted white boxes) with arrows indicating decay reactions (McDougall et al., 1999).

potassium found on Earth. 89.28% of the time it decays to ^{40}Ca , and 10.72% of the time it decays to ^{39}Ar . This explains the large amount of ^{40}Ar in Earth's atmosphere (0.93% by volume) and the relative abundances of the three argon isotopes: 99.6% ^{40}Ar compared to 0.34% ^{36}Ar and 0.06% ^{38}Ar (Fig. 2.19) (McDougall et al., 1999).

^{39}K is known to exist in constant proportion to ^{40}K and thus is a proxy for the amount of ^{40}K , allowing determination of $^{40}\text{Ar}^*/^{40}\text{K}$ where $^{40}\text{Ar}^*$ distinguishes radiogenic daughter product from ^{40}Ar naturally occurring in the atmosphere. For ^{40}Ar - ^{39}Ar dating, ^{39}Ar is created from ^{39}K by neutron irradiation in a nuclear reactor. $^{40}\text{Ar}/^{39}\text{Ar}$ dating offers greater precision than K-Ar dating as it uses ratios of isotopes rather than separate absolute measurements.

The age of a sample, t , can be calculated from equation 2.19, where the radioactive decay constant of ^{40}K $\lambda = 1.27 \times 10^9$ years, J is a measure of the neutron flux of irradiation and R is the $^{40}\text{Ar}/^{39}\text{Ar}$ ratio:

$$t = \frac{1}{\lambda} \ln(J \times R + 1) \quad 2.19$$

A number of assumptions are required for either K-Ar or Ar-Ar dating. The decay of the parent, ^{40}K , must be independent of its physical state. All radiogenic ^{40}Ar is assumed to result from ^{40}K decay. Since the event being dated, the sample must have been a closed system, with no gain or loss of Ar or K (Kelley, 2002). Compared to the age being determined, the closure of the system should be rapid. ^{38}Ar abundances must be corrected for a cosmogenic component. Cosmogenic ^{38}Ar and ^{36}Ar are produced by cosmic ray interactions while in space. ^{37}Ar is produced from Ca during irradiation, so acts as a proxy for Ca, and is thus generally correlated with cosmogenic $^{36}\text{Ar}_{\text{cos}}$, produced in feldspathic phases (Cassata & Borg, 2016). Measurements of ^{36}Ar and ^{37}Ar can be used in addition to the known cosmogenic $^{38}\text{Ar}/^{36}\text{Ar}$ ratio of 1.67 to correct ^{38}Ar abundances (Cartwright et al., 2013).

Corrections must be made for contaminating atmospheric ^{40}Ar , using the terrestrial $^{40}\text{Ar}/^{36}\text{Ar}$ ratio of 295.5, though complexity is added when considering trapped martian atmosphere. Measurements by the Curiosity rover suggests that Mars has 1.93% of ^{40}Ar in its atmosphere (Mahaffy et al., 2013). Once cosmogenic component corrections have been applied, the remaining Ar is a mixture of trapped and radiogenic components (Cartwright et al., 2013). The trapped component can be partly resolved using three-

isotope plots of $^{36}\text{Ar}/^{40}\text{Ar}$ vs $^{39}\text{Ar}/^{40}\text{Ar}$ and examining correlation of the Ar isotopes with Cl released (Cartwright et al., 2013).

Samples were irradiated for 24 hours in position B2W of the SAFARI-1 reactor, Pelindaba, South Africa (irradiation MN2016a) to turn ^{39}K (potassium) into ^{39}Ar (radioactive argon). This enables a single measurement of Argon isotopes to give $^{40}\text{Ar}/^{39}\text{Ar}$ results, provided a standard of known age is irradiated alongside the unknown samples. As only one measurement is needed, a very small sample can be used. After irradiation, a noble gas extraction system at the University of Manchester, UK with a laser port attached was used to evacuate the samples that were placed in 3 mm diameter wells in an aluminium disk. Ar blank levels were reduced by baking the samples at 150 °C overnight.

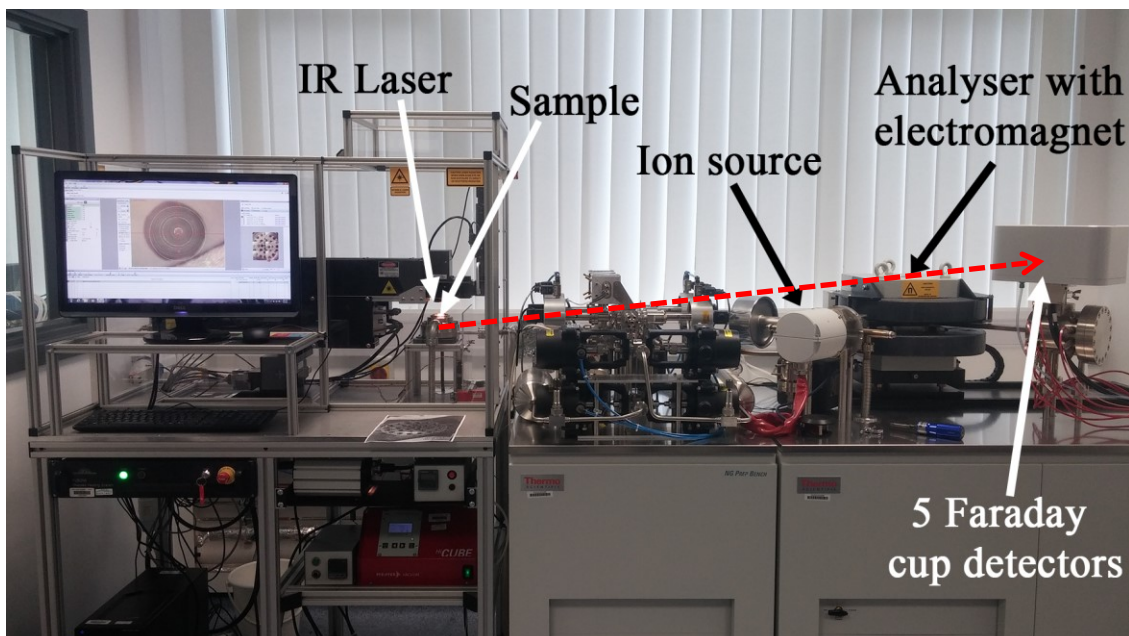


Fig. 2.20. Thermo Scientific Argus VI mass spectrometer, University of Manchester. The red dotted line shows the overall direction of the gas given off when the laser is fired at the sample, which travels through the preparation system before being ionised, where it is then analysed using a magnetic field of particular strength to deflect ions with the desired mass/charge ratios into the Faraday cup detectors.

The infrared 55 W CO₂ laser (Teledyne-Cetac Technologies Fusion 10.6 CO₂ laser system) was fired at each sample for 30 seconds in step heated intervals starting at 0.4% power (0.21 W), until it had all disintegrated (by 6 W). The laser beam had uniform energy distribution and was 3 mm in diameter with accelerating voltage of 2.5 kV. Between five and eleven steps were obtained for each sample, until the sample

fused. Before the noble gases were admitted to the mass spectrometer, a Zr-Al getter (SEAES NP10) was used to purify them for three minutes at 400 °C. The Thermo Scientific Argus VI mass spectrometer (Fig. 2.20) equipped with 5 Faraday detectors measured the argon isotopes.

Due to the presence of ^{40}Ar in the air, procedural blanks were analysed as a step without laser heating. The ^{40}Ar blank (equivalent to $2.68 \times 10^{-12} \text{ cm}^3$ at standard temperature and pressure) was monitored after every third heating step, staying relatively stable with less than 15% variation during all the experiments. Generally less than 30% (range 8% to 50%) of the ^{40}Ar released at each laser heating step corresponded to the blank levels. Aliquots of air with known volumes of Ar allowed the sensitivity of the instrument to be calculated and raw data to be converted to cm^3 at standard temperature and pressure. Air aliquots with a $^{40}\text{Ar}/^{36}\text{Ar} = 298.6$ were used to check the mass discrimination of the instrument and to apply a linear mass fractionation correction.

Neutron interference reactions, whereby K and Ca isotopes form Ar isotopes, were determined from examining high purity calcium fluoride and potassium sulphate samples. Aliquots of the international standard Hb3gr hornblende $t = 1081.0 \pm 2.4 \text{ Ma}$, 2σ ; (Renne et al., 2011) were irradiated with the unknown samples and then measured for ^{40}Ar - ^{39}Ar , in order to determine the fluence parameter J , which relates to the density of the neutron particle flux during the irradiation process, and α .

3 THERMAL HISTORY OF MARTIAN REGOLITH BRECCIA NORTHWEST AFRICA 8114

The majority of this chapter is in press at the journal *Geochimica et Cosmochimica Acta* (MacArthur et al., 2018). Scans provided by two of the co-authors and ^{40}Ar - ^{39}Ar dating work done with two collaborators at the University of Manchester are acknowledged in the text of the relevant sections. Other co-authors provided assistance, technical support with setting up instrumentation and feedback in their field of expertise.

3.1 Introduction

Meteorite Northwest Africa NWA 8114 and its paired stones, NWA 7034, 7475, 7533, 7906, 7907, 8171, 8674, 10922, 11220, 11522 and Rabt Sbayta 003 (all known as the martian breccia) provide the first opportunity to study an impact breccia from the surface or near-surface of Mars. The martian origin is confirmed from a trapped noble gas component similar to the modern martian atmosphere (Cartwright et al., 2014) together with oxygen isotope $\Delta^{17}\text{O}$ values that match and exceed those of other martian meteorites (Agee et al., 2013; Nemchin et al., 2014). The martian breccia contains a

wide range of crystalline clasts from low-Ca pyroxene to plagioclase and alkali feldspar, although olivine is largely absent. Iron oxides, Cl-apatite, chromite, and pyrite are also present in clasts and within the fine-grained matrix (Agee et al., 2013; Humayun et al., 2013; Muttik et al., 2014; Santos et al., 2015; Wittmann et al., 2015). Many of the pyroxene clasts exhibit exsolution lamellae with characteristics that indicate slow cooling rates and a range of parent rocks and formation depths, so must have developed prior to incorporation into the breccia (Leroux et al., 2016). There is also a diverse range of basaltic and alkaline igneous clasts (Santos et al., 2015) that were interpreted to be of impact melt origin (Humayun et al., 2013; Hewins et al., 2017).

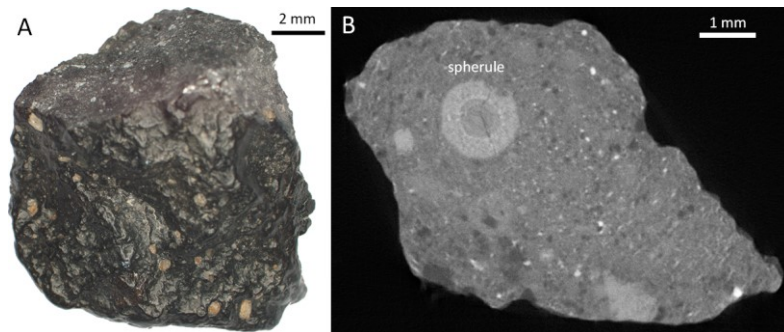


Fig. 3.1. (A) Main mass of NWA 8114 (~1.5 g) with visible clasts up to 0.5 mm in size. (B) A CT image of a slice from the middle of the NWA 8114 main mass, showing a 1.5 mm diameter spherule with concentric structure and layers.

Accretionary clasts and dust rims are also present in the martian breccia and may have formed in an ejecta plume (Wittmann et al., 2015). Melt spherules and clast-laden impact melt fragments have been identified in NWA 7533 (Humayun et al., 2013; Hewins et al., 2017), similar to melt clasts in NWA 7034 (Agee et al., 2013; Santos et al., 2015) and vitrophyre clasts in NWA 7475 (Wittmann et al., 2015). High Ni (1020 ppm) was measured in a vitrophyric clast confirming this as an impact melt product (Udry et al., 2014). Therefore, these polymict martian breccias have similarities to terrestrial suevite associated with base surges (i.e. density currents) (Wittmann et al., 2015; Hewins et al., 2017). Suevites are (usually polymict) impact breccias that contain inclusions of impact melt lithologies and the clastic matrix additionally contains melt particles (Stöffler & Grieve, 2007).

McCubbin et al. (2016) suggested that an impact process analogous to a pyroclastic fall deposit is responsible for the formation of the martian breccia samples, due to the clast

size and shape distribution. Regolith breccias are a subgroup of consolidated clastic impact debris that contain matrix melt and melt particles (Stöffler & Grieve, 2007).

The wide variety of ages found in the meteorite breccia suggests a complex history of its clast source terrains. Nyquist et al. (2016) found disturbed Rb-Sr systematics and a Sm-Nd isochron age of 4.42 ± 0.02 Ga interpreted as a “bulk” crystallisation age for the breccia components. This age is consistent with 4.3-4.4 Ga U-Pb ages obtained from zircons in monzonitic clasts or breccia matrix, whereas chlorapatite and some zircons yield younger U-Pb ages 1.35-1.7 Ga, possibly recording the effects of impacts that disturbed the Rb-Sr system (Humayun et al., 2013; Bellucci et al., 2015; McCubbin et al., 2016). The latter may represent the formation of the breccia from ancient precursor materials (Wittmann et al., 2015; Nyquist et al., 2016; Leroux et al., 2016). Further high precision U-Pb ages of seven zircons yield ages of 4.4763 ± 0.0009 Ga to 4.4297 ± 0.0001 Ga (Bouvier et al., 2018). The cosmic ray exposure age indicating the ejection event is suggested to be ~ 5 Ma (Cartwright et al., 2014).

Hydrated iron oxides have been identified in NWA 7034 (Muttik et al., 2014; Beck et al., 2015), and monazite-bearing apatite in the meteorite is thought to have required fluids and temperatures above 100 °C (Liu et al., 2016). The presence of hyalophane in veins in a spherule in paired rock NWA 7533 is consistent with hydrothermal activity (Hewins et al., 2017). NWA 7034 is the most oxidised known martian meteorite (Agee et al., 2013) as shown by the presence of maghemite and goethite (Gattacceca et al., 2014). These results suggest that this breccia, or components of it, might have experienced near-surface aqueous alteration. The high hydration of bulk NWA 7034 with ~ 6000 ppm water, shows two distinct δD components (Agee et al., 2013). While the high-temperature component $+300$ ‰ is most likely martian in origin, the low-temperature component with δD of -100 ‰ could reflect contamination by terrestrial water (Agee et al., 2013). A terrestrial origin for some of this hydration is likely, and NanoSIMS D/H analyses of δD of 10 ± 85 ‰ show a terrestrial origin for Fe oxyhydroxides through alteration of pyrite (Lorand et al., 2015). Further studies of the water content of paired stone NWA 7533 estimated ~ 8000 ppm (Beck et al., 2015) but Remusat et al. (2015) found less than 3600 ppm of martian water, with ilmenite containing 2000 ppm to 3600 ppm of water with δD between 1370 and 3130‰ and apatite containing 560 ppm to 3050 ppm of water with δD between 250 and 2230‰.

Any martian hydrous alteration in the breccia might be consistent with what has been determined through NIR spectroscopy (CRISM, OMEGA) of impact craters from orbit, some of which have been hypothesized to have preserved long-lived hydrothermal systems in the near-surface (Poulet et al., 2005; Bibring et al., 2006; Mustard et al., 2008; Schwenger & Kring, 2009; Marzo et al., 2010; Ehlmann, Mustard, Clark, et al., 2011; Ehlmann, Mustard, Murchie, et al., 2011; Mangold, Carter, et al., 2012)(Poulet et al., 2005; Bibring et al., 2006; Mustard et al., 2008; Schwenger & Kring, 2009; Ehlmann, Mustard, Clark, et al., 2011; Ehlmann, Mustard, Murchie, et al., 2011) These are more commonly seen in and around Noachian and Hesperian aged impact craters but are thought to be rarer during the Amazonian (Turner et al., 2016).

We use a combination of CT scanning, STEM, EDX, EPMA and synchrotron Fe-K XANES, XRD, FTIR to characterise the different mineralogical stages recording NWA 8114's thermal evolution and interaction with water. Four individual clasts were separated for ^{40}Ar - ^{39}Ar attempted age determinations. The goal is to constrain the formation and thermal history of the parent rocks, characterise high temperature effects in the regolith from the impact-forming event and investigate any interaction with water that it has experienced.

3.1.1.1 Clast Nomenclature

As this breccia is the first of its type, different authors have used various descriptive terms from volcanic, rock and mineral terminology to describe clasts and features within it. Table 3.1 provides a summary of some of the main classifications and terms and how they correspond between authors and with this study.

Chapter 3: Thermal History of Martian Regolith Breccia

Table 3.1. Different classifications of clasts within the martian breccias as described by different authors.

Agee et al. (2013)	Humayun et al. (2013)	Santos et al. (2015)	Wittmann et al. (2015)	Leroux et al. (2016)	Hewins et al. (2017)	This work
		Proto-breccia clasts	Sedimentary siltstone clasts		Fine grained sedimentary clasts	
Gabbroic clasts	Fine grained basaltic clasts, microbasalts Lithic plutonic noritic clasts	Basalt clasts Basaltic andesite clasts	Granular & subophitic clasts	Medium- and coarse-grained lithic clasts dominated by magmatic pyroxenes and feldspars	Fine grained basaltic clasts, microbasalts Lithic plutonic noritic clasts, containing inverted pigeonite & exsolution lamellae	
	Lithic plutonic monzonitic clasts	Trachyandesite clasts	Feldspathic clasts		Lithic plutonic monzonitic clasts	
Apatite-ilmenite-alkali feldspar cluster		Fe, Ti, P rich (FTP) clasts	Basalt clasts with ophitic textures of plag, K-spar, ilmenite, chlorapatite		Fe, Ti, P rich (FTP) clasts	
	Lithic leucocratic rock Clast II (NWA 7533-3)		Poikilitic noritic melt clasts			
	Crystal clasts, px and fp	Single mineral fragments	Monomineralic clasts, px and fp fragments		Crystal clasts, px and fp	Monomineralic clasts, px and fp
			Strongly shocked clasts, feldspar & px			Relict pyroxene clasts

Chapter 3: Thermal History of Martian Regolith Breccia

<p>Quenched melt clasts and reaction spheres “Plumose” groundmass</p>	<p>Clast-laden impact melt rock (CLIMR), melt rock, melt spherules Impact melt clasts</p>	<p>Melt clasts and reaction spheres shards, melt spherules</p>	<p>Vitrophyre impact melt clasts, melt shards, melt spherules</p>	<p>Clast-laden impact melt rock (CLIMR), melt rock, melt shards Melt spherules: microcrystalline, vitrophyric and altered</p>	<p>Spherule with accreted rim Clump-like aggregates of orthopyroxene surrounded by aureoles of plagioclase (within CLIMR) Relict pyroxene clasts with feldspar aureole</p>
---	--	---	---	--	--

3.2 Methods and samples

The 1.9 g main mass of NWA 8114 (Fig. 3.1) was found in 2013 and obtained by the University of Leicester, with classification reported by Ruzicka et al., (2015). The stone was split into two pieces. From the type specimen, held at the University of Leicester, a polished thin section (A) (Fig. 3.2), two polished thick sections (B, C), a polished block (D) and a double-polished wafer (F) of NWA 8114 were prepared. Four clasts were physically separated from the NWA 8114 stone, and split, with one half of each clast for ^{40}Ar - ^{39}Ar analyses at the University of Manchester, and the other fragments for complementary mineralogical studies.

3.2.1 SEM-EDX, EPMA and CT Scanning

Sections A, B, C, D, F were characterised using a Philips XL30 environmental scanning electron microscope (ESEM) and a Hitachi S-3600N ESEM with Oxford INCA 350 EDX spectroscopy system at the Advanced Microscopy Centre the University of Leicester. Back-scattered electron (BSE) images and normalised EDX spectroscopy element data for point analyses were obtained using an accelerating voltage of 20 kV and beam current of ~ 1.0 nA.

Standardised X-ray element maps of section C (Fig. 3.3) were generated using a JEOL 7001F FEG-SEM with Oxford Instruments X-Max 50 mm² energy dispersive spectroscopy (EDS) detector by collaborator Dr Natasha Stephen within Plymouth Electron Microscopy Centre at the University of Plymouth.

A detailed mineralogical map and modal mineralogy of section A (Fig. 3.2B) were obtained by collaborator Dr Elisabeth Steer using a Quanta 600 ESEM with two Bruker EDS spectrometers at the University of Nottingham.

EPMA data were obtained for pyroxenes and iron oxides in sections A, B, C using a Cameca SX100 at the Open University, with TAP, LTAP, LLiF, LPET and PET spectrometer crystals, a focused 1 μm beam, at an accelerating voltage of 20 kV and beam current of 20 nA.

An X-ray micro computerised tomography (CT) scan was taken of the remainder of the 1.9 g NWA 8114 main mass (after sections A-D were prepared, but before further material was consumed in preparing sections F) using a Nikon Metrology XT H 225

scanner at the University of Leicester. This provides a 3D image at high resolution of the internal structure and the composition of the bulk sample, processed using *VG Studio Max* (version 3) software (VG, 2017). The voxel size was $8 \times 8 \times 8 \mu\text{m}$.

3.2.2 FIB-SEM and TEM-STEM-EDX

Electron-transparent wafers were prepared using an FEI Quanta 200 3D dual Focused Ion Beam (FIB-SEM) at the University of Leicester from selected regions of interest in the clasts, using the methods described in section 2.2.3.

The wafers were analysed on a JEOL 2100 LaB₆ transmission electron microscope (TEM) with scanning-TEM (STEM) facilities and an Oxford Instruments system with Aztec EDX at the University of Leicester. All TEM, STEM and EDX work was carried out using an accelerating voltage of 200 kV and beam current of $\sim 110 \mu\text{A}$. STEM-EDX is described in more detail in sections 2.2.4 and 2.2.5.

3.2.3 Synchrotron techniques at the *Diamond Light Source*

The microfocuss beamline I-18 at the Diamond Light Source, Didcot, Oxfordshire, UK was used to determine the oxidation state of the Fe in NWA 8114 by analysing the $1s \rightarrow 3d$ transitions and characteristic absorption edge energy in the Fe-K XANES spectra. The beamline has an energy range of 2.0-20.7 keV, and a minimum spot size resolution of $\sim 2 \times 2.5 \mu\text{m}$, together with tuneable monochromators capable of resolving 0.1 eV spectra energy increments (Mosselmans et al., 2009).

3.2.3.1 Synchrotron X-ray Fluorescence (XRF)

XRF maps of the areas of interest were taken with a resolution of $2 \times 2.5 \mu\text{m}$ primarily to locate the iron for Fe-K XAS analyses. XRF measures elements up to Zn in atomic weight to produce elemental maps using a beam between 8.5 and 10.0 keV. These maps were analysed using *PyMca 4.4.1* software.

3.2.3.2 Fe-K X-ray Absorption Spectroscopy (Fe-K XANES)

Fe-K X-ray Absorption Near Edge Spectroscopy XANES measurements were taken at $2 \times 2.5 \mu\text{m}$ spot size. The spectra were taken over an energy range of 6900-7600 eV, with a high resolution of 0.1 eV over the region 7090-7145 eV, to accurately capture the $1s \rightarrow 3d$ pre-edge centroid and absorption edge positions. The data were processed and normalised through *Athena 0.9.24* software before analysing the $1s \rightarrow 3d$ pre-edge

centroids by fitting a baseline and calculating the energy position of the centroid, using the methods of Hicks et al. (2014). The proportion of Fe³⁺ to total iron ratio, Fe³⁺/ΣFe, has been calculated using the silicate calibration scale (Hicks et al., 2014). In addition to point measurements, Fe-K XANES maps were made of two areas to show the variation in iron oxidation state visually over the absorption edge energy range 6900-7300 eV, with the Fe-K XANES spectra for each pixel being normalised and analysed using *MANTISt 2.06*. An energy calibration was used derived in order to compare data measured during four separate beamtime sessions, as detailed in section 2.3.1.3.

3.2.3.3 Transmission X-ray Diffraction (XRD)

The same I-18 beamline was used for transmission XRD measurements of a variety of clasts taken at 13 keV for between 60 and 300 s with a detector capable of imaging 2θ angles ranging between ~4° and ~40°. This corresponds to an observable *d*-spacing range of ~1.4 Å to ~13.7 Å. Measurements on a LaB₆ standard with *Dawn 1.9* software (Basham et al., 2015) were used to calibrate the NWA 8114 data and obtain the *d*-spacings from the raw data. These were compared with measurements of other standards, magnetite, goethite, pyroxene, hematite etc and the ICDD database (ICDD, 2014) to identify the closest mineral match. Unit cell parameters were calculated after assigning *hkl* indices to the *d*-spacings and compared to unit cell parameters of mineral standards from the ICDD database (ICDD, 2014).

3.2.3.4 Fourier Transform Infrared Spectroscopy (FTIR)

Beamline B-22 at the Diamond Light Source was used to investigate sections A, B, C with reflectance FTIR, and section F with transmission FTIR (Cinque et al., 2011). B-22 has a spectral range of 10000 to 5 cm⁻¹ and beam size of 3-15 μm at the sample, with achievable resolution of 0.07 cm⁻¹. Both point and map measurements were made using a 10 × 10 μm or 15 × 15 μm spot size and resolution of either 4 cm⁻¹ (with 256 scans) or 8 cm⁻¹ (with 128 scans), with a spectral range of 4000–500 cm⁻¹. *OPUS 7.0* (Bruker Optik GmbH 2011) software was used to process the data and a Kramers-Kronig Transformation within it was used to obtain absorbance values from reflectance data.

3.2.4 ⁴⁰Ar-³⁹Ar dating

Four individual clasts were separated from NWA 8114 and subdivided into two fragments to investigate age and petrologic relationships. One fragment of each clast,

with estimated masses of 0.5-0.7 mg, was neutron-irradiated for ^{40}Ar - ^{39}Ar age determinations using the methodology described in section 2.5. The other fragment of each clast was mounted on carbon to characterise the mineralogy using SEM. The clast 3 fragment was subsequently made into a polished block for SEM-EDX analysis.

The data is uncorrected for martian (or terrestrial) trapped ^{40}Ar components, giving approximate maximum $^{40}\text{Ar}/^{39}\text{Ar}$ ages to compare to other radiometric ages from the martian breccia in the literature.

3.3 Results

3.3.1 Breccia and Clast Textures

NWA 8114 has a fresh distinctive black outer surface, a desert varnished relict of a fusion crust, with some visible feldspar and pyroxene clasts protruding (Fig. 3.1A) and a large spherule with concentric layers (Fig. 3.1B). However, minor terrestrial salt veins are apparent on the surface and in some of the polished sections. Some fracturing is seen, but no shock melt veins or maskelynite have been observed. The CT-scan in Fig. 3.1B shows a large spherule of diameter 1.5 mm with a central grain of ~ 0.6 mm and multiple further concentric layers including a fine-grained outer rim, similar to a spherule described by Wittmann et al. (2015) and another spherule described by Hewins et al. (2017).

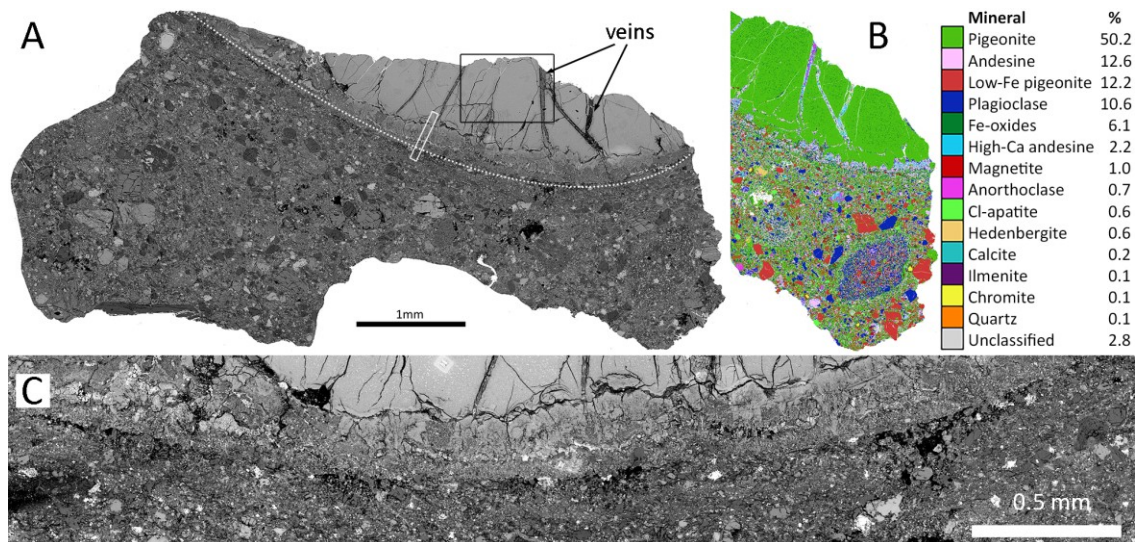


Fig. 3.2. (A) BSE image of section A of NWA 8114 showing varied clasts in the fine grained matrix. The black box denotes part of a large predominantly relict pigeonite clast where two FIB-TEM sections were taken (Fig. 3.12), the white box shows the area examined with Fe-K XANES (Fig. 3.13). Veins can be seen cutting the relict pigeonite clast and the partially melted accreted rim (white dotted line). (B) Mineral Liberation Analysis (MLA) map of the right hand side of section A. (C) Part of the accreted rim indicated by the white dotted line in A, shown at higher resolution with evidence of melting.

NWA 8114 has similar textural and mineralogical features to those described in NWA 7034 (Agee et al., 2013; Santos et al., 2015), NWA 7533 (Hewins et al., 2017; Humayun et al., 2013) and NWA 7475 (Wittmann et al., 2015). In section, the sample has a clastic, brecciated texture comprised of clasts of feldspar grains (26%), pyroxene (18%), Fe-Ti oxides (6%), small amounts of Cl-apatite as well as some melt rock, all

bound by a dark, fine grained matrix (50%). The SEM images of the sections (Fig. 3.2A, Fig. 3.3) show the range of clast size (5 μm to a few mm), and clast shape (from angular to rounded) bound in the fine grained ($<5 \mu\text{m}$) crystalline matrix. The pyroxenes are the main focus of this study, but alkali feldspar clasts were identified with cryptoperthite textures (Fig. 3.4H) indicating slow cooling for them at sub-solidus temperatures. An iron oxide intergrowth has a Ti-rich centre (Fig. 3.4C) and some iron oxide clasts contain pyrite inclusions (Fig. 3.4I), similar to those studied by Lorand et al. (2015), who found Fe-oxides to be terrestrial weathering products of martian pyrites.

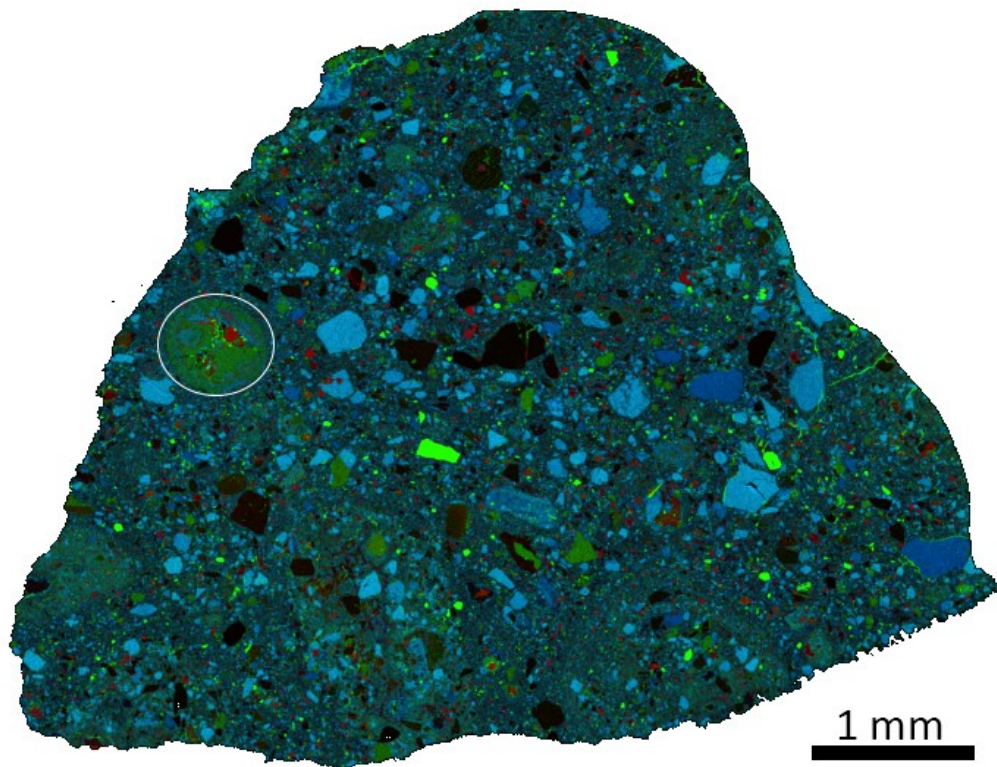


Fig. 3.3. Standardised EDS, combined X-ray element map of section C, where Fe=red, Ca=green, Al=blue. Thus, pyroxenes are dark green, iron oxides are red, plagioclase light blue, K-feldspar dark blue, Cl-apatite bright green. The black clasts are mostly Mg-rich pyroxene. The relict pyroxene with feldspar aureole, containing a goethite clast (Fig. 3.7), is shown by the white ellipse.

Many of the pyroxene clasts exhibit exsolution lamellae on the (001) lattice planes, including both augite lamellae in clasts which are mainly pigeonite pyroxene (Fig. 3.4D and F), and pigeonite lamellae in bulk augite clasts (Fig. 3.4E, Fig. 3.5). Some pyroxene clasts, including low-Ca pigeonite and augite, contain small crystals ($<2 \mu\text{m}$) of iron oxide (Fig. 3.4A,B,D-G, Fig. 3.6, Fig. 3.7A), like those examined by Leroux et al. (2016).

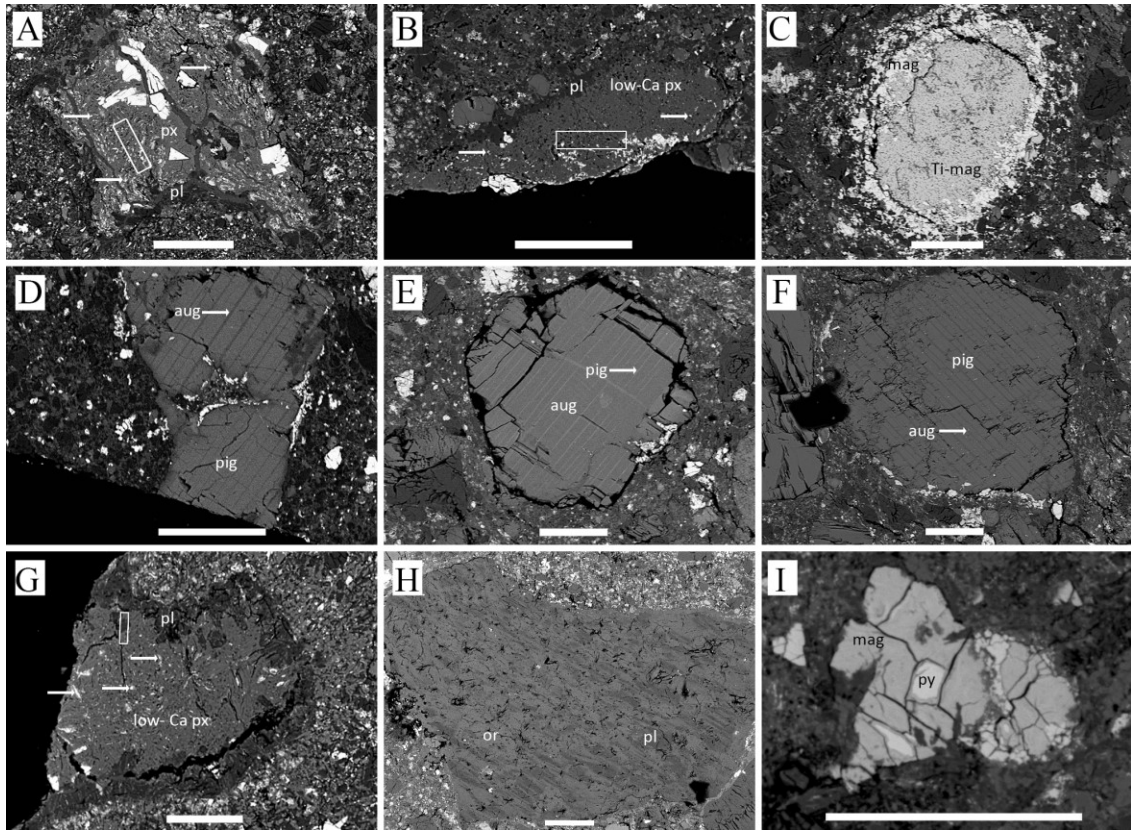


Fig. 3.4. Clasts from polished sections of NWA 8114, scale bars all 50 μm , white rectangles show FIB-TEM section locations (Fig. 3.11, Table 3.3). Px=pyroxene, aug=augite, pig=pigeonite, pl=plagioclase, or=orthoclase, mag=magnetite, py=pyrite. (A) Relict pyroxene $\text{En}_{53}\text{Fs}_{19}\text{Wo}_{28}$ with iron oxide grains (arrows), porosity and plagioclase $\text{An}_{25-55}\text{Ab}_{44-75}$ aureole, showing concave outer surfaces (FIB6). (B) Low-Ca relict pyroxene $\text{En}_{72}\text{Fs}_{26}\text{Wo}_2$ with iron oxide grains (arrows), porosity and $\text{An}_{40-52}\text{Ab}_{43-56}\text{Or}_{3-4}$ plagioclase aureole (FIB7). (C) Ti-rich magnetite core intergrowth with magnetite rim. (D) Bulk pigeonite $\text{En}_{44}\text{Fs}_{50}\text{Wo}_6$ with augite $\text{En}_{37}\text{Fs}_{26}\text{Wo}_{37}$ exsolution. (E) Bulk augite $\text{En}_{31}\text{Fs}_{24}\text{Wo}_{45}$ with pigeonite $\text{En}_{36}\text{Fs}_{47}\text{Wo}_{17}$ exsolution. (F) Bulk pigeonite $\text{En}_{52}\text{Fs}_{43}\text{Wo}_5$ with augite $\text{En}_{42}\text{Fs}_{18}\text{Wo}_{40}$ exsolution with iron oxide grains. (G) Low-Ca $\text{En}_{68}\text{Fs}_{30}\text{Wo}_2$ relict pyroxene with iron oxide grains, porosity and $\text{An}_{32-48}\text{Ab}_{49-63}\text{Or}_{2-5}$ plagioclase aureole (FIB2). (H) Cryptoperthite $\text{An}_{2-10}\text{Ab}_{8-95}\text{Or}_{3-91}$ feldspar. (I) Small pyrite inclusion in magnetite.

Some relict pyroxene fragments show strikingly high porosity of up to $\sim 5\%$ (Fig. 3.4A,B,G, Fig. 3.7A). These have plagioclase-rich rims (Fig. 3.4A,B,G) similar to clump-aureole structures (Hewins et al., 2017). The relict pyroxene with feldspar aureole (Fig. 3.4B) resembles dustball-like aggregates described by Hewins et al. (2017), Fig.S2d). The pyroxene clasts have been investigated further with STEM, XAS and XRD (Section 3.4).

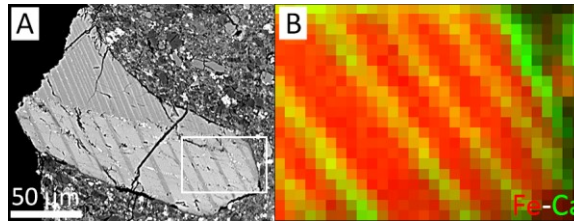


Fig. 3.5. (A) BSE image of an exsolution pyroxene clast, pigeonite composition $\text{En}_{41}\text{Fs}_{53}\text{Wo}_6$, augitic lamellae $\text{En}_{33}\text{Fs}_{26}\text{Wo}_{41}$ (C26, Fig. 3.8). (B) XRF map of the white box area in (A) showing Ca (green) and Fe (red) at $2\ \mu\text{m}$ per pixel resolution.

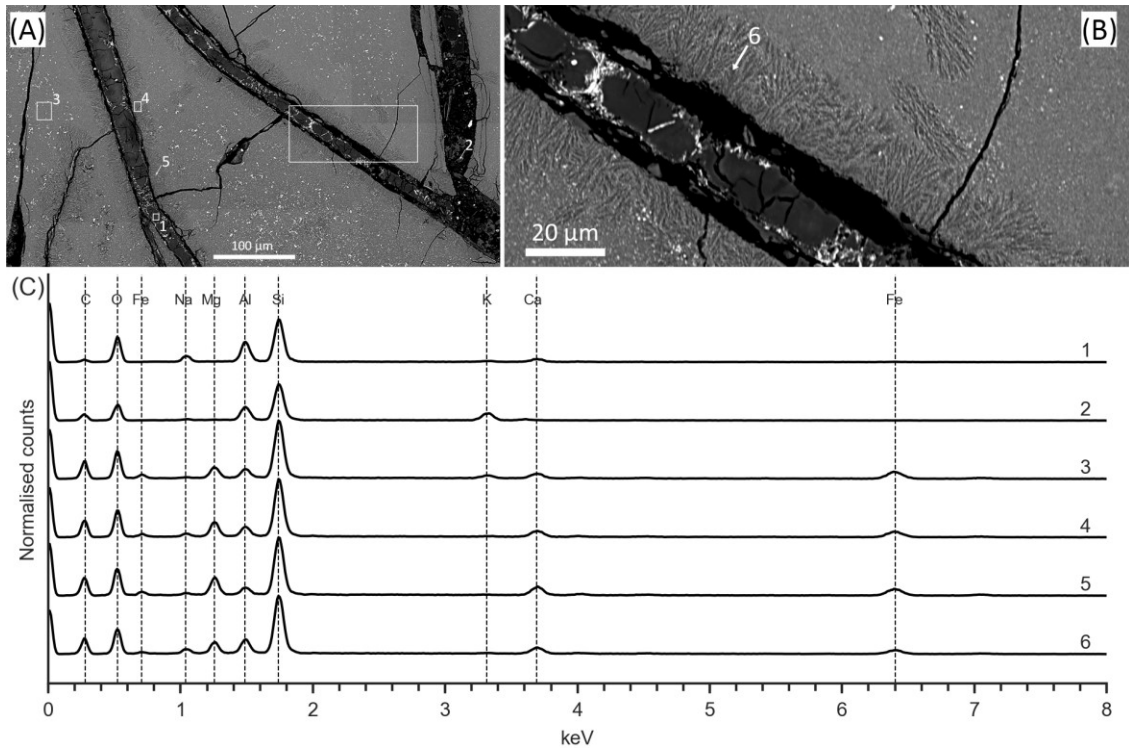


Fig. 3.6. BSE images of the large relict pigeonite clast from Fig. 3.2 showing (A) veins containing plagioclase feldspar. (B) Close up of the white box region from A, showing the partial melting beside the vein. (C) SEM-EDX spectra for locations 1-6 shown in A and B: (1) An area of feldspar $\text{An}_{18}\text{Ab}_{55}\text{Or}_{27}$ in the vein. (2) A point measurement of orthoclase $\text{Ab}_{13}\text{Or}_{87}$ in the vein. (3) An area of pigeonite with iron oxide grains (white). (4) Bulk composition of $\sim 20\ \mu\text{m}$ region each side of the vein containing (5) light grey stoichiometric pyroxene $\text{En}_{37}\text{Fs}_{42}\text{Wo}_{21}$ and (6) dark dendrites relatively enriched in Al, Na and K and depleted in Mg and Fe compared with the pyroxene.

Some angular clasts have fine-grained rims and feldspar veining as well. Some clasts show signs of limited melting taking place after the clast formed. One example of this is shown by the large relict pyroxene clast with iron oxide grains crosscut by feldspathic veins (Fig. 3.2, Fig. 3.6). In a region spanning $\sim 20\ \mu\text{m}$ either side of each vein there are fewer iron oxide grains and backscattered electron images show

devitrification and resultant microcrystalline axialites (Fig. 3.6B). In the same clast, the feldspar veins are truncated by a rim with accreted grains of up to 100 μm . This rim contains the ends of the veins and feldspar, giving evidence of melting with subsequent devitrification (Fig. 3.2C).

One clast consists of a 600 μm iron oxide grain (Fig. 3.7B) that is partially surrounded by terrestrial calcium carbonate veins. It also contains inclusions of pyrite and FeTi oxide. The data in section 3.5 demonstrates that this clast is composed of goethite.

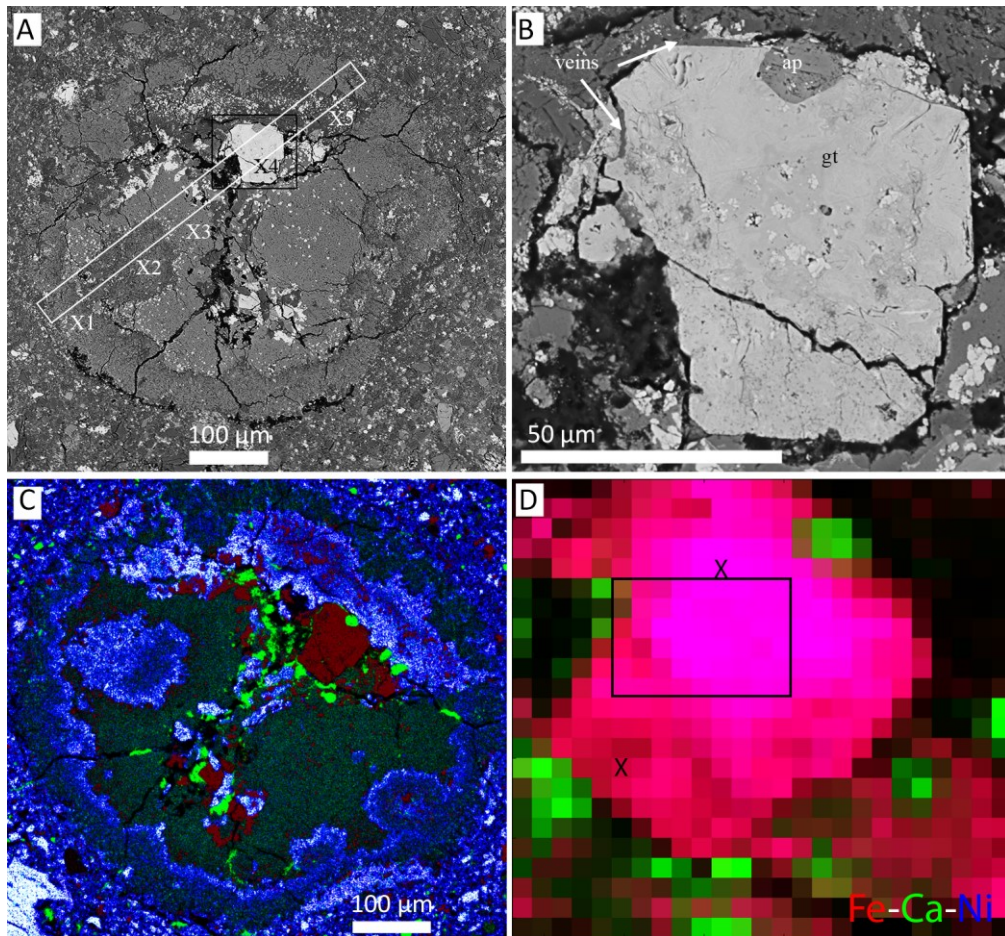


Fig. 3.7. BSE images of (A) Relict pyroxene ($\text{En}_{41-48}\text{Wo}_{26-39}\text{Fs}_{17-29}$), with plagioclase aureole ($\text{Ab}_{51-65}\text{An}_{18-40}\text{Or}_{2-22}$) and iron oxide grains. The black box highlights the goethite inclusion shown in B; the white box area was examined with Fe-K XANES (Fig. 3.13) and the X1-X5 points show XRD measurement locations (Table 3.5). (B) Goethite (gt) grain cross cut by calcium carbonate veins, with CI-apatite (ap) inclusion. (C) Standardised EDS, combined X-ray element false-colour element distribution map of A, Fe = red, Ca=green, Al=blue. (D) 5 μm synchrotron XRF map of the goethite grain, with the location of the XRD map (black rectangle) and XANES measurements (X), Fe is red, Ca is green, Ni is blue.

3.3.2 Mineral Compositions

NWA 8114 relict pyroxene clasts without exsolution lamellae include low-Ca pyroxene and pigeonite (Fig. 3.4B and G, Fig. 3.8) $\text{En}_{44-72}\text{Fs}_{26-50}\text{Wo}_{2-6}$, and augite (Fig. 3.4A, Fig. 3.8) $\text{En}_{31-53}\text{Fs}_{19-24}\text{Wo}_{28-45}$. Compositions of pyroxene clasts with exsolution lamellae are plotted in Fig. 3.8 and are similar to the ranges seen in the pyroxene clasts without exsolution lamellae. These include bulk pigeonite $\text{En}_{44}\text{Fs}_{50}\text{Wo}_6$ with augite $\text{En}_{37}\text{Fs}_{26}\text{Wo}_{37}$ exsolution lamellae (Fig. 3.4D), bulk augite $\text{En}_{31}\text{Fs}_{24}\text{Wo}_{45}$ with pigeonite $\text{En}_{36}\text{Fs}_{47}\text{Wo}_{17}$ exsolution lamellae (Fig. 3.4E) and bulk pigeonite $\text{En}_{52}\text{Fs}_{43}\text{Wo}_5$ with augite $\text{En}_{42}\text{Fs}_{18}\text{Wo}_{40}$ exsolution lamellae (Fig. 3.4F), although as the lamellae are only 1-2 μm wide the lamellae compositions may include some of the bulk clast.

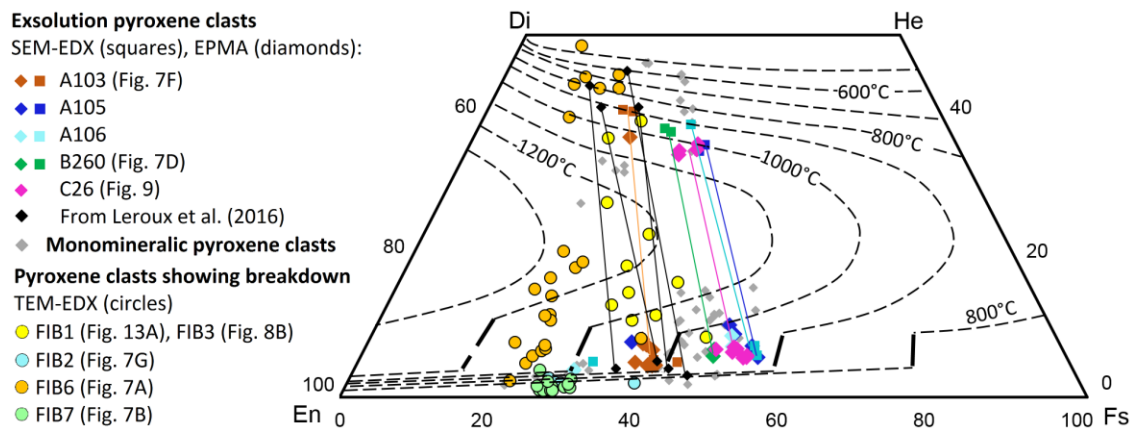


Fig. 3.8. Pyroxene quadrilateral showing: (1) the augite-pigeonite compositions in exsolution clasts with dotted tie lines overlaid on crystallisation temperatures showing a range of crystallisation temperatures from 900 to 1050 °C (Lindsley & Andersen, 1983), measured with EPMA (diamonds) or where lamellae were too narrow, measured with SEM (squares). (2) Monomineralic pyroxene clasts compositions (black diamonds). (3) FIB section compositions from pyroxene clasts showing breakdown measured with TEM-EDX (circles), also shown in Table 3.3.

The large relict pyroxene clast with a fine grained rim (Fig. 3.2A, Fig. 3.6) was found to be predominantly relict pigeonite with SEM-EDX composition $\text{En}_{30-33}\text{Fs}_{49-59}\text{Wo}_{11-18}$ with submicron grains of iron oxide and some likely fine submicron feldspar grains given the spectra show Al_2O_3 at 6.4% and traces of Na_2O 0.7%, and K_2O 2.5% (Table 1, Fig. 6A3). The veins cross-cutting it contained mainly plagioclase $\text{An}_{29}\text{Ab}_{64}\text{Or}_7$ (with a range of $\text{An}_{20-39}\text{Ab}_{60-72}\text{Or}_{0-19}$) though also small amounts of orthoclase $\text{An}_0\text{Ab}_{13}\text{Or}_{87}$ and hyalophane of $\text{An}_{12}\text{Ab}_{30}\text{Or}_{52}\text{Cn}_6$ were found, similar to veins seen in a spherule in paired stone NWA 7533 (Hewins et al., 2017). The $\sim 20 \mu\text{m}$ melt areas each side of the veins were found to be composed of stoichiometric pyroxene

$\text{En}_{37}\text{Fs}_{42}\text{Wo}_{21}$ (Table 3.2) in the light crystallites (Fig. 3.6A5), while the dark areas in BSE SEM images (Fig. 3.6A6) were non stoichiometric and relatively enriched in Al, Na and depleted in Fe, Mg and Ca compared to the light crystallites (Fig. 3.6A5, Table 3.2), likely feldspathic but the SEM spot size was too large to capture just stoichiometric feldspar and still included pyroxene.

The feldspar clasts compositions are $\text{An}_{12-46}\text{Ab}_{50-82}\text{Or}_{0-25}$ and alkali feldspar clasts show cryptoperthite texture with a range of $\text{An}_{0-10}\text{Ab}_{8-95}\text{Or}_{3-92}$ or $\text{An}_{1-5}\text{Ab}_{11-86}\text{Or}_{11-88}$ (Fig. 3.4H, Fig. 3.9). The compositional range of plagioclase-rich rims on pyroxene clasts is andesine, $\text{An}_{30-55}\text{Ab}_{43-66}\text{Or}_{2-5}$ (Fig. 3.4A,B,G, Fig. 3.9), which closely matches the range of plagioclase seen in the veins cutting the spherule (Fig. 3.2B).

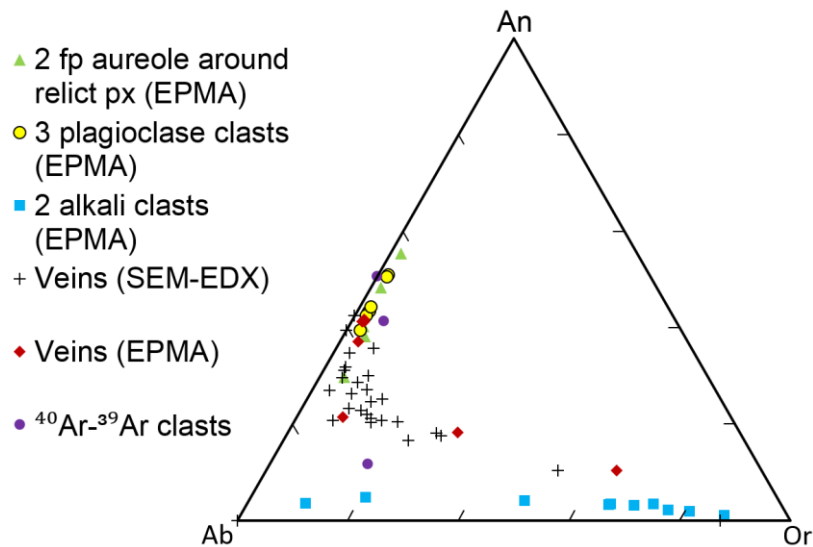


Fig. 3.9. Mineral compositions of feldspars, showing similarity between plagioclase in the veins, the plagioclase bordering pyroxene clasts (Fp borders), and in monomineralic plagioclase clasts. The K-rich feldspar clast compositions also match the K-rich feldspar found in the veins.

The EPMA map of the relict pyroxene clast with a plagioclase aureole (Fig. 3.7C) shows the areas with more plagioclase grains (blue = Al) ($\text{An}_{18-40}\text{Ab}_{51-65}\text{Or}_{2-22}$) versus those with more pyroxene grains (dark green = Ca with Fe) ($\text{En}_{41-48}\text{Fs}_{17-29}\text{Wo}_{26-39}$). Two measurements of the Fe oxide grain marked 'gt' (Fig. 3.7B) showed a total oxide weight of 77.3% and 78.1% (Fe was calculated as Fe^{2+} , (Table 3.2), indicating that it contains Fe^{3+} and/or a hydrated phase. This matches EPMA analyses for goethite in other planetary materials e.g. 75.7% (Zhu et al., 2012) and goethite measured as 86.5% Fe_2O_3 (equivalent to 77.8% FeO) (RRUFF Database, 2006). Both measurements also included 0.9 wt% NiO, which was rarely above 0.1 wt% in other measurements taken

across different clasts (predominantly pyroxene and feldspar) in NWA 8114. The goethite grain contains small amounts of Si, Al, Ti, S and P, consistent with possible titanomagnetite and pyrite and other precursor material. The goethite is likely a pseudomorph after euhedral pyrite, inheriting the Ni, similar in shape to pyrite and iron oxides seen in paired stones (Wittmann et al., 2015; Lorand et al., 2015; Hewins et al., 2017).

Other iron oxide grains in NWA 8114 include a Ti-rich magnetite intergrowth (Fig. 3.4C). Pyrite is present in very small quantities and usually within iron oxide clasts. Non-stoichiometric sulfide is also present, and this may be related to alteration. One large grain of Cl-apatite ($240 \times 100 \mu\text{m}$) was observed (Fig. 3.3: bright green), otherwise Cl-apatite is present as $<50 \mu\text{m}$ grains, or dispersed in the matrix.

3.3.2.1 Mineralogy of separated clasts for Ar- Ar

Four clasts that were less than one mm each in diameter were separated from the NWA 8114 stone. Half of each clast was dated using ^{40}Ar - ^{39}Ar (see section 3.3.7). Two clasts were highly zoned plagioclase: Clast 1: $\text{An}_{19-41}\text{Ab}_{53-73}\text{Or}_{5-8}$, Clast 2: $\text{An}_{47-51}\text{Ab}_{40-50}\text{Or}_{0-9}$. Clast 3 is an augitic pyroxene clast $\text{En}_{24-39}\text{Fs}_{13-26}\text{Wo}_{48-50}$ with up to 8% plagioclase inclusions $\text{An}_{12-55}\text{Ab}_{45-74}\text{Or}_{0-18}$ and a marginal band of terrestrial calcite (Fig. 3.9, Fig. 3.10A, Table 3.2). The pyroxene shows porosity of at least 3% throughout, together with small iron oxide grains, similar to relict pyroxene clasts with feldspar aureole seen in the polished sections (Fig. 3.4A,B,G, Fig. 3.7A). Iron oxides, Ti-magnetite and Cl-apatite inclusions were also present in clast 3. Clast 4 is a feldspar-rich clast.

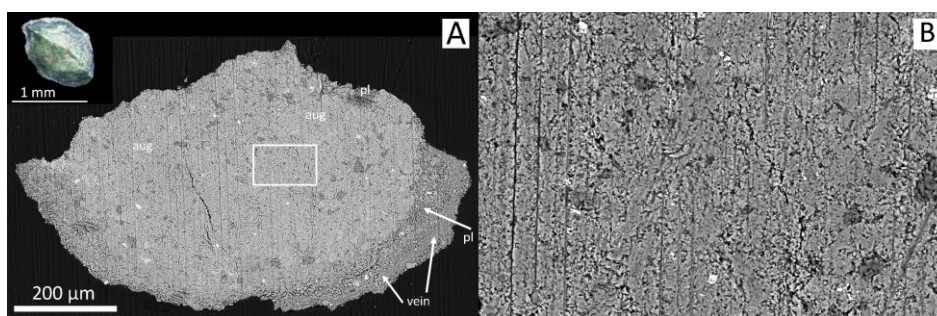


Fig. 3.10. (A) BSE image of part of the poorly polished augite clast 3 analysed with ^{40}Ar - ^{39}Ar in Fig. 3.17, showing predominantly augite (aug) $\text{En}_{24-39}\text{Fs}_{13-26}\text{Wo}_{48-50}$, plagioclase (pl) inclusions, $\text{An}_{12-84}\text{Ab}_{15-74}\text{Or}_{0-17}$ and a calcite vein. (Inset) Microscope image of part of clast 3, showing a rim and green pyroxene. (B) BSE image of augite shown in A (white rectangle) showing porosity (black) and iron oxide grains (white).

Chapter 3: Thermal History of Martian Regolith Breccia

Table 3.2: Representative SEM-EDX and EPMA compositions of the relict pigeonite clast with feldspar veins (Fig. 3.6A), the goethite clast (Fig. 3.7B), the pyroxene exsolution clast (Fig. 3.4F) and clasts 1, 2 (plagioclase = plag) and 3 (augite with plagioclase inclusions), dated with ^{40}Ar - ^{39}Ar (Fig. 3.10).

	SEM	SEM	SEM	SEM	SEM	SEM	EPMA	EPMA	EPMA	EPMA	SEM	SEM	SEM	SEM
	Vein	Vein	Clast	Vein	Vein	Vein	C5	C5	A103	A103	Clast 1	Clast 2	Clast 3	Clast 3
	Fig. 3.6A1	Fig. 3.6A2	Fig. 3.6A3	border: bulk Fig. 3.6A4	border: light Fig. 3.6A5	border: dark Fig. 3.6A6	Goethite Fig. 3.7B	Goethite Fig. 3.7B	Pigeonite Fig. 3.4F	Lamellae Fig. 3.4F	Zoned plag	Zoned plag	Augite Fig. 3.10	Plag. Fig. 3.10F
SiO ₂	62.0	64.7	49.1	49.6	47.2	52.8	3.6	1.8	51.7	51.0	56.6	54.5	53.2	67.2
TiO ₂	nd	nd	1.3	1.1	1.2	1.2	0.1	0.1	0.2	0.4	nd	nd	nd	nd
Al ₂ O ₃	22.5	19.0	6.4	7.1	4.9	10.5	0.2	nd	0.5	1.5	25.4	25.5	0.9	19.8
Cr ₂ O ₃	nd	nd	nd	nd	nd	nd	nd	nd	0.3	0.8	nd	nd	nd	nd
FeO	1.3	nd	26.4	21.5	24.2	15.4	71.8	73.7	25.1	12.7	nd	nd	9.9	nd
MnO	nd	nd	nd	nd	nd	nd	nd	nd	0.7	0.4	nd	nd	nd	nd
NiO	nd	nd	nd	nd	nd	nd	0.9	0.9	nd	nd	nd	nd	nd	nd
MgO	nd	nd	8.0	10.7	12.0	8.5	0.6	nd	19.5	14.7	nd	0.8	12.0	nd
CaO	5.8	nd	5.6	7.1	9.2	7.6	0.9	0.9	2.2	17.0	9.9	12.4	24.1	2.3
Na ₂ O	7.2	1.4	0.7	2.4	1.3	3.6	nd	nd	0.1	0.4	7.0	6.7	nd	7.7
K ₂ O	1.3	14.8	2.5	0.5	0	0.6	nd	nd	nd	nd	1.2	nd	nd	2.9
Total	100.1	99.9	99.9	100.0	100.0	100.2	78.1	77.3	100.3	98.9	100.1	99.9	100.1	99.9
An %	28.6	0.0									41.4	50.6		11.8
Ab %	63.9	12.7									52.8	49.4		70.5
Or %	7.5	87.3									5.8	0.0		17.7
En %					37.3				55.5	43.1				34.4
Fs %					42.1				40.0	21.0				15.9
Wo %					20.6				4.5	35.9				49.7

SEM-EDX given in oxide weight % normalized to 100%.

nd = not detected.

3.3.3 TEM Investigations of Pyroxene Texture

Seven TEM extracted wafers of NWA 8114 relict pyroxenes and their breakdown products were analysed. Two FIB-TEM extractions were taken from the relict pigeonite clast (Fig. 3.2A) containing iron oxide grains (FIB1 and FIB3, Fig. 3.11, Fig. 3.12). TEM-EDX revealed a porphyritic, submicron mixture of a K-bearing feldspathic, glassy material, iron oxide (~10-20%), with the remainder being discrete pyroxene laths up to 500 x 200 nm in size (Fig. 3.12C,D,E). A FIB-TEM extraction from a low-Ca $\text{En}_{72}\text{Fs}_{26}\text{Wo}_2$ relict pyroxene with feldspar aureole (Fig. 3.4B, Fig. 3.11B FIB7) showed the granoblastic texture, with many grain boundaries near 120° , evidence for re-crystallisation of the pyroxene. This clast had porosity of up to ~5%.

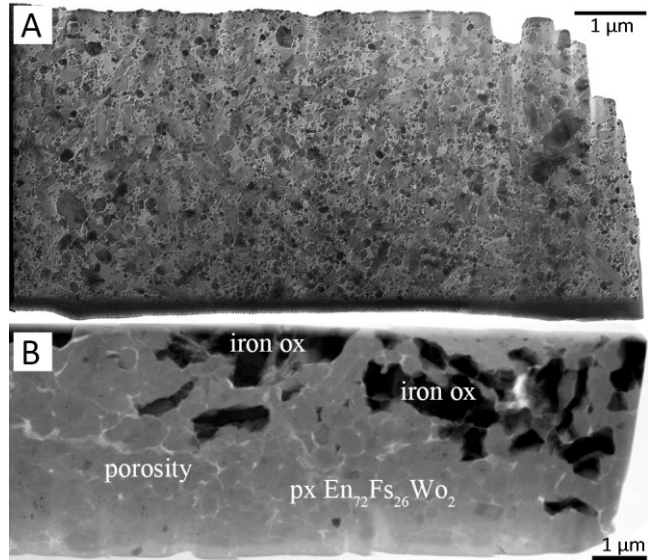


Fig. 3.11. (A) TEM bright field image of FIB1 taken from the relict pigeonite clast (Fig. 3.2A). (B) STEM bright field image of FIB7 taken from the relict pyroxene (px) $\text{En}_{72}\text{Fs}_{26}\text{Wo}_2$ shown in Fig. 3.4B, showing iron oxide (iron ox), porosity and a granoblastic texture with $\sim 120^\circ$ grain boundaries.

Table 3.3 gives TEM-EDX data for pyroxene from FIB1 and FIB3, with compositions ranging $\text{En}_{32-57}\text{Fs}_{21-51}\text{Wo}_{13-38}$, including both pigeonite and augite. The broader beam EPMA data suggests an Fe-rich bulk pyroxene, whereas the finer scale TEM-EDX resolution mostly indicates a lower Fs content in discrete pyroxene. This break down was also seen in another low-Ca relict pyroxene with feldspar aureole, $\text{En}_{65-68}\text{Fs}_{29-33}\text{Wo}_2$ (Fig. 3.4G). Iron oxide grains were present in the pyroxene but no aluminium silicate was observed. The apparent difference in Fs contents of pyroxene between EPMA and TEM-EDX analyses is likely due to submicron iron oxide grains being included in the EPMA point analyses.

Table 3.3: Representative TEM-EDX compositions of the pyroxenes studied, given in oxide weight % normalized to 100%.

Clasts:	Fig. 3.12A A140-FIB1	Fig. 3.12A A140-FIB3A	Fig. 3.12A A140-FIB3B	Fig. 3.4G C29-FIB2	Fig. 3.4A B202-FIB6A	Fig. 3.4A B202-FIB6B	Fig. 3.4B B245-FIB7A
SiO ₂	49.2	52.9	52.5	53.1	55.1	53.4	54.1
TiO ₂	1.0	0.4	0.5	0.8	0.4	0.1	0.4
Al ₂ O ₃	5.6	1.9	3.4	4.8	2.4	4.1	4.4
Cr ₂ O ₃	0.4	0.1	0.1	0.2	0.1	0.1	0.1
FeO	26.6	18.1	12.3	21.0	13.5	6.4	17.0
MnO	0.6	1.0	0.6	0.8	0.8	0.1	0.5
MgO	9.4	19.5	13.2	18.2	26.6	14.9	22.6
CaO	6.9	6.0	17.2	0.9	1.1	20.4	0.7
Na ₂ O	nd	nd	nd	nd	nd	0.1	nd
K ₂ O	0.3	0.1	0.2	nd	nd	0.1	nd
P ₂ O ₅	nd	nd	nd	0.3	nd	0.4	0.1
Total	100.0	100.0	100.0	100.1	100.0	100.1	99.9
Number of ions on the basis of 6 oxygens, for pyroxenes.							
Tetrahedral:							
Si	1.91	1.97	1.96	1.95	1.97	1.94	1.95
Al	0.09	0.03	0.04	0.05	0.03	0.06	0.05
Total:	2.00	2.00	2.00	2.00	2.00	2.00	2.00
Octahedral							
Ti	0.03	0.01	0.01	0.02	0.01	0.00	0.01
Al	0.17	0.05	0.11	0.16	0.07	0.12	0.14
Cr	0.01	nd	nd	nd	nd	0.00	0.00
Fe	0.86	0.56	0.38	0.65	0.40	0.19	0.51
Mn	0.02	0.03	0.02	0.02	0.02	0.00	0.01
Mg	0.54	1.08	0.73	1.00	1.42	0.81	1.22
Ca	0.28	0.24	0.69	0.03	0.04	0.80	0.03
Na	nd	nd	nd	nd	nd	0.01	nd
K	0.01	0.01	0.01	nd	nd	0.01	nd
P	nd	nd	nd	0.01	nd	0.01	0.00
Total:	1.92	1.98	1.95	1.89	1.96	1.95	1.92
En %	32.2	57.2	40.6	59.5	76.1	44.9	69.2
Fs %	50.9	30.0	21.2	38.4	21.6	10.8	29.3
Wo %	16.9	12.8	38.2	2.1	2.3	44.3	1.5

Uncertainties on the values are typically 3% for the major elements (Mg, Si, and Ca) and 10% on the minor elements (Al, Ca, Ti, Cr, Mn, and Fe).

nd = not detected.

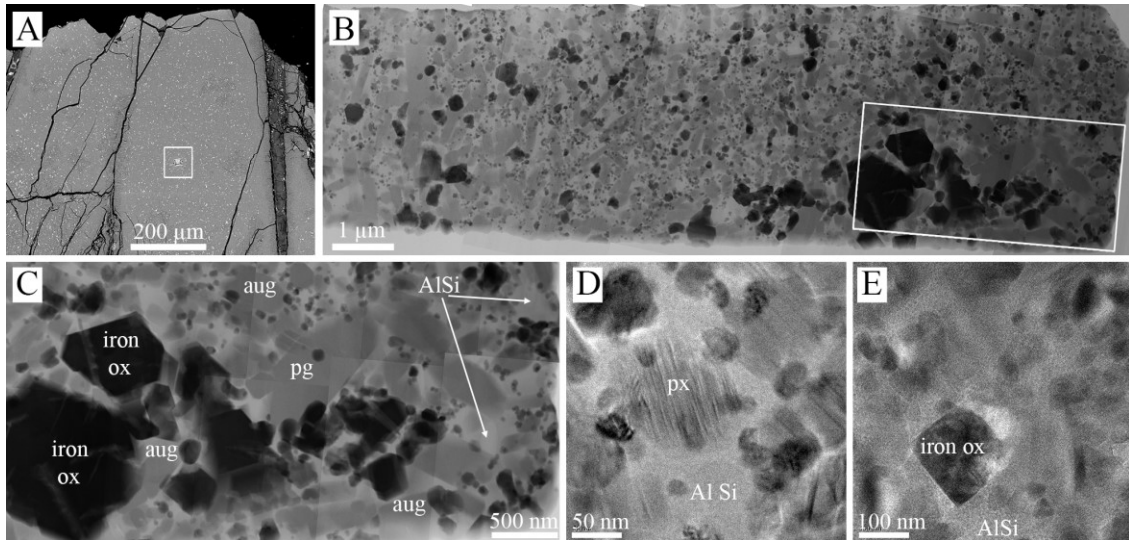


Fig. 3.12. (A) Black box area from Fig. 3.2 showing altered relict pigeonite $\text{En}_{30-33}\text{Fs}_{49-59}\text{Wo}_{11-18}$ with fine iron oxide and feldspar grains. (B) FIB-TEM section FIB3 taken from the location shown in A. (C) BF-STEM image of the white box area in B showing iron oxide (iron ox), pigeonite (pg), augite (aug) and aluminium silicate (AlSi). (D) BF-TEM image showing pigeonite and aluminium silicate. (E) BF-TEM image of iron oxide grain.

Iron oxide grains were also found in an augite-dominated relict pyroxene with feldspar aureole, $\text{En}_{53}\text{Fs}_{19}\text{Wo}_{28}$ (Table 3.3, FIB6A, 6B, Fig. 3.4A), but no aluminium silicate was seen in this sample, likely due to TEM-EDX analyses measuring more than one phase. Further TEM-EDX data showed an intermediate composition with enrichment in SiO_2 57.4 wt% and Al_2O_3 4.6 wt%, and lower FeO 3.7 wt% compared to stoichiometric pyroxene (53.4 wt% SiO_2 , 4.1 wt% Al_2O_3 , 6.4 wt% FeO). This suggests that some of the Fe in the pyroxene has been oxidised, resulting in the formation of separate magnetite grains and a mixture of pyroxene and a K-bearing feldspathic glassy material.

3.3.4 Iron Oxidation State

To investigate the oxidation state of the iron, XRF and Fe-K XANES maps (Fig. 3.13) were taken across the relict pigeonite clast (Fig. 3.2A, white box), where TEM showed the pyroxene breakdown occurring (Section 3.3.3), and the relict pyroxene with feldspar aureole (Fig. 3.7A, white box), which had similar small magnetite grains within the pyroxene and plagioclase. Fe-K XANES point measurements were taken on other similar relict pyroxene clasts with small iron oxide grains and porosity: the low-Ca relict pyroxene with feldspar aureole from which FIB2 was extracted (Fig. 3.4G), a

high-Ca relict pyroxene with feldspar aureole, from which FIB6A was extracted (Fig. 3.4A), and part of the augite pyroxene clast that also underwent ^{40}Ar - ^{39}Ar dating (Fig. 3.10).

Fig. 3.13 G and H show the normalized intensity across a range of energy values corresponding to the Fe-K absorption edge, the near-vertical line on the graph, where the 1s electron of Fe absorbs an X-ray photon. The small peak before the absorption edge corresponds to the pre-edge $1s \rightarrow 3d$, known as the pre-edge centroid. If the iron is more oxidized, then the pre-edge centroid and absorption edge shift to slightly higher energy values. Values for these are given in Table 3.4, and plotted in Fig. 3.14.

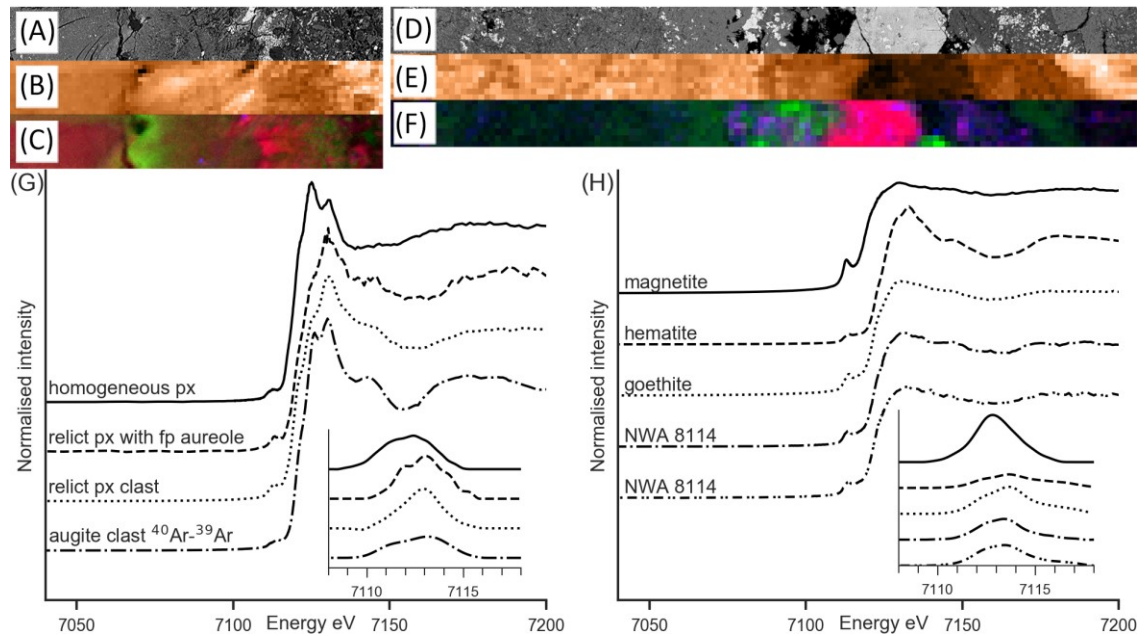


Fig. 3.13. (A) BSE image of part of the relict pigeonite clast (Fig. 3.2A white box) where a Fe-K XANES map was taken. (B) Fe-K XANES map, $65 \times 450 \mu\text{m}$ ($5 \mu\text{m}$ resolution), showing normalized intensity measured at 7120.0 eV , light areas = Fe^{2+} , dark areas = Fe^{3+} . (C) $2 \mu\text{m}$ XRF image of XANES area, Fe=red, Ca=green, Ti=blue. (D) BSE image of part of the relict pyroxene with feldspar aureole (Fig. 3.7A, white box) where a Fe-K XANES map was taken. (E) Fe-K XANES map, $40 \times 640 \mu\text{m}$ ($5 \mu\text{m}$ resolution), showing normalized intensity measured at 7120.0 eV , light areas = Fe^{2+} , dark areas = Fe^{3+} . (F) $5 \mu\text{m}$ XRF image of XANES area, Fe=red, Ca=green, Ti=blue. (G) Typical normalized Fe-K edges for a homogeneous pyroxene (px) clast, the pyroxene clast with feldspar aureole in area E, the relict pigeonite clast area B, and the augite clast from Fig. 3.10. Inset shows the pre-edge $1s \rightarrow 3d$ centroid for each of the four. For energy values, see Table 3.4. (H) Normalised Fe-K edges for NWA 8114 C5 goethite grain versus standards. Inset shows the pre-edge $1s \rightarrow 3d$ centroid. For energy values, see Table 3.4.

The pyroxene analyses indicate oxidation, as the pre-edge centroid and absorption edge are both noticeably higher when compared with unaltered monomineralic pyroxene clasts (Fig. 3.13G, Fig. 3.14, Table 3.4). Using the calibration scale of Hicks et al. (2014), the relict pigeonite clast, relict pyroxene with feldspar aureole, augitic and low-Ca relict pyroxenes with feldspar aureole have $\text{Fe}^{3+}/\Sigma\text{Fe} \leq 25\%$. Fe-K XANES measurements for unaltered monomineralic pyroxene clasts show negligible oxidised iron (Fe^{3+}) content (Fig. 3.13G, Fig. 3.14).

Two Fe-K XANES measurements on the Fe oxide grain (Fig. 10D) closely match the goethite standard analysis (Fig. 3.13H), with the $1s \rightarrow 3d$ pre-edge centroid 0.33 and 0.44 eV lower than the standard and the Fe-K absorption edge energy 0.40 eV higher than the standard (Table 3.4). The XRF map of this goethite grain (Fig. 3.7D) shows the presence of Ni throughout the grain, consistent with the EPMA measurement recording 0.9% NiO, higher than NiO recorded anywhere else in these samples. High NiO was previously seen in pyrite (Lorand et al., 2015), but no clasts of pyrite were observed in the three sections studied here (though pyrite clasts have been found in a fourth polished block of NWA 8114).

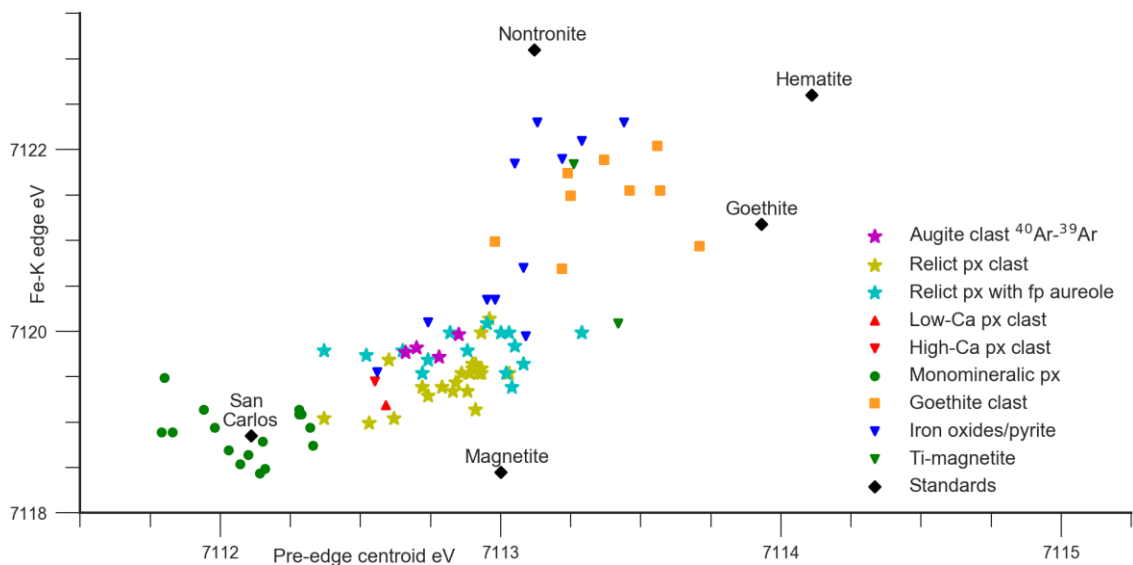


Fig. 3.14. Pre-edge centroid vs. Fe-K edge energies for monomineralic pyroxene clasts; pyroxene in the relict pyroxene (px) clast and relict pyroxene clast with feldspar (fp) aureole (Fig. 3.13G); a low-Ca relict pyroxene with feldspar aureole C29 (Fig. 3.4G); a high-Ca relict pyroxene with feldspar aureole B202 (Fig. 3.4A); goethite (Fig. 3.7B); iron oxides, pyrite, and Ti-magnetite (Fig. 3.4C) from NWA 8114, and standards (including San Carlos olivine). For energy values, see Table 3.4.

Table 3.4: Pre-edge centroid and Fe-K edge energies shown in Fig. 3.13G, H, and Fig. 3.14.

Material	Pre-edge centroid energy eV	Fe-K edge energy eV	Material	Pre-edge centroid energy eV	Fe-K edge energy eV	
Standards:			Low-Ca px clast (Fig. 3.4G)	7112.6	7119.2	
Hematite (Fig. 3.13H)	7114.1	7122.6	High-Ca px clast (Fig. 3.4A)	7112.6	7119.5	
Magnetite (Fig. 3.13H)	7113.0	7118.5	Px clast ⁴⁰ Ar- ³⁹ Ar (Fig. 3.10)	7112.7	7119.8	
Goethite (Fig. 3.13H)	7113.9	7121.2	Px clast ⁴⁰ Ar- ³⁹ Ar (Fig. 3.10)	7112.9	7120.0	
San Carlos olivine	7112.1	7118.9	Px clast ⁴⁰ Ar- ³⁹ Ar (Fig. 3.10)	7112.7	7119.8	
Nontronite	7113.1	7123.1	Px clast ⁴⁰ Ar- ³⁹ Ar (Fig. 3.10)	7112.8	7119.7	
NWA 8114:			Relict px (Fig. 3.2A, Fig. 3.13A)	7112.9	7119.6	
Monomineralic px clasts:			Relict px (Fig. 3.2A, Fig. 3.13A)	7112.9	7119.6	
104	7112.0	7118.9	Relict px (Fig. 3.2A, Fig. 3.13A)	7112.7	7119.3	
104	7112.3	7119.1	Relict px (Fig. 3.2A, Fig. 3.13A)	7112.8	7119.3	
103	7111.9	7119.1	Relict px (Fig. 3.2A, Fig. 3.13A)	7112.8	7119.4	
26	7111.8	7119.4	Relict px (Fig. 3.2A, Fig. 3.13A)	7112.6	7119.7	
9	7112.3	7118.7	Relict px (Fig. 3.2A, Fig. 3.13A)	7112.9	7119.6	
208	7112.3	7119.1	Relict px (Fig. 3.2A, Fig. 3.13A)	7112.9	7119.3	
130	7112.3	7119.1	Relict px (Fig. 3.2A, Fig. 3.13A)	7113.0	7120.1	
130	7112.3	7118.9	Relict px (Fig. 3.2A, Fig. 3.13A)	7112.9	7119.1	
129	7112.1	7118.5	Relict px (Fig. 3.2A, Fig. 3.13A)	7112.6	7119.0	
129	7112.1	7118.4	Relict px (Fig. 3.2A, Fig. 3.13A)	7112.4	7119.0	
3	7112.2	7118.5	Relict px (Fig. 3.2A, Fig. 3.13A)	7112.9	7119.5	
260	7112.0	7118.7	Relict px (Fig. 3.2A, Fig. 3.13A)	7112.9	7119.6	
260	7112.1	7118.6	Relict px (Fig. 3.2A, Fig. 3.13A)	7112.9	7119.5	
224	7111.8	7118.9	Relict px (Fig. 3.2A, Fig. 3.13A)	7112.9	7120.0	
224	7111.8	7118.9	Relict px (Fig. 3.2A, Fig. 3.13A)	7112.8	7119.4	
209(Fig. 3.13G)	7112.2	7118.8	Relict px (Fig. 3.2A, Fig. 3.13A)	7112.7	7119.4	
Goethite (Fig. 3.7, Fig. 3.13H)	7113.5	7121.6	Relict px (Fig. 3.2A, Fig. 3.13A)	7112.9	7119.5	
Goethite (Fig. 3.7, Fig. 3.13H)	7113.6	7121.6	Relict px (Fig. 3.2A, Fig. 3.13A)	7113.0	7119.5	
Goethite (Fig. 3.7, Fig. 3.13H)	7113.2	7121.7	Relict px (Fig. 3.2A, Fig. 3.13A)	7112.9	7119.5	
Goethite (Fig. 3.7, Fig. 3.13H)	7113.4	7121.9	Relict px (Fig. 3.2A, Fig. 3.13A)	7112.5	7119.0	
Goethite (Fig. 3.7, Fig. 3.13H)	7113.0	7121.0	Relict px with aureole (Fig. 3.7, Fig. 3.13B)	7113.0	7120.1	
Goethite (Fig. 3.7, Fig. 3.13H)	7113.3	7121.5	Relict px with aureole (Fig. 3.7, Fig. 3.13B)	7113.1	7119.6	
Goethite (Fig. 3.7, Fig. 3.13H)	7113.6	7122.0	Relict px with aureole (Fig. 3.7, Fig. 3.13B)	7112.7	7119.8	
Goethite (Fig. 3.7, Fig. 3.13H)	7113.2	7120.7	Relict px with aureole (Fig. 3.7, Fig. 3.13B)	7113.0	7120.0	
Goethite (Fig. 3.7, Fig. 3.13H)	7113.7	7120.9	Relict px with aureole (Fig. 3.7, Fig. 3.13B)	7113.1	7119.8	
Ti-magnetite (Fig. 3.4C)	114	7113.4	7120.1	Relict px with aureole (Fig. 3.7, Fig. 3.13B)	7112.7	7119.7
Ti-magnetite	206	7113.3	7121.8	Relict px with aureole (Fig. 3.7, Fig. 3.13B)	7112.8	7120.0
Fe-rich (Fig. 3.4A)	202	7113.4	7122.3	Relict px with aureole (Fig. 3.7, Fig. 3.13B)	7113.0	7119.4
Fe-rich (Fig. 3.4A)	202	7113.1	7122.3	Relict px with aureole (Fig. 3.7, Fig. 3.13B)	7113.0	7119.5
Iron oxide	233	7113.1	7120.7	Relict px with aureole (Fig. 3.7, Fig. 3.13B)	7113.0	7120.0
Iron oxide centre	273	7113.0	7120.4	Relict px with aureole (Fig. 3.7, Fig. 3.13B)	7113.3	7120.0
Iron oxide edge	273	7113.0	7120.4	Relict px with aureole (Fig. 3.7, Fig. 3.13B)	7112.9	7119.8
Iron oxide	267	7113.3	7122.1	Relict px with aureole (Fig. 3.7, Fig. 3.13B)	7112.5	7119.7
Fe-rich	267	7113.1	7121.9	Relict px with aureole (Fig. 3.7, Fig. 3.13B)	7112.4	7119.8
Fe-rich	206	7113.2	7121.9	Relict px with aureole (Fig. 3.7, Fig. 3.13B)	7112.7	7119.5

3.3.5 Mineral Identification by XRD

XRD measurements were taken across the full range of clasts and used in particular to distinguish between different iron oxides and hydroxides. Grains in the relict pyroxene with feldspar aureole marked ‘X’ (Fig. 3.7A) gave *d*-spacing peaks that matched the XRD measurement of a powdered magnetite standard (X1-X4, Fig. 3.15A, Table 3.5). These peaks were used to calculate unit cell dimensions, giving a calculated cubic cell parameter in two grains of $8.389 \pm 0.003 \text{ \AA}$ and $8.391 \pm 0.002 \text{ \AA}$ compared with magnetite standards 8.375 \AA to 8.405 \AA (ICDD, 2014). A measurement in the low-Ca relict pyroxene with feldspar aureole (C29, Fig. 3.15C) also gave the cubic cell parameter as $8.390 \pm 0.01 \text{ \AA}$ (Table 3.5). This shows that the sub-micron iron oxide grains in two of the clasts showing this texture are magnetite.

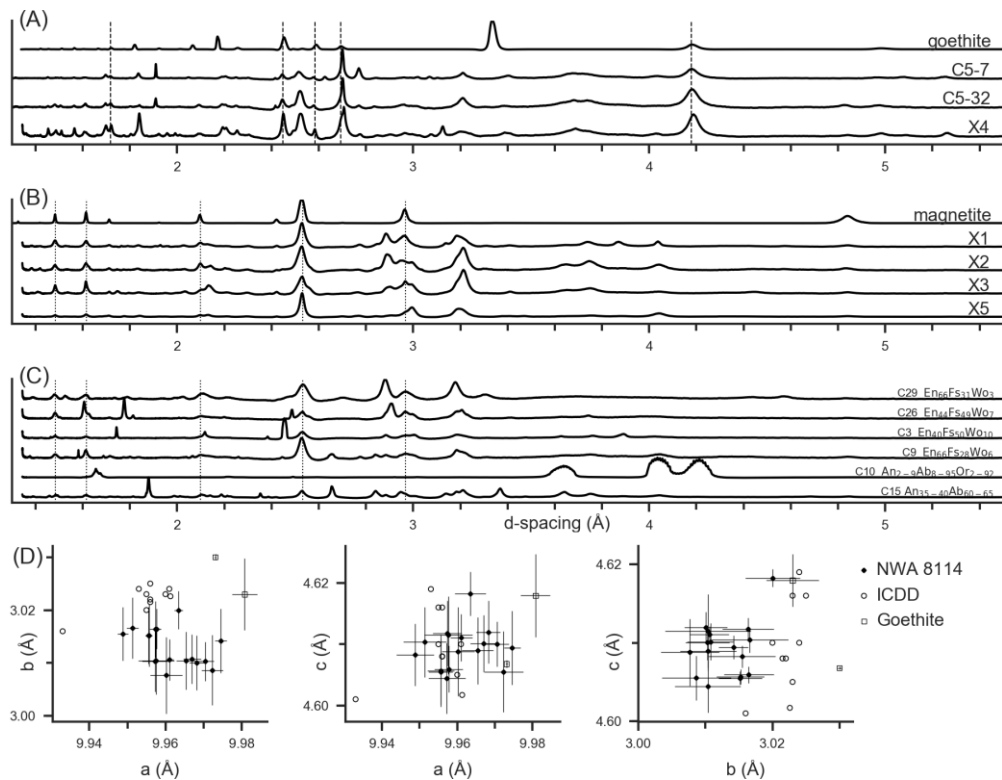


Fig. 3.15. XRD *d*-spacing peaks for (A) a goethite standard, two data points from the XRD map taken across the goethite grain in Fig. 3.7B (C5-7, C5-32), ‘X4’ shown in Fig. 3.7A, and the five expected most intense goethite peaks (dashed lines) (Gualtieri & Venturelli, 1999). (B) a magnetite standard, four of the five data points ‘X’ shown in Fig. 3.7A, and the five expected most intense magnetite peaks (dotted lines) (Wechsler et al., 1984). (C) four pyroxene and two feldspar clasts (two shown in Fig. 3.4GH) with the five expected most intense magnetite peaks (dotted lines) (Wechsler et al., 1984). (D) Calculated unit cell dimensions *a*, *b*, *c* (Å) plotted for *d*-spacing values from the XRD map data for the goethite grain (black diamonds) and the goethite standard (squares) with error bars, and goethite standards from the ICDD database (white circles) (ICDD, 2014).

The *d*-spacing peaks for the 'gt' grain in Fig. 3.7B indicate a good match with the goethite FeO(OH) standard, as seen by two typical measurements (Fig. 3.15B) taken from the fifty measurements of the XRD map across the clast (Fig. 3.7D). The second typical measurement C5-32 also shows *d*-spacings consistent with magnetite and/or maghemite (Table 3.5), confirming they co-exist with the goethite. The *d*-spacings were used to calculate unit cell dimensions (Table 3.5) together with further such calculated unit cell dimensions from the XRD map. These are plotted in Fig. 3.15B, showing a close fit against a population of goethite data (ICDD, 2014).

Measurements from a further three pyroxene clasts and one plagioclase and one K-feldspar clast are also shown in Fig. 3.15C. It can be seen that the pyroxene clasts often have peaks matching the magnetite standard, suggesting that where iron oxide grains are seen in pyroxene, these are usually magnetite.

Table 3.5: XRD measured d -spacings (Å) for indices hkl , as plotted in Fig. 3.15, with calculated unit cell dimensions a , b , c (Å). Measurements from the XRD map in the iron oxide grain (Fig. 3.7D, black box, C5), XRD point measurements across the relict pyroxene (px) with feldspar aureole showing sub-micron iron oxide grains (Fig. 3.7A, X1-X5) and the low-Ca relict pyroxene with feldspar aureole showing sub-micron iron oxide grains (C29, Fig. 3.4G) and reference standards.

Goethite	a (Å)	b (Å)	c (Å)	101	111	301	212	210	511	200	401	201	211	020	610	011	202	500
X4 38913	9.963(4)	3.020(1)	4.618(4)	4.189	2.451	2.704	1.721	2.583	1.565	-	-	-	2.254	1.510	1.455			1.992
C5-7	9.965(5)	3.010(3)	4.609(4)	4.181	2.446	2.701	1.717	2.576	1.563	4.975	2.191	-	2.249	-	-			
C5-32	9.961(4)	3.011(1)	4.611(3)	4.182	2.447	2.701	1.717	2.577	1.564	4.973	2.193	3.386	2.250	1.505	1.453	2.521	2.093	
Goethite ^a	9.981(7)	3.023(3)	4.618(4)	4.184	2.454	2.696	1.721	2.590	1.565	-	2.193	-	-	-	-			
Goethite ^b	9.9613	3.0226	4.6017	4.178	2.449	2.693	1.718	2.584	1.564	4.981	2.190	3.380	2.253	1.511	1.455	2.526		
Goethite ^c	9.956	3.0215	4.608															
Magnetite	$a = b = c$ (Å)			311	440	220	511	400	422	222	111	210	531	441	215	332		
X1 38910	8.389(3)			2.529	-	2.959	1.614	2.099	-	2.422	4.839	-	-	-				
X2 38911	8.391(2)			2.526	-	-	1.615	2.100	1.711	2.424	-	-	1.419	-				
X3 38912	8.376(8)			2.529	1.484	2.968	1.614	-	1.712	2.421	-	-	1.409	-				
X5 38914	8.387(3)			2.529	1.483	-	1.615	2.099	1.710	2.423	4.841	-	-	-				
C29	8.390(10)			2.532	1.488	2.970	1.614								1.526	1.789		
C5-21	8.379(5)			2.519	1.483	2.960	-	2.092		-	4.837	-	-	-				
C5-26	8.353(7)			2.521	-	2.961	-	-		2.420	-	-	-	-	1.453			
C5-32	8.365(9)			2.521	1.482	-	-	2.093		-	-	-	-	-	1.453			
C5-50	8.374(2)			2.522	-	2.958	1.612	2.093		2.419	4.840	3.740	-	-				
Magnetite ^a	8.3882			2.528	1.483	2.964	-	2.096	1.712	2.421	4.841	-	1.418	-				
Magnetite ^d	8.3961			2.532	1.484	2.969	1.616	2.099	1.714	2.424	4.848	-	-	-				
Maghemite ^c	8.3364			2.514	1.474	2.947	1.604	2.084	1.702	2.407	4.813	3.728	-	-				
Maghemite ^c	8.3474																	

Error estimates are given in parentheses and quoted in units of the least significant digit. Unit cell dimension error values calculated from standard deviation.

hkl planes for goethite and magnetite are ordered by intensity per ^b and ^d respectively.

^a Reference material. ^b Gualtieri and Venurelli (1999) ^c Cornell and Schwertmann (2003) ^d Wechsler et al. (1984) ^e Solano et al. (2014)

^{bdc} Referenced from American Mineralogical Crystal Structure Database (Downs & Hall-Wallace, 2003)

3.3.6 FTIR Search for Evidence of Hydration

FTIR reflectance data showed an absence of any hydration in the relict pigeonite clast described previously with TEM (Fig. 3.16) or across the rest of the relict pyroxene with feldspar aureole containing magnetite (Fig. 3.7A). FTIR reflectance data (Fig. 3.16) taken over the goethite grain marked gt (Fig. 3.7B) indicates a consistent absorption peak at 3145 cm^{-1} matching the synthetic goethite in Beck et al. (2015), and absorption peaks at 895 cm^{-1} and 795 cm^{-1} (Gotić & Musić, 2007), distinguishing it from other hydrated iron oxides.

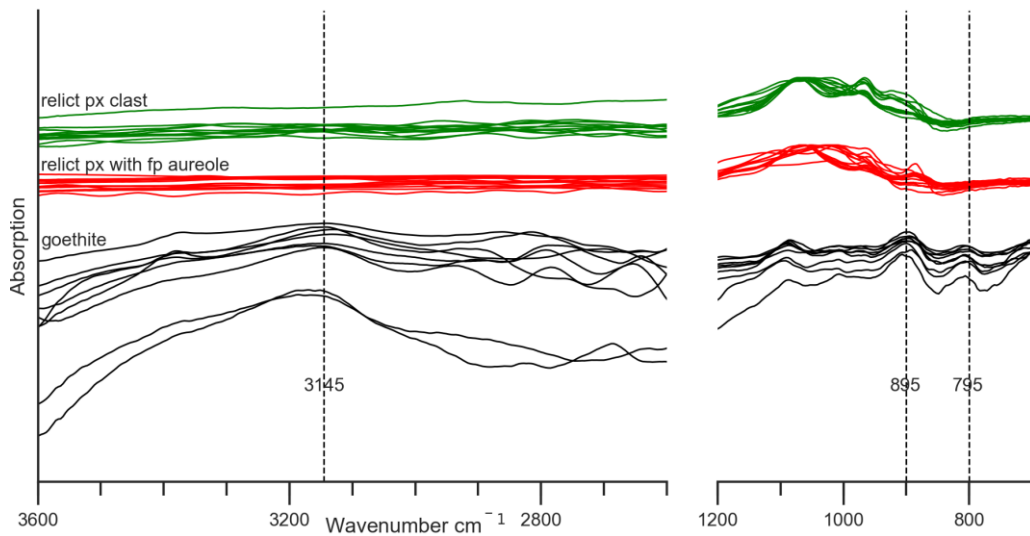


Fig. 3.16. Reflectance absorption of 9 measurements taken from a map across the goethite grain (black line) in the relict pyroxene with feldspar aureole (Fig. 3.7B). The dotted vertical lines show the characteristic absorption peaks for goethite at 3145 cm^{-1} (Beck et al., 2015), 895 cm^{-1} and 795 cm^{-1} (Gotić & Musić, 2007), whereas the relict pyroxene (px) clast (green) (Fig. 3.2) and the rest of the relict pyroxene with feldspar (fp) aureole (red) (Fig. 3.7A) show no evidence of H_2O or $-\text{OH}$ groups in this region.

3.3.7 ^{40}Ar - ^{39}Ar dating

Apparent age and Ca/K spectra are displayed for three alkali feldspar clasts (clasts 1, 2 and 4) and one predominantly augite clast (clast 3, Fig. 3.10) in Fig. 3.17 and the data are given in Table 3.6. Data for all samples show considerable scatter on $^{39}\text{Ar}/^{40}\text{Ar}$ - $^{36}\text{Ar}/^{40}\text{Ar}$ correlation diagrams (not shown), therefore it is not possible to establish if the sample contains trapped terrestrial or martian Ar components. Correction for assumed trapped terrestrial atmosphere results in a larger correction at low temperature, but a relatively minor correction at higher temperatures. Due to the uncertainty in the

trapped Ar composition, any ^{40}Ar excesses, and given that a proportion of the ^{36}Ar may have been formed by cosmic-ray interaction during transit of the parent meteoroid, the apparent ages shown in Fig. 3.17A represent maximum approximate age values. Precise ages and errors were not obtained due to the disturbed nature of the gas release patterns for the separated clasts.

The augite clast 3 shows a relatively flat spectrum (Fig. 3.17A) with apparent ages varying between 925 to 1293 Ma but with most spanning the interval 1100 to 1250 Ma. The high temperature step ages of 1130 Ma to 1250 Ma are regarded as more reliable, as there is a plateau in the gas release and Ca/K ratios. It is this approximate age range that is compared to other radiometric ages from the martian breccia (Fig. 3.18). The Ca/K spectrum of the augite (Fig. 3.17B) is reasonably stable for the initial 50% ^{39}Ar release with a value of a ~ 50 , and then rises steeply to a maximum of ~ 700 . This variation is considered to reflect the difference between the higher Ca in the augite, the lower Ca and higher K in the feldspar inclusions and higher Ca in the calcite vein in the clast (Fig. 3.10). EPMA data for comparable clasts confirms up to 2000 ppm of K in plagioclase and usually less than 200 ppm K in pyroxene, which suggests the 546 ppm K (Table 3.6) is predominantly pyroxene but with feldspar impurities. As calcite does not contain K, it is not expected to affect the ages.

The spectra for the feldspar clasts (Fig. 3.17) rise from a calculated ~ 500 Ma (clast 1 and 2) to maxima of 2620 Ma and 2640 Ma in clasts 1 and 4, but higher at 3440 Ma in clast 2. Staircase age spectra might indicate samples that have experienced diffusive loss of ^{40}Ar during thermal pulses or shock events. The K/Ca spectra for the feldspar have some variation throughout the releases (Fig. 3.17B) with the majority of steps having values between 28 and 31 (mol/mol). The data for the feldspar clasts is too imprecise to report any reliable ages resulting from shock resetting etc.

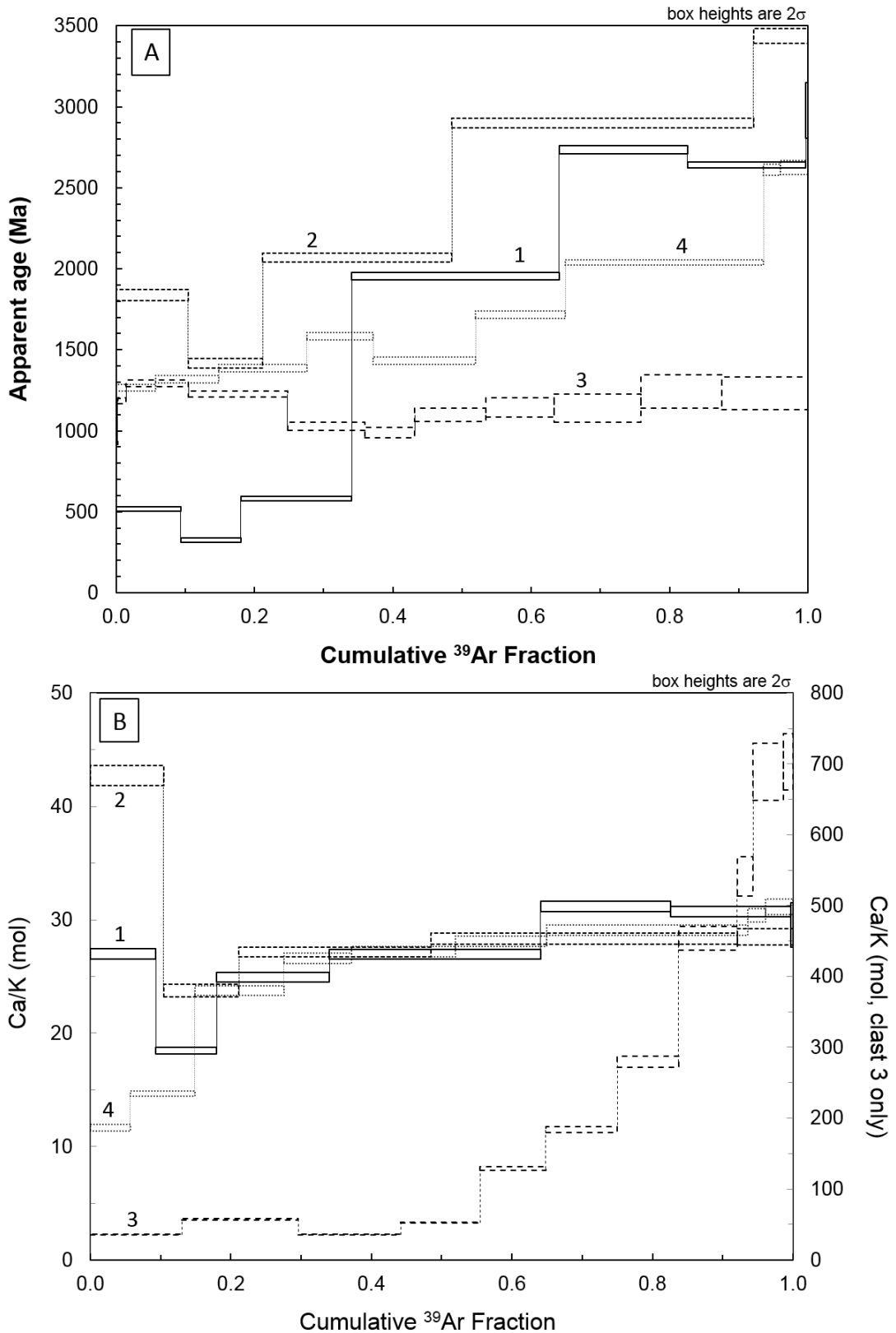


Fig. 3.17. ^{40}Ar - ^{39}Ar laser age determinations of clasts (1, 2 and 4 feldspar; 3 augite) showing (A) age and (B) Ca/K spectra. See data in Table 3.6. These data are uncorrected for any trapped martian atmospheric component. As a result the maximum approximate ages from these data are used i.e. 1130 Ma to 1250 Ma for the augite clast. The apparent ages for the feldspar clasts are too disturbed to give an age.

Chapter 3: Thermal History of Martian Regolith Breccia

Table 3.6. ^{40}Ar - ^{39}Ar analytical data for NWA 8114 clasts (1, 2 and 4 feldspar; 3 augite), produced by collaborators at the University of Manchester.

Laser Power (W)	Concentration (moles)					Cum.		Age (Ma) ^c
	^{36}Ar ($\times 10^{-18}$)	K ($\times 10^{-12}$) ^a	Ca ($\times 10^{-12}$) ^b	^{40}Ar ($\times 10^{-18}$)	^{39}Ar ($\times 10^{-12}$)	^{39}Ar (%)	$^{40}\text{Ar}/^{39}\text{Ar}$	
Clast 1 (feldspar)	mass = 0.00007 g							
0.31	4.00 ± 0.18	321.8 ± 3.8	8683 ± 108	1308 ± 15	7.29 ± 0.06	9.3	4.0 ± 0.1	517 ± 6
0.31	1.67 ± 0.21	299.7 ± 3.5	5533 ± 66	725 ± 14	6.8 ± 0.05	18.0	2.4 ± 0.1	325 ± 6
1.71	1.76 ± 0.21	553.5 ± 6.3	13802 ± 191	2582 ± 27	12.5 ± 0.1	34.0	4.6 ± 0.1	582 ± 6
2.38	7.28 ± 0.25	1036.1 ± 11.6	27933 ± 317	24838 ± 165	23.5 ± 0.2	64.1	23.7 ± 0.2	1955 ± 11
3.50	8.59 ± 0.73	639.4 ± 7.0	19932 ± 213	27849 ± 150	14.5 ± 0.1	82.6	43.1 ± 0.4	2734 ± 12
3.99	8.41 ± 1.57	591.0 ± 6.2	18163 ± 190	24079 ± 76	13.4 ± 0.1	99.7	40.3 ± 0.3	2641 ± 9
4.97	1.26 ± 0.55	10.3 ± 0.4	305 ± 17	534 ± 25	0.2 ± 0.0	100.0	51.1 ± 3.0	2978 ± 86
Total	32.97 ± 1.87	3451.8 ± 17.0	94351 ± 484	81915 ± 239	78.2 ± 0.2			
		1928 ± 5 ppm	0.64 ± 0.05 wt%					
Clast 2 (feldspar)	mass = 0.00005 g							
0.21	4.37 ± 0.15	65.4 ± 0.9	2793.2 ± 41.7	1418 ± 13	1.48 ± 0.02	10.9	21.5 ± 0.3	1837 ± 17
0.62	1.72 ± 0.12	67.3 ± 0.9	1598.9 ± 30.9	984 ± 10	1.52 ± 0.02	21.6	14.5 ± 0.2	1417 ± 14
1.19	5.95 ± 1.51	171.5 ± 1.7	4656.6 ± 51.7	4519 ± 46	3.88 ± 0.02	48.2	26.1 ± 0.3	2070 ± 14
1.71	4.08 ± 0.22	273.5 ± 3.3	7751.7 ± 87.1	13383 ± 95	6.20 ± 0.05	91.6	48.4 ± 0.5	2900 ± 16
2.38	0.91 ± 0.30	49.3 ± 0.7	1405.5 ± 29.1	3460 ± 37	1.12 ± 0.01	100.0	69.5 ± 1.0	3438 ± 23
Total	17.03 ± 1.57	627.0 ± 4.0	18205.9 ± 117.5	23764 ± 113	14.20 ± 0.06			
		490.3 ± 1.6 ppm	1.46 ± 0.00 wt%					
Clast 3 (augite)	mass = 0.00039 g							
0.21	7.38 ± 0.31	708.1 ± 7.9	17.9 ± 26.4	25271 ± 262	3.1 ± 0.2	13.0	8.1 ± 0.1	925 ± 6
0.62	11.39 ± 0.20	904.0 ± 10.8	244.9 ± 19.1	51693 ± 556	16.3 ± 0.1	29.6	11.3 ± 0.1	1187 ± 9
1.09	11.61 ± 0.20	794.2 ± 9.2	259.2 ± 20.3	28165 ± 312	119.9 ± 0.5	44.2	12.7 ± 0.1	1293 ± 9
1.45	15.63 ± 0.35	616.0 ± 7.5	120.8 ± 21.0	32326 ± 366	189.5 ± 0.7	55.5	11.8 ± 0.1	1226 ± 10
1.87	28.62 ± 0.49	508.0 ± 8.2	106.7 ± 15.1	65382 ± 724	148.8 ± 0.4	64.8	9.3 ± 0.1	1028 ± 12
2.38	40.23 ± 0.60	555.2 ± 11.4	75.0 ± 32.0	101855 ± 1142	95.7 ± 0.7	75.0	8.8 ± 0.2	988 ± 15
2.95	56.92 ± 0.53	476.1 ± 12.5	88.3 ± 38.1	133054 ± 1442	136.2 ± 1.0	83.7	10.2 ± 0.3	1098 ± 21
3.57	74.07 ± 0.56	456.1 ± 16.4	125.2 ± 23.4	207091 ± 2169	131.0 ± 0.4	92.1	10.8 ± 0.4	1145 ± 30
4.3	23.26 ± 0.28	122.9 ± 6.2	110.6 ± 11.8	66539 ± 739	166.1 ± 0.5	94.3	10.7 ± 0.5	1139 ± 43
4.97	42.24 ± 0.56	235.6 ± 13.6	75.0 ± 15.1	162222 ± 1738	155.4 ± 0.5	98.7	12.0 ± 0.7	1243 ± 52
6.32	12.51 ± 0.42	72.5 ± 4.1	86.7 ± 21.2	50969 ± 536	165.2 ± 0.6	100.0	11.9 ± 0.7	1232 ± 51
Total	323.86 ± 1.43	22683.9 ± 94.3	1712.4 ± 81.7	924567 ± 3616	2016.3 ± 2.4			
		546.3 ± 1.7 ppm	9.24 ± 0.02 wt%					
Clast 4 (feldspar)	mass = 0.00005 g (estimated)							
0.31	1.06 ± 0.21	89.7 ± 1.1	1045 ± 22	1117 ± 9	2.03 ± 0.02	5.7	12.3 ± 0.1	1265 ± 11
0.88	1.27 ± 0.14	145.2 ± 1.6	2128 ± 28	1913 ± 18	3.29 ± 0.02	14.9	13.0 ± 0.2	1317 ± 11
1.40	1.73 ± 0.22	200.4 ± 2.4	4765 ± 65	2841 ± 22	4.54 ± 0.04	27.5	14.0 ± 0.2	1387 ± 11
1.92	1.77 ± 0.09	152.2 ± 1.8	4047 ± 52	2622 ± 21	3.45 ± 0.03	37.2	17.0 ± 0.2	1584 ± 12
2.33	2.78 ± 0.13	234.0 ± 2.6	6363 ± 79	3476 ± 30	5.30 ± 0.04	52.0	14.7 ± 0.2	1432 ± 11
2.75	2.00 ± 0.12	204.5 ± 2.4	5744 ± 62	3977 ± 28	4.63 ± 0.04	64.9	19.3 ± 0.2	1715 ± 12
3.21	6.32 ± 1.12	452.9 ± 4.8	13181 ± 153	11648 ± 23	10.26 ± 0.06	93.6	25.5 ± 0.2	2040 ± 8
3.68	1.46 ± 0.42	39.0 ± 0.5	1186 ± 19	1558 ± 13	0.88 ± 0.01	96.1	39.5 ± 0.5	2612 ± 17
4.46	1.19 ± 0.15	62.1 ± 0.9	1934 ± 30	2502 ± 22	1.41 ± 0.02	100.0	39.9 ± 0.6	2625 ± 21
Total	19.6 ± 1.27	1579.9 ± 7.3	40394 ± 207	31652 ± 65	35.78 ± 0.10			
		1235.4 ± 2.8 ppm	5.40 ± 0.01 wt%					

^a Determined from $^{39}\text{K}(n,p)^{39}\text{Ar}$: $K = (^{39}\text{Ar}/J) \cdot (K/^{40}\text{K}) \cdot (\lambda/\lambda_0)$ (mole/mole); $\lambda/\lambda_0 = 9.54$; $K/^{40}\text{K} = 1.167 \times 10^4$; $J = 0.08260 \pm 0.00036$

^b Determined from $^{40}\text{Ca}(n,\alpha)^{36}\text{Ar}$: $\text{Ca} = 8.042 \times 10^4 \cdot (^{37}\text{Ar}/a \cdot J)$ (mole/mole); $\alpha = ((K/\text{Ca}) \cdot (^{37}\text{Ar}/^{39}\text{Ar}))_{\text{Hb3gr}}$; $(K/\text{Ca})_{\text{Hb3gr}} = 0.1674$; $\alpha = 0.5051 \pm 0.0002$

^c Excludes uncertainties on the J value.

Errors are given at the 2 σ level of uncertainty

3.4 Discussion

Based on the mineralogical and Ar-Ar studies, five distinct events have been identified in the history of the NWA 8114 parent breccia, ordered here from earliest to last. Stages 2 to 4 are considered to have occurred in quick succession as a result of the impact event that formed the breccia. The results are discussed in the context of impact

crater ejecta blankets and the thermal structure of the regolith on Mars, and provide a simple Fourier cooling model constrained by the mineralogical data.

3.4.1 Five Distinct Events in the Martian Breccia's Formation

3.4.1.1 Stage 1: Original magmatic crystallisation

The compositions of the pigeonite host pyroxenes and their augite exsolution lamellae for six exsolution-bearing clasts suggest that these originally crystallised from a magmatic event with subsequent subsolidus cooling recorded between 900 °C to 1050 °C (Fig. 3.8, Lindsley and Andersen, 1983). The lamellae are the result of slow cooling from the original magmatic event(s). As the exsolution lamellae vary in width and distance of separation (Fig. 3.4D,E,F), these pyroxenes likely cooled at different depths and may have originated from different parent rocks. This was also noted by Leroux et al. (2016) who measured the lamellae in a TEM study of three augite clasts bearing pigeonite lamellae, and one pigeonite clast containing augite exsolution lamellae in paired stone NWA 7533. The Ti-magnetite, Cl-apatite, plagioclase and alkaline feldspar are also magmatic precursor material, likely originating from more than one magmatic event as trends in pyroxene REE chemistry and Mg# suggest that the igneous clasts cannot be related by fractional crystallisation (Santos et al., 2015). Cryptoperthite feldspar also indicates a slow-cooling magmatic history (Fig. 3.4H). ^{147}Sm - ^{143}Nd dating of whole rock and mineral separates suggest that these magmatic precursors and impact melt rocks probably formed ~4.44 Ga ago (Nyquist et al., 2016).

3.4.1.2 Stage 2: Formation of accretionary lapilli and formation of the breccia

The spherule with diameter 1.5 mm seen with the CT scan shows distinct layers of different compositions (Fig. 3.1B), comparable to accretionary lapilli from other planetary materials (Branney & Brown, 2011). Accretionary lapilli are found throughout Earth's stratigraphic record at large impact sites on the Earth; at the 1850 Ma (Krogh et al., 1982) Sudbury impact basin, (Huber & Koeberl, 2017), the 65 Ma (indicated by the K/T boundary), ~195 km diameter, multi-ring Chicxulub crater (Gulick et al., 2008; Yancey & Guillemette, 2008), and the 14.8 Ma (Schmieder et al., 2018), ~26 km diameter, Ries crater (Graup, 1981; Siegert et al., 2017). They are also present in the Apollo lunar samples, formed in impact events (Mckay & Morrison, 1971). They appear similar to pyroclastic accretionary lapilli, that start to form in the

hot volcanic plume where water vapour facilitates the accretion of dust into pellets, which fall out into a pyroclastic density current (Gilbert & Lane, 1994; Schumacher & Schmincke, 1995). The pellets circulate in the upper turbulent flow where concentric dust layers accrete as they harden, and these accretionary lapilli tend to be found in the upper layers of the current deposit, ignimbrites, with pellet and ash fallout layers occurring afterwards (Brown et al., 2010; Branney & Brown, 2011).

Molten silicate, or any condensable material in the ejecta curtain could be the binding agent for impact-derived accretionary lapilli (Johnson & Melosh, 2014), as higher temperatures are reached compared to volcanic plumes that consist mainly of hot gas and solid ash particles. This would explain how they can form on the Moon and Mars without there being much atmosphere or large volumes of water vapour present.

Wittmann et al. (2015) suggested the accretionary dust rims seen in the martian breccia may have formed due to sintering in a hot ejecta plume, though they also drew parallels with accretionary lapilli in terrestrial suevites thought to have formed under base surge conditions. A base surge formation mechanisms would also explain the presence of impact melt rock clasts. Fluidized ejecta patterns are observed at craters on Mars and base-surge deposits on the Moon show radial flow patterns (Mckay & Morrison, 1971), providing further evidence that depositional processes via density currents may occur around large impacts, even if the mechanism for them is not currently understood. By this scenario, accretion of the breccia followed immediately after the presence of the envisaged density flow current.

3.4.1.3 Stage 3: The breakdown of pyroxene under high temperature, oxidising conditions.

Immediately after the impact, the regolith breccia was assembled and compacted in a thick, hot ejecta blanket, likely experiencing sustained high temperatures, of at least 700 °C based on the oxidation studies described later in this section, from the impact event for some weeks or months. The TEM data shows that the large relict pigeonite clast with iron oxide grains $\text{Wo}_{12-18}\text{En}_{31-34}\text{Fs}_{47-56}$ (Fig. 3.12) has partially melted and partially devitrified to form magnetite and K-bearing feldspathic glassy material at a submicron scale (Fig. 3.12B-E). The iron oxide is assumed to be magnetite as a pyroxene clast with similar grains was shown to be magnetite with XRD (Fig. 3.15, Table 3.5). The pyroxene breakdown was associated with oxidation, as shown by the

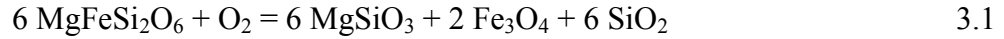
Fe-K XANES data (Table 3.4), which indicate up to 25% $\text{Fe}^{3+}/\Sigma\text{Fe}$ (Hicks et al., 2014) compared to no oxidation seen in unaltered monomineralic pyroxene clasts (Table 3.4). FTIR suggests this alteration assemblage is anhydrous (Fig. 3.16). However, although now anhydrous, the original oxidative breakdown and formation of accretionary clasts may have involved the action of water vapour. This water vapour would have been driven off during cooling from high temperature in the porous regolith. Many pyroxene clasts in NWA 8114, from low-Ca to high-Ca pyroxene, show submicron magnetite grains within them (Table 3.3, Fig. 3.11). TEM-EDX results for these also show an intermediate, non-stoichiometric composition enriched in SiO_2 and Al_2O_3 and depleted in FeO compared to pyroxene, indicating that some of the Fe from the pyroxene has been oxidised, forming the separate magnetite grains (Table 3.3, Fig. 3.11). Not all pyroxenes show this breakdown. However, it is seen in some examples of augite, pigeonite and orthopyroxenes so the breakdown occurrence does not depend upon exact pyroxene composition.

Some iron oxide grains have also been observed in those clasts formed of pyroxene with exsolution lamellae. These iron oxide grains tend to be larger, over a micron in size, and are often present along cracks (Fig. 3.4D,F). They are not aligned or associated with the exsolution lamellae from original crystallisation, suggesting they formed later. As Leroux et al. (2016) noted, trails of magnetite and silica inclusions resemble fluid inclusion trails.

Oxidation of planetary pyroxene has been associated with shock effects in previous studies of meteorites. The breakdown of both Ca-rich and Ca-poor pyroxene to iron oxide observed in NWA 8114, and also seen in pyroxenes in paired stone NWA 7533 (Hewins et al., 2017; Leroux et al., 2016), has some analogies with the breakdown of pyroxene in ureilites by impact smelting. In ureilites, it has been suggested ~50% of the pigeonite has been reduced by impact smelting and contains a fine distribution of Fe-metal, and diverse felsic glasses containing SiO_2 and Al_2O_3 (Warren & Rubin, 2010). The impact event(s) on Mars took place under much more oxidising conditions, calculated from magnetite-ilmenite pairs to be FMQ + 2 to FMQ + 4 log units (Santos et al., 2015). Thus, iron oxide grains (rather than Fe-metal) and a K-bearing feldspathic glassy material are observed. Furthermore, the impact shock of the breccia was lower than that of ureilites, with the former's maximum shock pressure estimated at 5-15 GPa

from pyroxene and feldspar fractures, occasional shock melt veins (Wittmann et al., 2015), and the absence of any maskelynite (Santos et al., 2015).

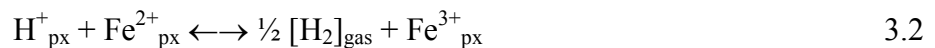
An appropriate, simplified pyroxene oxidation reaction adapted from Leroux et al. (2016) is:



In reality, some of the Fe remains as FeO in the pyroxene so pure enstatite is not predicted from this reaction.

The altered pyroxene in LAR 04315 ureilite is unusually porous, with pre-terrestrial porosity estimated to be 9% to 12% (Warren & Rubin, 2010). The porosity is thought to have been caused by the impact smelting, as the pyroxene still shows near optical continuity after smelting, suggesting it was coherent beforehand. The breccia clasts showing pyroxene breakdown (Fig. 3.4A,B,G, Fig. 3.7A) show similar porosity of up to 5% in the breccia clasts, and this porosity is also observed in the augitic clast 3 that was dated to provide approximate maximum ages using ^{40}Ar - ^{39}Ar (Fig. 3.10).

In another approach to shock effects in pyroxene minerals, McCanta and Dyar (2017) used experimental shock analyses (21 GPa to 59 GPa) of pyroxene to show the Fe^{3+} increased by a factor of $\times 2$ to $\times 6$, even without free oxygen, overprinting the original magmatic $f\text{O}_2$ values. Mössbauer data showed this increase was within the pyroxene structure itself; BSE and TEM imaging showed no new phases. The mechanism of incorporating H^+ ions in the crystal structure is suggested, as hydrogen diffusivity increases as total Fe content increases and nearly all natural clinopyroxene contains ppm levels of H (McCanta & Dyar, 2017). The redox exchange reaction suggested by McCanta and Dyar (2017) incorporating hydrogen is:



This mechanism provides some insight to the overall link to shock processes causing oxidation, however, in NWA 8114 the oxidation in pigeonite is associated with the formation of submicron-sized magnetite grains, rather than the oxidation being incorporated into the pyroxene structure. An oxidising agent is required, assuming the original pyroxene before breakdown and relict pyroxene afterwards have a similar level of oxidation, in order for the magnetite to form. Equation 3.2 offers one possible mechanism. Alternatively, transient water may have been present at the time of the

impact event, perhaps from melting subsurface ice in the regolith, to cause the oxidation and breakdown of pyroxene observed. This would be consistent with the formation of accretionary rims around clasts e.g. (Gilbert & Lane, 1994) within the martian breccia.

Studies have also explored the oxidation of iron within the silicate matrix of pyroxenes, at a variety of temperatures (400 °C to 1000 °C) and for different durations up to 28 days (Straub et al., 1991). Mossbauer reflectance spectra confirmed that the proportion of Fe³⁺ ions in oxidised pyroxene increases at higher temperatures and after longer heating time periods. Nanophase hematite formed in both enstatite oxidised at 700 °C for 28 days and pigeonite oxidised at 1000 °C for 14 days. However, oxidation of augite at 700 °C for 28 days and 800 °C for 3 days showed structural Fe³⁺ ions were present in the pyroxene structure, rather than nanophase hematite.

Similarly, an analogue martian sample was oxidised in air at 700 °C for 1, 3 or 7 days (Minitti et al., 2002). This was a calculated melt sample composition representative of the SNC meteorites, low in Al₂O₃ (~8.0 wt%) and high in total FeO (~19 wt%) relative to terrestrial basaltic melts (Johnson et al., 1991), prepared for a range of different crystallinities (0% to 80% crystalline). Electron and spectral microscopy showed nanophase hematite as the dominant oxidation product in pigeonite, while the behaviour of the 1.0 and 2.3 µm visible and near-infrared (VISNIR) absorptions for augite were consistent with the development of Fe³⁺ (Minitti et al., 2002).

Both of these studies show the production of submicron iron oxide grains in pigeonite at high temperatures, similar to that observed in NWA 8114 suggesting it also experienced a high temperature oxidation process, likely due to heat from an impact event. Both show that oxidised augite tends to retain the Fe³⁺ within its structure.

Olivine in some martian shergottites has been shown to contain iron metal nanoparticles, which are responsible for heterogeneously darkening the olivine to brown as a result of shock (Takenouchi et al., 2017). It is thought that the disproportionation reaction of olivine ($3\text{Fe}^{2+}_{\text{olivine}} \rightarrow \text{Fe}^0_{\text{metal}} + 2\text{Fe}^{3+}_{\text{olivine}} + V_{\text{olivine}}$ where V_{olivine} is a vacancy in olivine) is responsible for this, requiring temperatures over 1500 K, pressures over 30 GPa and a shock duration of at least ~90 ms (Takenouchi et al., 2017). These pressures are higher than those experienced by NWA 8114 but similarly show shock-induced oxidation in some martian shergottites.

Our results show the decomposition and oxidation of pyroxene in NWA 8114, similar to paired meteorite NWA 7533 (Leroux et al., 2016). By comparison to the studies above, it is identified to be the result of shock oxidation and heating. Leroux et al. (2016) suggested this reaction occurred ~ 1000 °C and only affected some of the pyroxenes, so concluded it was a separate high temperature event to that which formed the breccia. The above studies suggest oxidation could take place at $\sim 700+$ °C and thus it is likely to be the same impact event that resulted in the formation of the breccia and accretionary rims around some of the clasts. The ^{40}Ar - ^{39}Ar potential maximum age range for the predominantly augitic pyroxene clast 3 (Fig. 3.10, Fig. 3.17) that shows porosity and iron oxide grains similar to the pyroxene breakdown texture described above in the polished sections, indicates the high temperature shock event was approximately 1.13 Ga to 1.25 Ga.

Comparing with other available data (Fig. 3.18), this is in good agreement with ten whole rock ^{40}Ar - ^{39}Ar ages of 1.159 to 1.407 Ga in pair NWA 11522 (Cassata et al., 2018). It is also consistent with two of the three U-Th-total Pb ages of monazite in apatite reported as 1.0 ± 0.4 Ga, 1.1 ± 0.5 Ga and 2.8 ± 0.7 Ga, and interpreted to have been formed by hydrothermal alteration (Liu et al., 2016). K-Ar whole rock ages of ~ 1.56 Ga (Cartwright et al., 2014) are in reasonable agreement with the augite age from this study, given that the K-Ar age is a bulk measurement.

^{40}Ar - ^{39}Ar plateau ages of 1.411 ± 0.009 Ga for a plagioclase sample, 1.361 ± 0.003 Ga for an alkali feldspar sample together with 0.798 ± 0.052 Ga for another alkali feldspar sample for paired stone NWA 7533 are reported by (Lindsay et al., 2014), Further work for NWA 7034 feldspars shows ^{40}Ar - ^{39}Ar plateau ages from 1.4 to 2.3 Ga, noting 1.285 ± 0.004 Ga for a bulk sample of 202 μg and suggests the bulk sample age is a result of averaging the three age groups observed in the separated feldspar samples: >2.0 Ga, 1.4 to 1.6 Ga and 0.8 Ga (Lindsay et al., 2016).

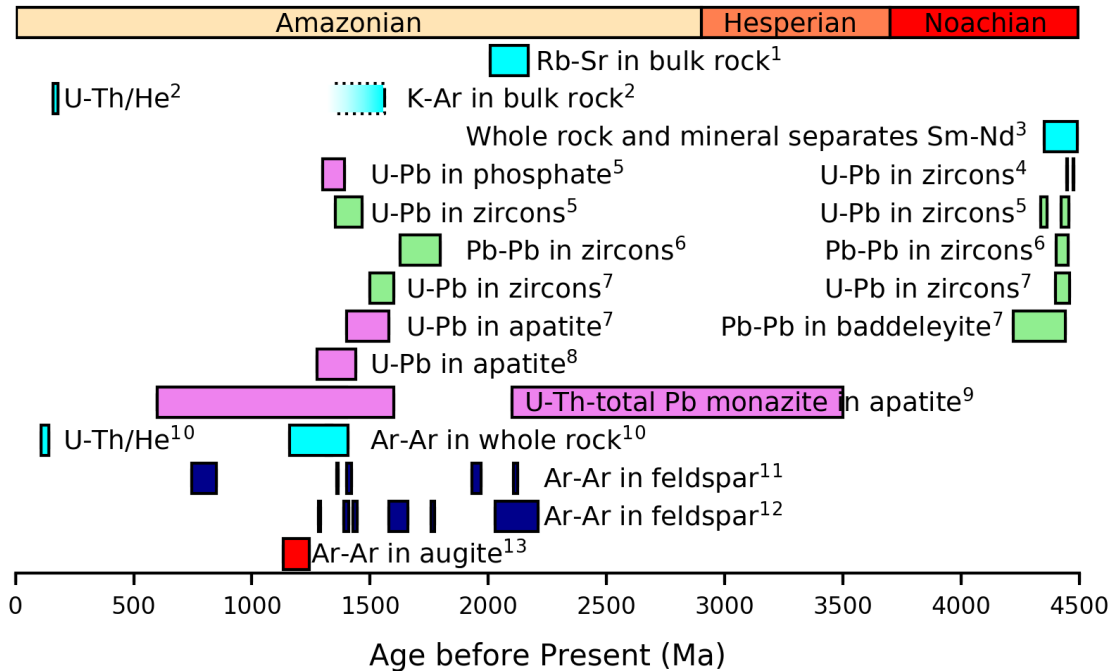


Fig. 3.18. Reported ages for bulk rock and mineral separates from pairs of NWA 8114. Coloured rectangles represent age and 2σ uncertainty for ¹Agee et al. (2013), ³Nyquist et al. (2016), ⁴Bouvier et al. (2018), ⁵Yin et al. (2014), ⁷McCubbin et al. (2016), ⁸Bellucci et al. (2015), ⁹Liu et al. (2016), ¹⁰Cassata et al. (2018), 1σ uncertainty for ⁶Humayun et al. (2013), ¹¹Lindsay et al. (2014), ¹²Lindsay et al. (2016) and the upper limit for the age from ²Cartwright et al. (2014) and uncorrected ages, 1130 Ma to 1250 Ma, for the Ar-Ar dating of the augite clast in this study¹³.

Cl-apatite U-Pb ages of 1.35-1.5 Ga (Yin et al., 2014; Bellucci et al., 2015; McCubbin et al., 2016) and zircon U-Pb young ages of ~1.4-1.7 Ga (Humayun et al., 2013; Yin et al., 2014; Nemchin et al., 2014; Bellucci et al., 2015; McCubbin et al., 2016) show some variation. These different isotopic dating methods have higher closure temperatures than the Ar system, which could - taken at face value - suggest the 100 Ma to 300 Ma difference is an indication that the Ar-isotope system stayed open for a longer time. However, with the uncertainties in the excess Ar corrections, those values are indistinguishable from the ~1.1 to 1.4 Ga ages discussed above (Lindsay et al., 2014; Lindsay et al., 2016; Cassata et al., 2018) considering the analytical error, and 1.13 Ga to 1.25 Ga may date the main high temperature event within the regolith, immediately after the main impact event associated with the breccia.

3.4.1.4 Stage 4: The formation of feldspathic veins

Textural evidence shows that the feldspar veins crosscut and postdate the impact oxidised relict pigeonite clast (Fig. 3.2, Fig. 3.6). The presence of a 20 μm region each

side of each vein with recrystallised grains of pigeonite among dendrites enriched in Na and Al, likely submicron plagioclase (Fig. 3.6) suggests a possibility that the temperature at which the veins were emplaced caused some melting and recrystallization in the oxidised relict pigeonite clast. Some of the clast's accretionary rim shows signs of melting and feldspar migration (Fig. 3.2).

However, orthoclase-rich veins on Earth often occur as a result of hydrothermal alteration below 500 °C (McSwiggen et al., 1994; Deer et al., 2001), which is suggested as a mechanism for the formation of similar veins seen in NWA 7533 (Hewins et al., 2017). Hewins et al. (2017) also described hyalophane veins. Hyalophane contains 5% to 65% celsian, and terrestrial examples include hyalophane-zoisite veins in shales near Litosice, Czech Republic (Zak, 1991) and Ba-bearing alkali feldspars, hyalophane $An_{0.3}Ab_{8.2}Or_{25.8}Cn_{65.7}$ and celsian in the green mica schists of Hemlo-Heron Bay in Ontario (Pan & Fleet, 1991), both being a result of hydrothermal alteration. In this study a small amount of hyalophane $An_{12}Ab_{30}Or_{52}Cn_6$ is present in NWA 8114 veins, but there is little clear mineralogical evidence of other hydrothermal assemblages or alteration in the meteorite. If the temperature did not go above ~400 °C it is hard to explain the recrystallized grains in the ~20 µm area bordering the veins, but the nature of the veins and terrestrial analogues do leave open the alternative possibility of a hydrothermal origin.

To explain the feldspar veins in the breccia clasts, it is suggested that the impact event may have aggregated the breccia in a thick, hot insulated ejecta blanket, where high enough temperatures were maintained to remobilise and melt feldspar rich domains (Fig. 3.6). The diopside-anorthite-albite ternary eutectic lies at ~1150 °C, though temperatures are unlikely to have reached this given some zircons did not reset (~1000 °C) and pyroxene exsolution lamellae are preserved (~900 °C). Impurities and other components would lower the eutectic, and the liquidus temperature for a monzonite could be as low as 800 °C, which is in agreement with a textural study of the degree of melting in the submicron matrix (McCubbin et al., 2016).

The andesine-rich $An_{29}Ab_{64}Or_7$ veins that crosscut the relict pigeonite clast and the Na and Al enrichment in the dendritic texture bordering the veins, are evidence of *in situ* melting, of a feldspar-rich domain. Similar andesine is also seen in the fine grained rim of this clast, sometimes with a melted texture in the adjacent pyroxene. The range of

feldspar in the veins is also similar to feldspar $An_{33.8}Ab_{62.6}Or_{3.6}$ observed in veins by Hewins et al. (2017).

Other pyroxene clasts with crystalline andesine rims $An_{25-55}Ab_{43-75}Or_{2-5}$ (Fig. 3.4A,B,G) rather than accretionary rims, closely match the An_{32-56} rims of ‘oval somewhat spherulite-like clump-aureole structures’ by Hewins et al. (2017). Clasts in Fig. 3.4A,B,G also show concave margins in pyroxene which indicate vesicle walls, consistent with vesiculated melts (Hewins et al., 2017). These authors suggested formation as spherulitic growth on remnants of pyroxene or hydrated dust pellets.

The evidence of high temperatures – either melting or possibly hydrothermal action – identified here is further evidence to the previously described pyroxene breakdown textures, that shortly after formation, the breccia was maintained at high temperatures.

3.4.1.5 Stage 5: Low temperature aqueous alteration and goethite formation

The presence of goethite $FeO(OH)$ within the relict pyroxene with feldspar aureole as shown by the XRD and FTIR analyses, indicates that water was also present at a low temperature stage in the regolith’s history. Possible precursor phases that the NWA 8114 goethite may have replaced under aqueous conditions include magnetite, maghemite or pyrite. Of the total iron oxides in NWA 8114, magnetite and maghemite make up 70% and 30% respectively (Agee et al., 2013). The goethite grains contain small amounts of Ti and S, consistent with precursor phases that contained some Ti-magnetite and pyrite.

A range of factors including temperature, pH, particle size, composition, concentration, structure and morphology can all play a part in the various possible interconversion reactions among the iron oxides. Studies suggest submicron magnetite and titanomagnetite oxidise rapidly to maghemite and goethite, whereas coarse-grained magnetite oxidises slowly to haematite (Xu et al., 1997; He & Traina, 2007). Magnetite (Fe_3O_4) will also transform to maghemite (Fe_2O_3) under hydrothermal conditions, and maghemite will then likely transform to haematite or goethite. Goethite may also form directly from magnetite via dissolution and reprecipitation (He & Traina, 2007). With silicate species, sulphate and/or Al present and lower pH, goethite formation will be promoted over magnetite or haematite (Cornell & Schwertmann, 2003). Lower temperatures favour goethite formation over hematite. Ferrihydrite, identified in NWA

7533 (Beck et al., 2015), could also potentially be an intermediate product of similar reactions.

If pyroxenes and Fe-Ti oxides such as magnetite in NWA 8114 were exposed to sulphurous hydrothermal fluids, then magnetite may have first been converted to pyrite (Wittmann et al., 2015; Lorand et al., 2015):



Lorand et al. (2015) suggested this would occur at temperatures below 500 °C, from the maximum Ni contents and that pyrite formed on Mars as a late alteration mineral. They concluded the goethite they found in NWA 7533 was terrestrial alteration of the pyrite, with goethite postdating shock fractures in the pyrite and based on the D/H ratio of $10 \pm 85\%$ of five grains of Fe oxyhydroxides, via the following reaction



A similar terrestrial origin for the NWA 8114 goethite clast is likely. Lorand et al. (2015) noted that the high-Ni concentration spots in NWA 7533 pyrite increase the weathering resistance, as seen by Ni-rich pyrite being less susceptible to alteration.

The oxygen isotope ratio of bulk NWA 7034 water suggests that most of it is extra-terrestrial, with $\Delta^{17}\text{O}$ above the terrestrial fractionation line (Agee et al., 2013). The bulk rock D/H isotope ratio of NWA 7034 water shows two distinct components, a negative value of about -100% likely to be terrestrial contamination, but also a positive value of 300% to 327% . The latter is similar to the range of 250% to 900% values seen in the nakhlites though lower than those for shergottites of 1200% to 2100% or martian atmosphere at 4000% (Leshin et al., 1996), nevertheless it is clear there is some martian water within the breccia.

This leaves open the possibility that the goethite formation and an associated phase of hydrous activity could have occurred on Mars. Goethite has been detected on Mars before by NASA's *Spirit* rover together with Fe^{3+} -sulphate at Gusev crater in the rocks at Columbia Hills on Mars, and this is one of the mineralogical lines of evidence of past aqueous processes (Ming et al., 2006; Morris et al., 2006).

3.4.2 Formation of Regolith Ejecta Blankets

NWA 7034 and its breccia pairs have been interpreted as fragments of impact regolith due to the meteoritic siderophiles (e.g., Ni, Ir) found in them. These indicate a component of at least a 3% carbonaceous chondrite material (Humayun et al., 2013; Wittmann et al., 2015). Thus, understanding the processes that create and change impact regolith on Mars are key to unravelling the evolution of NWA 8114. Consideration of the thermal evolution of an impact regolith on Mars is necessary to understand the mineralogical history of NWA 8114.

The thickness, t , of regolith ejecta blankets has been modelled from nuclear, terrestrial craters, lab experiments and estimates for lunar craters, and found for all of the examples to be a function of range:

$$t = 0.14 R^{0.74} (r/R)^{-3.0} \quad 3.5$$

where R is crater radius and r is range from the centre of the crater (McGetchin et al., 1973). Thus, a 20 km crater could create a 10 m thick ejecta blanket up to 50 km from the centre, a 50 km crater could create an ejecta blanket 100 m thick up to 80 km from the centre, and a 100 km crater could create a 200 m thick ejecta blanket up to 150 km from the centre.

A thick regolith layer can provide substantial insulation, which can maintain high temperatures at depth for long durations after impact events. Numerical modelling using HYDROTHERM showed that for a 100 km diameter crater on early Mars in the absence of fluid flow, isotherms over 900 °C can extend laterally for 10 km and persist for well over 4,000 years within the top 1 km of the crust (Abramov & Kring, 2005). A 30 km width crater is likely to have cooled below 400 °C within 25 years, whereas a 180 km crater would have temperatures over 900 °C extending 25 km, to nearly the crater rim in the top km depth, and over 1200 °C in the centre at 4000 years (Abramov & Kring, 2005).

3.4.3 Thermal Structure of the Martian Breccia Parental Regolith and Simple Cooling Model.

The properties of the martian regolith are important in constructing a thermal model for its evolution. Current surface temperatures on Mars range from -113 °C to -7 °C with an average of -58 °C at the equator (Carr, 2007) though may vary seasonally as much

as from $-153\text{ }^{\circ}\text{C}$ at the poles to $20\text{ }^{\circ}\text{C}$ at the equator. Thermal models require knowledge of crustal density, porosity with conductivity and ideally surface heat flow. The density of the crust has most recently been calculated as $2580 \pm 210\text{ kg m}^{-3}$ from gravitational and topography measurements (Goossens et al., 2017), in good agreement with the uncompressed density of basalt of 2600 kg m^{-3} (Abramov & Kring, 2005). The heat capacity of basalt is $800\text{ J kg}^{-1}\text{ K}^{-1}$ (Abramov & Kring, 2005), while Apollo soil has a value of $760\text{ J kg}^{-1}\text{ K}^{-1}$ at 300 K (Ledlow et al., 1992). However, the geothermal gradients on Mars, including impact regolith terrains, are not well constrained as no surface heat flow measurements have yet been made. Babeyko and Zharkov (2000) did calculate a geothermal gradient of $13.5 \pm 7.5\text{ K km}^{-1}$ based on a possible range of surface heat flow $30, 40$ and 45 mW m^{-2} and crustal thermal conductivity of $2.5 \pm 0.5\text{ W m}^{-1}\text{ K}^{-1}$. The authors based this model on the considered fraction of heat-producing radionuclides (K, Th, U) transported into the crust (Babeyko & Zharkov, 2000). The thermal conductivity of $2.5\text{ W m}^{-1}\text{ K}^{-1}$ (Abramov & Kring, 2005; Babeyko & Zharkov, 2000) is also in good agreement with Robertson (1988), who noted that thermal conductivity varies as a function of $(1 - \text{porosity})^2$ for vesicular basalts. Thermal conductivity of $1.7\text{ W m}^{-1}\text{ K}^{-1}$ was used for ejecta and $2.5\text{ W m}^{-1}\text{ K}^{-1}$ for ice in modelling post-impact runoff at the Noachian Eberswalde crater (Mangold, Kite, et al., 2012). The porosity of the martian crust is modelled as decreasing exponentially with depth, starting with a value of 20% at the surface (Abramov & Kring, 2005). The sort of temperatures that the NWA 8114 parent regolith experienced would only be achieved at unrealistically great depths, within the mantle, unless there was an enhanced geothermal gradient resulting from the residual effects of the associated impact.

Studies of paired breccias have confirmed Cl-apatite U-Pb ages of 1.35 Ga to 1.5 Ga (Yin et al., 2014; Bellucci et al., 2015; McCubbin et al., 2016). The U-Pb system for apatite has a low closure temperature of $450\text{ }^{\circ}\text{C}$ to $500\text{ }^{\circ}\text{C}$, suggesting that the breccia must have experienced temperatures above $500\text{ }^{\circ}\text{C}$ to reset them (Cherniak et al., 1991; Nemchin et al., 2009). Zircons have been divided into two age populations, both ancient ($\sim 4.4\text{ Ga}$) and younger (1.4 Ga to 1.7 Ga), with the suggestion that the younger metamict zircons experienced later alteration from low temperature fluids (Humayun et al., 2013; Yin et al., 2014; Nemchin et al., 2014; Bellucci et al., 2015; McCubbin et al., 2016). As many of the zircons have not been reset, the breccia could not have experienced temperatures above $900\text{ }^{\circ}\text{C}$ (Ireland & Williams, 2003). Similarly, if

temperatures had exceeded 900 °C then pyroxene exsolution textures seen would not have survived. The breccia is likely to have experienced temperatures above 700 °C for some time in order to have mobilised and melted feldspar-rich parts of the breccia, as evidenced by the incipient melting textures along the margin of feldspar veins within pyroxene clasts. Thus, a temperature range from 500 °C to 900 °C has been used in considering a thermal model that would allow the high temperature oxidation seen in pyroxene clasts, which is in agreement with a textural study of melting in the submicron matrix (McCubbin et al., 2016).

A simple cooling model has been constructed using Fourier's Law, which gives the cooling times from a starting temperature of 800 °C, for a 1 m thick slab of martian regolith, area 100 m², density 2600 kg m⁻³, buried at two different depths, 5 m and 20 m (Fig. 3.19). The heat capacity used is 800 J kg⁻¹ K⁻¹, and two examples are shown using thermal conductivity of (A) 2.0 W m⁻¹ K⁻¹ and (B) 0.3 W m⁻¹ K⁻¹ based on lunar breccia samples (Weiss & Head, 2016). Radiative cooling has not been taken into account in this model but would lead to faster cooling rates than calculated.

Temperatures in the regolith at a burial depth of 5 m were maintained at above 700 °C for over 28 days, which is sufficient for nanophase hematite to form (Minitti et al., 2002) (Fig. 3.19). Cooling from 800 °C at a depth of at least ~10 m maintains temperatures above 760 °C for 4 weeks, similar to the conditions needed to form analogous oxidation in enstatite (Straub et al., 1991). Oxidation was also reported in pigeonite samples oxidised in experiments at 700 °C for 7 days, but a larger effect was seen at 1000 °C for 14 days (Straub et al., 1991). This shows that even if the breccia formed close to the surface, in a relatively thin regolith blanket, of the order of 5 m deep, it would still experience elevated temperatures for weeks and up to months, consistent with the experimental results from pyroxene oxidation studies.

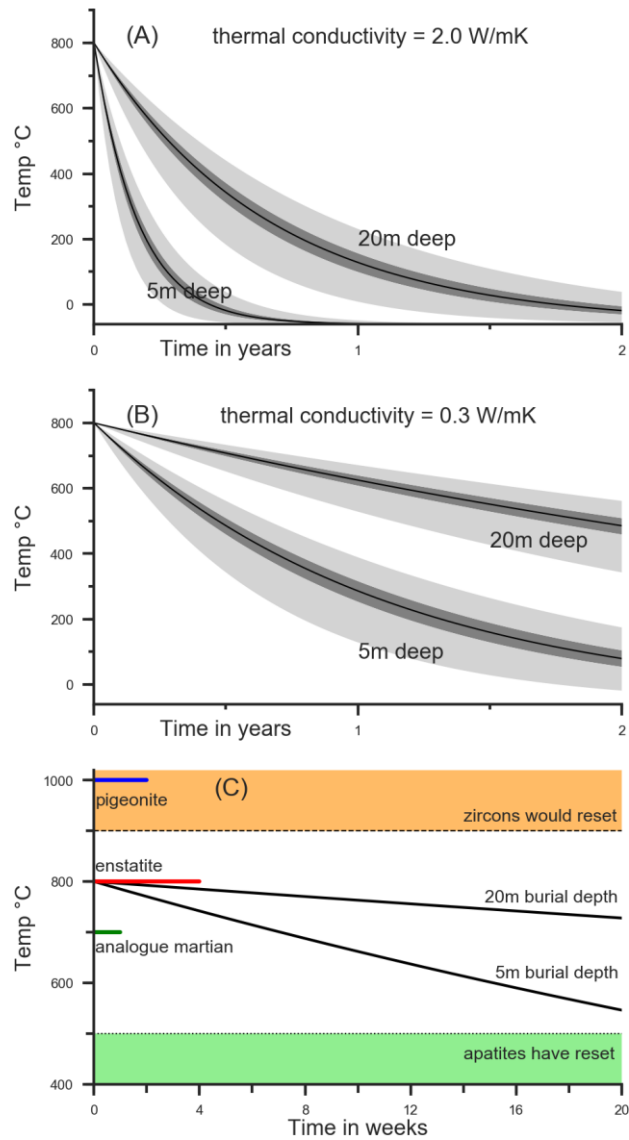


Fig. 3.19: Modelled cooling profiles using Fourier's law for a 1 m thick slab of martian regolith with surface area 100 m^2 , density 2600 kg m^{-3} buried at two different depths, 5 m and 20 m, starting at $800 \text{ }^\circ\text{C}$. The martian surface temperature is assumed as $-60 \text{ }^\circ\text{C}$. The heat capacity used is $800 \text{ J kg}^{-1} \text{ K}^{-1}$, the effect of varying this by $\pm 10\%$ or $\pm 40\%$ is shown by the dark grey and light grey areas respectively. Thermal conductivity is estimated as (A) $2.0 \text{ W m}^{-1} \text{ K}^{-1}$ based on basalt values and (B) $0.3 \text{ W m}^{-1} \text{ K}^{-1}$ based on lunar breccia values (Weiss & Head, 2016). (C) Detailed cooling profiles with parameters the same as (B) over the first 20 weeks compared with oxidation studies showing nanophase hematite forming in pigeonite, enstatite (Straub et al., 1991) and analogue martian samples (Minitti et al., 2002). As some of the zircons have not been reset by the breccia formation event at $\sim 1.25 \text{ Ga}$ and there is not extensive evidence of melting in the matrix, it is unlikely that temperatures exceeded $900 \text{ }^\circ\text{C}$ (orange area). As Cl-apatite grains have had their U-Pb system reset 1.35 Ga to 1.5 Ga (Yin et al., 2014; Bellucci et al., 2015; McCubbin et al., 2016), temperatures must have exceeded $500 \text{ }^\circ\text{C}$ (green area). This model shows a burial depth of $\sim 5 \text{ m}$ would be sufficient to provide enough heat to partially oxidise the pyroxene and produce the micron and submicron grains of magnetite observed.

The cooling curves at 5 m depth or greater all maintain temperatures above 700 °C for at least six weeks, with a 20 m burial depth taking over twenty weeks to cool below this (Fig. 3.19). Thus, cooling at a depth of at least 5 m provides a thermal environment with temperatures high enough and cooling slow enough to produce the crystalline plagioclase seen in the veins.

3.5 Conclusions

The martian regolith breccia, NWA 8114 is paired with NWA 7034 and others. This study of clasts within it used SEM, EPMA, FIB-STEM, synchrotron Fe-K XANES, XRD, XRF, FTIR and additionally, individual clasts have been separated and analysed with ^{40}Ar - ^{39}Ar . This has revealed a combination of early magmatic events overprinted in some clasts by breakdown of pyroxene and feldspar veining at high temperature within the impact regolith.

- The NWA 8114 martian breccia includes a range of crystal clasts, including pyroxenes, plagioclase and alkali feldspar, with minor volumes of iron oxides, Cl-apatite, and also feldspar veins and aureoles. Pyroxene exsolution textures and feldspar cryptoperthite textures indicate slow cooling and a record of magmatic events prior to the impact-related processes.
- I have focused on the pyroxenes, investigating a texture where many pyroxene clasts contain sub-micron iron oxide grains and high porosity (~2 %). Some clasts have accreted rims, requiring time spent in an ejecta plume or density current, perhaps in the presence of water vapour, likely caused by the impact event that formed the breccia.
- FIB-TEM-EDX and XANES analyses reveal oxidation of up to 25% $\text{Fe}^{3+}/\Sigma\text{Fe}$ and the breakdown of clasts that were predominantly pyroxene, at high temperature, to iron oxide and a K-bearing feldspathic glassy material, with an associated porous texture. This was shown to be anhydrous by micro FTIR analyses, so any early water vapour was rapidly lost in the cooling regolith breccia on Mars. In one of these relict pyroxenes with a feldspar aureole, XRD was used to identify iron oxide as magnetite. This breakdown assemblage occurs in low-Ca pyroxene, relict pigeonite and some augite-dominated pyroxene clasts. The oxidation could arise from the loss of H^+ ions from the pyroxene structure, or the presence of transient water at the time of the impact

event.

- The NWA 8114 parent rock was maintained at high temperature in the regolith. By analogy with published experimental studies, the oxidation and partial pyroxene breakdown are likely due to being held at a temperature above 700 °C for at least 7 days in an oxidising regolith environment as a result of the impact event. Temperatures above 700 °C would also be sufficient for *in-situ* melting of feldspar-rich domains forming feldspathic veins crosscutting the oxidised pyroxene. The area ~20 µm each side of the veins shows some textural evidence for partial melting and subsequent devitrification of the pyroxene host clasts. These could however, alternatively be hydrothermal feldspar veins, as a small amount of hyalophane is observed.
- A separated clast of augite showing the partial breakdown texture, yielded an approximate, maximum ^{40}Ar - ^{39}Ar age of ~1.13 Ga to 1.25 Ga, in line with the 1.1 Ga to 1.4 Ga ages suggested by comparable studies. This age range is interpreted as dating the pyroxene breakdown in the impact regolith at elevated temperatures of at least 700 °C.
- A simple cooling model suggests that the high temperature processing could have occurred within a regolith breccia of the order of ≥ 5 m depth.
- XRD, XANES and FTIR identify goethite, which is evidence of late stage low temperature hydrous alteration. In the absence of textural evidence to the contrary, this is probably the result of terrestrial alteration of martian pyrite.

4 SYNCHROTRON ANALYSES OF COMET WILD 2 AND ANALOGUE CHONDRITES

This chapter aims to provide a direct comparison between different carbonaceous chondrite types and comet 81P/Wild 2. It details my characterisation of comet terminal grains returned by the NASA *Stardust* spacecraft in four keystones that have not been examined before, using non-destructive synchrotron techniques: Fe-K X-ray absorption near edge structure (XANES), X-ray fluorescence (XRF) and X-ray diffraction (XRD), and comparing to reference standard materials. Then, to compare and investigate the similarities between *Stardust* comet grains and carbonaceous chondrites, I have prepared and characterised carbonaceous chondrite samples which were shot into aerogel and prepared as keystones, analogous to the *Stardust* capture process. The terminal grains were examined with the same synchrotron techniques.

A prologue about comets and cometary science missions to date can be found in chapter 1, and future science in chapter 6. This chapter introduces the *Stardust* mission and samples and looks at the body of knowledge from the first ten years of analysing *Stardust* grains. It then looks at the similarities and differences between comets and carbonaceous chondrites. The methods detail the samples, processes and techniques used and then the results are given and discussed. The work in this chapter has contributed to Hicks et al. (2017) and Wickham-Eade et al. (2017).

4.1 Introduction

4.1.1 Comet 81P/Wild 2

Comet 81P/Wild 2, first discovered in 1978, previously took ~ 43 years to orbit the Sun between 4.9 AU and 25 AU (Brownlee et al., 2003; Brownlee et al., 2012). Due to a close encounter with Jupiter's gravitational influence in 1974, it was brought into the inner Solar System as a Jupiter-family comet (JFC). It is now in a ~ 6 year orbit between 1.58 AU and 5.2 AU (Brownlee et al., 2003).

Emissions showing depletion of C_2 suggest Wild 2 originated in the Kuiper belt between 30 AU to 50 AU from the Sun (Brownlee et al., 2012). Perturbations from the outer planets most likely caused the gradual migration of Wild 2 from beyond Neptune, to its current JFC orbit, over a few million years (Levison & Duncan, 1997). Therefore, this recently deflected comet, now accessible within the inner Solar System, offers pristine 'left over' material from the early Solar System as Wild 2 had only made five near solar passes between becoming a Jupiter-family comet and the *Stardust* encounter. The comet has otherwise been stored at temperatures below 50 K beyond Neptune and likely undergone little or no alteration since, prior to the *Stardust* mission encounter.

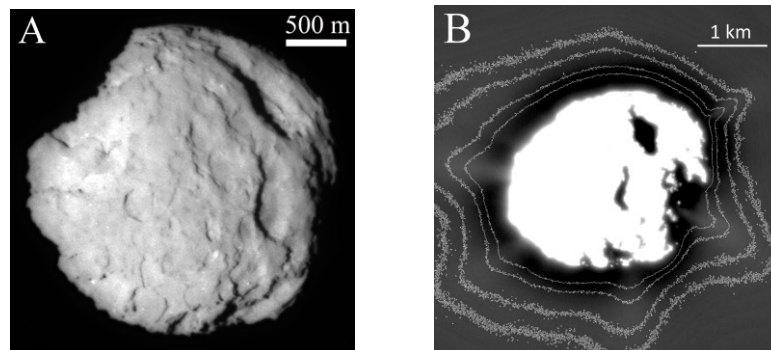


Fig. 4.1 (A) The closest image taken of the nucleus of comet Wild 2 from the *Stardust* spacecraft. (B) The nucleus of comet Wild 2, surrounded by lines of constant brightness in the dust, with bumps indicating jets. (NASA/JPL-Caltech 2004)

Wild 2 is found to be an oblate ellipsoid, showing a fairly constant cross section as it rotates about its shortest axis. Fitting a triaxial ellipsoid, with radii of $1.65 \times 2.00 \times 2.75 \text{ km} \pm 0.05 \text{ km}$ (Duxbury et al., 2004) to camera images of the nucleus (Fig. 4.1A) gives a diameter of 4.0 km (Sekanina et al., 2004). Twenty jets of solid particles from multiple sources were observed (one angle shown in Fig. 4.1B) (Sekanina et al., 2004).

Doppler data suggests the maximum mass of the nucleus is 5×10^{15} kg (Anderson et al., 2004) assuming a density for the nucleus of 0.5 g cm^{-3} .

When assessing Wild 2 as a suitable target for a possible sample-return mission within NASA's Discovery program constraints, a 7-year trajectory was calculated. This trajectory allowed suitable speeds at which to encounter the comet at a distance of 1.86 AU (Anderson et al., 2004), capture grains and return the sample, while requiring only modest fuel, and led to the mission being selected by NASA in 1995 (Brownlee et al., 2003). The collected grains should allow the non-volatile component of the comet nucleus to be analysed (Brownlee et al., 2006).

4.1.2 The *Stardust* mission

The primary aim of the NASA *Stardust* mission was to collect over 1000 particles over $15 \mu\text{m}$ in diameter from the coma of comet Wild 2 and return them to Earth for analysis. The secondary objectives were to collect 100 interstellar particles (ISP) particles over $0.1 \mu\text{m}$ in diameter during the cruise phase for return to Earth, and to acquire at least 65 images of the nucleus at a minimum resolution of $67 \mu\text{r}$ (micro rad)/pixel, and to analyse the composition of cometary particles in situ (Brownlee et al., 2003).

Launched in February 1999, the spacecraft spent two periods totalling 95 days collecting interstellar particles. On 2 January 2004, it flew past the nucleus of comet Wild 2 at a distance of 234 km and a speed of 6.1 kms^{-1} (Brownlee et al., 2006), collecting an estimated 2800 ± 500 particles of $> 15 \mu\text{m}$ in diameter from the Dust Flux Monitor Instrument measurements (Tuzzolino et al., 2004). During the period of closest approach the nucleus was imaged at ten second intervals, with fourteen metre per pixel resolution for the closest image (Brownlee et al., 2004). Seven likely ISPs have been identified (Westphal et al., 2014), though probably no more than a dozen ISPs over one picogram in mass were collected (Westphal et al., 2017). The sample collector landed in the Utah desert on 15 January 2006, and the samples were subsequently curated at the Johnson Space Centre (JSC).

The spacecraft also made a flyby of asteroid Annefrank (2 November, 2002) that tested its instruments in preparation for studying comet Wild 2. After successfully completing its primary mission, the spacecraft performed a bonus mission, *Stardust-NExT*, flying

past comet Tempel 1 on 14 February 2011, making its final transmission to Earth on 24 March 2011.

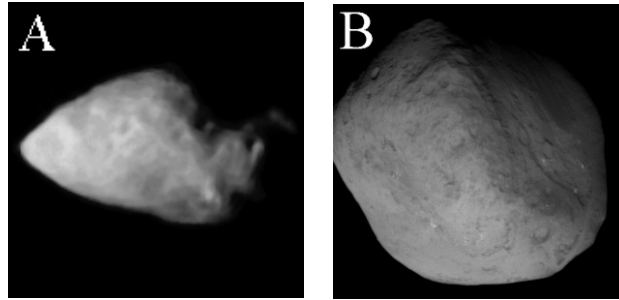


Fig. 4.2. (A) Asteroid Annefrank, $6.6 \times 5.0 \times 3.4$ km, imaged by *Stardust* from a distance of 3,300 km. Composite image created from over 40 images (Nov 2, 2002, NASA / JPL / Ted Stryk). (B) The nucleus of comet Tempel 1, 7.6 km \times 4.9 km, imaged by *Stardust*-NExT from a distance of 181 km, (Feb 14, 2011, NASA/JPL-Caltech/Cornell).

4.1.3 The *Stardust* Spacecraft

An artist's impression of NASA's *Stardust* spacecraft at Wild 2 shows its main features in Fig. 4.3. The Sample Return Capsule (SRC) contained the *Stardust* Wild 2 and Interstellar Sample Collection and Earth Return (WISCER) instrument (Tsou et al., 2003), which deployed the sample tray assembly (STA) during the encounter. The STA comprised the 3 cm thick Cometary Tray 2 (C2) for Wild 2 grains, and the 1 cm thick Interstellar Tray 1 (I1) for interstellar grains, back to back mounted aluminium trays. These trays contained aerogel varying in density to decelerate the particles during capture. The STA was retracted and locked three minutes after the closest point of the flyby for Earth return. During collection, the STA extended beyond the high-gain antenna and main spacecraft dust 'Whipple shields' that protect the spacecraft from hypervelocity particle impacts (Fig. 4.3). The following three science instruments collected complementary measurements throughout the close flyby of the coma of comet Wild 2 in January 2004.

The engineering Optical Navigation Camera (NavCam) utilised components from the Voyager mission and a spare Cassini CCD array with 1024×1024 pixels, alongside new components with inherited designs. This gave a resolution of 59.4 microradian per pixel resolution (Newburn et al., 2003).

The Comet and Interstellar Dust Analyzer (CIDA) is a time-of-flight mass spectrometer, a derivative of an instrument used on the Giotto spacecraft's flyby of

Halley's comet. Impact ionization mass spectrometry can detect relatively volatile molecular species in-situ from the comet, which would not be retained in the aerogel cells (Kissel et al., 2003).

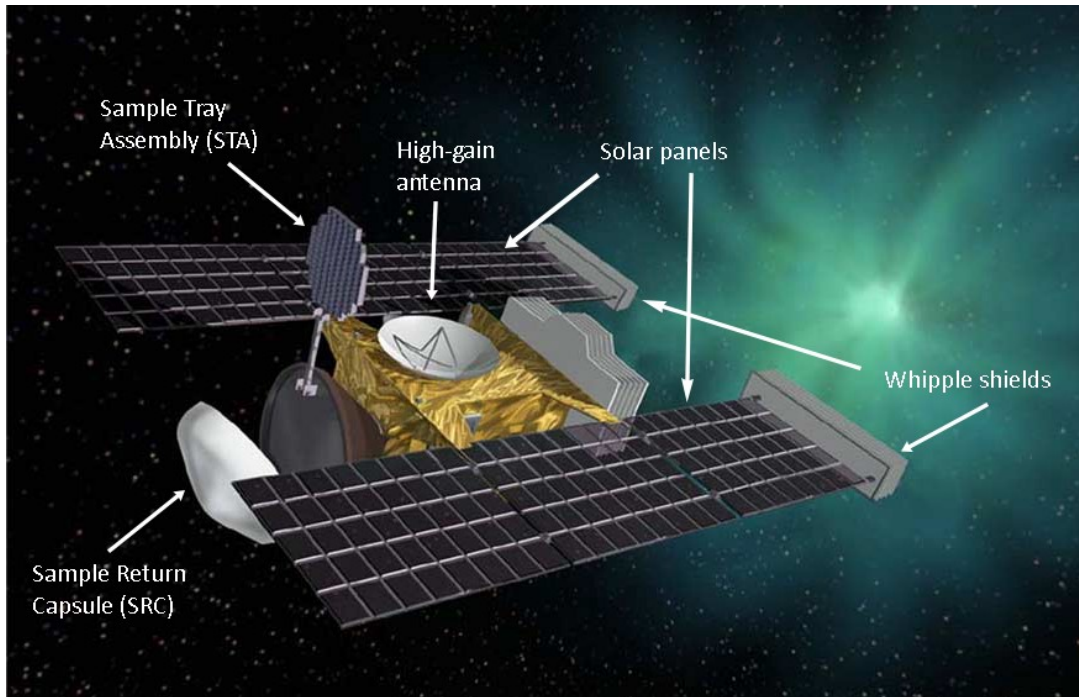


Fig. 4.3. Artist's concept of the *Stardust* spacecraft at comet Wild 2 with the Sample Tray Assembly aerogel detector fully deployed (NASA).

The Dust Flux Monitor investigation is a polyvinylidene fluoride particle penetration dust flux monitor, a duplicate of part of the Cosmic Dust Analyzer instrument used for the Cassini mission to Saturn. This classifies impacting dust particles with mass $< 10^{-4}$ g into seven particle mass thresholds (Tuzzolino et al., 2003). Additionally, half of the main Whipple shield has piezoelectric acoustic sensors to detect larger particles, a larger area in order to detect the expected lower flux (Tuzzolino et al., 2003).

4.1.4 The *Stardust* Samples

Both the Cometary and Interstellar Tray have 132 aerogel cells. This silica aerogel has very high spongy porosity, in which more than 99% of the volume is space, and is ideal for capturing hypervelocity particles, as it is nearly

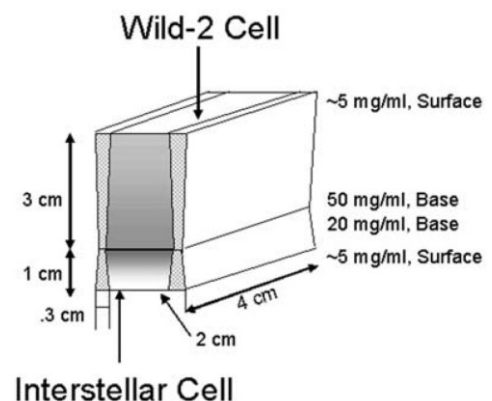


Fig. 4.4. Aerogel cell (Tsou et al., 2003)

transparent, allowing microscopic study. The cells have a continuous gradient density to decelerate the particles during capture, starting at $\sim 5 \text{ mg/ml}$ (kg m^{-3}) at the surface of each to 50 mg/ml at the base of the cometary side, and to 20 mg/ml (20 kg m^{-3}) at the base of the interstellar side (Fig. 4.4). The tray wall frames are wrapped in aluminium foils to facilitate extraction of the aerogel. The total surface area exposed to Wild 2 was 1039 cm^2 of aerogel (87%) and 153 cm^2 (13%) of aluminium foil (Fig. 4.5) (Tsou et al., 2003).

Techniques were developed for curating and handling the samples at NASA’s JSC and University of California Berkeley, including cutting keystones from the aerogel (Westphal et al., 2004; Mark J. Burchell et al., 2006), and using acrylic resin to embed compressed grains and tracks for ultramicrotomy samples in order to study them with electron microscopy (Matrajt & Brownlee, 2006). Epoxy was sometimes used instead of acrylic to avoid any compression and preserve the original shape of an entire track (Nakamura-Messenger et al., 2011)

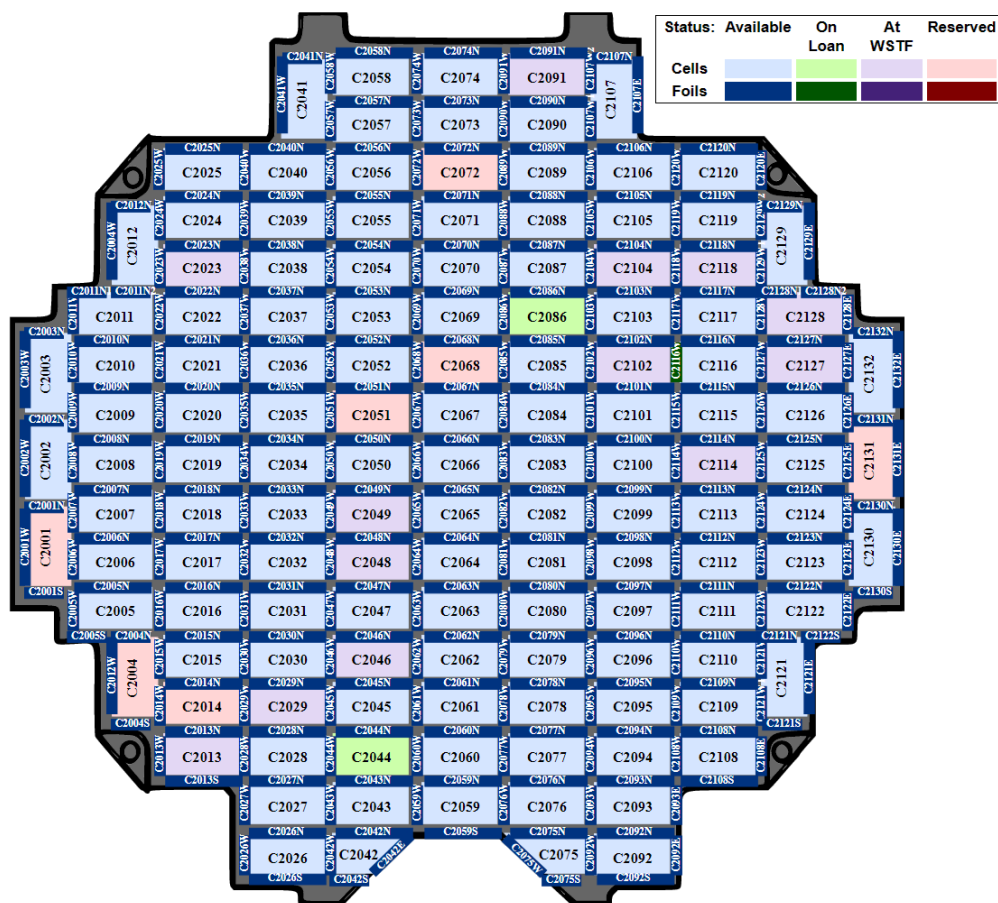


Fig. 4.5. *Stardust* Cometary Tray 2, showing the status of the 132 aerogel cells and foil areas between them as at 23 September, 2018 (NASA-JSC, 2018).

4.1.4.1 Nomenclature of tracks

The names for *Stardust* samples use the following system. “C2” refers to Cometary Tray 2, and “I1” refers to Interstellar Tray 1 (the others C1, C3, I2, I3 were built as flight spares). The next part is the name of the aerogel cell from 001 to 132, so all the *Stardust* samples are numbered from C2001 to C2132 (Fig. 4.5).

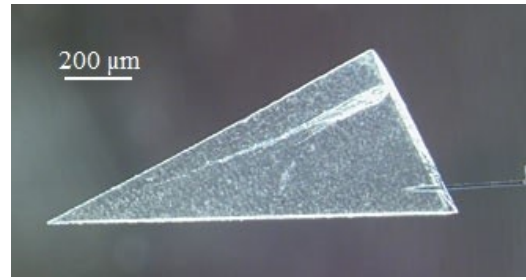


Fig. 4.6 Extracted aerogel keystone (credit Christopher Snead/UC Berkeley)

The second part of the name is the sequential number of the piece of aerogel containing the captured particle(s), starting from “0”. These are known as keystones and are often triangular (Fig. 4.6).

The third part is the sequential number of the impact track features, in the order they were removed from the aerogel cells or first sampled. In this thesis I abbreviate the samples by their track numbers #187, #188, #189 and #190.

Any following numbers denote the parent of any further sub-samples, with commas in between each. For example, C2009,20,77,1,6 is TEM grid 6, made by JSC from microtomed slices of grain 1 from track 77 in the 20th keystone cut from aerogel cell C2009. This chapter focuses on complete *Stardust* tracks, so the last two numbers are 0,0 for all samples.

4.1.4.2 Preliminary sample overview, track types

The total mass of the comet particles collected is estimated to be ~300 μg and the distribution is shown in Fig. 4.7 (Hörz et al., 2006). The deepest aerogel track is 21.9 mm long, the widest is 9.6 mm and the largest crater in the foil is 680 μm in diameter (Hörz et al., 2006). The aerogel tracks have been classified as type A ‘carrot’, type B ‘bulbous’ with a slender terminal portion or type C ‘bulbous’ without a terminal extension (Fig. 4.8). Similar track morphologies have been successfully created experimentally for comparison, by firing known projectiles into aerogel using a light gas gun of speeds up to 7 km s^{-1} (Hörz et al., 2006).

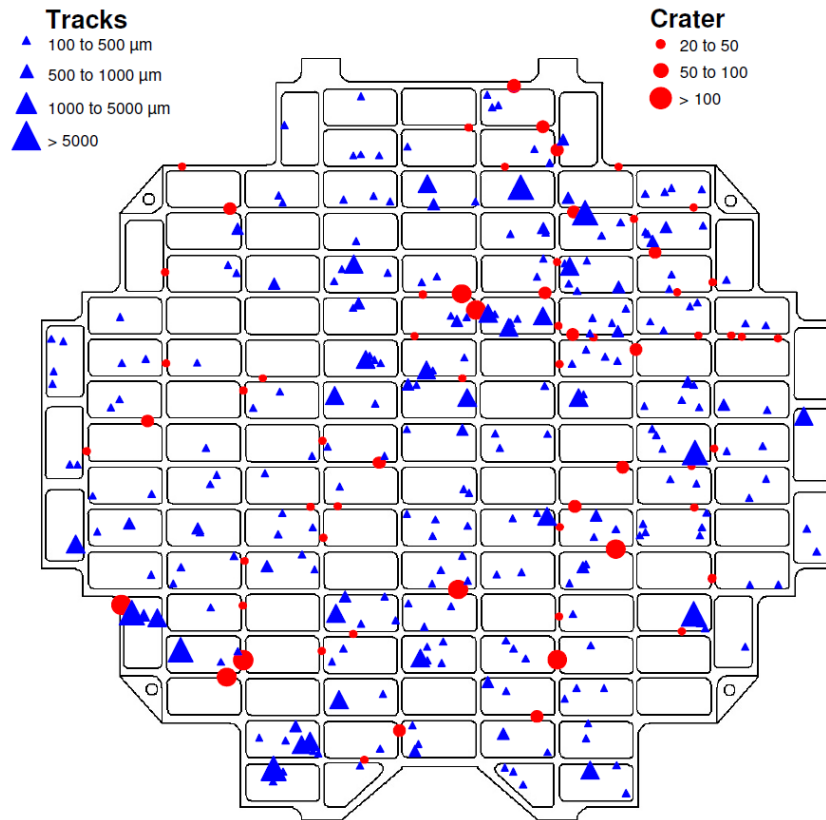


Fig. 4.7. Distribution of all aerogel tracks $> 100 \mu\text{m}$ in diameter and craters in the foil $> 20 \mu\text{m}$ in the Cometary Tray (Hörz et al., 2006).

A study of 186 tracks found 65% Type A, 33% type B and 2% type C (Burchell et al., 2008). Most tracks less than $300 \mu\text{m}$ are type A, whereas tracks over $500 \mu\text{m}$ are approximately half A and half B (Burchell et al., 2008). These preliminary studies estimated in total 158-180 particles over $15 \mu\text{m}$ in diameter were collected, and ~ 1200 particles over $1 \mu\text{m}$ in diameter (Hörz et al., 2006; Burchell et al., 2008). 95% of the samples are still available to analyse (Westphal et al., 2017).

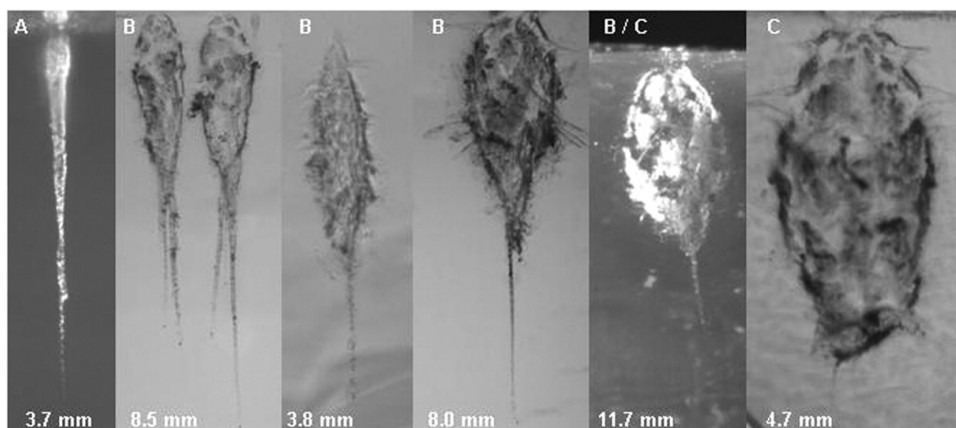


Fig. 4.8. Examples of type A, B and C *Stardust* tracks (Hörz et al., 2006).

The aluminium foil was also bombarded with hypervelocity particles leading to impact crater features, giving a range of shapes and sizes with melted and unmelted residue (Brownlee et al., 2006). This forms an important complementary data set to the grains captured in aerogel.

4.1.4.3 Capture effects

The upper parts of tracks contain melted aerogel with dissolved projectile, but further down the amount of melting decreases leaving largely unmelted comet fragments in the lower region (Brownlee et al., 2006). Components under 1 μm were often strongly modified by the capture process, experiencing temperatures of over 2000 K locally, but those over 1 μm appear well preserved (Brownlee et al., 2006). Spacecraft contamination in the aerogel is very limited (Zolensky et al., 2006).

If comet Wild 2 were to contain chondrules and CAIs, they would not be expected to remain intact during the *Stardust* capture process. However, terminal grains offer the possibility that fragments of these would survive. Light gas gun experiments in aerogel suggest that grains $>4 \mu\text{m}$ would not have experienced temperatures over 300 °C in their centre. This would also allow phyllosilicates to survive (Noguchi et al., 2007). For analogue experiments using light gas guns to fire projectiles into aerogel, the acceleration may affect and alter grains, though it is not possible to distinguish these effects from the effects of possible alteration from the impact into aerogel.

We have chosen to study terminal grains as these are generally larger and show the least evidence of alteration by the capture process, with cores of grains over 1 μm likely to offer the most pristine material captured by the *Stardust* mission (Changela et al., 2012).

4.1.5 *Stardust* science: affinities with carbonaceous chondrites

Stardust grains were originally expected to resemble chondritic porous interplanetary dust particles (CP-IDPs), formed at low temperatures and thought to be derived from comets. Surprisingly, they instead contain refractory minerals such as forsterite and enstatite (Brownlee et al., 2006) that have more in common with inner Solar System material and, in particular, carbonaceous chondrites.

Carbonaceous chondrites are thought to have more than eight parent bodies, as indicated by the different classes, CV, CR, CK, CH, CB, CI, CM, CO as well as

ungrouped specimens. Most are matrix-rich but CH and CB are matrix-poor (Weisberg et al., 2006). All contain minerals formed at high temperatures, and chondrules and CAIs (calcium-aluminium inclusions) are present in all types except CI chondrites.

CI chondrites have the most primitive solar-like composition, but being type 1 with heavy aqueous alteration, it is unclear whether CI chondrites are entirely composed of matrix, or whether they originally contained chondrules and CAIs (calcium-aluminium inclusions) that were destroyed by alteration (Weisberg et al., 2006). All CV chondrites are type 3, having undergone little or no thermal or aqueous alteration, with a high abundance of CAIs and AOAs. Most CR chondrites are type 2, with some aqueous alteration, and a low abundance of CAIs and AOAs. Both CV3 and CR2 chondrites contain abundant, large ~1 mm size chondrules, often with rims (Weisberg et al., 2006). Most chondrules in unequilibrated chondrites share characteristics. They have porphyritic and poikilitic textures, indicative of high temperature melting and rapid cooling (Nakamura et al., 2008). They are dominated by Mg-rich olivine and low-Ca pyroxene microphenocrysts set within feldspathic glassy mesostasis (Nakamura et al., 2008).

The possible formation mechanisms for chondrules are highly debated. The prevailing view has been that chondrules experienced high temperature melting and fast cooling in the solar nebula, and existed as individual chondrules in the protoplanetary disk, before they accreted to small asteroids (Brearley & Jones, 1998; Connolly & Jones, 2016). Models have been offered for nebular shock waves or lightning in the early protoplanetary disk, shock-melting clumps of dust. However, it is unknown if these processes did actually occur in the disk (Connolly & Jones, 2016).

It has been suggested that chondrules could have formed in a planetary regolith (Bridges et al., 1998). More recently it has been suggested that chondrules formed from partially molten planetesimals colliding (Asphaug et al., 2011). An impact jetting model demonstrates that with an impact velocity $> 2.5 \text{ kms}^{-1}$, material is melted and ejected at high speeds with the igneous textures and characteristics of chondrules (Johnson et al., 2015). This would make chondrules a by-product of planet building, rather than the building blocks of the planets (Johnson et al., 2015).

CAIs are traditionally thought to have a different formation mechanism to chondrules, as they are ~2 Ma older, they have isotopic anomalies and excess ^{26}Mg indicating the

past presence of live ^{26}Al and they formed in a more reducing environment (Russell et al., 2006). However, as they are igneous with similar thermal histories and cooling rates to chondrules, a simpler solution would be that they formed by a similar mechanism to chondrules, but distinct in time and perhaps space, which led to their different compositions (Connolly & Jones, 2016).

Oxygen isotope ratios for four olivine and pyroxene chondrule-like *Stardust* particles cover the full range of O isotopes measured in carbonaceous chondrites (Nakamura et al., 2008). This shows an affinity with carbonaceous chondrites rather than ordinary or enstatite chondrites (Nakamura et al., 2008).

Initial studies suggested Wild 2 material is depleted in S and Fe relative to Si, and enriched in Cu, Zn and Ga, when compared to CI chondrite composition (Flynn et al., 2006). These two features are also observed in fine grained anhydrous IDPs (Flynn et al., 2006). Six CAI-like *Stardust* grains have been studied (Simon et al., 2008; Matzel et al., 2010; Joswiak et al., 2017) as well as Al,Ti clinopyroxenes and Mg-Al spinel, consistent with CAI-like material (Joswiak et al., 2012; Joswiak et al., 2017). Melilite was found in the refractory CAI-like *Stardust* grain ‘Inti’, a major phase in CAIs in CV3, CH, CO and CM2 chondrites, formed at temperatures over 1400 K (Simon et al., 2008).

Other investigations have yielded two Al-rich chondrule-like fragments (Bridges et al., 2012; Joswiak et al., 2014), and ferromagnesian chondrule-like fragments, with Mg-rich olivine and low-Ca pyroxene and minor Fe-metal inclusions (Nakamura et al., 2008; Oglione et al., 2012; Bridges et al., 2012; Joswiak et al., 2014; Nakashima et al., 2015). *Stardust* grains contain nearly the complete range of olivine, Fo_{3-100} , with a strong peak at Fo_{99} (Zolensky et al., 2006; Zolensky et al., 2008; Dobrică et al., 2009; Stodolna et al., 2012; Frank et al., 2014). Stodolna et al. (2012) showed that Fe, Mg and S abundances in larger *Stardust* particles ($>1 \mu\text{m}$) converged to the average CI composition value.

Iron oxides have been identified in *Stardust* kestones. Magnetite and magnetite-hematite mixtures (Bridges et al., 2010; Stodolna et al., 2012; Changela et al., 2012) have been found along track walls and magnetite has been found in terminal grains (Hicks, 2015). Carbonaceous chondrites are known to contain magnetite as the result of aqueous alteration on the parent body (Brearley, 2006), thus magnetite found in

Stardust may be evidence for a similar alteration formation mechanism and suggests further similarities with carbonaceous chondrite mineralogy. Ni, Cu and Zn bearing iron sulphides (including cubanite) and comparison to the CI Orgueil meteorite, provide further evidence for low temperature hydrothermal processing (Berger et al., 2011). However, no hydrous phases or phyllosilicates have been observed in *Stardust* grains, which is interpreted as evidence for a lack of hydrothermal alteration (Westphal et al., 2017), although could be the result of sample bias if phyllosilicates were destroyed during the capture process (Wozniakiewicz et al., 2015).

Stardust grains also have similarities with chondritic porous interplanetary dust particles (CP-IDPs). CP-IDPs are the only meteoritic materials known to contain >50% by volume of GEMS, glass with embedded metal and sulphides, and crystalline silicate enstatite whiskers and platelet morphologies (Ishii et al., 2008). GEMS are easily destroyed by aqueous alteration or heating (Westphal et al., 2017). GEMS-like melted material has been found along *Stardust* tracks, but it has also been shown to be created during capture by melting and mixing with the aerogel (Fig. 4.9). The bulk compositions differ from GEMS found in IDPs, so it is not possible to prove original cometary GEMS exist in the *Stardust* samples (Ishii et al., 2008). Only one enstatite whisker embedded in a silicate matrix has been found in Wild 2, whereas whiskers in IDPs are not usually embedded (Stodolna et al., 2014). A study of ~50 coarse grains from a single large CP-IDP yielded three CAIs and a likely AOA, so future study will allow comparison of CAIs and AOAs between the *Stardust* samples, IDPs and chondrites (Westphal et al., 2017).

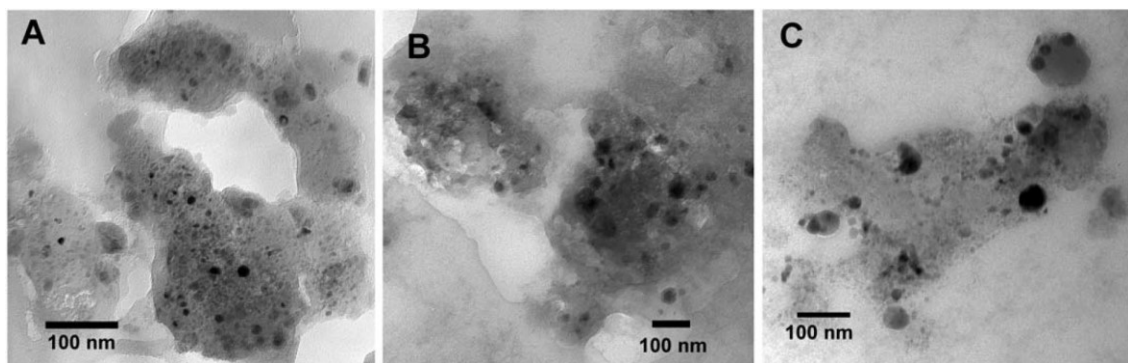


Fig. 4.9. Bright field transmission electron micrographs of (A) GEMS in CP-IDP U220A19 (B) GEMS-like melted material in a *Stardust* track and (C) GEMS-like material from a pyrrhotite grain shot into aerogel with a light gas gun at similar speeds to *Stardust* capture (Ishii et al., 2008).

Although the proportion of presolar grains found in *Stardust* tracks is much lower than the proportion found in IDPs, analogue experiments show that presolar grains tend to be destroyed during the capture process (Floss et al., 2013). After correcting for this, the abundances of the two populations are similar (Floss et al., 2013).

Over half of all Wild 2 tracks contain “Kool” assemblages (Kosmochloric high-Ca pyroxene and Fe-rich olivine) which are also found in IDPs, but not in chondrites (Westphal et al., 2017). These high-Ca pyroxene grains are usually Na- and Cr-rich (Joswiak et al., 2009). One *Stardust* grain, Iris (C2052,12,74), has similar oxygen isotopes and olivine composition to CR type II chondrules (Gainsforth et al., 2015). However, it is also Na- and Cr-rich and appears related to the Kool assemblages (Joswiak et al., 2009), evidence that perhaps Kool grains may be precursors for chondrule-forming processes (Gainsforth et al., 2015).

4.1.6 Selection of CV3 and CR2 chondrites as analogues

CR2 and CV3 chondrites were chosen for this study as they contain chondrules, CAIs, ferromagnesian silicates such as olivine (end members being forsterite Fo, Mg_2SiO_4 and fayalite Fa, Fe_2SiO_4) and pyroxene, FeNi sulphides, and magnetite Fe_3O_4 grains, and are thus potentially close analogues as all these materials have been identified in the *Stardust* tracks. The characterisation of iron oxides is of particular interest in providing further information about possible past aqueous alteration.

Stardust samples are found to have low iron and MnO enrichment (LIME) in some olivine and pyroxene grains (Brownlee et al., 2006; Zolensky et al., 2006; Nakamura et al., 2008). This is also seen in CR chondrule olivine and CM2 matrix olivine (Ebel et al., 2012).

Dobrică et al. (2009) note that the abundance ratio of low-Ca pyroxene to olivine varies from ~ 1 for CR meteorites and Antarctic micrometeorites, to ~ 0.2 for CM meteorites. *Stardust* ratios are approximately ~ 1 as estimated from a population of 169 grains (Dobrică et al., 2009), though more accurate measurement is needed for this to be better constrained (Westphal et al., 2017). This suggests CR meteorites may be a closer match for *Stardust* than CM meteorites, and I seek to test this hypothesis.

Oxygen isotopes measured for Wild 2 ferromagnesian grains suggest a trend of $\Delta^{17}\text{O}$ values increasing with decreasing Mg#, which is most similar to chondrules reported

for CR chondrites (Nakashima et al., 2012). Formation ages of a ferromagnesian *Stardust* particle and oxygen isotope ratios suggest similarities with late-forming CR3 chondrules (Nakashima et al., 2015).

Analysis of D/H isotopes in water found in carbonaceous chondrites shows CR meteorites, with a value of 1.71×10^{-4} (with error of $+0.17 \times 10^{-4}$, -0.10×10^{-4}), to be the closest to the only value measured in a Jupiter-family comet, 103P/Hartley 2, of $1.61 \pm 0.24 \times 10^{-4}$ (Alexander et al., 2012). CM, CI, CV, CO meteorite values are all below this, less than 0.865×10^{-4} (± 0.036) (Alexander et al., 2012).

CR meteorites have similar CAI abundances to those found in comet Wild 2 (Joswiak et al., 2017). As the CR parent body is the youngest of the CCs, formed ~ 3.6 Ma after CAIs, the materials accreted at this time may have been most similar to those materials carried by the radial gas outflow, which could have reached comet-forming regions within a few Ma (Desch et al., 2018). CV meteorites have higher CAI abundances, and the parent body formed >2.6 Ma after CAIs (Doyle et al., 2015), whereas the CR parent body is thought to be a bit later, $\sim 3.5 \pm 0.5$ Ma (Sugiura & Fujiya, 2014).

Magnetite is more abundant in the aqueously altered CR2 and CR1 meteorites and rare in CR3 meteorites (Abreu & Brearley, 2010). The CR2 meteorite chosen for this study has $\sim 1\%$ magnetite.

To explore these chondrite analogues to Wild 2, the carbonaceous chondrite samples were prepared under similar conditions to those for the capture of *Stardust* grains and analysed using the same techniques (see the next section). This work aims to provide an accurate comparison of two selected carbonaceous chondrite types and comet Wild 2.

4.2 Methods

4.2.1 Sample preparation

Three *Stardust* keystones were obtained from the NASA-JSC Curation Facility in Houston, containing four type B tracks:

C2065,4,187,0,0 (#187); Tg1, Tg2, Tg3

C2098,4,188,0,0 (#188); Tg

C2119,4,189,0,0 (#189); Tg1, Tg2, Tg3

C2119,5,190,0,0 (#190); Tg

These were compared with a *Stardust* microtomed terminal grain, from a type B track, examined with TEM (Chapter 5) C2009,20,77,1,6 (#77) and terminal grains from previous studies: C2045,3,177,0,0 (#177), Tg1 in a type A track: and C2045,4,178,0,0 (#178) Tg1a, Tg1b, Tg2 in a type B track (Hicks, 2015).

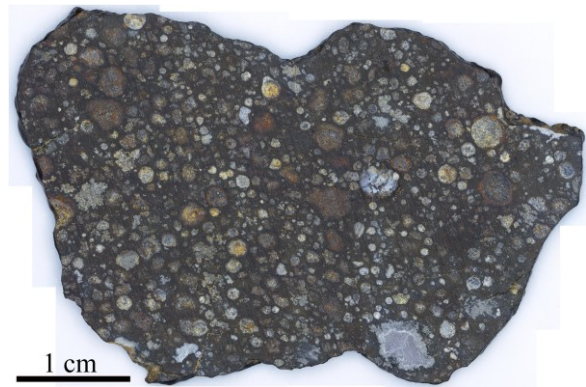


Fig. 4.10. NWA 10256 CR2 slice showing varied large >1mm chondrules in a fine grained matrix.

Carbonaceous chondrites NWA 4502, type CV3, and NWA 10256, type CR2 (Fig. 4.10), were used to make two polished thin sections. Interior parts of the chondrites, away from the crust and any terrestrial weathering, were used to grind a powder with grain size 25 μm to 200 μm . Half of the powders were fired into aerogel of density gradient 25 mg cm^{-3} to 55 mg cm^{-3} at speeds of 6.1 km s^{-1} to 6.3 km s^{-1} using the University of Kent light gas gun (Burchell et al., 1999) (Fig. 4.11) to

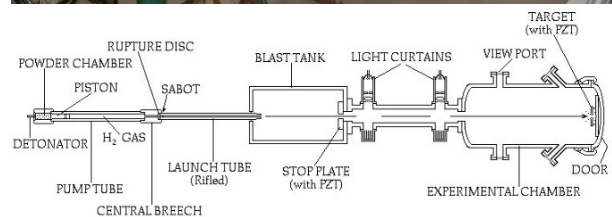
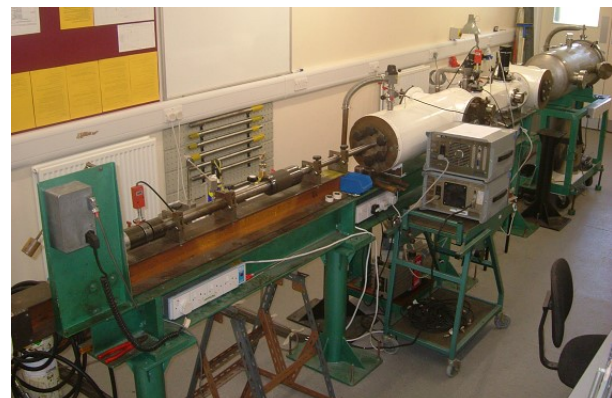


Fig. 4.11. Kent light-gas gun (top) and schematic (bottom) (Burchell et al., 1999).

simulate the *Stardust* grain capture process. Polished blocks were made from the other half for further compositional analysis. The impact tracks in aerogel were then made into kestones at the University of Berkeley using the same methods as for *Stardust* (Westphal et al., 2004). Three of these kestones, containing three CR2 tracks #1, #2 and #3 and three CV3 tracks, #4, #5 and #6, were then analysed at the Diamond synchrotron.

4.2.2 Techniques

The chondrite sections and blocks were characterised using an optical microscope, and a Philips XL30 environmental scanning electron microscope (ESEM) with Oxford INCA 350 energy dispersive X-ray (EDX) system at the University of Leicester. Back scattered electron (BSE) mosaic images of the sections were analysed with *Adobe Photoshop 2015.5.0* software using thresholding tools and pixel counts to give the proportions of chondrules, CAIs and matrix (Fig. 4.12b,d).

MicroRaman spectroscopy analyses were carried out at the University of Kent using a Horiba LabRam-HR Raman spectrometer, incorporating four lasers at 473 nm, 532 nm, 633 nm, and 785 nm with a spot size of $\sim 5 \mu\text{m}$ (M. J. Burchell et al., 2006). The 532 nm laser was used at low power, giving a maximum of 3 mW of power at the sample, to ensure it would not cause heating affects or alteration (Wickham-Eade et al., 2017). MicroRaman was used to characterise the powders before firing, and the impact tracks in aerogel after firing (Wickham-Eade et al., 2017).

These carbonaceous chondrite thin sections and the analogue tracks with terminal grains, together with the four *Stardust* tracks, and suitable standards for comparison and identification purposes, were studied at the Diamond Light Source. The terminal grains were located using X-ray fluorescence (XRF), then Fe-K X-ray absorption near-edge structure (XANES) and X-ray diffraction (XRD) point measurements and maps were taken over the relevant areas. The settings and data processing procedures, including calculation of the Fe-K pre-edge centroid and edge energy and calculating the unit cell dimensions for XRD *d*-spacing intensities, are detailed in chapter 2.

4.3 Results

4.3.1 Characterisation of carbonaceous chondrites

CV3 NWA 4502 has 38% matrix, 14% CAIs and 48% other chondrules (Fig. 4.12A,B). The chondrules contain pyroxene $\text{En}_{50-98}\text{Wo}_{0-34}\text{Fs}_{0-2}$ and olivine Fo_{66-100} , the matrix has FeNi sulfide, metal and olivine Fo_{36-50} , pyroxene $\text{En}_{64}\text{Wo}_{36}$.

CR2 NWA 10256 has 42% matrix, 58% chondrules (Fig. 4.12C,D). Pyroxene $\text{En}_{27-99}\text{Wo}_{0-6}\text{Fs}_{1-67}$ and olivine Fo_{66-99} are found in chondrules, with more fayalitic olivine Fo_{41-81} , Fe-sulfides, FeNi metal, and Fe-oxides in the matrix.

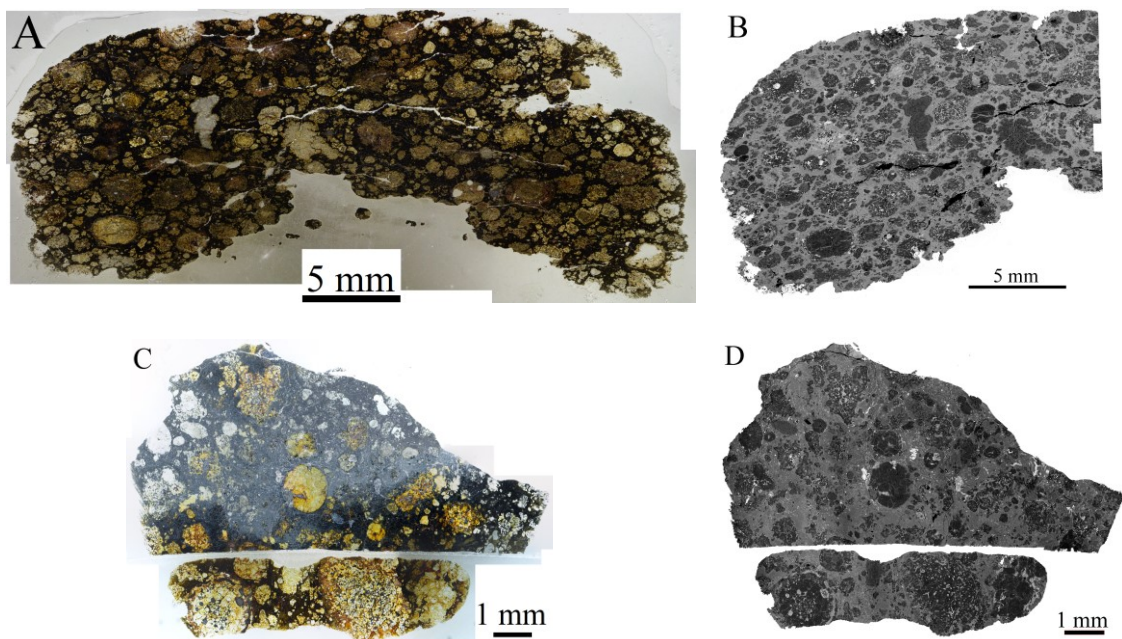


Fig. 4.12. (A) Optical transmitted light microscope image and (B) BSE image of NWA 4502, a CV3 meteorite. (C) Microscope image and (D) BSE image of NWA 10256, a CR2 meteorite.

120 Raman spectra measurements of the CR2 powder before the shot showed ~47% olivine: Fo_{43-57} (7%), Fo_{70-82} (29%), Fo_{88-99} (64%), ~46% enstatite, ~7% hematite (Wickham-Eade et al., 2017). The olivine compositional range is similar to the range seen in *Stardust* grains (Fig. 4.13). After the shot, Raman analyses identified hematite, enstatite and forsterite in three of the aerogel tracks of the CR2 powdered sample.

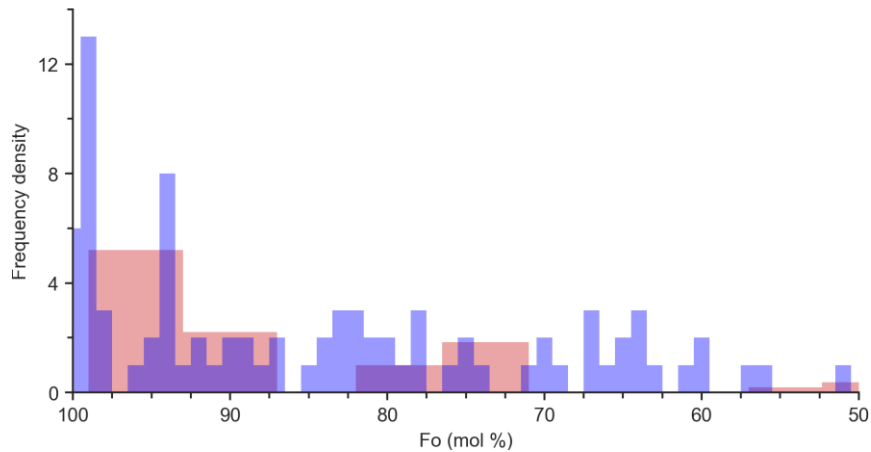


Fig. 4.13. Histogram showing olivine compositions from (Red) 58 Raman measurements of the CR2 meteorite powder, before being shot into aerogel (Wickham-Eade et al., 2017). (Blue) 84 *Stardust* grains in aerogel tracks examined by TEM and/or synchrotron techniques compiled by Dobrică et al. (2009) from Zolensky et al. (2006), Tomeoka et al. (2008), Leroux, Rietmeijer et al. (2008) and Leroux, Stroud et al. (2008).

4.3.2 Characterisation of *Stardust* terminal grains

In this section, the results for each *Stardust* track are examined in turn.

4.3.2.1 C2065,4,187,0,0 (#187)

This type B track #187 contains three terminal grains, Tg1, Tg2, Tg3 (Fig. 4.14).

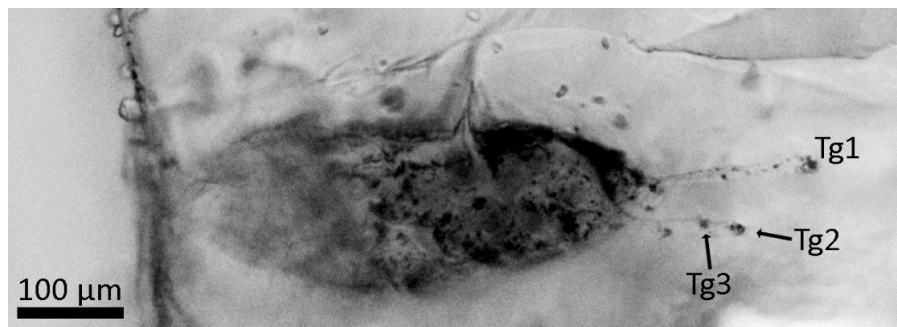


Fig. 4.14. Track #187: a Type B track, 590 μm in length, with at least two styli featuring three terminal grains, consisting of magnetite (Tg1), olivine (Tg2), and troilite (Tg3).

An XRF map across Tg1 shows abundant Fe, high counts for Ni (1566-27057), with small amounts of Cr, Ti, Mn and Ca (Fig. 4.15).

The Fe-K XANES measurement of #187 Tg1 is a close match with the dilute magnetite powder (Fig. 4.16), with its pre-edge centroid energy of 7113.5 eV and edge energy of 7121.0 eV compared with the dilute magnetite powder having a pre-edge centroid of 7113.2 eV and edge of 7120.8 eV (Table 4.2).

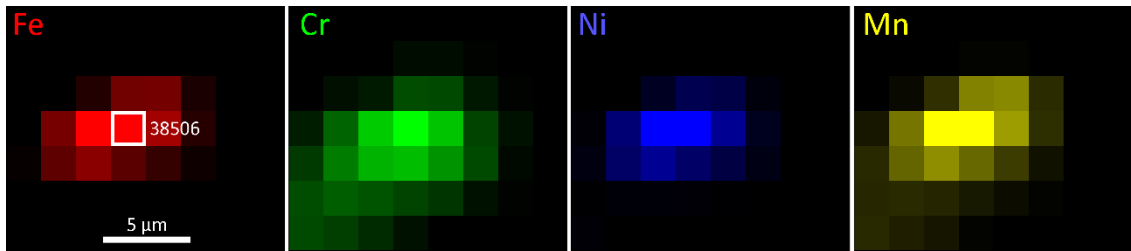


Fig. 4.15. XRF map of the $\sim 5 \mu\text{m}$ first terminal grain (Tg1) in #187 showed the presence of Fe, Cr, Ni and Mn. The location for the XAS measurement is shown by the white box and data number (Fig. 4.16). The brightest and darkest points show the maximum and minimum counts respectively for each element. XRF map data number: 38505. Counts: Fe 2773-470728, Cr 917-4291, Ni 1566-27057, Ti 410-1705, Mn 587-5472.

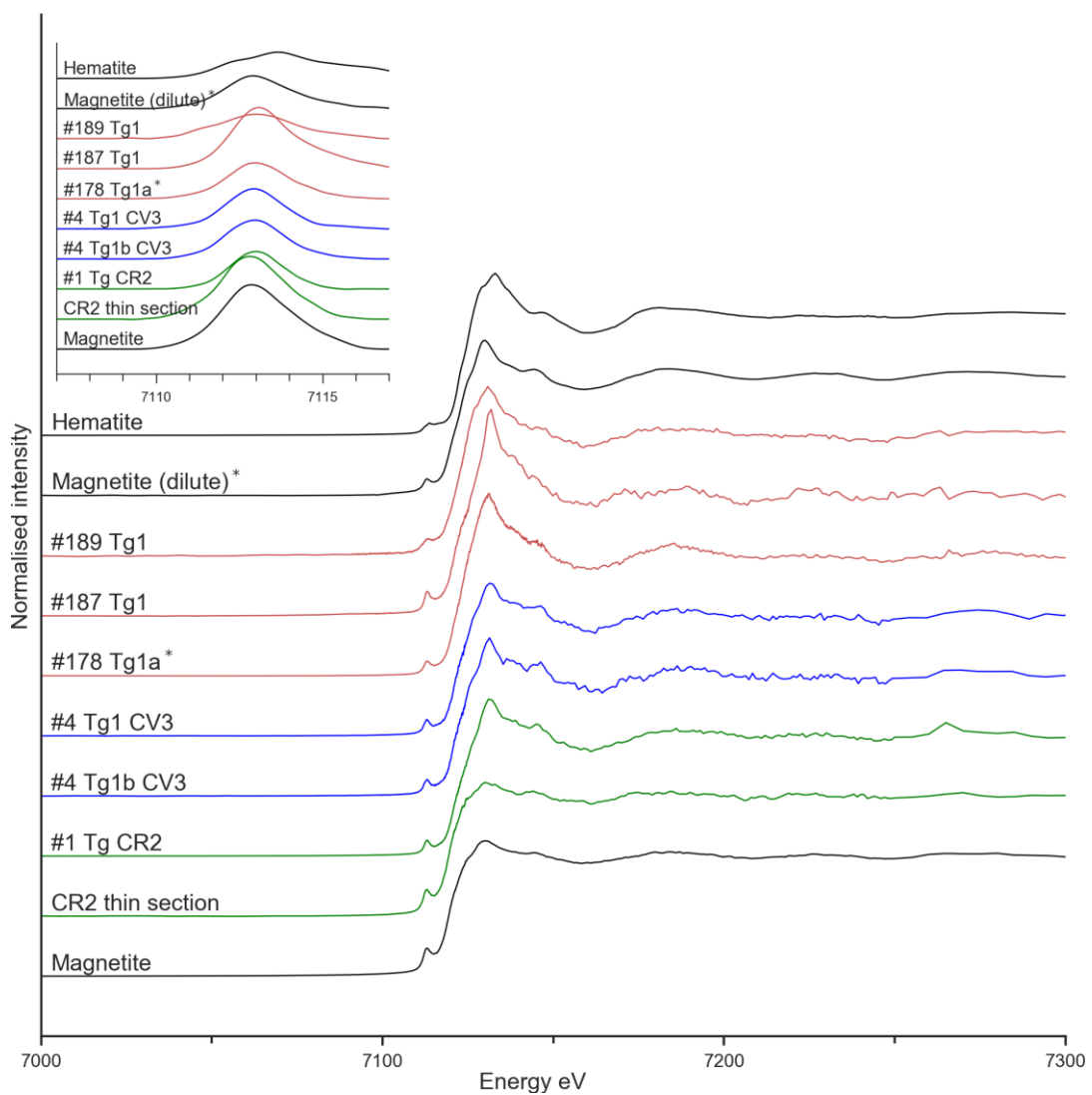


Fig. 4.16. Fe-K XAS of *Stardust* terminal grains (red) found in #178*, #187 and #189 compared with CV3 (blue) and CR2 (green) terminal grains, CR2 in thin section, with standards (black) of hematite (top), dilute magnetite powder* (2nd top) and concentrated magnetite powder with self-absorption (bottom). *(Hicks et al., 2017).

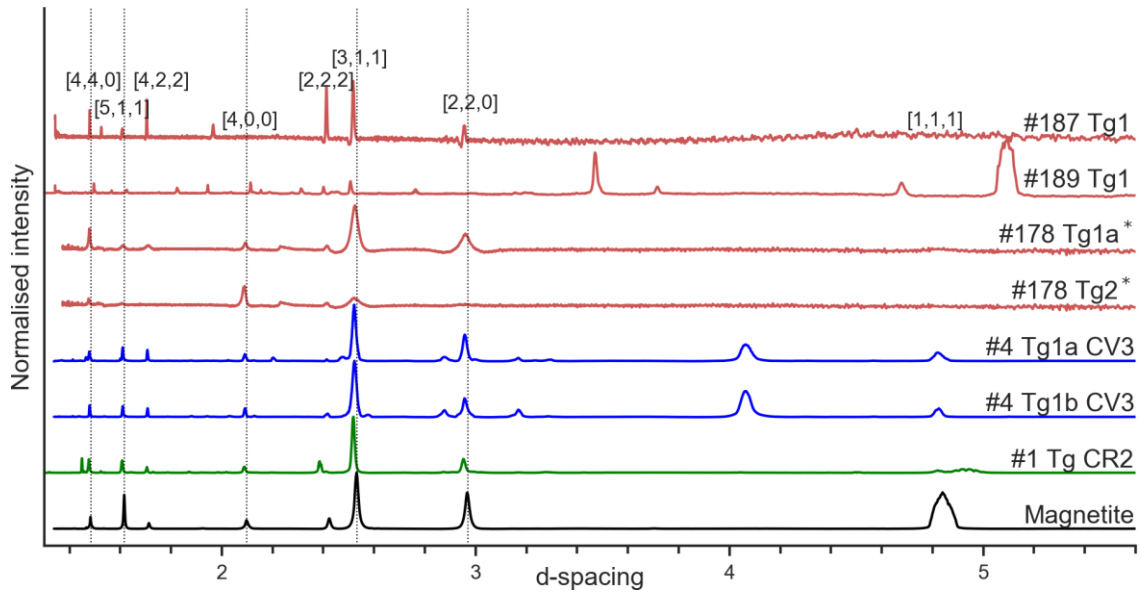


Fig. 4.17. Normalised SR-XRD d -spacing peaks for terminal grains in *Stardust* tracks #178*, #187, #189 (red) compared to #4 CV3 (blue) and #1 CR2 (green) terminal grains and a magnetite powder standard (black). Vertical dotted lines show the five most intense hkl planes for magnetite. The terminal grains show d -spacing peak intensities that closely match to magnetite (Table 4.3).

The XRD d -spacings for #187 Tg1 are a close match with the magnetite powder standard (Fig. 4.17) (Table 4.3). Given the indicated match with magnetite, which has a cubic unit cell, the hkl indices matching the d -spacing peaks observed were used to calculate the unit cell dimension a (Å), assuming that the unit cell was cubic (Table 4.3).

An XRF map across Tg2 shows abundant Fe, high counts for Ni (1783-8601), with small amounts of Cr, Ti, Mn and Ca (Fig. 4.18).

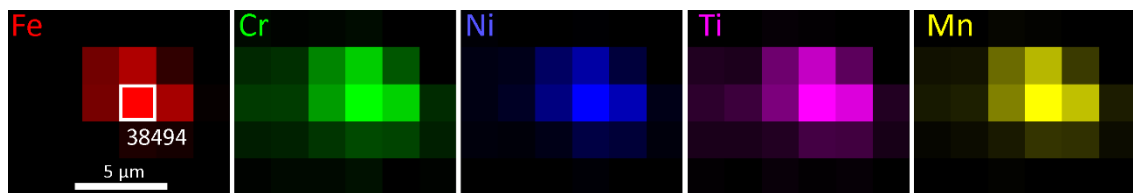


Fig. 4.18. XRF map of the ~ 5 μm second terminal grain (Tg2) in #187 showed the presence of Fe, Cr, Ni, Ti and Mn. The location for the XAS measurement is shown by the white box and data number (Fig. 4.19). The brightest and darkest points show the maximum and minimum counts respectively for each element. XRF map data number: 38493. Counts: Fe 3117-96631, Cr 986-3400, Ni 1783-8601, Ti 506-2725, Mn 693-4210, Ca 2070-7741.

The Fe-K XANES measurement of #187 Tg2 is a close match with olivine (Fig. 4.18), with its pre-edge centroid energy of 7112.3 eV and edge energy of 7119.2 eV

compared with the San Carlos olivine standard having a pre-edge centroid of 7112.1 eV and edge of 7118.8 eV (Table 4.2).

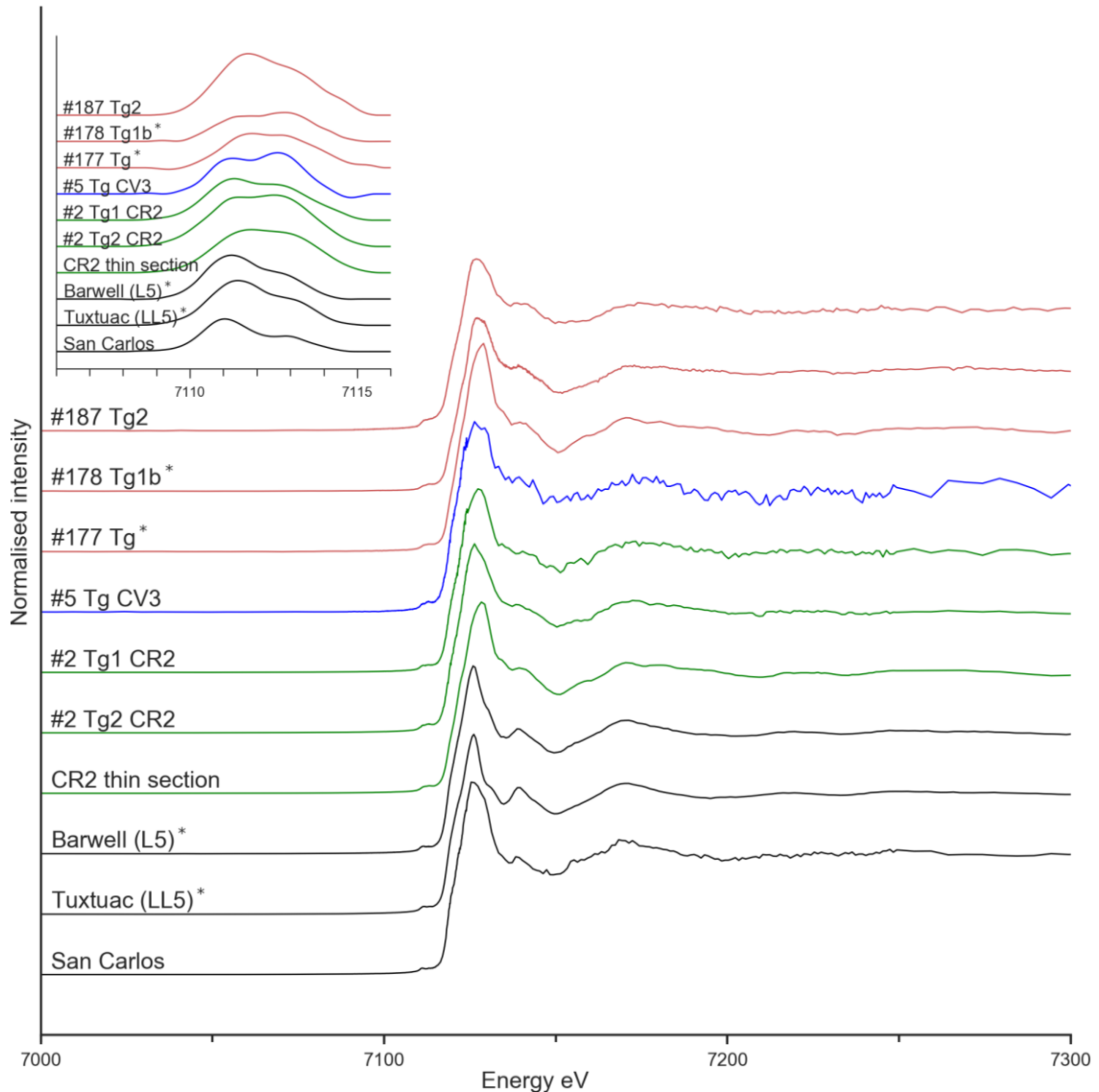


Fig. 4.19. Fe-K XAS of *Stardust* #177*, #178* and #187 terminal grains (red) compared with #5 CV3 (blue) and #2 CR2 (green) terminal grains and with standards (black) of San Carlos olivine, and olivine measurements from chondrites Barwell and Tuxtuac. *(Hicks, 2015)

The XRD normalised intensities for the d -spacings for #187 Tg2 show noisy data as the intensities were very low (Fig. 4.20). There are two tiny peaks showing a provisional match with two of the lattice planes with highest intensities for olivine, [1,1,2] and [1,3,1] as well as a peak at ~ 2.27 that matches [1,2,2].

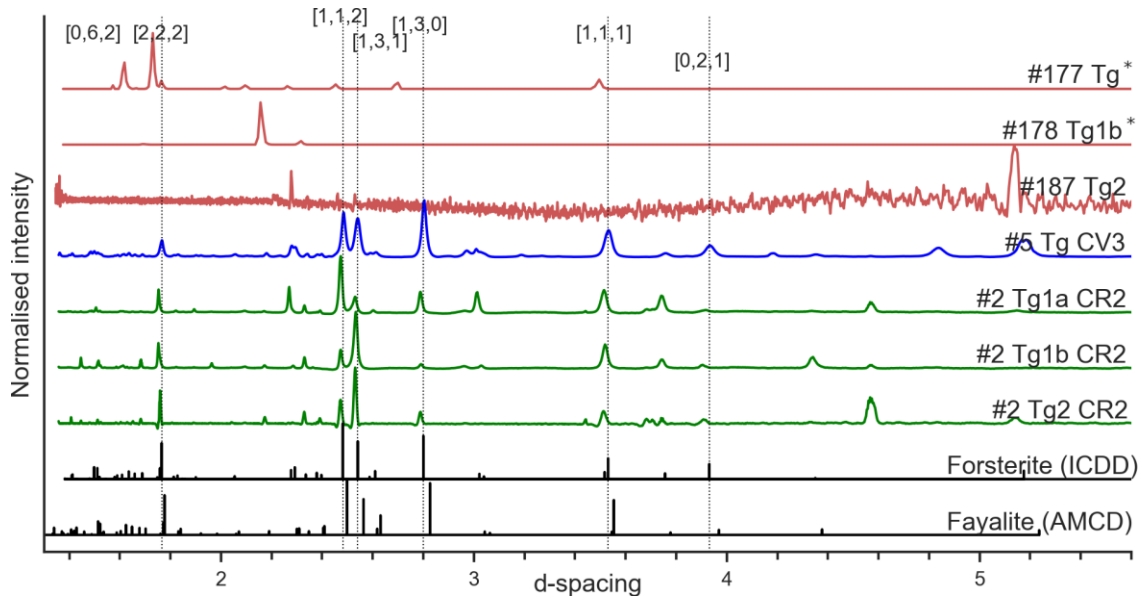


Fig. 4.20. Normalised SR-XRD of #2 CR2 (green) and #5 CV3 (blue) terminal grains with forsterite from the ICDD (2014), fayalite from the American Mineralogical Crystal Structure Database (Downs & Hall-Wallace, 2003) (black) and comparison to terminal grains in *Stardust* tracks #177*, #178*, #187 (red). Vertical dotted lines show the six most intense hkl planes for forsterite. The CV3 and CR2 terminal grains show d -spacing peak intensities that closely match to forsterite (Table 4.3). * (Hicks, 2015)

An XRF map across Tg3 shows abundant Fe, high counts for Ni (1646-78334), with small amounts of Cr, Ti, Mn and Ca (Fig. 4.21).

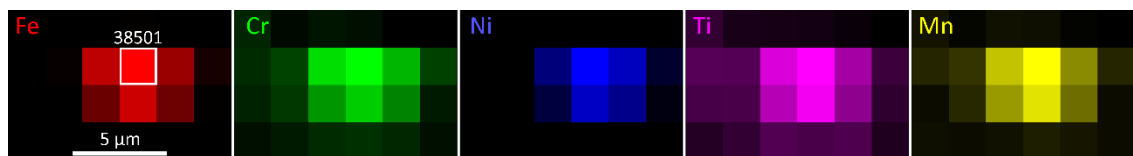


Fig. 4.21. XRF map of the ~ 5 μm third terminal grain (Tg3) in #187 showed the presence of Fe, Cr, Ni, Ti and Mn. The location for the XAS measurement is shown by the white box and data number (Fig. 4.22). The brightest and darkest points show the maximum and minimum counts respectively for each element. XRF map data number: 38500. Counts: Fe 2814-397259, Cr 821-2398, Ni 1646-78334, Ti 408-1332, Mn 573-2630, Ca 1707-3230.

The Fe-K XANES measurement of #187 Tg3 shows a similar shape to those for the iron sulphides, pyrrhotite and troilite (Fig. 4.22). The pre-edge centroid energy of 7111.8 eV and edge energy of 7117.0 eV are similar to those for pyrrhotite, which has a pre-edge centroid energy of 7112.0 eV and edge energy of 7116.7 eV and troilite (centroid 7111.8 eV, edge 7116.0 eV) (Table 4.2) though the edge has a slight double peak structure more similar to the pyroxenes.

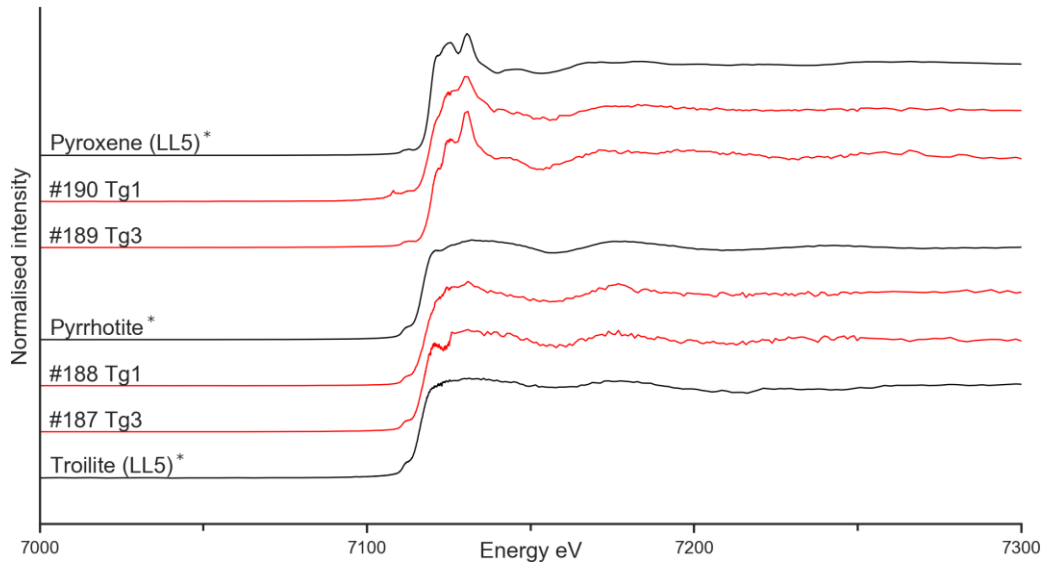


Fig. 4.22. Fe-K XANES of *Stardust* terminal grains #187 Tg3, #188 Tg1, #189 Tg3, #190 Tg1 (red) compared with pyroxene, pyrrhotite and troilite reference materials (black).

The XRD *d*-spacings for #187 Tg3 show a lot of noise in the data as the only two definite peaks were very small, and thus no further compositional conclusions can be drawn (Fig. 4.23).

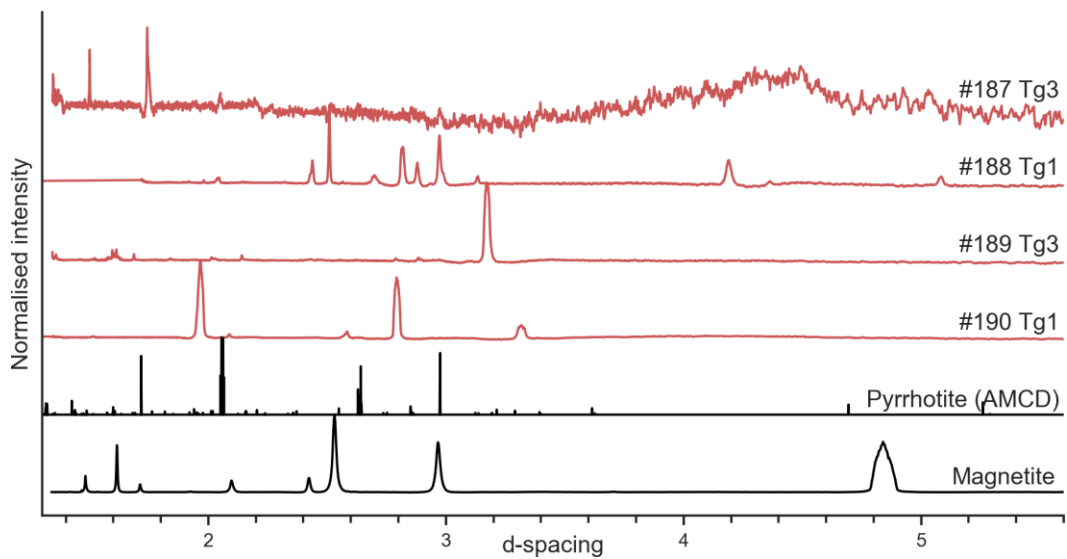


Fig. 4.23. XRD *d*-spacing measurements for *Stardust* terminal grains #187 Tg3, #188 Tg1, #189 Tg3, #190 Tg1 (red) and reference materials (black) pyrrhotite from the American Mineralogical Crystal Structure Database (Downs & Hall-Wallace, 2003) and a magnetite standard.

4.3.2.2 C2098,4,188,0,0 (#188)

This type B track #188 contains one terminal grain, Tg (Fig. 4.24). XRF maps across the grain shows it to have abundant Fe, high counts (over 9000) for Cr, Ni and Mn, with small amounts of Ti and Ca (Fig. 4.25).

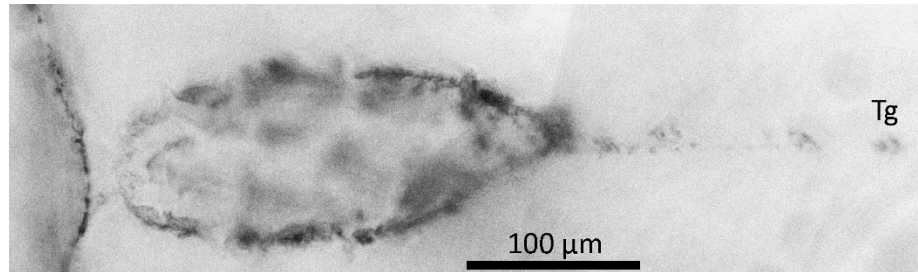


Fig. 4.24. Track #188 is type B and is 460 μm long, with one stylus and one terminal grain (Tg).

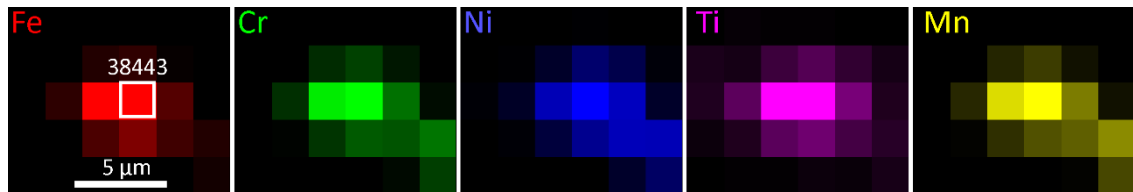


Fig. 4.25. XRF map of the ~5 μm terminal grain (Tg) in #188 showed the presence of Fe, Cr, Ni, Ti and Mn. The brightest and darkest points show the maximum and minimum counts respectively for each element. The location for the XAS measurement is shown by the white box and data number (Fig. 4.22). XRF map data number: 38442. Counts: Fe 2003-414883, Cr 637-8307, Ni 1188-8444, Ti 347-1758, Mn 411-14001, Ca 1398-3568.

The Fe-K XANES measurement of #188 Tg shows a similar shape to those for the iron sulphides, pyrrhotite and troilite (Fig. 4.22). The Tg pre-edge centroid energy of 7111.8 eV and edge energy of 7117.5 eV are similar to those for pyrrhotite, which has a pre-edge centroid energy of 7112.0 eV and edge energy of 7116.7 eV and troilite (centroid 7111.8 eV, edge 7116.0 eV) (Table 4.2).

The XRD *d*-spacings for #188 Tg are shown in Fig. 4.23. Although two peaks match magnetite, there were insufficient peaks matching for a conclusive identification.

4.3.2.3 C2119,4,189,0,0 (#189)

This type B track #189 contains three terminal grains, Tg1, Tg2, Tg3 (Fig. 4.26).

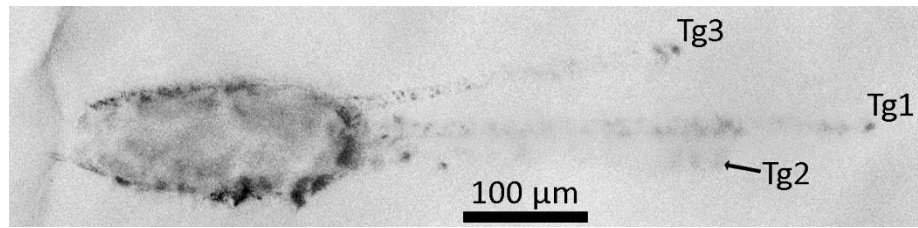


Fig. 4.26. Track #189 is type B and is 740 μm long, with three styli containing one terminal grain each (Tg1, Tg2, Tg3).

XRF maps across Tg1 showed abundant Fe and Ca, high counts (377-9503) for Mn, with small amounts of Cr, Ni, Ti and Ca (Fig. 4.27).

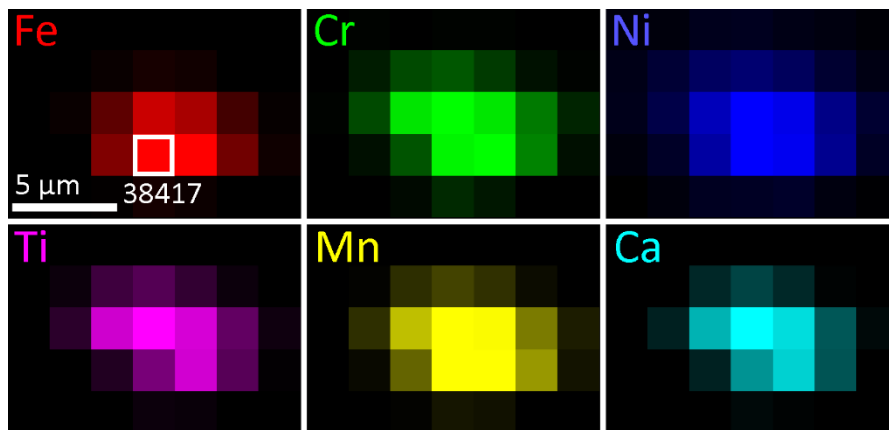


Fig. 4.27. XRF map of the ~7 μm first terminal grain (Tg1) in #189 showed the presence of Fe, Cr, Ni, Ti, Mn and Ca. The brightest and darkest points show the maximum and minimum counts respectively for each element. The location for the XAS measurement is shown by the white box and data number (Fig. 4.16). XRF map data number: 38406. Counts: Fe 1857-29784, Cr 576-3957, Ni 1063-3787, Ti 328-4902, Mn 377-9503, Ca 1145-16033.

The Fe-K XANES measurement of #189 Tg1 is a close match with the dilute magnetite powder (Fig. 4.16), with its pre-edge centroid energy of 7113.1 eV and edge energy of 7121.1 eV compared with the dilute magnetite powder having a pre-edge centroid of 7113.2 eV and edge of 7120.8 eV (Table 4.2).

The XRD *d*-spacings for #189 Tg1 are not a good match with the magnetite powder standard (Fig. 4.17) (Table 4.3). Although the XANES data (Fig. 4.16) indicated that #189 Tg1 could be magnetite, insufficient *d*-spacing peaks matched so the unit cell dimension was not calculated for this sample.

The second terminal grain, #189 Tg2, could not be located with XRF so was not measured with XANES or XRD.

An XRF map across Tg3 showed it to have abundant Fe, high counts (428-10913) for Mn, with lesser amounts of Cr, Ni, Ti and Ca (Fig. 4.28).

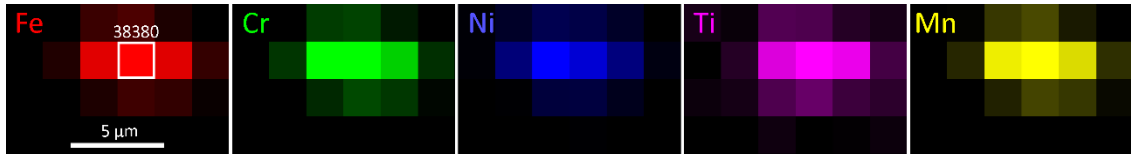


Fig. 4.28. XRF map of the $\sim 6 \mu\text{m}$ third terminal grain (Tg3) in #189 showed the presence of Fe, Cr, Ni, Ti, and Mn. The brightest and darkest points show the maximum and minimum counts respectively for each element. The location for the XAS measurement is shown by the white box and data number (Fig. 4.22). XRF map data number: 38379. Counts: Fe 2060-186626, Cr 645-6255, Ni 1129-3708, Ti 346-787, Mn 428-10913, Ca 1189-2025.

The Fe-K XANES measurement of #189 Tg3 showing the double peak, is like that shown for the LL5 pyroxene reference material (Fig. 4.22). The pre-edge centroid energy of 7112.3 eV and edge energy of 7119.5 eV are comparable to that measured for the LL5 pyroxene pre-edge centroid energy of 7112.1 eV and edge energy of 7118.9 eV (Table 4.2). The XRD d -spacings for #189 Tg3 are shown in Fig. 4.23. There are insufficient peaks to identify any minerals present.

4.3.2.4 C2119,5,190,0,0 (#190)

This type B track #190 contains one terminal grain, Tg (Fig. 4.29). XRF maps across the grain shows it to have abundant Fe, high counts for Cr, with small amounts of Ni, Ti, Mn and Ca (Fig. 4.30).

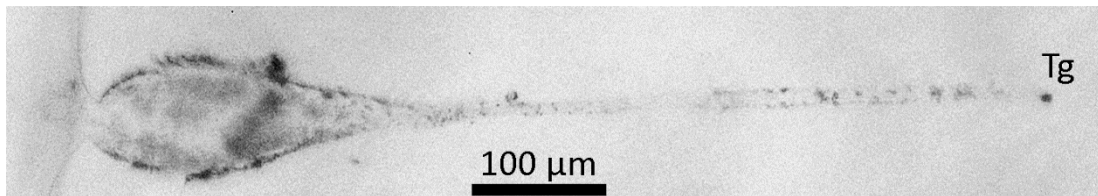


Fig. 4.29. Track #190 is Type B and is $810 \mu\text{m}$ long with one stylus and one terminal grain (Tg).

The Fe-K XANES measurement of #190 Tg showing the double peak, is similar to that shown for the LL5 pyroxene reference material (Fig. 4.22). The pre-edge centroid for the Tg contained glitches so it was not possible to calculate the energy position. The edge energy for #190 Tg of 7118.7 eV is comparable to that measured for the LL5 pyroxene of 7118.9 eV (Table 4.2).

The XRD d -spacings for #190 Tg are shown in Fig. 4.23. There are insufficient peaks to identify any minerals present.

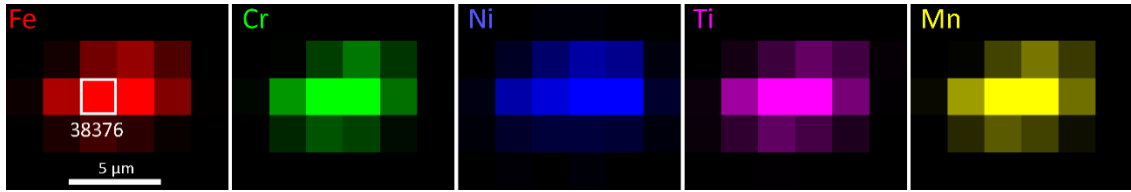


Fig. 4.30. XRF map of the $\sim 7 \mu\text{m}$ terminal grain (Tg) in #190 showed the presence of Fe, Cr, Ni, Ti and Mn. The brightest and darkest points show the maximum and minimum counts respectively for each element. The location for the XAS measurement is shown by the white box and data number (Fig. 4.22). XRF map data number: 38375. Counts: Fe 1968-51664, Cr 622-16754, Ni 1146-3335, Ti 338-1824, Mn 393-6595, Ca 1212-3466.

4.3.3 Characterisation of carbonaceous chondrite terminal grains

Five light gas gun shots of carbonaceous chondrite powders into aerogel were carried out at the University of Kent. One example type A ‘carrot’ track 22 mm long (Fig. 4.31) shows similarities with the type A *Stardust* tracks, albeit at a much larger scale, as most *Stardust* type A tracks are generally under $200 \mu\text{m}$ long, although the longest *Stardust* track measured 21.9 mm (Hörz et al., 2006).



Fig. 4.31. Example of a 22 mm impact track in aerogel made by CR2 carbonaceous chondrite (NWA 10256) powder fired at 6.28 km s^{-1} . A terminal grain is visible at the end of the track. This track has not yet been made into a keystone.

The analogue tracks are longer than *Stardust* tracks and contain bigger terminal grains, suggesting the starting powder had a larger particle size and/or the particles were more cohesive than the *Stardust* comet grains. *Stardust* tracks have smaller terminal grains and more powdery material along the track walls, particularly for type B tracks, thought to be the result of aggregate particles breaking up during capture. The carbonaceous chondrite tracks were longer than could be made into a keystone, so the ends of the tracks containing the terminal grains were made into three keystones (Fig. 4.32). The

tracks cannot be classified as type A or B as I have not seen the full track and whether there was a bulbous region or not.

The Fe-K XANES measurements of the 20 μm Tg in track #1 (Fig. 4.32c) and the 36 μm Tg1 in track #4 (Fig. 4.32f) are a close match with the dilute magnetite powder (Fig. 4.16), with similar pre-edge centroid and edge energy values (Table 4.2). The XRF maps for these grains (Fig. 4.33a,d) show high Fe counts and Ni counts, with also moderately high counts for Mn in #4.

The XRD d -spacings for track #1, Tg (Fig. 4.32c) and #4, Tg1 (Fig. 4.32f) are a close match with the magnetite powder standard (Fig. 4.17) (Table 4.3). Given the indicated match with magnetite, the hkl indices matching the d -spacing peaks observed were used to calculate the unit cell dimension a (\AA), assuming that the unit cell was cubic (Table 4.3, section 4.3.4).

An attempt was made to measure the second terminal grain (Tg2) in track #4 but the data was too noisy for comparison to reference materials.

The Fe-K XANES measurements of the broken two-piece grain Tg1, $\sim 5+5$ μm and ~ 6 μm Tg2 in track #2 (Fig. 4.32d), and the ~ 12 μm Tg2 in track #5 (Fig. 4.32g) and an olivine in the CR2 thin section, are a close match with olivine standards (Fig. 4.19). These also have similar pre-edge centroid and edge energy values to the olivine standards (Table 4.2). The XRF maps for these grains (Fig. 4.33b,c,e) show high Fe counts in all, with high counts of Ni and Mn in Tg1 #2 and high counts of Cr in Tg2 #5.

The XRD d -spacings for track #2, Tg1, Tg2 (Fig. 4.32d), #5, Tg2 (Fig. 4.32g) are a close match with the forsterite standard (Fig. 4.17) (Table 4.3). Given the indicated match with olivine, the hkl indices matching the d -spacing peaks observed were used to calculate the unit cell dimension a (\AA) (Table 4.3).

The data taken on the grains in tracks 3 and 6 was inconclusive so their mineralogy could not be ascertained.

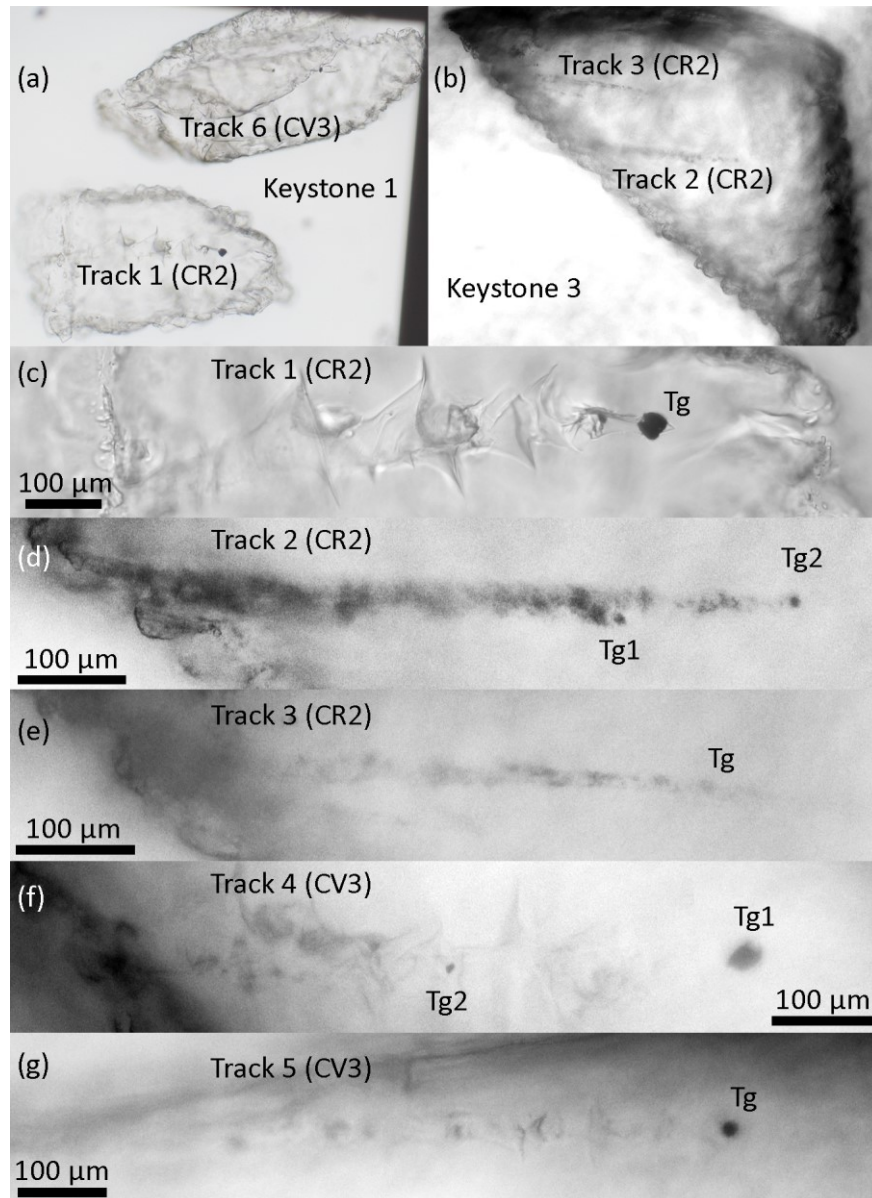


Fig. 4.32. Microscope images for carbonaceous chondrite impact tracks in aerogel from three keystones. (a) Keystone 1 containing impact track #1 (CR2) and impact track #6 (CV3) in aerogel. (b) Keystone 3 containing CR2 impact tracks #2 and #3. (c) Impact track #1 (CR2) shown in (a) with $\sim 30 \mu\text{m}$ magnetite terminal grain Tg1 (Fig. 4.16, Fig. 4.17). The track stylus, minus the bulbous region, measures $\sim 650 \mu\text{m}$. (d) Impact track #2 (CR2) shown in (b) measuring $\sim 620 \mu\text{m}$ (full original track $\sim 1500 \mu\text{m}$), containing olivine grains Tg1 $\sim 2 \times 5 \mu\text{m}$ and Tg2 $\sim 6 \mu\text{m}$ (Fig. 4.19, Fig. 4.20). (e) Impact track #3 (CR2) shown in (b) $\sim 495 \mu\text{m}$ containing one Tg. (f) Composite image of impact track #4 (CV3) in keystone 2 measuring $\sim 610 \mu\text{m}$ with two terminal grains. Measurements of Tg1 $\sim 36 \mu\text{m}$ showed magnetite (Fig. 4.16, Fig. 4.17). (g) Impact track #5 (CV3) in keystone 2 measuring $\sim 710 \mu\text{m}$ with Tg $\sim 12 \mu\text{m}$ olivine (Fig. 4.19, Fig. 4.20).

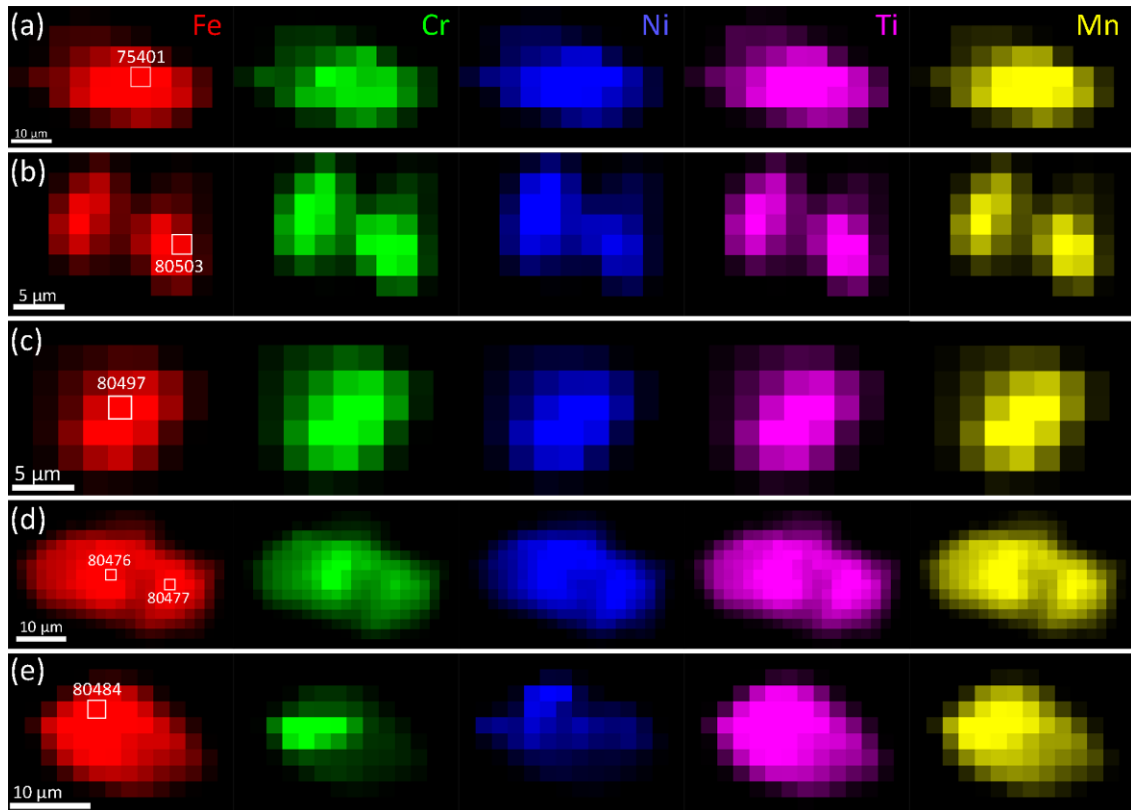


Fig. 4.33. XRF maps of the carbonaceous chondrite terminal grains, where the darkest and brightest points show the minimum and maximum counts respectively for each element. The white boxes show where the XAS measurements were taken. Table 4.1 shows the grain sizes, XRF file number, minimum and maximum counts for each element, and a reference to where the XAS data is plotted.

Table 4.1. Data giving the range of counts for each XRF map shown in Fig. 4.33.

	Grain	Size	File							XAS
			no.	Fe	Cr	Ni	Ti	Mn	Ca	
(a)	#1 Tg1	~30 μm	75400	24-214410	0-1983	6-17054	0-719	0-2890	0-993	Fig. 4.16
(b)	#2 Tg1	~2 \times 5 μm	80504	864-619719	170-5680	607-26597	106-3369	159-10112	106-1391	Fig. 4.19
(c)	#2 Tg2	~6 μm	80496	284-430495	61-4229	189-18506	50-2452	69-6317	65-1123	Fig. 4.19
(d)	#4 Tg1	~36 μm	80475	373-760069	19-3942	143-15833	19-3942	47-13863	21-1995	Fig. 4.16
(e)	#5 Tg1	~12 μm	80483	217-508792	36-16669	123-13224	18-2586	35-9637	19-2752	Fig. 4.19

4.3.4 Unit cell fit for magnetite and olivine terminal grains

As magnetite is cubic, all three unit cell dimensions are the same. This dimension was calculated as 8.359(3) Å for #187 Tg1, 8.3624(6) Å for CV3 #4 Tg1a, 8.3660(7) Å for CV3 #4 Tg1b, and 8.3521(8) Å for CR2 #1 Tg and it was 8.395(3) Å for the magnetite standard (Table 4.3). The *Stardust* and carbonaceous chondrite grains show consistency at ~8.35-8.37 Å, whereas the standard is a little higher at ~8.40 Å.

The slightly smaller unit cell dimension for the more oxidised cubic maghemite, Fe₂O₃, of 8.3364 Å and 8.3474 Å (Table 4.3) show that the grains studied here may have a mixture of magnetite and maghemite. This implies the grains are more oxidised than the magnetite standard, consistent with the slightly higher pre-edge centroid and edge energies (Table 4.2).

The orthorhombic unit cell dimensions for the grains identified as olivine were calculated from the XRD *d*-spacing intensities (Table 4.3) and are compared with olivine from the ICDD (2014) in Fig. 4.34. Previous data collected (Hicks, 2015) was used to calculate the unit cell for #177, though #178 Tg1b had insufficient peaks for a calculation to be possible. The unit cell dimensions for olivine increase as the Mg# decreases, by Vegard's rule, which states the lattice parameters vary linearly with the concentrations of the constituent elements, at constant temperature.

The Mg# is determined by calculating applying the methods of Shinno (1980) to the calculated unit cell dimensions, which are used to give the idealised *d*-spacing value for the [130] plane. The forsterite composition is calculated via:

$$\text{Fo (mol\%)} = 4401.1 - 1555.5 \times d\text{-spacing for [130]} \quad (\text{Shinno, 1980})$$

CR2 #2 Tg1 is Fo_{60±2} and Tg2 is Fo_{62±1} and the CV3 #5 Tg is Fo_{43±2}. For *Stardust* grains, the approximate olivine composition for #177 Tg1 is Fo_{64±10}, and #187 Tg2 is Fo_{69±13}, as the intensities were very low for the *d*-spacings measured for the much smaller grains, giving larger experimental error. STEM-EDX shows C2009,20,77,1,6 (Track #77) to have Fo₇₁₋₇₄ (Chapter 5).

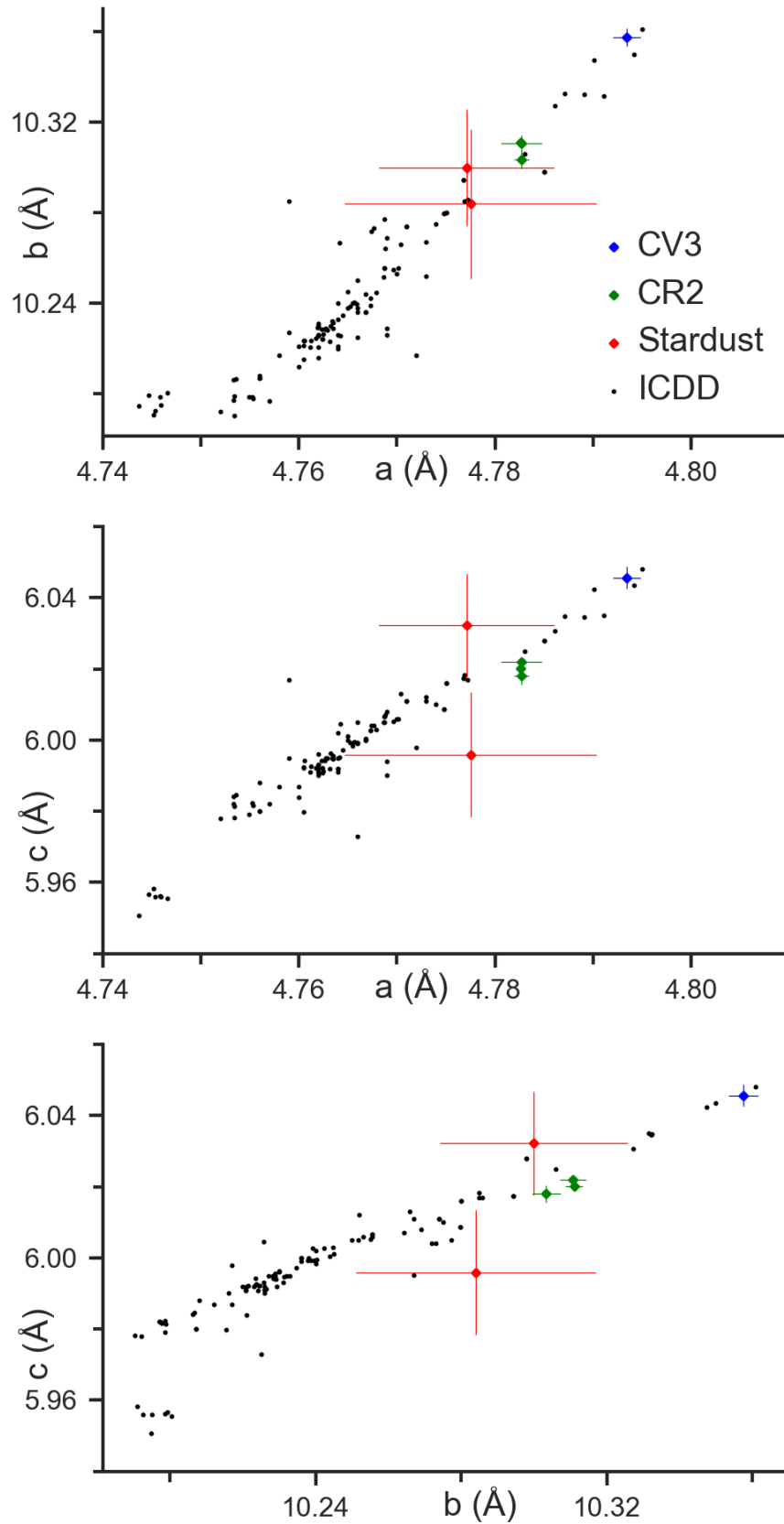


Fig. 4.34. Olivine unit cell dimensions a , b , c calculated from XRD data for the CV3, CR2 and *Stardust* grains identified as olivine, plotted against representative forsterite (Fo_{51-100}) from the ICDD (2014).

4.3.5 Summary of results

Table 4.2. Fe-K XAS analysis of *Stardust* cometary grains, CR2 and CV3 analogue samples and reference materials.

Sample, Track #No.	Grain	Type/size	XANES 1s → 3d Centroid (±0.05 eV)	XANES Fe-K Absorption Edge (±0.05 eV)	XRF detected composition	Concluding Mineral Type
<i>Stardust</i> Tracks						
#177 [^]	Tg	~4 μm	7112.5*	7119.6*	Fe-rich with Cr	Olivine
#178 [^]	Tg1a	10 μm	7113.1*	7121.5*	Fe-rich	Magnetite
	Tg1b	6 μm	7112.3*	7120.2*	Fe-rich	Olivine
#187	Tg2	~6 μm	-	-	Fe-rich	Magnetite
	Tg1	5 μm	7113.5	7121.0	Fe-rich	Magnetite
	Tg2	5 μm	7112.3	7119.2	Fe-rich	Olivine
#188	Tg3	~5 μm	7111.8	7117.0	Fe-rich with Ni	Fe-Ni-sulfide [^]
	Tg	~5 μm	7111.8	7117.5	Fe-rich	Fe-sulfide [^]
#189	Tg1	~7 μm	7113.1	7121.1	Fe-Ca-rich with Mn	Magnetite [^]
	Tg3	~6 μm	7112.3	7119.5	Fe-rich	Pyroxene
#190	Tg=	~7 μm	-	7118.7	Fe-rich with Cr	Pyroxene [^]
Analogue sample NWA 10256						
CR2 #1	Tg	~30 μm	7113.1	7121.7	Fe-rich with Ni	Magnetite
CR2		Section	7113.0	7119.4	Fe-rich	Magnetite
CR2 #2	Tg1	~2 x 5 μm	7112.0	7119.0	Fe-rich with Ni, Mn	Olivine
CR2 #2	Tg2	6 μm	7112.1	7119.0	Fe-rich with Ni, Mn	Olivine
CR2		Section	7112.3	7117.2	Fe-rich	Olivine
Analogue sample NWA 4502						
CV3 #4	Tg1	~36 μm	7113.0	7121.7	Fe-rich with Ni, Mn	Magnetite
CV3 #4	Tg1b	~36 μm	7113.1	7121.5	Fe-rich with Ni, Mn	Magnetite
CV3 #5	Tg	12 μm	7112.0	7118.8	Fe-rich, Cr, Ni	Olivine
Reference materials used						
Magnetite		Dilute powder	7113.2*	7120.8*		Magnetite
Magnetite		Self-absorbing	7113.1	7119.4		Magnetite
Hematite		Powder	7114.1	7122.6		Hematite
Fe-metal		Foil	7113.1*	7121.9*		Fe-metal
San Carlos		Section	7112.1	7118.8		Olivine
Barwell (L5)		Section	7111.7*	7118.7*		Olivine
Tuxtuac (LL5)		Section	7111.9*	7118.8*		Olivine
Tuxtuac (LL5)		Section	7112.1*	7118.9*		Pyroxene
Pyrrhotite		Powder	7112.0*	7116.7*		Pyrrhotite
Tuxtuac (LL5)		Section	7111.8*	7116.0*		Troilite

[^] This identification is uncertain due to insufficient XRD peaks and a lack of good comparisons with reference materials.

* Data taken from Hicks et al. (2017), collected prior to this thesis.

Table 4.3. XRD measured d-spacings (Å) for indices hkl , as plotted in Fig. 4.17 and Fig. 4.20 with calculated unit cell dimensions a, b, c (Å). Measurements from the *Stardust* tracks, CR2 and CV3 analogue samples and reference standards.

Magnetite	a=b=c	File	311	440	220	511	400	422	222	111	210	531	441	215	521
#178 Tg1a*	8.370(6)	Hicks et al	2.526	1.479	2.959	1.610	2.093	1.710	2.413						
#178 Tg2*	8.357(10)	Hicks et al	2.522	1.475		1.607	2.090		2.416						
#187 Tg1	8.359(3)		38491	2.518	1.480	2.956	1.608		1.704	2.412					1.525
#189 Tg1															
CV3 #4 Tg1a	8.3624(6)		80480	2.522	1.478	2.957	1.610	2.091	1.707					1.413	
CV3 #4 Tg1b	8.3660(7)		80481	2.522	1.479	2.958	1.610	2.091	1.708	2.415	4.823			1.414	
CR2 #1 Tg	8.3521(8)		75396-T4	2.517	1.476	2.950	1.608	2.088	1.705						
Magnetite	8.395(3)	Jul16 std	75209	2.528	1.483	2.964	1.614	2.096	1.712	2.421	4.841	-		1.418	
Magnetite ^a	8.3882	which sess	Same as	2.528	1.483	2.964		2.096	1.712	2.421	4.841	-		1.418	-
Magnetite ^b	8.3961			2.532	1.484	2.969	1.616	2.099	1.714	2.424	4.848	-	-	-	-
Maghemite ^c	8.3364			2.514	1.474	2.947	1.604	2.084	1.702	2.407	4.813	3.728	-	-	
Maghemite ^d	8.3474														

Olivine	a	b	c	Fo%	112	222	130	131	021	062	004	240	111	122	211	133	022	042
#177*	4.777(9)	10.30(3)	6.03(1)	64(10)		1.765												
#187 Tg2	4.78(1)	10.28(3)	6.00(2)	69(13)	2.460		2.766	2.530						2.279			2.585	1.955
CV3 #5 Tg	4.793(1)	10.358(4)	6.046(3)	43(2)	2.485	1.766	2.803	2.540	3.934	1.499			3.532		2.180	1.636		
CR2 #2 Tg1a	4.782(2)	10.311(4)	6.022(1)	60(2)	2.473		2.789	2.529			1.506	1.753	3.514					
CR2 #2 Tg1b	4.783(1)	10.311(2)	6.020(1)	60(1)	2.474		2.791	2.533				1.753	3.519					
CR2 #2 Tg2	4.783(1)	10.303(4)	6.018(2)	62(1)	2.473	1.760	2.789	2.531					3.514					
San Carlos	4.739(7)	10.225(3)	5.994(4)															
Fayalite ^c	4.8180	10.4710	6.0860		2.499	1.777	2.827	2.564	3.969	1.514	1.5215	1.7726	3.5534	2.3091	2.1904	1.6481	2.6309	
Forsterite ^c	4.7600	10.2210	5.9840		2.461	1.751	2.775	2.518	3.893	1.483	1.497	1.744	3.503	2.272	2.163	1.621	2.585	

Error estimates are given in parentheses and quoted in units of the least significant digit. Unit cell dimension error values calculated from standard deviation. hkl planes for olivine and magnetite are ordered by intensity per X and d respectively.

*Data from Hicks (2015). ^aReference material. ^bWechsler et al. (1984). ^cSolano et al. (2014). ^dCornell and Schwertmann (2003).

^{bce} Referenced from American Mineralogical Crystal Structure Database (Downs & Hall-Wallace, 2003).

4.4 Discussion

My results build directly on previous work (Bridges et al., 2010; Changela et al., 2012; Hicks, 2015) and contribute to Hicks et al. (2017) and Wickham-Eade et al. (2017), and provide further evidence that carbonaceous chondrites are close analogues to the Wild 2 terminal grains.

4.4.1 Classifications of CR2 and CV3 carbonaceous chondrites

The CV3 meteorite, NWA 4502, is classified as oxidised with shock level S2 and weathering degree W1 (Ruzicka et al., 2015). My results for proportions of chondrules (48%), CAIs and AOAs (14%) and matrix (38%) agree exactly with the classification results, and are similar to their compositional ranges for matrix olivine Fo₄₆₋₅₂ and chondrule olivine Fo₆₁₋₉₈ (Ruzicka et al., 2015).

The CR2 meteorite, NWA 10256, is classified with an apparent mean chondrule size of 625±325 µm, with the largest up to 3 mm in diameter, and contains a few very small CAIs (Bouvier et al., 2017). A similar proportion of matrix (40%) and olivine compositions were found (Bouvier et al., 2017).

4.4.2 Mineralogy of *Stardust* and carbonaceous chondrite terminal grains

The compositions found in *Stardust* grains are consistent with previous reports. *Stardust* grains #187 Tg3 is provisionally identified as Fe-Ni sulphide and #188 Tg1 as iron sulphide from XAS (Fig. 4.22), although insufficient XRD *d*-spacing intensities were observed to be able to confirm these.

Stardust grains #189 Tg3 and #190 Tg are potentially pyroxene from XAS similarities (Fig. 4.22), although insufficient XRD *d*-spacing intensities were observed to be able to confirm these.

4.4.2.1 Comparing olivine in comet Wild 2 with carbonaceous chondrites

Stardust grain #187 Tg2 has been revealed as olivine and calculated to be approximately Fo_{69±13}, where the forsterite Fo mol% is Mg/(Mg+Fe). Hicks (2015) identifies #177 Tg1 to be olivine from XAS; I have used the XRD *d*-spacing data from Hicks (2015) in order to calculate the unit cell and show the olivine to be Fo_{64±10}. Using the size of the unit cell to calculate the Fo mol% has uncertainty from both the

synchrotron measurement, and the software programme used to calculate the best fit dimensions for the unit cell (section 2.3.4). The two olivine grains are more iron rich than the average olivine compositions measured in *Stardust* grains previously (Fig. 4.13). The *Stardust* terminal grain from Track #77 is shown by STEM-EDX to have olivine Fo₇₁₋₇₄ (Chapter 5).

Olivine was identified in two carbonaceous chondrite tracks, CR2 #2 Tg1 is Fo_{60±2} and Tg2 is Fo_{62±1} and the CV3 #5 Tg is Fo_{43±2}. Frank et al. (2014) report olivine ranges from carbonaceous chondrite matrices to be CR2 Fo₅₄₋₉₉ and CV3 Fo₃₋₉₉. Chondrules typically have a higher Mg content, so the olivine in these analogue shots is more likely to be from the matrices of the CR2 and CV3 meteorites.

4.4.2.2 Magnetite in Comet Wild 2 and carbonaceous chondrites

Stardust grains #187 Tg1 and #189 Tg1 have been identified as magnetite. These add to magnetite revealed in track #178 (Hicks, 2015) and a grain found in the mid-track #134 (Changela et al., 2012), as well as fragments in close to the track entrance in #41 and terminal grains from #121 (Bridges et al., 2010). Cr-rich magnetite was identified in a 30 µm × 20 µm particle in track #183 (De Gregorio et al., 2017). Further magnetite was identified in sub grains in track walls (Stodolna et al., 2012).

Magnetite was identified in two carbonaceous chondrite tracks, CR2 #1 Tg1 and #CV3 #4 Tg1. This is surprising considering magnetite only comprises ~1 % of the CR2 and <1% of the CV3. Identifying magnetite in a CR2 track (Hicks et al., 2017) and now also in a CV3 track reinforces the suggestion that it is preferentially preserved during capture.

4.4.3 Formation of magnetite

Ti-bearing magnetite on Earth is usually a late forming high temperature igneous mineral. This is also found in achondrite meteorites like the angrites and martians (McSween Jr. & Treiman, 1998; Mittlefehldt et al., 1998) and some equilibrated chondrites. Magnetite with high Ti-contents are a diagnostic feature of CK chondrites (Greenwood et al., 2010), which have undergone higher degrees of metamorphism than some of the other carbonaceous chondrites.

Terrestrial magnetites that do not contain Ti tend to form via low temperature oxidation and alteration reactions of Fe metal or primary ferromagnesian silicate minerals

(Haggerty & Baker, 1967; Sanderson, 1974). The same mechanism forms Ti-free magnetite in carbonaceous chondrites, mainly as a result of aqueous alteration on the parent body asteroid (Brearley & Jones, 1998; Hutchison, 2004; Weisberg et al., 2006) though some magnetites found in chondrites form due to weathering on Earth (King & King, 1981; Gooding, 1986; Bland et al., 2006).

The most likely mechanism to produce the required liquid is the melting of icy particles, which accreted to the carbonaceous chondrite parent bodies during formation. The decay of radiogenic ^{26}Al would have produced sufficient heat within the first few million years of the asteroid's history (Ghosh & McSween, 1998; Merk et al., 2002).

Studies of aqueously altered CI and CM meteorites suggest mechanisms for the aqueous alteration of anhydrous coherent lithified rock in a closed-system (Palguta et al., 2010). Numerical studies suggest large scale water transport over 10s of kms on parent asteroids, but this would cause fractionation of soluble elements which is not observed (Bland et al., 2009). Chondrite precursors are thought to have low permeability due to the extremely fine grain size which would restrict liquid water flow (Bland et al., 2009). The range in ^{18}O requires varying temperatures and water-rock ratio over small scales, which is hard to achieve in a closed system. Bland and Travis (2017) suggest that at this time, the accreted body would have high-porosity and no process would have lithified the material, so large-scale mud convection may have acted to reduce variation in temperature and produce size-sorted chondrules. Full mixing of the system would remove any solubility-related fractionation and allow the original chemistry to be preserved, explaining why the most aqueously altered are the most chemically pristine (Bland & Travis, 2017).

Ti-free magnetites are far more abundant in carbonaceous chondrites than Ti-magnetites, and they are the second most abundant phase in CI chondrites (Weisberg et al., 2006). Magnetite abundances in carbonaceous chondrites vary from 120 mg/g in CI to ~80 mg/g in CV, to less than 8 mg/g in CM (0.5 vol%, McSween, 1979) and CR (Kallemeyn et al., 1994). Kallemeyn et al. (1994) suggest hydrothermal alteration of metal-rich precursors is responsible for the formation of magnetite in CI and CR chondrites, and the lower abundance of magnetite in CM relative to CI is due to the CM parent body being metal poor. The similar abundance of magnetite in the CM and CR parent bodies is explained by the CR parent body having a higher Fe-Ni content but a

much lower degree of hydrothermal alteration.

Oxygen isotopes for magnetite and fayalite in CO3 and CV3 meteorites were demonstrated to be in disequilibrium with olivine in the chondrules (Krot et al., 1998; Doyle et al., 2015). This shows the magnetite and fayalite did not originate in the same high-temperature environment as the chondrules. Together with chronology data showing fayalite ages younger than CV and CO parent asteroid accretion ages, a later low-temperature aqueous alteration formation mechanism is supported (Doyle et al., 2015).

Magnetite can form by aqueous alteration of ferromagnesian silicates, eg the alteration of fayalite:



The abundance of magnetite is expected to correlate with the abundance of other alteration products, such as phyllosilicates (serpentine, smectite). The relative degree of hydrous alteration is reflected in the chondrite classification scheme from unaltered type 3.0 (< 0.05 phyllosilicate) to type 1.0 (phyllosilicate > 0.95) (Howard et al., 2015), which corresponds well with previous classification schemes (Weisberg et al., 2006).

This was found to be the case in examining CM-chondrites ranging from mild alteration (type 2) to almost completely altered (type 1), with Mg-serpentine and magnetite abundances found to increase with increased alteration, from ~1% to ~3% vol% for magnetite (King et al., 2017). An alteration model is suggested whereby the Fe,Ni-metal is oxidised first to magnetite, before Mg-rich silicates were altered to phyllosilicates (King et al., 2017). This model opens up the possibility of a limited amount of alteration, whereby some magnetite is formed but insufficient alteration takes place to produce phyllosilicates. When examining terrestrial weathering reactions, Bland et al. (2006) found that magnetite formed as a result of direct dissolution of FeNi metal, whereas other primary minerals (pyroxene, olivine) were more likely to form ferrihydrite before further dissolution.

In oxidised CV3 meteorites, similar to NWA 4502 used for this study, magnetite abundances were 1.6 vol% to 6.1 vol%, whereas in reduced CV3 meteorites they were lower, 1.4 vol% to 1.8 vol%, with the anomalous Allende, an oxidised CV3, having 0.3 vol% (Bland et al., 2004; Howard et al., 2010). Reduced CV3 meteorites are not

thought to have undergone alteration, given the relative absence of phyllosilicates (Howard et al., 2010).

CK chondrites are highly oxidised with 1.2% to 8.1% (vol%) magnetite in two different populations, micron-sized grains, and rounded aggregates up to 1mm in size, with average 4 wt% Cr₂O₃, <1 wt% TiO₂ (Geiger & Bischoff, 1995). It is suggested that magnetite replaced sulphides (Geiger & Bischoff, 1995). Studies suggest that CK chondrites are metamorphosed CV chondrites and should be reclassified as one group, CK making up for the missing CV types 4 to 6 (Greenwood et al., 2010; Wasson et al., 2013). However, differences in magnetite compositions (higher Cr₂O₃, NiO and TiO₂) are difficult to reconcile with a single parent body history for both groups (Dunn et al., 2016).

The lack of phyllosilicates observed in Wild 2 could indicate that the Wild 2 material is anhydrous (Frank et al., 2014; Westphal et al., 2017), or by analogy with CM chondrites, perhaps comet Wild 2 was only oxidised enough to form magnetite, not phyllosilicates (King et al., 2017). However, it could instead be sampling bias, as phyllosilicates may be destroyed during collection (Wozniakiewicz et al., 2015). Experimental hypervelocity studies of CM2 and phyllosilicate powders fired into aerogel showed they were reduced to less than 20% of their original size and experienced significant melting and fracturing (Noguchi et al., 2007). While temperatures in the interior of the grains did not exceed 300 °C, the captured grains would need to be larger than 4 µm to retain their original mineralogy (Noguchi et al., 2007). Hypervelocity shots into foils of CV3 and CI meteorite powders showed less than 3% organic material survived (Wozniakiewicz et al., 2018).

Hypervelocity impact studies have demonstrated a correlation between the relative densities of the penetrator and target material, with penetration depth (Dehn, 1987; Christiansen & Friesen, 1997). A coherent mineral such as magnetite (density 5150 kg m⁻³) would thus be expected to penetrate further than a low-density mineral such as phyllosilicate. This offers an explanation for the preferential preservation of magnetite and absence of phyllosilicates observed in *Stardust* grains (Hicks et al., 2017).

Magnetite can form as a result of oxidation of metallic iron. It is proposed that magnetite in track #183 formed, in an environment with water/ice and carbon, via oxidation of iron, originally condensed as reduced EH3-chondrite-like metal (De

Gregorio et al., 2017). However, the combination of cohenite and Cr-rich magnetite found in #183 has not been observed in the enstatite chondrites.

Magnetite is found in CP-IDPs, though some of this forms due to heating during atmospheric entry (Germani et al., 1990). Wooden (2008) suggests that the grains forming Wild 2, including magnetite grains, migrated from various locations under different reducing-oxidising conditions in the solar nebula, rather than the magnetite forming by selective aqueous alteration in the comet. As parent-body processing should not have affected the oxidation state of anhydrous CP-IDPs (Zolensky & Thomas, 1995), a synchrotron study compared the Fe oxidation state of these with *Stardust* tracks. (Ogliore, 2010). This found a 2σ difference with CP-IDPs being more oxidised, unlikely to be caused by sampling bias or effects, as *Stardust* contains more Fe metal (Ogliore, 2010). Thus, anhydrous CP-IDPs do not originate from a comet of Wild 2 composition (Ogliore, 2010).

Direct condensation of magnetite from a nebula gas is ruled out, as it would only be stable at temperatures below 400 °C or lower. Fe is more likely to condense as metal grains or as Fe-bearing olivine, Fe-bearing carbides and other minerals at much higher temperatures (De Gregorio et al., 2017).

The VIRTIS (Visible, Infrared and Thermal Imaging Spectrometer) on the Rosetta mission, visiting Jupiter-family comet 67P/Churyumov-Gerasimenko, did not identify any hydrated minerals (Quirico et al., 2016). They conclude a lack of connection with the CI, CR and CM chondrites (Quirico et al., 2016).

Fe metal and ferromagnesian silicates are abundant in the *Stardust* samples, so by analogy with carbonaceous chondrites, it is most likely that magnetite formed via low temperature aqueous alteration reactions. However, carbonaceous chondrites containing magnetite formed by alteration usually have abundant phyllosilicates in the matrix, and the absence of phyllosilicates and lack of context for the Wild 2 samples prohibits proof. This study shows that higher density minerals like magnetite may have been preferentially preserved (Hicks et al., 2017), and other studies (Wozniakiewicz et al., 2015) show phyllosilicates may have been destroyed during the capture process. This would explain the absence of phyllosilicates.

4.4.4 Complementary Raman studies

58 Raman spectra measurements taken before shooting CR2 carbonaceous chondrite grains into aerogel, were identified as olivine (Wickham-Eade et al., 2017), and show a similar compositional range to that observed in *Stardust* grains (Fig. 4.13). These were compared with six Raman spectra identified as olivine, taken afterwards (Wickham-Eade et al., 2017). These suggest that there was a change in at least three of the olivine compositions of up to ten forsterite units to a lower Mg content, due to shock and heating effects (Wickham-Eade et al., 2017). However, due to the difficulties of getting a strong enough signal to measure in the aerogel after shooting, and the method for calculating forsterite content only offering accuracy to ± 10 Fo units (Kuebler et al., 2006), more data is needed to confirm this effect.

4.4.5 Formation in the early solar system

Any dynamical model to explain the formation and mixing of materials in the early Solar System needs to take into account the spatial and temporal constraints from the following overlapping themes of study:

1. Analysis of minerals in all planetary materials, to understand the constraints on the time and place of their formation, from radiometric and thermodynamic studies.
2. The constraints on planet formation positions given their size, composition and locations today, and how efficiently material was transported in the protoplanetary disc.
3. Linking the meteorite collection accurately with parent bodies and their locations today.

The refractory grains found in Comet Wild 2 formed at high temperature, similar to CAIs and chondrule fragments, require either that they were formed in situ, at distances of 30 AU+, or they were formed in the inner Solar System and transported outwards to comet forming regions (Brownlee et al., 2006). The similarities with carbonaceous chondrites, thought to form much closer to the Sun than comets, support the latter possibility of large scale transport.

Comet Wild 2 contains crystalline silicates and refractory particles that resemble chondrule fragments. Ciesla (2010) studied the dynamics of the paths that these refractory objects could have taken, to achieve the large scale transport in the

timescales available. It was found that objects formed in the first few $\times 10^5$ years would make up over 90% of those that survive throughout the nebula, as a larger number formed in this period, and the initial angular momentum transport assisting fast spreading of the protoplanetary disk helped preserve the earlier formed grains rather than the later formed grains.

Hughes and Armitage (2010) examined advection and turbulent diffusion in a protoplanetary disk, finding that this could transport particles up to 20 μm in size outwards. This would need to be quickly accreted by icy bodies to avoid fallback from the mean inward gas flow in the disk. A range of favourable models show original compact protoplanetary disks that undergo rapid expansion in the earliest phase of disk evolution, within 1-2 Ma, offer efficient outwards transport (Hughes & Armitage, 2010).

Spectral analysis of asteroids supports spatial differences for formation, as enstatite and ordinary chondrites have similarities with inner belt asteroids at ~ 1.9 AU while CCs have more in common with asteroids at 2.75 and 3.0 AU, with carbonaceous material becoming more abundant with heliocentric distance (Gaffey et al., 1993).

Warren (2011) suggests that the highest classification distinction for meteorites should be between carbonaceous (C), formed in the outer solar system and non-carbonaceous (NC), formed in the inner solar system, based on differences in their Ti and Cr isotopes. Warren (2011) comments that Jupiter is an obvious potential barrier between the two groupings. Mo isotopes were also observed to be anomalous in carbonaceous chondrites (Burkhardt et al., 2011; Budde et al., 2016) and additional work on Mo and W isotopes has found that the same two distinct groupings, C and NC, exist in iron meteorites (Kruijer et al., 2017). Furthermore, thermal modelling suggests the NC iron meteorite parent body cores formed earlier, likely within < 0.4 Ma after CAI formation, whereas the C iron meteorite parent bodies accreted later, ~ 0.9 Ma after CAI formation (Kruijer et al., 2017). As we have no samples of intermediate composition, the two reservoirs must have remained separate until after the chondrite parent bodies were fully formed at 3-4 Ma after CAI formation (Budde et al., 2016; Kruijer et al., 2017).

Rubin (2018) studied the C-iron meteorites and NC-iron meteorites, revealing longer cosmic-ray exposure (CRE) ages for the C-iron meteorites. The smaller number of C-irons is likely to be a result of both the longer residence in interplanetary space and

more fragmentation via collisions due to formation further from Earth than NC-irons, and also the C-iron precursors having smaller cores with less metal as they were more oxidised (Rubin, 2018).

Kruijer et al. (2017) suggested Jupiter's early formation < 1 Ma opened a gap, in the disk, preventing exchange between these two different genetic systems. This would also prevent fall back of particles transported further outwards in the disk, solving one of the issues highlighted by Hughes and Armitage (2010). Desch et al. (2018) notes that a similar pressure gap could have existed beyond Saturn ~ 15 AU, and possibly the CI chondrite parent formed there by 4 Ma, without CAIs or chondrules, as fragments of CAIs and chondrules took longer to be transported out to these distances.

The Grand Tack dynamical model, starting from a protoplanetary disk of about 1 AU radius, manages to reproduce characteristics of the terrestrial planets, including Mars' small mass, which was a problem for previous models (Walsh et al., 2011). This proposes that Jupiter migrated inward to 1.5 AU, similar to observed exoplanets, and then outwards due to a resonance with Saturn, noting that the formation of C-type asteroids occurs beyond Jupiter, near or beyond the snow line and nearer to comets than to S-type asteroids (Walsh et al., 2011). The CR chondrite parent body is one of the youngest at ~ 3.6 Ma after CAI formation, constraining the earliest time Jupiter could have migrated outwards (Budde, Kruijer, et al., 2018).

Desch et al. (2018) offer the most comprehensive model so far, linking the three initial themes mentioned in this section, to overcome the issue of CAIs being abundant in CCs but not in ordinary chondrites. This solves the CAI storage problem, of CAIs forming very early on, before chondrules and chondrite parent bodies, and surviving to accrete to the CC parent bodies, rather than plunging into the Sun due to gas tidal pressures. The model accurately reproduces the compositions of 18 classes of chondrites, lunar and martian meteorites, and finds that radial gas outflow is reasonable to support comets having nearly as many CAI fragments, ~ 0.5 vol%, (Joswiak et al., 2017) as CM and CR chondrites (Desch et al., 2018). Similar ideas have been put forward (Scott et al., 2018; Melosh et al., 2018) but Desch et al. (2018) have developed the first quantitative model.

These latest modifications suggested to the Grand Tack model with Jupiter creating a tidal barrier until its outward migration, explain many key compositional differences

between the carbonaceous and ordinary chondrites. It also allows for the storage and transport of CAIs to neatly explain their presence in carbonaceous chondrites and comet samples. This suggests wide scale mixing in the protoplanetary disk is responsible for the combination of refractory silicate minerals and icy minerals found in comets. Small amounts of radiogenic heat could cause partial melting to react with ferromagnesian silicates to form the magnetite observed.

Alternatively, a radical model based on ‘tidal downsizing’ for planet formation in situ is suggested, whereby instability in the outer protoplanetary disc gives rise to massive (~10 Jupiter masses) gas giant planet embryos, hot (up to ~1500 K) and dense due to contraction of the gas regions (Nayakshin et al., 2011). These were disrupted, with some particles mixing with outer solar system material to form comets, and the rest leaving planetary cores, such as possibly Uranus and Neptune (Nayakshin et al., 2011). This model suggests there would be more planets at long distances (up to 100 AU) from their parent star, which is unlikely to occur via the core accretion or the disc instability models for planet formation, so may be testable with future observation (Nayakshin et al., 2011).

4.4.6 Best carbonaceous chondrite match for comet Wild 2

This work shows that magnetite and forsterite Fo₆₀₋₆₂, Fo₄₃ grains from the matrix of CR2 and CV3 chondrites survive a capture process analogous to the *Stardust* mission. This supports the idea of preferential preservation, due to the higher density of magnetite (5150 kg m⁻³), as magnetite comprises ~1% of the CR2 and <1% of the CV3 chondrite powders used and is not thought to be one of the dominant phases in *Stardust* grains. This potential selection bias would also explain the lack of phyllosilicates observed in comet Wild 2 so far.

From these results, both are good analogues. Combining my work with other results and models discussed, more investigation is recommended into the close similarities with CR meteorites, though comet Wild 2 may contain a mixture of materials from different carbonaceous chondrite classes.

4.5 Conclusions

The mineralogy of *Stardust* terminal grains and carbonaceous chondrite analogue terminal grains have been studied and compared with synchrotron XRF, XAS and XRD. Raman analyses on these samples have been carried out by colleagues at the University of Kent.

1. Track C2065,4,187,0,0 (#187) contains three terminal grains. Tg1 magnetite, Tg2 olivine $\text{Fo}_{69\pm 13}$, Tg3 provisionally Fe-Ni sulphide.
2. Track C2098,4,188,0,0 (#188) Tg Fe sulphide.
3. Track C2119,4,189,0,0 (#189); Tg1 magnetite, Tg3 pyroxene.
4. Track C2119,5,190,0,0 (#190); Tg pyroxene.
5. CR2: 3 tracks: #1 Tg1 magnetite, Track #2 Tg1 is $\text{Fo}_{60\pm 2}$ and Tg2 is $\text{Fo}_{62\pm 1}$, #3 not identified.
6. CV3: 3 tracks: #4 Tg1a and 1b magnetite, #5 Tg is olivine $\text{Fo}_{43\pm 2}$, #6 not identified.
7. CR2 and CV3 powders were shot into aerogel at 6.1 km s^{-1} and made into keystones, analogous to the *Stardust* capture process. This was to test the similarities between *Stardust* grains and carbonaceous chondrites. These results verify the preservation of magnetite and olivine in terminal grains from each of the CR2 and CV3 powders.
8. This work confirms carbonaceous chondrites as a close match with *Stardust* and provides evidence of a possible density selection bias, whereby a minor phase of high density like magnetite is preferentially preserved. This would also provide a reason why low density phyllosilicates may have been preferentially destroyed, if present in comet Wild 2.
9. Alternatively, given the presence of magnetite and lack of phyllosilicates identified in *Stardust* comet grains, and by analogy with the two stage timing model suggested for CM meteorite alteration, it is suggested that the degree of aqueous alteration in comet Wild 2 only allowed the initial oxidation of metal FeNi to magnetite and there was insufficient aqueous solution to produce phyllosilicates. However, further work would be needed to substantiate that this process could be two discrete stages and would require a very specific amount of alteration, so I favour the density selection bias theory.

5 STEM-EDX ANALYSES OF COMET WILD 2

Five terminal grains captured by the *Stardust* mission have been investigated using scanning transmission electron microscopy (STEM) bright field (BF) and dark field (DF) imaging and energy dispersive X-ray (EDX) spectroscopy techniques as described in sections 2.2.4, 2.2.5 and 2.2.6. Ultramicrotomed slices mounted on copper grids were allocated by the Johnson Space Centre (JSC).

The purpose of this work is to characterise the mineralogy of the terminal grains to increase the overall population of *Stardust* grains examined, compare with previous studies, and consider the origin and formation of the grains.

A general background to cometary science is given in Chapter 1, and a detailed introduction to the *Stardust* mission and particles captured can be found in Chapter 4. This chapter gives an overview of previous transmission electron microscopy (TEM) *Stardust* studies, introduces the samples and describes the sample preparation processes undertaken by JSC. It then gives the results, characterising the grains and discusses them in the context of other studies.

5.1 Introduction

The *Stardust* spacecraft and the cometary tray used to capture particles from the coma of comet Wild 2 and return them to Earth are described in section 4.1. Grains from comet Wild 2 have been found to contain ferromagnesian silicates (pyroxenes, olivines, feldspars), iron oxides such as magnetite, chondrule-like fragments and particles similar to calcium aluminium inclusions (CAIs) (Brownlee et al., 2006; Zolensky et al., 2006; Zolensky et al., 2008; Bridges et al., 2010; Joswiak et al., 2012). Kosmochloric (Ko-, meaning enriched in Na and Cr) high-calcium pyroxene grains have been identified, and Kool (Ko-olivine) grain populations (Joswiak et al., 2009). Material similar to glass embedded metal and sulphides (GEMS) has been seen but cannot unambiguously be proven indigenous to the comet rather than formed from possible reaction with the melted aerogel (Ishii et al., 2008).

Finding refractory minerals, chondrule-fragments and CAI-like particles in comet Wild 2 was a surprise, as these materials are thought to have formed in the early hot inner Solar System. The discovery that up to 10% of comet Wild 2's mass may have been transported from the inner Solar System to the cold outer comet-forming regions provides evidence for widespread mixing in the early Solar System (Brownlee et al., 2006).

Chondrules are ferromagnesian igneous droplets up to one millimetre in size that experienced flash heating and fast-cooling, usually composed of olivine and low-Ca pyroxene in a feldspathic glassy mesostasis (Fig. 5.1) (Scott & Krot, 2007). Type 1 magnesian chondrules are thought to have

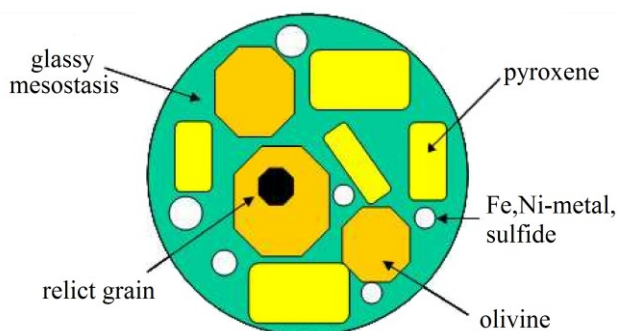


Fig. 5.1. Constituents of a ~1 mm ferromagnesian chondrule (Jones et al., 2005).

formed in a reducing environment, as they have large amounts of metallic iron as FeNi-metal and iron sulphide (predominantly troilite, FeS) nodules and very little iron oxide (Fig. 5.1). Thus, compositions close to forsterite (Mg_2SiO_4) and enstatite (MgSiO_3) are usually seen for olivine and pyroxene respectively, with Mg# over 0.9, where $\text{Mg}\# = \text{Mg}/(\text{Mg}+\text{Fe})$ (Jones et al., 2005). The glassy mesostasis usually has a feldspathic

plagioclase composition and was the last liquid to solidify as the chondrule cooled (Jones et al., 2005). Over 95% of chondrules in CV, CR, CM and CO carbonaceous chondrites are type 1 (Scott & Krot, 2007).

Type 2 chondrules, with Mg# less than 0.9, are thought to have formed under more oxidising conditions, so their pyroxene and olivine contains more FeO and they are generally more volatile rich (Jones et al., 2005). Chondrules are often described and grouped further by their textural properties, but as there is no textural context for the *Stardust* comet grains, discussion is restricted to comparing their compositions.

An experimental study suggest that type 1 chondrules may be precursors for type 2, and that chondrules could have formed in vapor plumes from impacts on planetesimals, with the most oxidising conditions experienced closest to the plumes (Villeneuve et al., 2015). Other possible chondrule formation mechanisms are discussed in section 4.1.5.

The terminal grains found in aerogel tracks are thought to be the most pristine material captured from comet Wild 2, as they are the largest grains that retained their integrity through the capture process, suffering less melting than fragments found along track walls (Bridges et al., 2010). Section 4.1.5 describes the material further and compares mineralogical resemblances with carbonaceous chondrites and interplanetary dust particles (IDPs).

Analytical transmission electron microscopy has been highlighted as one of the most important techniques available to determine modal mineralogy and concentrations of minor phases in the cometary tracks, look for evidence of aqueous alteration, determine the distribution of iron in olivine, and whether samples are crystalline or amorphous (Westphal et al., 2017). Together with isotopic results from other high precision techniques, these can be compared with other analyses of extraterrestrial materials in order to learn what comets are made of, how and where they may have formed, and how material might have been transported and mixed in the protoplanetary disk (Westphal et al., 2017).

5.2 Samples and methods

Stardust terminal grains from tracks #77, #81, #108 and #153 were ultramicrotomed and mounted on grids by the Johnson Space Center for transmission electron microscopy (TEM) study. These samples were borrowed for this study and are all type

B tracks (section 4.1.4.1). This work examines five grains, comparing their mineralogy with previous studies.

Procedures were developed for excavating individual grains as small as 3 μm using microneedles, extracting them with microtweezers and embedding them in an epoxy resin (Embed-812) before ultramicrotoming them (Westphal et al., 2002; Westphal et al., 2004). Microtomed slices that were electron transparent (70-100 nm thick) were then mounted onto copper TEM grids. A later refinement using acrylic resin instead of epoxy has the advantage of being soluble and reversible, so that carbon and insoluble organics can be analysed (Matrajt & Brownlee, 2006).

This section describes the samples using the JSC documentation where available. Details of the TEM and calibration procedure used for STEM-EDX are in sections 2.2.4, 2.2.5, and 2.2.6.

5.2.1 Track #77, terminal grain 1 (Tg1)

Samples 2009-20-77-1-6 and 2009-20-77-1-12 were provided from the twentieth aerogel keystone containing track #77, being TEM grids 6 and 12 made from microtoming Tg1. Grid 6 is shown in Fig. 5.2; no images were available of grid 12.

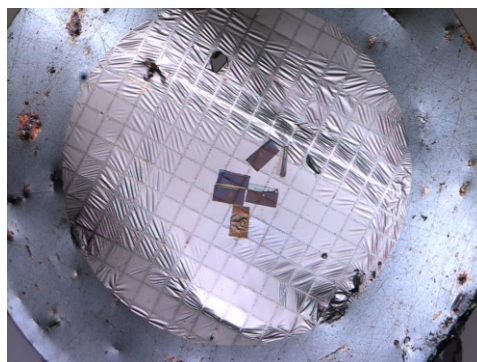


Fig. 5.2. Grid 6 (2009-20-77-1-6) has five slices.

Both grids were previously allocated to D.

Brownlee (30 December 2006) (NASA-JSC, 2018). Tg1 was also named Puki, Puki-A, and Puki-1, Puki-2 (7 μm x 4 μm), Puki-3 for different fragments/slices of the terminal grain (Matrajt et al., 2007; Brownlee et al., 2010; Joswiak et al., 2009). TEM of Tg1 has diopside and Fe-olivine (Matrajt et al., 2007). Time-of-flight secondary ion mass spectrometry (TOF-SIMS) work on TEM grid 11 (2009-20-77-1-11) reported Mg-rich olivine and noted the bulk Si/Mg ratio of 1.1 was near to chondritic values (Stephan, 2009). Puki contains Fo_{62-67} , a one μm grain of Ko-diopside and FeNi/FeS nanobeads in a SiO_2 melt rim and thus is described as a Kool-grain (Brownlee et al., 2010; Joswiak et al., 2012). Full analysis of further fragments from track #77 was reported by Joswiak et al. (2012) and XANES of Fe metal of 53 fragments from track #77 was examined by (Ogliore, 2010).

5.2.2 Track #81, terminal grains 1 and 2

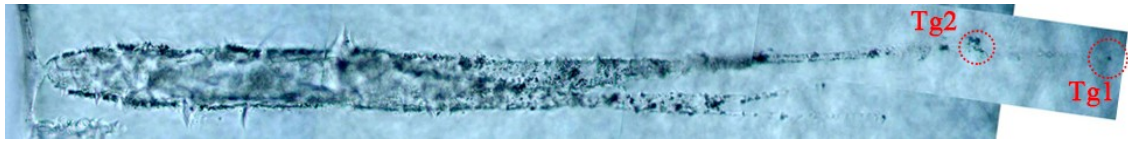


Fig. 5.3. Track #81, type B, length 2040 μm , with the *Stardust* grains entering the aerogel from the left hand side, with terminal grain 1 (Tg1) and terminal grain 2 (Tg2). Image: K. Nakamura-Messenger, NASA-JSC.

Samples 2092-7-81-1-4 and 2092-7-81-1-7 were provided from the seventh aerogel keystone containing track #81 (Fig. 5.3), being TEM grids 4 and 7 made from microtoming terminal grain 1. TEM grid 4 contains slices 13 to 18 and TEM grid 7 contains slice 22 of this grain, numbered by JSC (Fig. 5.4).

An extra grid was stuck to the first sample, which has been identified as the 5th TEM grid of terminal grain 2, sample 2092-7-81-2-5. This contains four slices (Fig. 5.5).

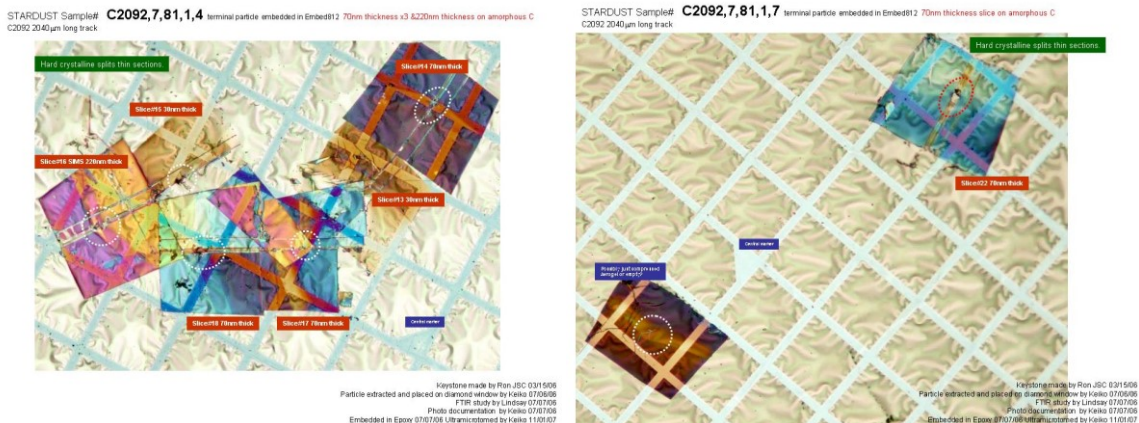


Fig. 5.4. Optical micrographs of (Left) 2092-7-81-1-4: Slice 13 is only 30 nm thick, no useful data collected. Slice 14 overlaps the copper grid. Slice 15, no grain was found. Images and EDX measurements were collected from slices 16-18. (Right) 2092-7-81-1-7: Slice 22. Images: NASA-JSC.

Terminal grain one (Tg1) from #81 was recorded as $\sim 15 \times 20 \mu\text{m}$ (2092-7-81-1-0) and named Pyxie or F1/T81 (Nakashima et al., 2012; Nakashima et al., 2015). It consists of low-Ca pyroxene ($\text{En}_{92}\text{Wo}_3$) and plagioclase ($\text{An}_{65}\text{Ab}_{35}$) (Nakashima et al., 2012; Nakashima et al., 2015). Similar analyses were seen from the tenth TEM grid of Tg1 (2092-7-81-1-10): low-Ca pyroxene $\text{En}_{80-95}\text{Wo}_{1-8}$, high-Ca pyroxene $\text{En}_{52-63}\text{Wo}_{32-38}$ and plagioclase $\text{An}_{45-85}\text{Ab}_{13-55}\text{Or}_{0-2}$ (Dobrică & Brearley, 2011).

TEM grid 2092-7-81-1-4 was previously allocated to M. Fries (24 September 2008) (NASA-JSC, 2018). Crystalline graphite was identified by Raman spectroscopy, though considered likely to have crystallised after contact with molten aerogel, as analogue studies indicated graphite would be strongly disrupted by the capture process (Fries et al., 2009).

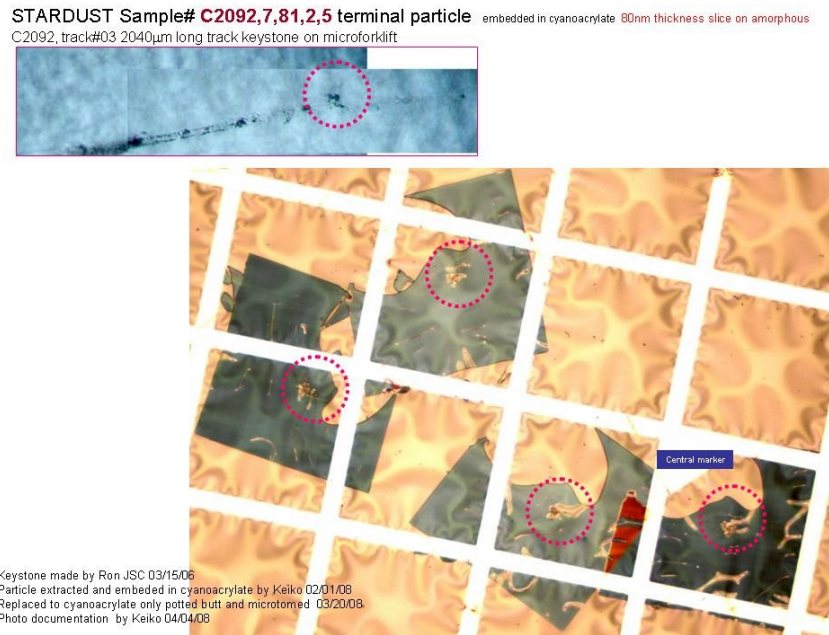


Fig. 5.5. Optical micrographs of 2092-7-81-2-5 with four microtome slices each with part of terminal grain 2. Image: NASA-JSC.

5.2.3 Track #108, terminal grain 20

Samples 2081-1-108-20-1 and 2081-1-108-20-3 were provided from the first aerogel keystone containing track #108 (Fig. 5.6), being TEM grids 1 and 3 made from microtoming terminal grain 20 (Fig. 5.7). This track was 13210 μm long, with 8 stylii coming out of the bulb and 30 terminal grains.

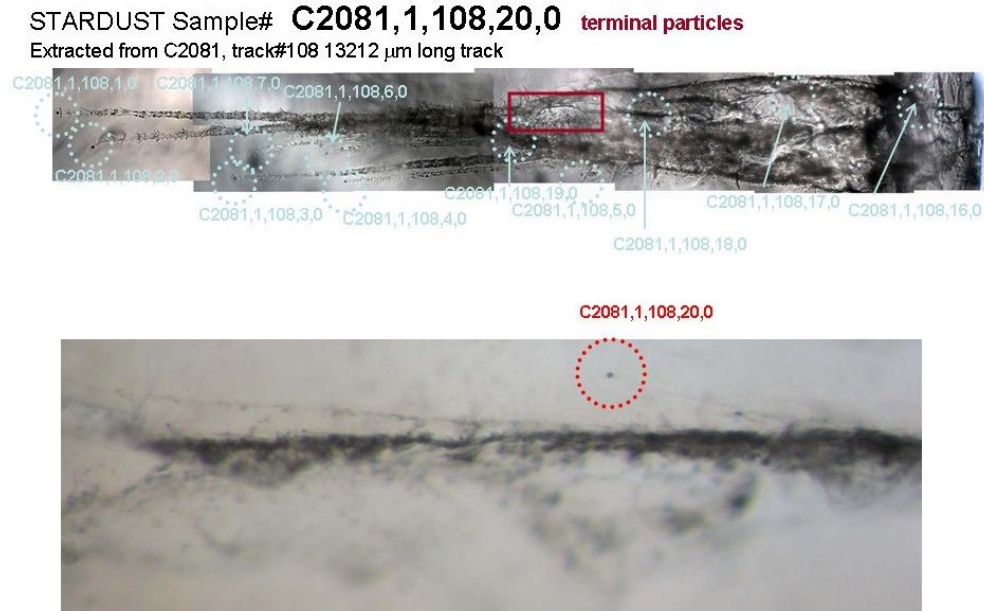


Fig. 5.6. Microscope images of track #108, type B, with the *Stardust* grains entering from the right hand side. (Top) length 13210 μm , with 8 stylii coming out of the bulb, containing a total of 30 terminal grains (Bottom) Terminal grain 20 is highlighted. Image: NASA-JSC.



Fig. 5.7. Optical micrographs of (Left) 2081-1-108-20-1 with four slices, two containing the terminal grain. (Right) 2081-1-108-20-3 with one slice containing the terminal grain. Image: NASA-JSC.

Terminal grains previously studied from track #108 are 2081-1-108-1, Gozen-sama, (40 μm) with two olivine Fo_{95} grains enclosed in low-Ca pyroxene, $\text{En}_{95}\text{Fs}_4\text{Wo}_1$, and 2081-1-108-7 has pigeonite, $\text{En}_{84}\text{Fs}_5\text{Wo}_{11}$ and low-Ca pyroxene, $\text{En}_{97}\text{Fs}_1\text{Wo}_2$ (Nakamura et al., 2008).

5.2.4 Track #153, terminal grain 2

Samples 2035-3-153-2-7 and 2035-3-153-2-8 were provided from the third aerogel keystone containing track #153, being TEM grids 7 and 8 made from microtoming terminal grain 2 (Fig. 5.8). The microtome slices are numbered here as slices 1 to 9 for grid 7 and slices 1 to 7 for grid 8.

Grid 7 contained nine microtome slices but only slices 1, 4, 5 and 7 were observable as the others overlapped the copper grid (Fig. 5.8B). Grid 8 contained seven slices, where six of them could be analysed with the TEM (Fig. 5.8C).

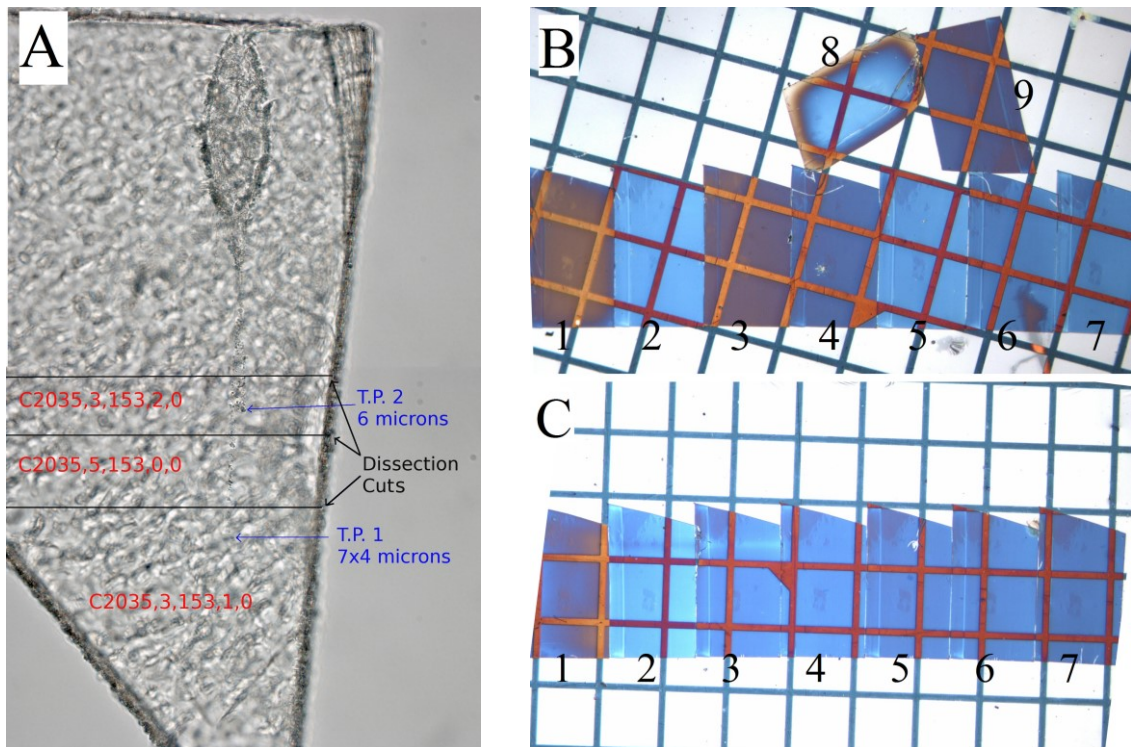


Fig. 5.8. Optical micrographs of (A) Track #153 made by *Stardust* grains entering the aerogel from the top, causing the bulbous type B cavity seen. Terminal grain 2 is 6 μm . The track length is 1131 μm , the bulb width 29 μm and depth 530 μm . (B) Sample 2035-3-153-2-7 contains nine slices. (C) Sample 2035-3-153-2-8 contains seven slices. Images: NASA-JSC.

5.3 Results

As the silica aerogel has often partly melted and mixed with the captured *Stardust* grains, it is very hard to measure indigenous Si, present in the cometary grains, precisely (Zolensky et al., 2006; Leroux, Rietmeijer, et al., 2008; Jacob et al., 2010). Some of the silicate mineralogy observed in this section is not stoichiometric for that reason, but as the proportions of other minerals should not change, this does not hinder reporting and discussing the pyroxene, olivine and feldspar grains found.

5.3.1 Terminal grain 1 from Track #77

Grid 6 (2009-20-77-1-6) contains a terminal grain slice, imaged with DF and BF mosaic images in Fig. 5.9. This was identified to be the same as the fragment examined previously by Joswiak et al. (2012) (Fig. 5.9C), with mineralogical information also available from their studies in the *Stardust* sample database (NASA-JSC, 2018).

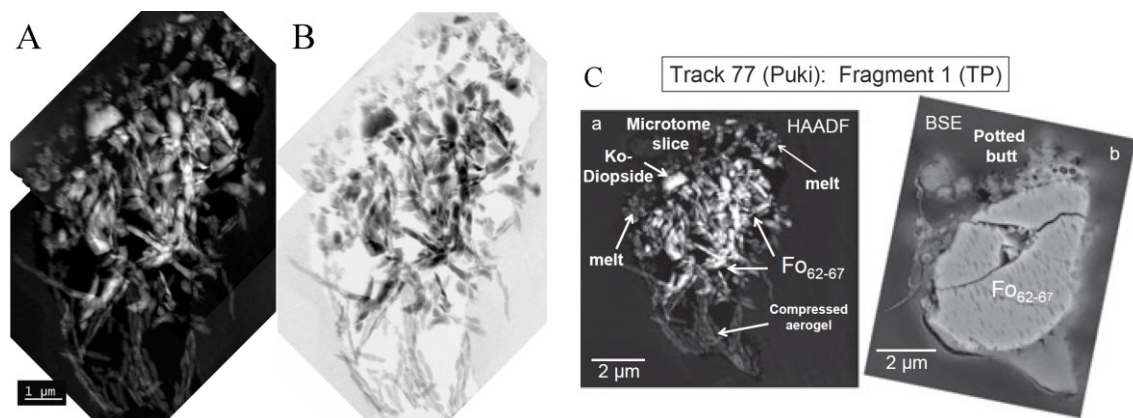


Fig. 5.9. (A) Dark field image and (B) Bright field image of 2009-20-77-1-6, mainly Fo₇₁₋₇₃, some En₇₇Fs₂₁Wo₂. (C) Labeled image of the slice by Joswiak et al. (2012).

STEM-EDX point measurements gave a range of olivine Fo₆₉₋₇₃ and the Ko-diopside grain was measured to be En₅₂Fs₁₁Wo₃₇ (Table 5.1). Comparable measurements from Puki-2 have a slightly lower olivine range Fo₆₂₋₆₇ (Joswiak et al., 2012) (Table 5.1).

Grid 12 has a slice of the terminal grain (Fig. 5.10A). STEM-EDX maps have Mg, Si and Fe throughout with no other major element contribution (Fig. 5.10B). Three measurements across the grain report olivine Fo₇₀₋₇₃ (Table 5.1). No area of high calcium or possible diopside was seen in this slice of the grain.

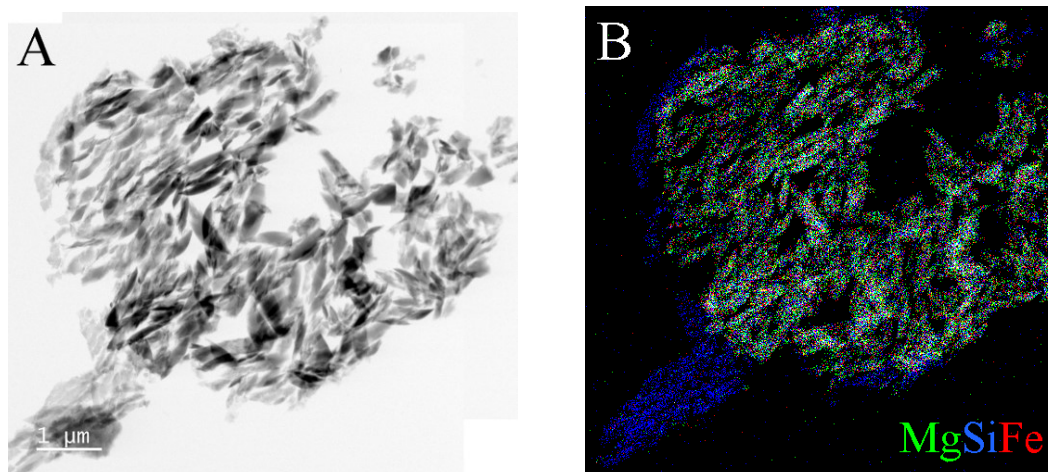


Fig. 5.10. (A) Bright field image of 2009-20-77-1-12. (B) EDX map of A with olivine Fo_{70-73} .

Table 5.1. Normalised STEM-EDX data for olivines and pyroxenes identified, compared with previous measurements.

	77-1-6	77-1-12	77-1-6	Puki-A*	Puki-A*
	olivine	olivine	Ko-diopside	olivine	Ko-diopside
SiO_2	37.8	37.9	59.3	37.4	56.4
TiO_2					0.3
Al_2O_3			0.9	0.2	0.5
Cr_2O_3	0.5	0.4	1.3	0.1	1.4
FeO	25.6	26.0	6.1	27.5	6.7
MnO		0.3		0.4	0.2
MgO	36.2	35.2	15.7	34.3	14.2
CaO		0.2	15.7	0.2	19.4
Na_2O			1.0		1.0
Total	100.1	100.0	100.0	100.0	100.0
Si/O	0.25	0.25	0.35	0.25	0.34
Mg#	71.6	70.6		69.2	
En %			51.7		44.3
Fs %			11.2		12.4
Wo %			37.0		43.7

*(Joswiak et al., 2009)

Further material in a different slice of grid 6 has very small iron sulphide beads, measurements suggest $\text{Fe}_{0.95}\text{S}$, though there is Si contamination.

5.3.2 Terminal grain 1 from Track #81

Grid 4 (2092-7-81-1-4) was examined. Slices 13 and 15 were noted to be only 30 μm thick (JSC). No useful data was obtained from slice 13, and the grid appeared ripped and no grain could be found in slice 15. The grain in slice 14 was mounted on top of the copper grid so no measurements could be made. The grain was found in slice 16 (Fig. 5.11), slice 17 (Fig. 5.12) and slice 18 (Fig. 5.13). Grid 7 (2092-7-81-1-7) was examined and the grain was found in slice 22 (Fig. 5.14).

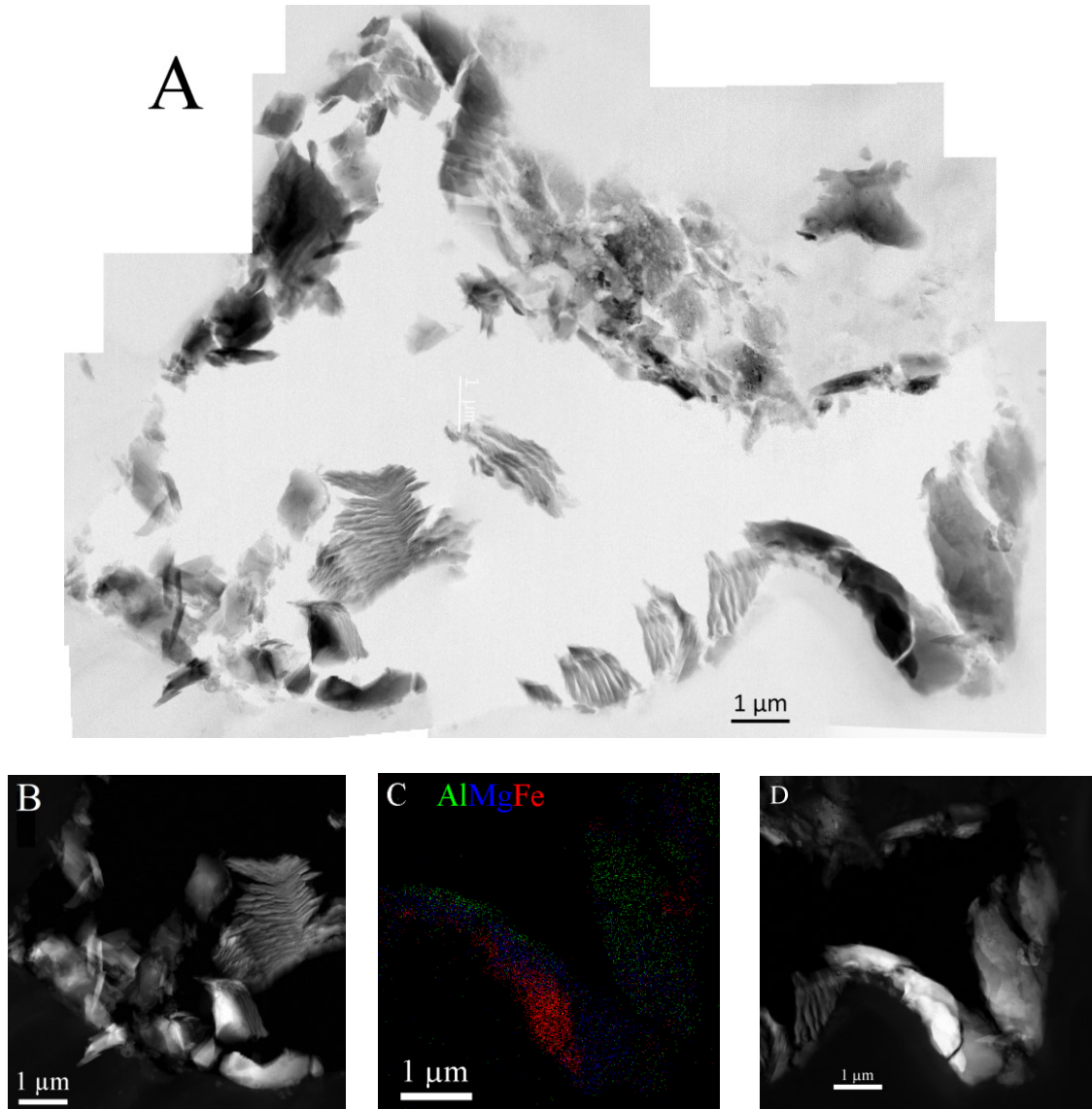
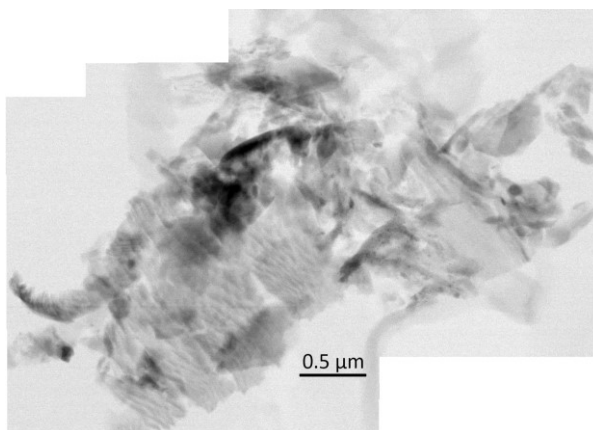


Fig. 5.11. (A) BF image of 2092-7-81-1-4 slice 16 of a terminal grain with an area of $\sim 16 \mu\text{m} \times 12 \mu\text{m}$. (B) DF image of bottom left of A consisting mainly of pyroxene. (C) EDX map of area in D with Al indicating feldspar, Mg for pyroxene, and the iron rich area also contains sulphur, $\text{Fe}_{0.82}\text{S}$. (D) DF image showing the area in C, from the bottom right of A.

Pyroxene, feldspar and iron sulphide were found in all four slices and no olivine was seen, similar to previous studies (Nakashima et al., 2015; Dobrică & Brearley, 2011). The pyroxene is enstatite with a range of $\text{En}_{85-97}\text{Fs}_{2-9}\text{Wo}_{0-11}$ from thirty-one stoichiometric measurements. The plagioclase feldspar has a range of $\text{Ab}_{29-64}\text{An}_{36-71}\text{Or}_0$ from twenty-eight stoichiometric measurements. Table



5.2 gives representative measurements from each slice. Fig. 5.12. BF image of 2092-7-81-1-4 slice 17 of a terminal grain showing material with an area of $\sim 4 \mu\text{m} \times 2.5 \mu\text{m}$.

5.2 gives representative measurements from each slice.

Table 5.2. Normalised STEM-EDX data for pyroxenes and feldspars identified.

Slice	16	16	17	17	18	18	22	22
	px	fp	px	fp	Px	fp	Px	fp
Data pt	15-70	15-57	2-8	1-2	11-59	12-62	5-15	2-6
SiO ₂	57.4	56.3	57.4	53.3	57.9	53.1	57.7	53.5
TiO ₂							0.1	
Al ₂ O ₃	1.1	24.6	2.3	30.1		30.7		30.9
Cr ₂ O ₃	1.2		1.0		1.0		1.1	0.4
FeO	2.0	1.2	1.3		2.6		3.6	0.3
MnO	0.5				1.0		0.9	
MgO	36.9		32.6		37.0		36.2	
CaO	1.0	14.1	4.7	9.8	0.5	8.3	0.5	10.3
Na ₂ O		3.7		5.7		7.9		4.6
Total	100.1	99.9	99.9	100.0	100.0	100.0	100.1	100.0
Si/O	0.33	0.32	0.33	0.30	0.33	0.30	0.33	0.3
(Mg+Fe+Ca)/Si	1.00		0.96		1.00		1.00	
En %	95.3		88.5		95.3		93.9	
Fs %	2.9		2.2		3.7		5.2	
Wo %	1.8		9.2		1.0		0.9	
Ab %		32.2		51.4		63.4		44.5
An %		67.8		48.6		36.6		55.5
Or %		0.0		0.0		0.0		0.0

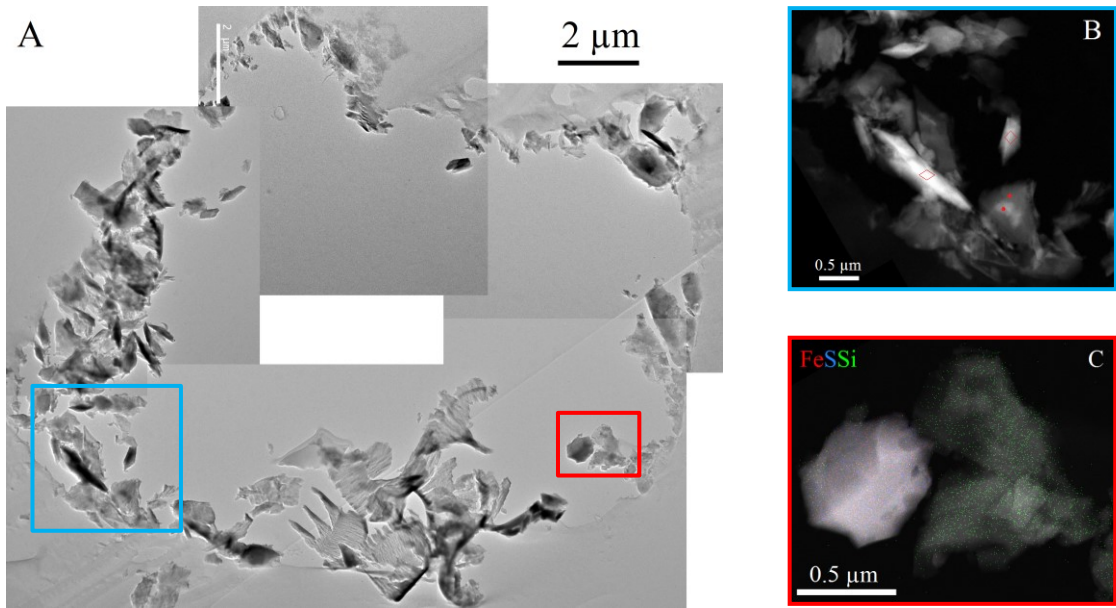


Fig. 5.13. (A) Gatan image of 2092-7-81-1-4 slice 18 of terminal grain material with an area of $\sim 19 \mu\text{m} \times 14 \mu\text{m}$. (B) DF image of the blue rectangle area from A with four stoichiometric enstatite analyses locations (red). (C) DF image with STEM-EDX map of an $\text{Fe}_{0.8}\text{S}$ pyrrhotite droplet (left), from the red rectangle area in A.

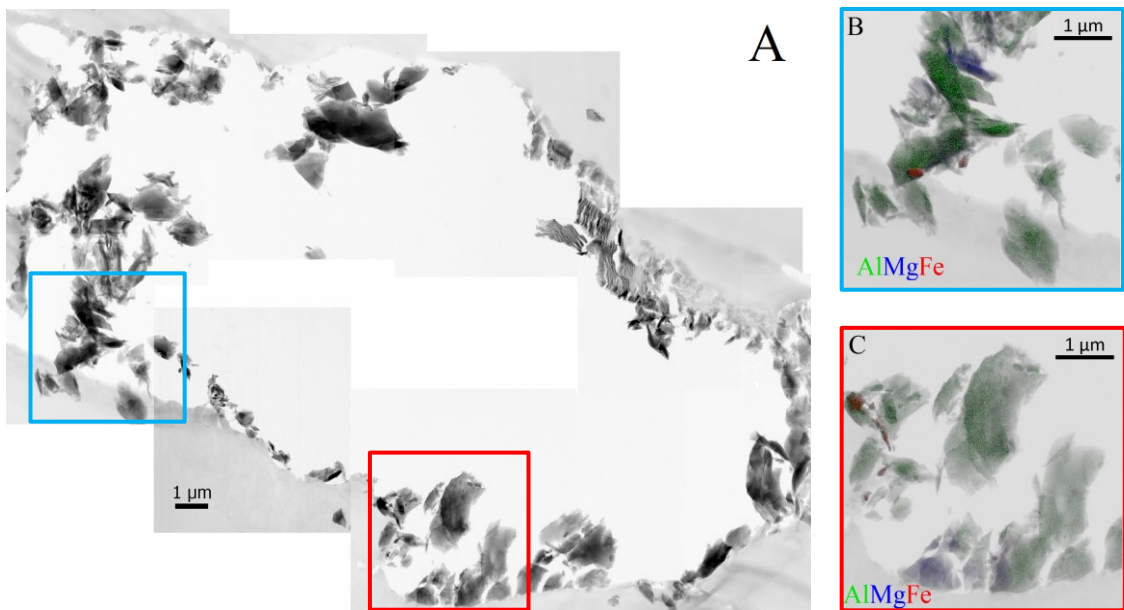


Fig. 5.14. BF images of (A) 2092-7-81-1-7 slice 22 of terminal grain material with an area of $\sim 28 \mu\text{m} \times 14 \mu\text{m}$. (B) A STEM-EDX map for the blue rectangle area in A: Al indicates plagioclase $\text{Ab}_{42-48}\text{An}_{52-58}$, Mg shows Px $\text{En}_{95}\text{Fs}_4\text{Wo}_1$, Fe is metal and pyrrhotite $\text{Fe}_{0.9}\text{S}$. (C) STEM-EDX map for the red rectangle area in A: Al indicates plagioclase $\text{Ab}_{52}\text{An}_{48}$, Mg shows Px $\text{En}_{94}\text{Fs}_5\text{Wo}_1$, Fe shows pyrrhotite $\text{Fe}_{0.8}\text{S}$.

5.3.3 Terminal grain 2 from Track #81

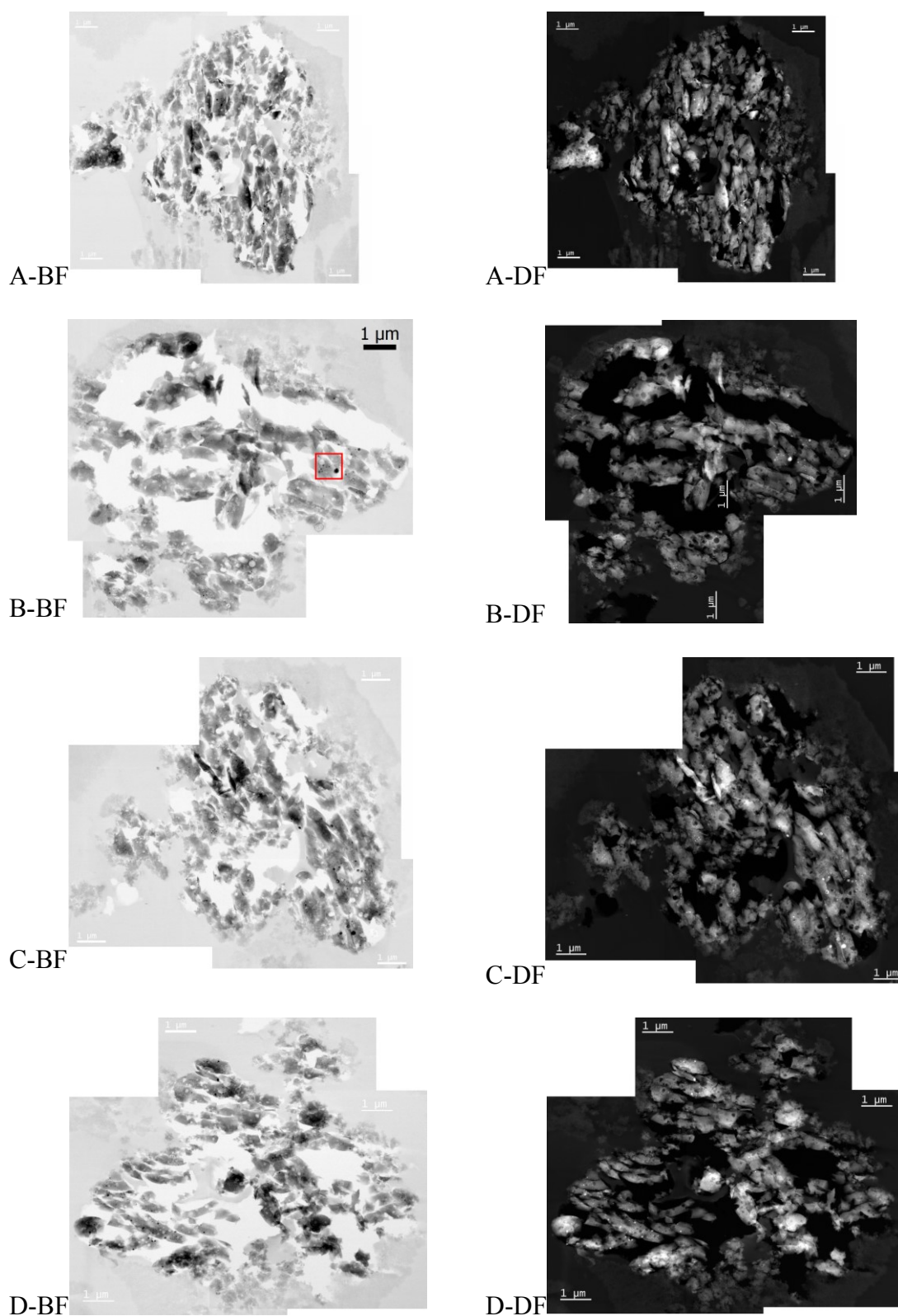


Fig. 5.15. BF and DF images of the four slices A-D from terminal grain 2 (2092-7-81-2-5) with abundant small Fe-Ni-S beads.

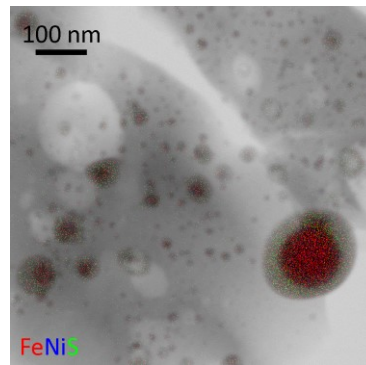


Fig. 5.16. Slice B contains the largest Fe metal sphere with an iron sulphide rim (red box area from Fig. 5.15B-BF).

Grid 5 (2092-7-81-2-5) was examined (Fig. 5.5). The grain was found in all four slices, all containing abundant Fe-Ni beads with iron sulphide rims (Fig. 5.15). EDX compositions of these are plotted in Fig. 5.23 with a compositional range of $\text{Fe}_{50-89}\text{Ni}_{3-9}\text{S}_{1-46}$. A few analyses showed near-troilite compositions but the majority of the analyses varied with lower sulphur content, indicative of capture heating effects liberating some of the volatile sulphur. The EDX map (Fig. 5.16) contains one of the largest Fe-Ni beads with an iron sulphide rim.

5.3.4 Terminal grain 20 from Track #108

Grid one (2081-1-108-20-1) had two slices of the terminal grain (Fig. 5.7). Some Mg and Si was observed along the top area, with one fragment containing Ni-Ti (Fig. 5.17B). However, counts were very low, so no stoichiometric identifications could be made.

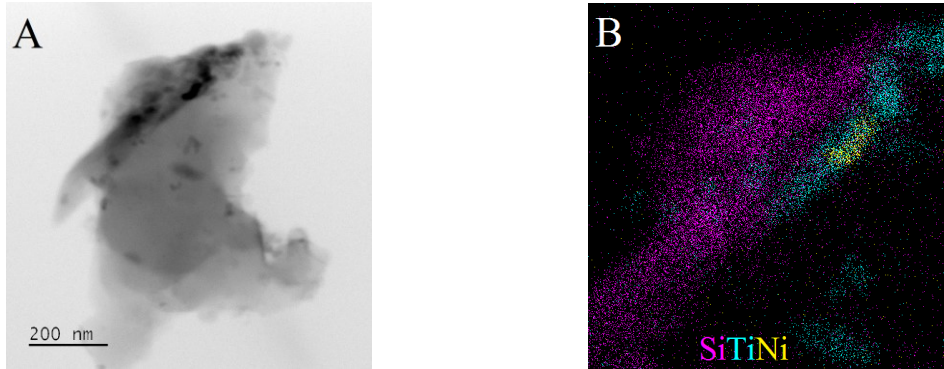


Fig. 5.17. (A) BF image of the grain (2081-1-108-20-1). (B) EDX map of the top part of the grain showing the darker material in A.

Grid 3 (2081-1-108-20-3) had one slice of the terminal grain (Fig. 5.18A). EDX spectra for parts of the grain report high Fe (39-45 at%) with some Ni (1-5 at%) though also high Si (10-20 at%) contamination from the aerogel (Fig. 5.18B). EDX spectra gave low counts and SiO_2 was predominantly identified elsewhere in this grain, as there was little surviving material. No evidence was found for olivine or pyroxene, observed in other terminal grains in this track (Nakamura et al., 2008).

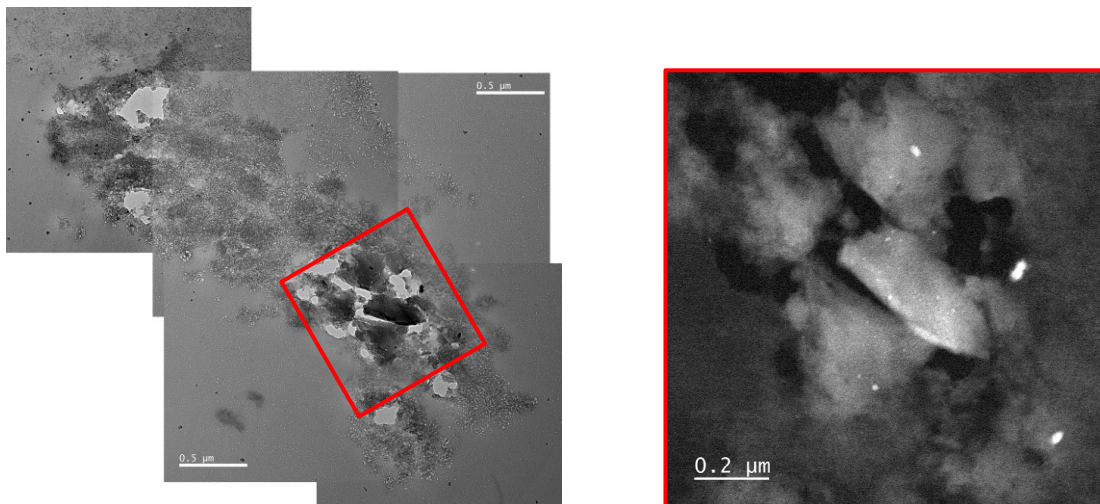


Fig. 5.18. (A) Gatan image of the slice from grid 3 (2081-1-108-20-3). (B) DF image of part of the slice in A (red box).

5.3.5 Terminal grain 2 from Track #153

EDX spectra for grid 7 (2035-3-153-2-7, Fig. 5.8B) slice 4 contained TiO_2 (Fig. 5.19A). A grain was found in the expected location for slice 1 but the EDX counts were too low to identify any minerals (Fig. 5.19B). The locations for slices 5 and 7 were examined but no convincing *Stardust* material was observed.

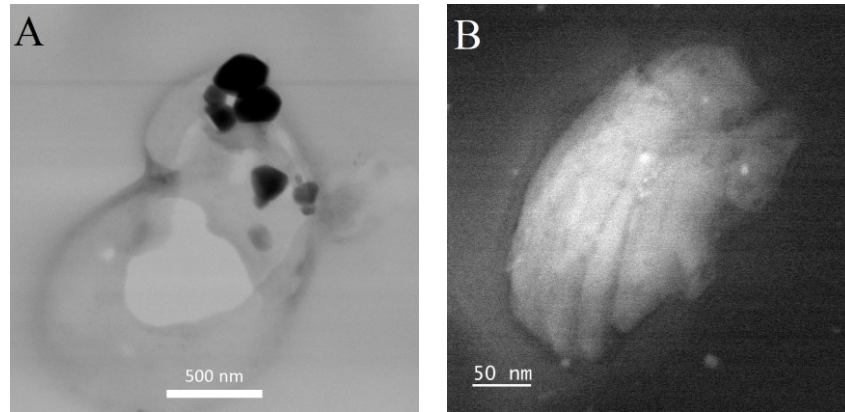


Fig. 5.19. (A) BF image of #153-2-7, slice 4. (B) DF image of #153-2-7, slice 1.

Grid 8 (2035-3-153-2-8, Fig. 5.8C) had grain fragments in slice 1 (Fig. 5.20). The EDX spectra for both fragments contained Fe (35 to 46 at%), Ni (16 to 22 at%), Cr (17 to 22 at%) and Mn (1.1 to 1.7 at%) (Fig. 5.20A,C).

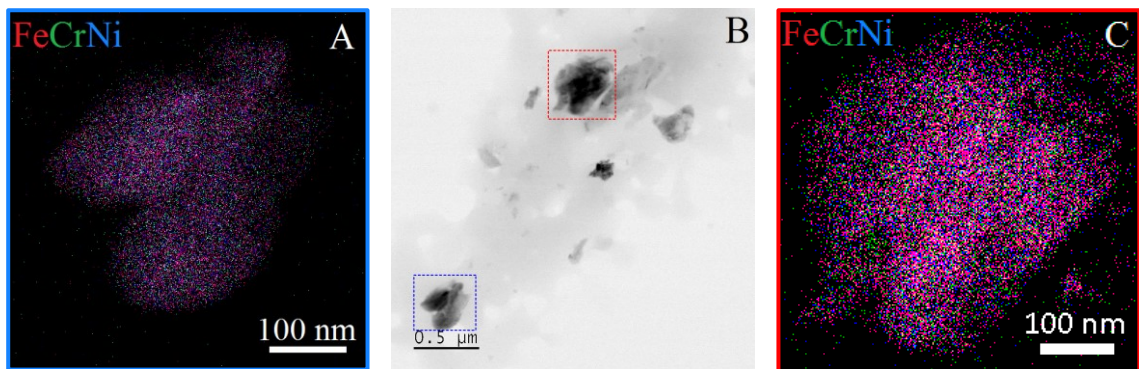


Fig. 5.20. (A) EDX of the lower left grain in image B. (B) BF image of slice 1 on grid 8. (C) EDX of the upper middle grain in image B. All particles contain TiO_2 .

5.3.6 Comparisons of mineralogy with previous results

Stardust grains contain both low-Ca pyroxene, mainly enstatite, and high-Ca pyroxene (Fig. 5.21). All observed pyroxene is Mg-rich. Pyroxene and olivine, within the same *Stardust* grain, have a similar proportion of magnesium compared with iron, $Mg/(Mg+Fe)\%$. Joswiak et al (2009) noted that tie lines between the average composition of co-existing pyroxene and olivine, for different grains, do not cross. This suggests that the Fe-Mg in pyroxene and co-existing olivine shared a similar evolution.

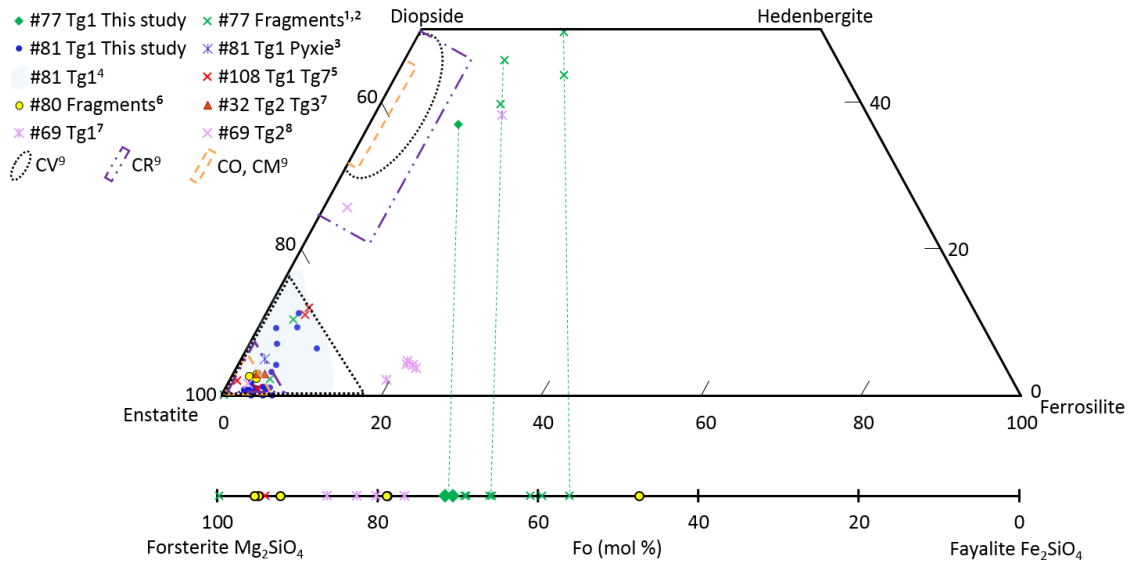


Fig. 5.21. Pyroxene quadrilateral and line plot of olivine forsterite% with STEM-EDX compositions of the *Stardust* grains studied here, #77 (Table 5.1) and #81 (Table 5.2), and previous measurements from the literature, compared with pyroxene in chondrules in different carbonaceous chondrites, types CV, CR, CO and CM. # = track number, Tg = terminal grain. ¹TEM (Joswiak et al., 2012), ²(Joswiak et al., 2009), ³EPMA (Nakashima et al., 2015), ⁴TEM (Dobrică & Brearley, 2011), ⁵EPMA (Nakamura et al., 2008), ⁶STEM (Stodolna et al., 2012) ⁷TEM (Jacob et al., 2010), ⁸TEM (Leroux, Jacob, et al., 2008). ⁹Brearley & Jones (1998).

The range of olivine in Fig. 5.21 is comparable with the measurements of olivine in *Stardust* and a CR2 meteorite powder together with their relative abundances (Fig. 4.13). Track #77 olivine Fo_{69-73} has a rarer higher iron content compared to more abundant Fo_{90-100} *Stardust* olivine compositions (Fig. 4.13) and the co-existing Ko-diopside grain was $En_{52}Fs_{11}Wo_{37}$. The terminal grain compositions from this study have parallel tie-lines between their olivine and pyroxene compositions when compared with other fragments from track #77 (Fig. 5.21) (Joswiak et al., 2009).

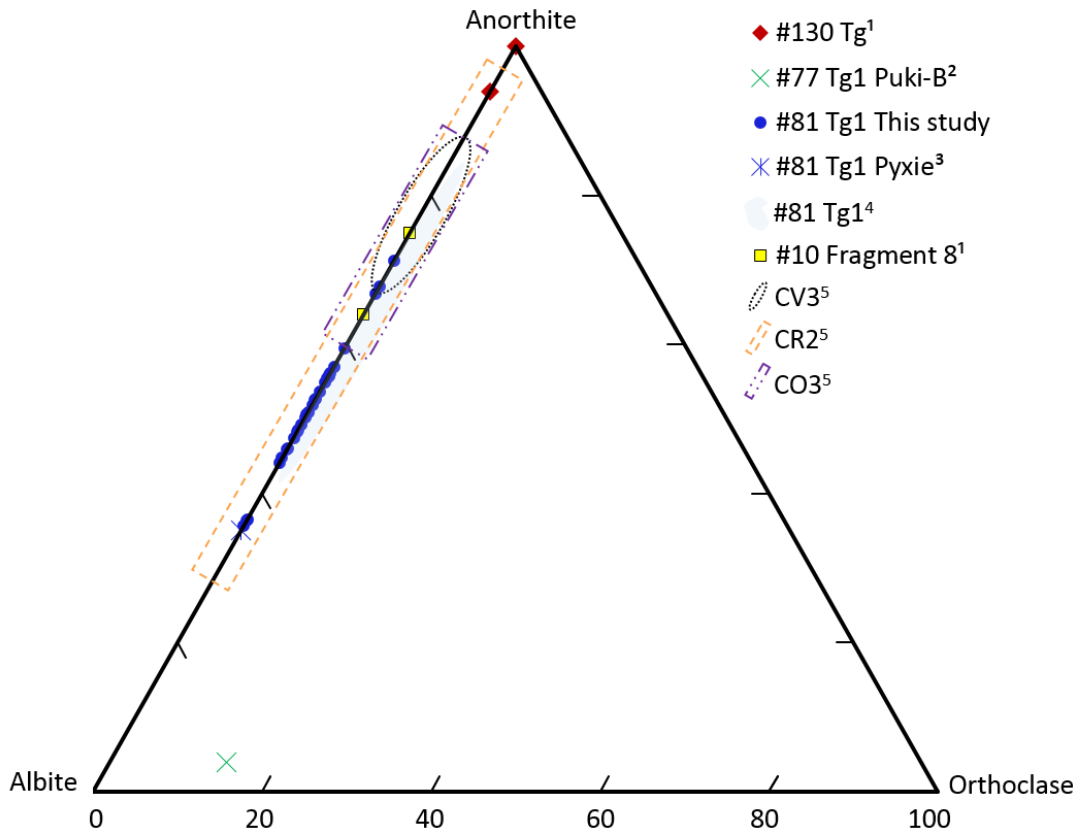


Fig. 5.22. Feldspar ternary with STEM-EDX compositions of the *Stardust* grains studied here and previous measurements from the literature, compared with feldspar in chondrules in different carbonaceous chondrites, types CV3, CR2, and CO3. # = track number, Tg = terminal grain. ¹TEM (Joswiak et al., 2012), ²(Joswiak et al., 2009), ³EPMA (Nakashima et al., 2015), ⁴TEM (Dobričá & Brearley, 2011) ⁵Brearley & Jones (1998).

Feldspar observed in *Stardust* and carbonaceous chondrites is usually plagioclase, with negligible orthoclase content (Fig. 5.22). Crystalline plagioclase or feldspathic glassy mesostasis is susceptible to aqueous alteration, thus feldspathic compositions are rarely seen in aqueously altered CM chondrites. The range of compositions seen in *Stardust* is similar to that seen in chondrules, with CR chondrites being the closest match (Fig. 5.22).

Track #81 low-Ca pyroxene is nearly pure enstatite $\text{En}_{85-97}\text{Fs}_{2-9}\text{Wo}_{0-11}$, overlapping with pyroxene compositions of CV, CR, CO and CM chondrules (Fig. 5.21). The $\text{Ab}_{29-64}\text{An}_{36-71}$ composition of the #81 plagioclase overlaps with plagioclase seen in CR chondrules (Fig. 5.22). Small spheres of Fe-Ni-S, pyrrhotite, were also observed in #81 (Fig. 5.23).

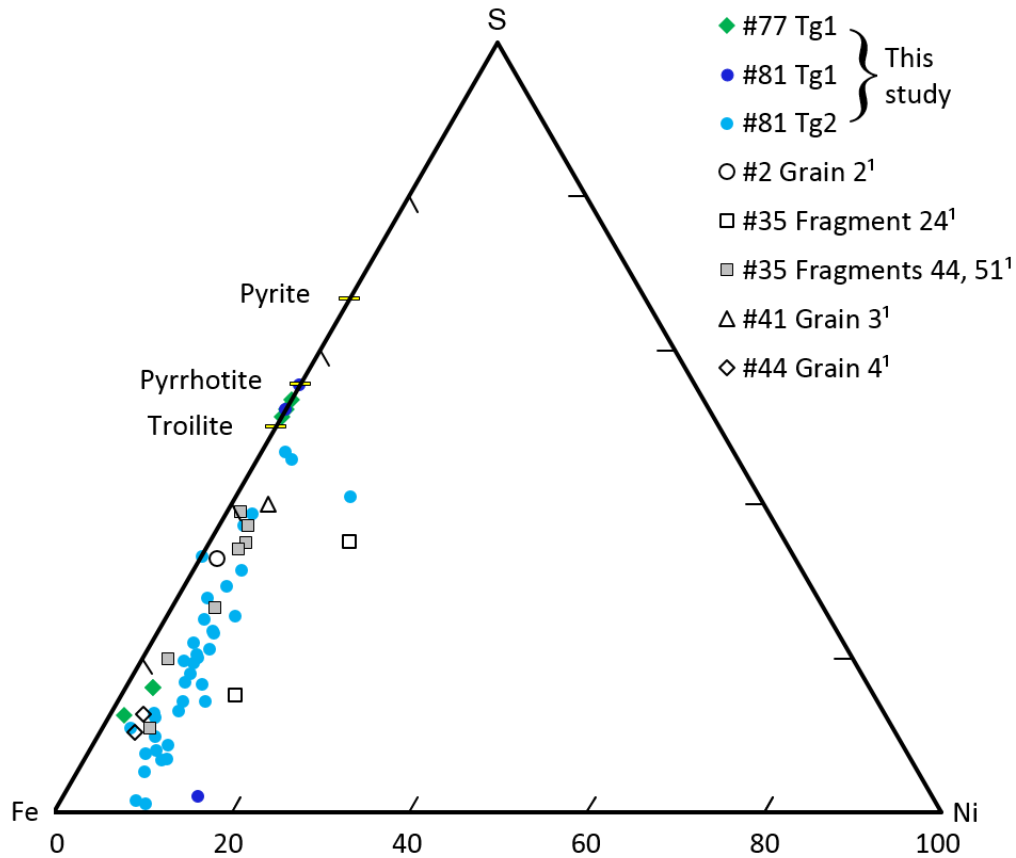


Fig. 5.23. Fe-Ni-S ternary with STEM-EDX compositions of the *Stardust* grains studied here and previous average measurements from the literature, ¹TEM (Leroux, Rietmeijer, et al., 2008). # = track number, Tg = terminal grain.

Troilite (FeS) and pyrrhotite (Fe_{0.8-1}S) are present in *Stardust* tracks #77 Tg1 and #81 Tg1, though there is also a large scatter of analyses with a range of Fe₅₀₋₈₉Ni₃₋₉S₁₋₄₆, (Fig. 5.23). This is likely due to effects of capture heating leading to loss of some of the volatile sulphur content (Zolensky et al., 2008). Thirteen fragments studied previously showed similar scatter, with one track also having more Ni-rich material (C2054,0,35,24, fragments 1 and 7) (Leroux, Rietmeijer, et al., 2008). The average composition of 11-59 analyses for each fragment was plotted for comparison here (Leroux, Rietmeijer, et al., 2008).

Only troilite and pyrrhotite are present in anhydrous chondritic IDPs, with hydrous chondritic IDPs having Ni-rich sulphides such as pentlandite (Zolensky & Thomas, 1995).

5.4 Discussion

5.4.1 Chondrule-like fragments

Track #77 Tg1 contains olivine throughout two slices with one grain of diopside. Track #81 Tg1 has enstatite and andesine assemblages in all four slices of the terminal grain. These mineral assemblages are similar to those seen in chondrule fragments.

The low-Ca pyroxene $\text{En}_{85-97}\text{Fs}_{2-9}\text{Wo}_{0-11}$ in the terminal grain of track 81 is similar to that seen in type 1 chondrules. Type 1 (low-iron) chondrules are the most abundant, and present in all chondrite types (Jones et al., 2005). Oxygen isotope analyses of *Stardust* grains overlap with oxygen isotopes seen in carbonaceous chondrite, and distinguishes them from oxygen isotopes in ordinary chondrites, rumuruti and enstatite chondrites (Nakamura et al., 2008; Nakashima et al., 2012). Both low-Ca pyroxene and high Ca-pyroxene in carbonaceous chondrites have similar compositions for the different types (CV, CR, CM, CO) so it is not possible to distinguish further or suggest a closer affinity with one type than another (Fig. 5.21).

Anhydrous IDPs were found to be the closest match for the large range of low-Ca pyroxene from Fs_0 to Fs_{48} observed in seven *Stardust* tracks (Zolensky et al., 2008), broader than the range seen in most chondrites. The Fe-rich pyroxenes observed in *Stardust* may instead have affinities with chondrite matrix that also has a broader range of pyroxene compositions, though more accurate compositional data for chondrite matrix minerals via TEM analyses is needed for comparisons (Zolensky et al., 2008).

The range of Fe-rich olivine in *Stardust* also suggests similarities with chondrite matrix, particularly with aqueously altered matrix of CM, CO and CI chondrites (Zolensky et al., 2008). A larger study of the fayalite content (mol%) of thirty-six particles from twenty-six *Stardust* tracks were compared with both ordinary and carbonaceous chondrite matrix (Frank et al., 2014). This study concluded that the FeO-rich olivine observed was more similar to type II chondrules (Frank et al., 2014).

The plagioclase $\text{Ab}_{29-64}\text{An}_{36-71}$ in the terminal grain of #81 suggests a closer affinity with plagioclase seen in CR2 chondrules, as CV3 and CO3 compositions from other studies usually have a higher anorthite content, above An_{60} .

Chondrule-like fragments have been seen in multiple tracks in comet Wild 2 grains. Previous reports include fragments resembling both type 1 and type 2 ferromagnesian chondrules (Nakamura et al., 2008; Gainsforth et al., 2015; Joswiak et al., 2012), Al-rich chondrules in tracks #154, #130 (Joswiak et al., 2009; Bridges et al., 2012; Joswiak et al., 2017). Five refractory-rich CAI-like particles were all found in type B tracks (Joswiak et al., 2017).

The presence of chondrule fragments and CAIs indicates that these refractory materials were present both in the inner Solar System regions where asteroids accreted, and in the outer regions where comets formed, as discussed in section 4.4.5. It is difficult to model a high temperature process in the outer Solar System that could have made a range of material so similar in composition to chondrules formed in the inner Solar System (Westphal et al., 2017). Thus, the presence of chondrule fragments in comet Wild 2 strengthens the evidence for models of large-scale mixing in the early Solar System.

5.4.2 Fe-Ni metal and sulphides

Four slices of Tg2 from track #81 contain numerous nanophase Fe, Ni metal beads with Fe sulphide rims ($\text{Fe}_{50-89}\text{Ni}_{3-9}\text{S}_{1-46}$), similar to compositions in tracks previously studied (Leroux, Rietmeijer, et al., 2008; Joswiak et al., 2012).

Laboratory experiments firing pyrrhotite grains into aerogel, similar to the *Stardust* capture process, demonstrated that sulfide-metal beads formed in silicate glass (Ishii et al., 2008). These sulfide-metal beads resemble GEMS-like objects, making it hard to definitively identify GEMS in *Stardust*, as the beads may just be an affect of capture heating (Stodolna et al., 2012). Further work, investigating fine-grained GEMS-like material thought to have been shielded by a larger terminal particle, also concluded the material was likely created by the effects of deceleration and heating in the aerogel (Ishii, 2018).

CR, CV, CO chondrites have up to 8 vol% Fe and Ni metal, whereas CI, CM and CK chondrites have less than 0.1 vol% Fe and Ni metal (Krot et al., 2009). Fe-Ni metal has been observed here in the two *Stardust* terminal grains of track 81, and terminal grain 2 of track #153 contains Cr-rich Fe-Ni metal. Fe or Fe-Ni metal was also seen in terminal grains 1 and 2 of track #176 studied previously at the *Diamond Light Source* (Hicks,

2015). This provides further evidence for CR, CV and CO chondrites being closer analogues for *Stardust* than the other types of carbonaceous chondrites.

5.4.3 Limitations and future investigations

As more *Stardust* tracks have been analysed, it has become apparent that further information is needed for the elemental compositions of chondrite matrix, micrometeorites and silicates in IDPs, in order to have high quality data sets available to compare with the wide range of materials seen in the comet grains (Zolensky et al., 2008).. More TEM work on chondrite matrix is needed as it is too fine-grained for microprobe analyses to be useful (Zolensky et al., 2008).

The lack of any textural evidence for the *Stardust* grains prevents any textural comparisons with chondrule or IDPs. Although the *Stardust* mission represents a huge step forward in collecting the first samples of pristine cometary material and showing the heterogeneous nature of comet Wild 2, the next generation of asteroid sample return missions will hopefully successfully return samples collected in-situ. This will remove the difficulties associated with distinguishing between capture heating effects due to the high speed impact into aerogel, and original material.

6 CONCLUSIONS

This chapter discusses the key results obtained from the techniques employed, as set out in the earlier chapters, together with suggestions for future work. Advancements in techniques and instrumentation for sample analysis are reviewed. The future for planetary material analysis is reviewed in the context of present and future meteorite discoveries and space missions that will lead to new discoveries in planetary science.

6.1 Thermal history of martian meteorites

The analysis of the martian breccia described in Chapter 3 shows the power of using a variety of complementary techniques to analyse small valuable samples, enabling a large amount of information to be obtained.

The work in this thesis has provided constraints on the formation conditions of this breccia, Northwest Africa (NWA) 8114, near an impact crater on Mars. The combination of transmission electron microscopy with synchrotron X-ray absorption spectroscopy (XAS) confirmed that clasts showing the partial breakdown of pyroxene, into a potassium-bearing feldspathic glassy material and iron oxide, were also partially oxidised, $\sim 20\% \text{ Fe}^{3+} / \Sigma\text{Fe}$. Subsequent Fourier transform infrared spectroscopy (FTIR) investigations indicated that these clasts were anhydrous. Compared with shock oxidation experiments, this suggests the pyroxenes experienced temperatures above 700 °C for at least 7 days. This temperature could have occurred at a burial depth in the regolith of over five metres. The lack of alteration detected with the range of techniques

used, together with the general absence of hydration seen with FTIR, suggests the breccia did not experience significant hydrothermal alteration on Mars.

Synchrotron X-ray diffraction (XRD) and FTIR allowed the precise determination of an iron oxide to be goethite. Different iron oxides and iron hydroxides are difficult to distinguish with any other technique, so this is important for mineralogists, particularly with such small extra-terrestrial samples. In this instance, the goethite is most likely to have formed due to terrestrial alteration rather than martian alteration. Following up this identification of goethite with deuterium-hydrogen analyses, using an ion microprobe or nanoscale secondary ion mass spectrometry, could resolve the origin of the water in the breccia.

A detailed trace element study would also help resolve the similarities and differences between clasts in the breccia, and which clasts may have shared a similar thermal history before compaction of the breccia.

This work will contribute towards a better understanding of this heterogeneous breccia and its thermal history. The detailed compositional study of NWA 8114 will be useful for comparisons with studies of rocks on Mars by the Mars Science Laboratory *Curiosity* rover, and for comparisons with other martian meteorites, as we continue to identify more.

6.2 Magnetite and silicates identified in comet Wild 2

XAS and XRD have been used to identify the mineralogy of further *Stardust* comet grains and compare them with carbonaceous chondrite analogue samples, extending the work of Changela et al. (2012) and Hicks (2015). Five out of seven carbonaceous chondrite terminal grains were identified, two contained magnetite and three contained olivine (Chapter 4).

Magnetite is a likely result of water-rock interaction on the comet, although other possibilities are also discussed (section 4.4.3). Finding magnetite in two out of five grains, albeit a small sample, is unexpected when magnetite comprises no more than ~1% of the original CR2 or CV3 material. This evidence suggests a density selection bias, where magnetite, a coherent high density mineral, is preferentially preserved during the capture process. If this is the case, it also implies that low density

phyllosilicates in *Stardust* grains, if present in comet Wild 2, may be preferentially destroyed during capture.

Further cometary missions are needed to understand the presence or absence of phyllosilicates in comets, and the extent to which aqueous alteration processes occur on comets and throughout the Solar System.

Chondrule-like fragments rich in feldspar and pyroxene have been observed by TEM in *Stardust* terminal grains in Chapter 5. The large range of pyroxene and olivine compositions, particularly the more iron-rich, suggest affinities with the rarer type 2 chondrules as well as type 1 chondrules being represented by the enstatite and forsterite found. A range of iron sulphide and metal beads were also found in terminal grains, indicating pyrrhotite was originally present, although capture heating effects have led to a loss and variable range of sulphur content.

This work adds to the database of characterised Wild 2 comet grains that have transformed original ideas of comets being icy bodies, and demonstrates widespread mixing must have taken place in the early Solar System. Missions to asteroids and comets in the future will help to match meteorites to parent bodies, and sample-return missions, with context, will provide further constraints on when and where planetary bodies formed, and refine possible Solar System formation models such as the Grand Tack, discussed in Chapter 4.

6.3 Advancement in sample analysis capabilities

Work is always ongoing at synchrotrons to improve and extend the capabilities offered to users. The I-18 beamline has had a number of upgrades; in early 2017 the X-ray fluorescence (XRF) mapping software was rewritten, which combined with new Xspress-3 detector readout electronics, allow for two-way scanning (Diaz-Moreno et al., 2018). This avoids the overhead of wasted time in resetting at the end of each row when mapping. Both XRF and XAS mapping are considerably faster as a result.

The hard X-ray nanoprobe I-14 beamline at *Diamond Light Source* came online for first users in March 2017. The beam size of just 50 nm with a range of 5 keV to 23 keV is optimised for XAS, XRF and XRD, and is achieved by maximising the distance between the sample and the focusing optic (~185 m), with the experiment hutch (Fig. 6.1) and control cabin in a new building. Samples can be mounted on both 3 mm

circular TEM grids and Omniprobe half grids, or on silican nitride membranes. The University of Leicester have already utilised it once in September 2018 to study further martian and other meteorite samples, as well as some grains returned from an asteroid by the *Hayabusa* mission. Studies of the martian breccia using I-14 would enable further investigation of the smallest clasts and matrix, that are not resolvable with I-18.



Fig. 6.1. The I-14 nanoprobe beamline at *Diamond Light Source* (Image: J. Piercy).

6.4 The future for planetary materials

This section discusses the future for planetary materials. Developments in the search for meteorites are noted, and a brief overview of some of the latest martian meteorite discoveries is given, together with planned future martian sample return missions. The collection and curation of interplanetary dust particle (IDP) and *Stardust* samples for future study are considered. Finally, it reviews the current active and proposed space missions to asteroids, comets and the Moon.

Many space missions have allowed remote sensing measurements of planetary bodies, including asteroids and comets, and in-situ surface measurements on the Moon and Mars. However, returning more samples for detailed laboratory analysis on Earth would greatly assist in understanding the evolution of the Solar System. Accurate compositional measurements and isotope analysis provide constraints as to where and when meteorites could have formed in the Solar System, but pristine samples from

asteroids and comets with their context are needed, to match meteorites to parent bodies.

For example, only rocks from Earth and the Moon have been dated accurately, and the Curiosity rover Sample Analysis at Mars (SAM) instrument obtained an age of 4.21 ± 0.35 Ga (K-Ar) for a mudstone in Gale crater (Farley et al., 2014). Meteorites have also been dated accurately, but apart from lunar and martian meteorites, parent bodies have not been conclusively identified. Surface ages for the outer planets and moons currently rely on crater counting techniques that use an estimate of the collision flux in the early Solar System, which is hard to constrain accurately. Returning samples with context from Mars, asteroids and further planetary bodies would allow for accurate surface dating.

6.4.1 New meteorites

Meteor tracking networks such as ‘Fireballs in the Sky’ are expanding operations from Australia to the UK, and comparable systems are resulting in many more meteorites being found as a result of witnessed falls. In the last eight months these systems have led to success in finding eight new falls globally. This is important for science because if the meteorites are found quickly, they spend minimal time on the Earth’s surface and are less likely to undergo terrestrial weathering. This is particularly important when trying to resolve whether reactions took place on a parent body or on Earth.

6.4.1.1 New discoveries of martian meteorites

Further unusual martian shergottites have been discovered in the last few years. NWA 8159 is a single 150 g stone purchased in 2013 (Ruzicka et al., 2015) and NWA 10416 is a 964.8 g stone purchased in 2015 (Bouvier et al., 2017). Both are martian because of their characteristic oxygen isotopes, Fe/Mn ratios and An-content in plagioclase. A preliminary age of 400-500 Ma (^{40}Ar - ^{39}Ar) for NWA 10416 has been suggested, similar to other shergottites (Cassata et al., 2016). NWA 8159 has a formation age of 2.37 ± 0.25 Ga (Sm-Nd; Herd et al., 2017), and could be launch-paired with NWA 7635, a 196 g martian meteorite purchased in 2012, age 2.403 ± 0.140 Ga (Sm-Nd; Lapen et al., 2017). This Amazonian older age is different to the rest of the younger shergottites (all <500 Ma) so samples a second igneous suite of rocks from Mars. Although they are classed as shergottites, NWA 10416 and NWA 8159 are far less

shocked than other shergottites. NWA 10416 has <10% and NWA 8159 has <50% of the plagioclase converted to maskelynite. Further study of NWA 10416 is being carried out at the University of Leicester.

6.4.2 Interplanetary dust particles (IDPs)

The range and distribution of compositions of interplanetary dust from all bodies in the Solar System represent a challenge to differentiate the origin of the dust between cometary, asteroidal and Kuiper belt objects. Understanding the creation, evolution and loss of IDPs will help to match particles to their source regions and parent bodies (Espy et al., 2011; National Research Council, 2011).

The stratosphere, between 30 km to 48 km, is the best region for sampling to find IDPs, as it is above the levels of contaminating dust from anthropogenic activities. DUSTER (Dust in the Upper Stratosphere Tracking Experiment and Retrieval) is a sampling device for meteoric dust 200 nm to 40 μm in size in this region (Ciucci et al., 2011; Della Corte et al., 2014). It aims to improve the efficiency of collection, to be able to cut down the length of time to collect a similar number of particles, by using pumps to sample larger volumes of air, and for the collector to operate autonomously.

Large micrometeorites (> 100 μm) have been collected from rooftops in towns, with significant numbers (500) retrieved and identified. Entering the atmosphere causes the silicate cosmic spherules to melt, and they are found as magnesian olivine, and iron-bearing olivine in glass, sometimes with Ni-rich metal sulphide beads (Genge et al., 2017).

6.4.3 *Stardust* samples

Over 95% of the *Stardust* grains returned in 2006 are available for analysis (Westphal et al., 2017). Plans are underway at the Johnson Space Center to cut keystones from all the remaining aerogel cells. Given the specialisation of both sample preparation and analysis techniques, it will take time to prepare larger numbers of terminal grains for TEM analysis, and access to synchrotrons to examine keystones continues to be competitive. However, the data set has been gradually building throughout the last decade and there is plenty of material to increase this further and answer some of the outstanding questions (Westphal et al., 2017). Some samples will be preserved for future generations of scientists and new developments in instrumentation.

Co-ordinating future studies of these grains is very important, in order to identify the best candidate particles that may help to answer key questions. For example, the lack of Al-rich, low-Mg phases has made it challenging to date the age of the cometary materials relative to CAIs, and oxygen isotope studies require high-precision analysis on small unaltered samples (Westphal et al., 2017). Further use of non-destructive synchrotron techniques for compositional analysis will be needed in order to identify possible grains that may be suitable for such analysis (Westphal et al., 2017).

6.4.4 Sample return missions

Techniques for analysing small samples will continue to be tested and improved from sample return missions.

6.4.4.1 Asteroid sample return missions

JAXA's *Hayabusa 2* is currently at type-C asteroid 162173 Ryugu (1999 JU3), thought to be similar to the parent body of the CM carbonaceous chondrite meteorites (Okada et al., 2017). As carbonaceous asteroids contain some of the most pristine materials in the Solar System, detailed spacecraft observation will provide evidence for understanding the dynamic evolution of the Solar System, including the origin of water and organic compounds (Tachibana et al., 2014).

Since its arrival in July 2018, it is carrying out an eighteen month survey. High resolution images are being taken and studied to select the best landing sites for sampling (Fig. 6.2). It will collect up to ten grams of sample from three locations and return it to Earth in December 2020. A projectile will be used each time, which impacts onto Ryugu's surface, then reflecting material will be collected by the sampler horn (SMP) and placed into one of the three chambers in the sampling container (Tsuda et al., 2013).

Two MINERVA-III (Micro Nano Experimental Robot Vehicle for Asteroid) robot rovers were successfully deployed to the surface of Ryugu on 21st September, 2018. They are designed as autonomous 'hoppers', able to move 15 metres in any direction and stay afloat for 15 minutes due to the weak gravity. The European MASCOT (Mobile Asteroid Surface Scout) 10 kg rover will free fall from about 100 metres to land on the asteroid in October 2018, and be able to jump up to 70 metres to explore

Ryugu with four scientific instruments (Ho et al., 2017). Another MINERVA-II2 rover will be deployed in 2019.

A two metre crater will be generated by a high speed impactor, deployed at an altitude of 500 metres and accelerated to 2 kms^{-1} before impact (Saiki et al., 2013). Before detonation, the Hayabusa 2 spacecraft will move away to the opposite side of the asteroid to ensure no damage is done to the spacecraft (Tsuda et al., 2013).

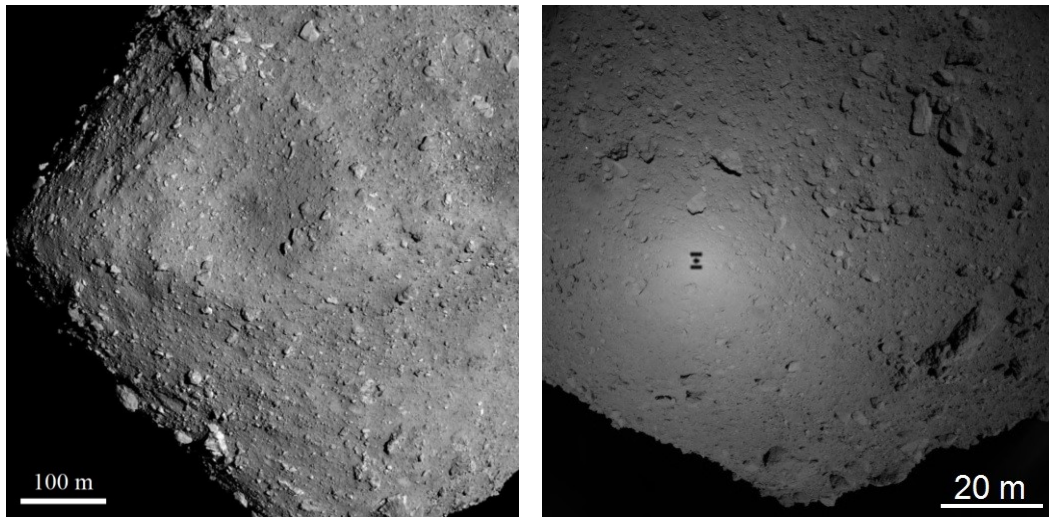


Fig. 6.2. Asteroid Ryugu from an altitude of: (A) 6 km, taken with the telescopic Optical Navigation Camera (ONCT) on 20 July 2018 by the Hayabusa 2 spacecraft, with a 6.5° field of view. (B) ~ 80 m during the Minerva II-1 lander deployment on 21 September 2018, with the shadow of the spacecraft clearly visible. Taken with the wide-angle camera (ONC-W), with a 65° field of view, with the north pole at the bottom. Credit: JAXA, University of Tokyo and collaborators.

The *OSIRIS-REx* (Origins, Spectral Interpretation, Resource Identification, Security, Regolith Explorer) NASA spacecraft will rendez-vous with asteroid 101955 Benu (1999 RQ36) in December 2018. This pristine, ~ 1 km wide, carbonaceous B-type asteroid is thought to be most similar to the parent body of the CI or CM meteorites (Clark et al., 2011). A spectral investigation found that type CI carbonaceous chondrites heated above 700°C were the closest compositional match for B-type asteroids (Clark et al., 2011).

The spacecraft will study Benu for eighteen months to allow global mapping, extensive documentation of the context of the sample site, as well as ground truth astronomical measurements collected for this asteroid and improve estimates of its future trajectory and possible impact with another body (Lauretta et al., 2017). The five science instruments include imaging cameras, an imaging LIDAR system, a thermal

emission spectrometer, a visible and near-infrared spectrometer and an X-ray emission spectrometer. A Touch and Go Sample Acquisition Mechanism (TAGSAM) will be delivered to within 25 m of the selected sample site and collect an asteroid regolith sample between 60 g and 2 kg, by releasing a jet of nitrogen gas to excite the regolith into the sample chamber (Bierhaus et al., 2018). In addition to this, there are 24 surface contact pads on the TAGSAM that will collect regolith material by trapping particles in a velcro steel hook and loop system (Snead et al., 2018). The sample canister will be put into the Sample Return Capsule (SRC), based on the *Stardust* SRC, and return it to Earth in September 2023 (Lauretta et al., 2017).

Work is underway to build new cleanrooms in both Japan and Houston, USA, for the future curation of Hayabusa 2 and OSIRIS-Rex asteroid samples (Pace et al., 2018; Yada et al., 2018). A memorandum of understanding assigns 10% of the Hayabusa 2 sample to NASA, and half a percent of the OSIRIS-REx sample to JAXA, 0.1 grams and 0.3 grams respectively, if each mission manages to collect its minimum target sample. 4% of the OSIRIS-Rex sample will be claimed by Canada in return for their contribution of a laser altimeter sensor to the mission.

Development of techniques for the characterisation, handling and storage for small particles, less than 100 microns in size, are underway at the Astromaterials Acquisition and Curation office at NASA JSC. Replica OSIRIS-REx contact pads are being tested for sample extraction, and tungsten carbide needles have been found the best at handling particles larger than 20 microns (Snead et al., 2018). Custom N₂ gloveboxes will be designed to accommodate a range of small sample processing requirements (Snead et al., 2018).

6.4.4.2 Cometary sample return mission

In December 2017, *CAESAR* (Comet Astrobiology Exploration Sample Return) was selected as one of two finalists for NASA's New Frontiers programme. This would neatly combine the legacy from the *Stardust* and *Rosetta* missions by returning a sample from comet 67P/Churyumov–Gerasimenko, with a “touch and go” sample collection mechanism similar to OSIRIS-REx (Fig. 6.3). The wealth of scientific context, from the *Rosetta* mission having already visited the comet, would increase the chance of mission success. *CAESAR* aims to launch by 2025 and return a 100 g sample to Earth in 2038, 100,000 times more than returned from *Stardust*. The mission hopes

to protect the sample from alteration and collect it at ambient temperatures, to avoid the heat-capture effects seen in the *Stardust* samples (Glavin et al., 2018).



Fig. 6.3. *CAESAR* mission concept (Credit: NASA)

6.4.4.3 *Martian sample return missions*

Following on from the ongoing successful Mars Science Laboratory ‘Curiosity’ rover mission, NASA’s Mars 2020 rover will be based on the same design. As well as looking for evidence past habitable conditions on Mars, it will seek for signs of past microbial life and test new technology to extract oxygen from the carbon-dioxide rich martian atmosphere. The Mars 2020 rover will have a drill to collect core samples of rocks and soils, and cache up to 32 samples for eventual future return to Earth. Two further missions will be required, one to launch the samples from the surface of Mars into orbit around Mars, and a second mission to collect the samples from orbit and bring them home.

JAXA’s *Martian Moons eXploration* (MMX) mission aims to launch in 2024, characterise the two martian moons, Phobos and Deimos, and return a sample of Phobos to Earth in 2029. The mission aims to understand the origin and evolution of the satellites. If they contain lots of volatiles, they are more likely to be primordial captured asteroids, but if they are dry they are more likely to have formed from a large impact event on Mars that ejected enough material to form moons.

6.4.4.4 *Lunar sample return*

The Moon is thought to have been formed in a collision between Earth and a Mars-sized body, Theia (Cameron & Benz, 1991). It is suggested that Theia must have

formed between Earth and Mars, between 1.16 A.U. and 1.20 A.U. to have remained in a stable orbit for 70 to 110 Ma prior to the collision (Dvorak et al., 2017; Halliday, 2008). Dynamical models suggest that the Moon should be made of 70% to 90% Theia and only 10% to 30% Earth material (Canup & Asphaug, 2001; Cameron & Benz, 1991). The identical nature of stable isotopes and compositions between the Earth and the Moon today, suggest that Theia must have formed at a similar distance to the Sun as the Earth (Wiechert et al., 2001). Although this was originally considered unlikely, Melosh et al. (2018) suggest that the idea of gaps in the protoplanetary disk discussed in Chapter 4 (Desch et al., 2018; Kruijer et al., 2017; Budde, Burkhardt, et al., 2018) may be quite common, as observations of exoplanet systems sometimes show up to four planets appearing to form at the same distance from their sun. This could explain that Theia and Earth forming in nearly the same orbit may not be as unlikely as initially thought (Melosh et al., 2018).

The Chang'e 5 Chinese lunar exploration mission plans to land on the Moon in 2019 and return a sample from Mons Rümker in Oceanus Procellarum. It will dig two metres below the surface for a 1.3 Ga basalt, younger than Apollo samples returned previously.

A sample return mission to the South Pole Aitken Basin on the Moon was submitted to NASA's Discovery program in 2000 (Duke, 2003). An initial proposal to return a one kilogram sample of regolith fines and rock fragments would test the hypothesis for lunar differentiation of a lunar magma ocean, and test whether the Moon experienced a strong peak in bombardment by meteorites at ~3.9 Ga, the 'lunar terminal cataclysm' (Tera 1973,74) or if it may be a result of sampling bias. Lunar meteorites do not show this peak, which suggests the terminal cataclysm was not a short interval (Michael et al., 2018). NASA's Decadal survey agreed the importance of a sample return mission to this location in order to determine the age of the oldest and largest basin on the Moon (National Research Council, 2011). Studies from 2008 to 2012 that mapped the best locations for every scientific goal culminated in a report of scientifically rich landing sites (Kring & Durda, 2012) and a database where *ArcGIS* map layers can be utilised (CLSE, 2018).

6.4.5 Asteroid and comet missions

Space missions can greatly enhance our understanding of asteroids and comets by visiting them and provide detailed information that can prove or disprove theories about possible parent bodies of meteorites that have been studied. NASA's Discovery programme is building two spacecraft that will improve understanding and knowledge of asteroids and help constrain possible parent bodies of meteorite samples in our collections.

Lucy will launch in 2021, flyby a main belt asteroid in 2025, then will conduct flybys of six Jupiter Trojan asteroids between 2027 and 2033 (Levison et al., 2017). *Lucy* will be mapping the surface geology and composition, determining interior properties and determining the properties of any satellites or rings. There are three different spectral types (C, D and P) of Trojan asteroids, P and D types are thought similar to icy bodies in the Kuiper Belt and C-types are in the outer main belt of asteroids. Thus the Trojan asteroids likely formed at different locations and were mixed together by planet formation and migration. By visiting at least two examples of each type, this mission hopes to provide further evidence towards answering priority questions in NASA's Decadal Survey (National Research Council, 2011), such as where did primordial organic matter originate, how did the giant planets accrete and did they migrate, what were the processes and conditions of Solar System formation and what influence did impacting projectiles have (Levison et al., 2017).

After a 2023 launch, NASA's *Psyche* orbiter will arrive at a unique giant metal asteroid, 16 Psyche, 210 km in diameter, in 2030 (Fig. 6.4). Asteroid Psyche, made of iron and nickel, is thought to be either the core of a planetesimal that was once molten, or possibly metal-rich materials that accreted but never melted in the early Solar System (Elkins-Tanton, 2018). Models suggest that collisions in the early Solar System could remove the silicate mantle from a differentiated body, which is the leading formation theory for Psyche. This mission potentially offers the first glimpse of a differentiated iron core that should help us better understand the Earth and terrestrial planets, and will shed light on the process of differentiation in the early Solar System (Elkins-Tanton, 2018).



Fig. 6.4. Artists's concept of the *Psyche* spacecraft at the metal asteroid. Image: SSL/ASU/P. Rubin/NASA/JPL-Caltech

In July 2018, ESA issued a call for a Fast (F) mission, to be a co-passenger to the *Ariel* or *Plato* medium sized (M) missions, specifically mentioning Near-Earth Objects or main belt comets as possible targets. This may give a renewed opportunity to the *Castalia* mission, unselected at previous M4 and M5 calls, which aimed to visit a main belt comet. Main belt comets are icy bodies between Mars and Jupiter in the main asteroid belt that could be remnants of a population that supplied the early Earth with water. *Castalia* would characterise a comet in the asteroid belt and perform the first in situ measurements of water (Snodgrass et al., 2017).

APPENDIX A: PUBLICATIONS LIST

PEER REVIEWED JOURNALS

In press:

MacArthur J.L., Bridges J. C., Hicks L.J., Burgess R., Joy K.H., Branney M.J., Hansford G.M., Baker S.H., Schwenzer S.P., Gurman S.J., Stephen N.R, Steer E.D, Piercy J.D. and Ireland T.R. (2018) Mineralogical Constraints on the Thermal History of Martian Regolith Breccia Northwest Africa 8114. *Geochimica et Cosmochimica Acta*.

<https://doi.org/10.1016/j.gca.2018.11.026>

Published:

Hicks L. J., MacArthur J.L., Bridges J.C., Price M.C., Wickham-Eade J.E., Burchell M.J., Hansford G.M, Butterworth A.L., Gurman S.J. and Baker S.H. (2017) Magnetite in Comet Wild 2: Evidence for parent body aqueous alteration. *Meteoritics & Planetary Science* Vol 52 No.10 pp. 2075-2096.

<https://onlinelibrary.wiley.com/doi/abs/10.1111/maps.12909>

Wickham-Eade J.E., Burchell M.J., Price M.C., Hicks L.J., MacArthur J.L. and Bridges J.C. (2017) Raman identification of olivine grains in fine grained mineral assemblages fired into aerogel. *Procedia Engineering*, 204, pp. 413-420.

<https://doi.org/10.1016/j.proeng.2017.09.796>

CONFERENCE ABSTRACTS

Wiley Award for outstanding student presentation: MacArthur J.L., Bridges J.C., Hicks L.J., Burgess R., Joy K.H., Branney M.J. and Piercy J.D. (2018) Constraining the thermal history of martian breccia Northwest Africa 8114. *81st Annual Meteoritical Society Meeting*, Abstract #6330.

<https://www.hou.usra.edu/meetings/metsoc2018/pdf/6330.pdf>

MacArthur J.L., Hicks L.J., Bridges J.C., Price M.C., Wickham-Eade J.E., Burchell M.J., Hansford G.M and Butterworth A.L. (2018) Comparing aqueous alteration in

comet Wild 2 and carbonaceous chondrites. *81st Annual Meteoritical Society Meeting*, Abstract #6342.

<https://www.hou.usra.edu/meetings/metsoc2018/pdf/6342.pdf>

MacArthur J.L., Bridges J.C., Hicks L.J., Price M.C., Wickham-Eade J.E., Burchell M.J., Hansford G.M and Butterworth A.L. (2017) Carbonaceous chondrites as an analogue for Stardust comet grains. *80th Annual Meteoritical Society Meeting*, Abstract #6011.

<https://www.hou.usra.edu/meetings/metsoc2017/pdf/6011.pdf>

MacArthur J.L., Bridges J.C., Hicks L.J., Branney M.J., Hansford G.M. and Steer E.D. (2017) Thermal history of Northwest Africa 8114, *80th Annual Meteoritical Society Meeting*, Abstract #6108.

<https://www.hou.usra.edu/meetings/metsoc2017/pdf/6108.pdf>

MacArthur J.L., Bridges J.C., Hicks L.J. (2017) The thermal and alteration history of martian regolith breccia. NWA 8114, *MMC 2017*.

MacArthur J.L., Bridges J.C., Branney M.J. (2017) Clastic meteorite from Mars: petrological and textural insights. *Joint Assembly TSG-VMSG-BGA*.

MacArthur J.L., Bridges J.C., Hicks L.J., Hansford G.M. and Paget L. (2016) Goethite in Northwest Africa 8114. *Extraterrestrial Materials Meeting 2016*.

Hicks L.J., Bridges J.C., MacArthur J.L., Baker S. (2016) Using microfocus spectroscopy and FTIR to investigate planetary materials. *Diamond SR User Meeting*.

MacArthur J.L., Bridges J.C., Hicks L.J., Hansford G.M. and Paget L. (2016) Goethite in Northwest Africa 8114. *79th Annual Meteoritical Society Meeting* Abstract #6020.

<https://www.hou.usra.edu/meetings/metsoc2016/pdf/6020.pdf>

Hicks L.J., Bridges J.C., MacArthur J.L., Wickham-Eade J.E., Price M.C., Burchell M.J., Butterworth A.L. and Baker S.H. (2016) Analogues for Wild2: carbonaceous chondrites shot into aerogel. *79th Annual Meteoritical Society Meeting*, Abstract #6428.

<https://www.hou.usra.edu/meetings/metsoc2016/pdf/6428.pdf>

MacArthur J.L., Bridges J.C., Hicks L.J., Paget L., Burgess R., Joy K.H. (2016) Water and the evolution of NWA 8114 Martian Regolith. *National Astronomy Meeting*.

MacArthur J.L., Bridges J.C., Hicks L.J., Burgess R. and Joy K.H. (2016) Water and the Formation of the Northwest Africa 8114 Martian Regolith. *47th Lunar and Planetary Science Conference*, Abstract #2916.

<https://www.hou.usra.edu/meetings/lpsc2016/pdf/2916.pdf>

MacArthur J.L., Bridges J.C., Hicks L.J., Price M.C., Burchell M.J., Franchi I.A. and Gurman S.J. (2015) Magnetite in Stardust Terminal Grains: Evidence for Hydrous Alteration in the Wild2 Parent Body. *Royal Society "The origin, history and role of water in the evolution of the inner Solar System" meeting*.

Bridges J.C., MacArthur J.L., Hicks L.J., Price M.C., Burchell M.J. and Wozniakiewicz P.J. (2015) Magnetite in Stardust Terminal Grains: Hydrous Alteration of the Wild2 Parent Body. *RAS General Discussion Meeting*.

MacArthur J.L., Bridges J.C., Hicks L.J., Burgess R. and Joy K.H. (2015) The alteration history of a martian impact regolith NWA 8114. *Astrobiology Society of Britain 6th biennial conference, Natural History Museum Barwell meeting*.

Bridges J.C., MacArthur J.L., Hicks L.J., Burgess R. and Joy K. (2015) Alteration of a martian impact regolith recorded in NWA 8114. *78th Annual Meteoritical Society Meeting*, Abstract #5284.

<https://www.hou.usra.edu/meetings/metsoc2015/pdf/5284.pdf>

Bridges J.C., Hicks L.J., MacArthur J.L., Price M.C., Burchell M.J., Franchi I.A., and Gurman S.J. (2015) Magnetite in Stardust Terminal Grains: Evidence for Hydrous Alteration in the Wild2 Parent Body. *European Planetary Science Congress*.

<http://meetingorganizer.copernicus.org/EPSC2015/EPSC2015-866-1.pdf>

MacArthur J.L., Bridges J.C., Hicks L.J. and Gurman S.J. (2015) The thermal and alteration history of NWA 8114 martian regolith. *4th UK in Aurora Programme meeting*.

MacArthur J.L., Bridges J.C., Hicks L.J. and Gurman S.J. (2015) The thermal and alteration history of NWA 8114 martian regolith. *46th Lunar and Planetary Science Conference*, Abstract #2295.

Price M.C., Bridges J.C., MacArthur J.L., and Hicks L.J. (2015) Carbonaceous and magnetite-bearing Stardust cometary grains from tracks 187, 188, 189, 190. *46th Lunar and Planetary Science Conference*, Abstract #2000.

<https://www.hou.usra.edu/meetings/lpsc2015/pdf/2000.pdf>

MacArthur J.L. Bridges J.C., Hicks L.J. and Gurman S.J. (2015) The thermal and alteration history of NWA 8114 martian regolith. *Early Career Scientists' Meeting*.

MacArthur J.L. and Bridges J.C. (2014) Clast classification in martian meteorite NWA 7034/NWA 8114. *Early Career Scientists' Meeting, Comparative Planetology Meeting, MPSE Warsaw, UCL CPS Summer Meeting*.

BIBLIOGRAPHY

- Abramov, O. & Kring, D.A. (2005) Impact-induced hydrothermal activity on early Mars. *Journal of Geophysical Research: Planets*, 110 (E12), p.E12S09.
- Abreu, N.M. & Brearley, A.J. (2010) Early solar system processes recorded in the matrices of two highly pristine CR3 carbonaceous chondrites, MET 00426 and QUE 99177. *Geochimica et Cosmochimica Acta*, 74 (3), pp.1146–1171.
- Agee, C.B., Muttik, N., Ziegler, K., McCubbin, F.M., Herd, C.D.K., Rochette, P. & Gattacceca, J. (2014) Discovery of a new martian meteorite type: augite basalt - NWA 8159. *LPSC XLV*, Abstract #2036.
- Agee, C.B., Wilson, N.V., McCubbin, F.M., Ziegler, K., Polyak, V.J., Sharp, Z.D., Asmerom, Y., Nunn, M.H., Shaheen, R., Thiemens, M.H., Steele, A., Fogel, M.L., Bowden, R., Glamoclija, M., Zhang, Z. & Elardo, S.M. (2013) Unique Meteorite from Early Amazonian Mars: Water-Rich Basaltic Breccia Northwest Africa 7034. *Science*, 339 (6121), pp.780–785.
- A'Hearn, M.F., Belton, M.J.S., Delamere, W.A., Feaga, L.M., Hampton, D., Kissel, J., Klaasen, K.P., McFadden, L.A., Meech, K.J., Melosh, H.J., Schultz, P.H., Sunshine, J.M., Thomas, P.C., Veverka, J., Wellnitz, D.D., Yeomans, D.K., Besse, S., Bodewits, D., Bowling, T.J., Carcich, B.T., Collins, S.M., Farnham, T.L., Groussin, O., Hermalyn, B., Kelley, M.S., Kelley, M.S., Li, J.-Y., Lindler, D.J., Lisse, C.M., McLaughlin, S.A., Merlin, F., Protopapa, S., Richardson, J.E. & Williams, J.L. (2011) EPOXI at Comet Hartley 2. *Science*, 332 (6036), pp.1396–1400.
- A'Hearn, M.F. & Combi, M.R. (2007) Deep Impact at Comet Tempel 1. *Icarus*, 187 (1), pp.1–3.
- Alexander, C.M.O., Bowden, R., Fogel, M.L., Howard, K.T., Herd, C.D.K. & Nittler, L.R. (2012) The Provenances of Asteroids, and Their Contributions to the Volatile Inventories of the Terrestrial Planets. *Science*, 337 (6095), pp.721–723.
- Altwegg, K., Balsiger, H., Bar-Nun, A., Berthelier, J.J., Bieler, A., Bochsler, P., Briois, C., Calmonte, U., Combi, M., Keyser, J.D., Eberhardt, P., Fiethe, B., Fuselier, S., Gasc, S., Gombosi, T.I., Hansen, K.C., Hässig, M., Jäckel, A., Kopp, E., Korth, A., LeRoy, L., Mall, U., Marty, B., Mousis, O., Neefs, E., Owen, T., Rème, H., Rubin, M., Sémon, T., Tzou, C.-Y., Waite, H. & Wurz, P. (2014) 67P/Churyumov-Gerasimenko, a Jupiter family comet with a high D/H ratio. *Science*, 347 (6220), p.1261952.
- Anderson, J.D., Lau, E.L., Bird, M.K., Asmar, S.W., Clark, B.C., Giampieri, G., Gilliland, K.V. & Pätzold, M. (2004) Stardust dynamic science at comet 81P/Wild 2. *Journal of Geophysical Research: Planets*, 109 (E12). Available from: <<https://agupubs.onlinelibrary.wiley.com/doi/full/10.1029/2004JE002323>> [Accessed 24 March 2018].
- Aoudjehane, H.C., Avice, G., Barrat, J.-A., Boudouma, O., Chen, G., Duke, M.J.M., Franchi, I.A., Gattacceca, J., Grady, M.M., Greenwood, R.C., Herd, C.D.K., Hewins, R., Jambon, A., Marty, B., Rochette, P., Smith, C.L., Sautter, V., Verchovsky, A.,

- Weber, P. & Zanda, B. (2012) Tissint Martian Meteorite: A Fresh Look at the Interior, Surface, and Atmosphere of Mars. *Science*, 338 (6108), pp.785–788.
- Asphaug, E., Jutzi, M. & Movshovitz, N. (2011) Chondrule formation during planetesimal accretion. *Earth and Planetary Science Letters*, 308 (3), pp.369–379.
- Babeyko, A.Y. & Zharkov, V.N. (2000) Martian crust: a modeling approach. *Physics of the Earth and Planetary Interiors*, 117 (1), pp.421–435.
- Balsiger, H., Altwegg, K., Bühler, F., Geiss, J., Ghielmetti, A.G., Goldstein, B.E., Goldstein, R., Huntress, W.T., Ip, W.-H., Lazarus, A.J., Meier, A., Neugebauer, M., Rettenmund, U., Rosenbauer, H., Schwenn, R., Sharp, R.D., Shelley, E.G., Ungstrup, E. & Young, D.T. (1986) Ion composition and dynamics at comet Halley. *Nature*, 321 (6067s), pp.330–334.
- Barrat, J.A., Jambon, A., Ferrière, L., Bollinger, C., Langlade, J.A., Liorzou, C., Boudouma, O. & Fialin, M. (2014) No Martian soil component in shergottite meteorites. *Geochimica et Cosmochimica Acta*, 125, pp.23–33.
- Basham, M., Filik, J., Wharmby, M.T., Chang, P.C.Y., El Kassaby, B., Gerring, M., Aishima, J., Levik, K., Pulford, B.C.A., Sikharulidze, I., Sneddon, D., Webber, M., Dhesi, S.S., Maccherozzi, F., Svensson, O., Brockhauser, S., Náray, G. & Ashton, A.W. (2015) Data Analysis Workbench (DAWN). *Journal of Synchrotron Radiation*, 22 (Pt 3), pp.853–858.
- Bassan, P., Byrne, H.J., Bonnier, F., Lee, J., Dumas, P. & Gardner, P. (2009) Resonant Mie scattering in infrared spectroscopy of biological materials – understanding the ‘dispersion artefact’. *Analyst*, 134 (8), pp.1586–1593.
- Beck, P., Pommerol, A., Zanda, B., Remusat, L., Lorand, J.P., Göpel, C., Hewins, R., Pont, S., Lewin, E., Quirico, E., Schmitt, B., Montes-Hernandez, G., Garenne, A., Bonal, L., Proux, O., Hazemann, J.L. & Chevrier, V.F. (2015) A Noachian source region for the “Black Beauty” meteorite, and a source lithology for Mars surface hydrated dust? *Earth and Planetary Science Letters*, 427, pp.104–111.
- Becker, R.H. & Pepin, R.O. (1984) The case for a martian origin of the shergottites: nitrogen and noble gases in EETA 79001. *Earth and Planetary Science Letters*, 69 (2), pp.225–242.
- Bellucci, J.J., Nemchin, A.A., Whitehouse, M.J., Humayun, M., Hewins, R. & Zanda, B. (2015) Pb-isotopic evidence for an early, enriched crust on Mars. *Earth and Planetary Science Letters*, 410, pp.34–41.
- Berger, E.L., Zega, T.J., Keller, L.P. & Lauretta, D.S. (2011) Evidence for aqueous activity on comet 81P/Wild 2 from sulfide mineral assemblages in Stardust samples and CI chondrites. *Geochimica et Cosmochimica Acta*, 75 (12), pp.3501–3513.
- Bibring, J.-P., Langevin, Y., Mustard, J.F., Poulet, F., Arvidson, Raymond, Gendrin, A., Gondet, B., Mangold, N., Pinet, P., Forget, F., Berthé, M., Bibring, J.-P., Gendrin, A., Gomez, C., Gondet, B., Jouglet, D., Poulet, F., Soufflot, A., Vincendon, M., Combes, M., Drossart, P., Encrenaz, T., Fouchet, T., Merchiorri, R., Belluci, G.,

- Altieri, F., Formisano, V., Capaccioni, F., Cerroni, P., Coradini, A., Fonti, S., Korablev, O., Kottsov, V., Ignatiev, N., Moroz, V., Titov, D., Zasova, L., Loiseau, D., Mangold, N., Pinet, Patrick, Douté, S., Schmitt, B., Sotin, C., Hauber, E., Hoffmann, H., Jaumann, R., Keller, U., Arvidson, Ray, Mustard, J.F., Duxbury, T., Forget, François & Neukum, G. (2006) Global Mineralogical and Aqueous Mars History Derived from OMEGA/Mars Express Data. *Science*, 312 (5772), pp.400–404.
- Bieler, A., Altwegg, K., Balsiger, H., Bar-Nun, A., Berthelier, J.-J., Bochsler, P., Briois, C., Calmonte, U., Combi, M., Keyser, J.D., Dishoeck, E.F. van, Fiethe, B., Fuselier, S.A., Gasc, S., Gombosi, T.I., Hansen, K.C., Hässig, M., Jäckel, A., Kopp, E., Korth, A., Roy, L.L., Mall, U., Maggiolo, R., Marty, B., Mousis, O., Owen, T., Rème, H., Rubin, M., Sémon, T., Tzou, C.-Y., Waite, J.H., Walsh, C. & Wurz, P. (2015) Abundant molecular oxygen in the coma of comet 67P/Churyumov–Gerasimenko. *Nature*, 526 (7575), pp.678–681.
- Bierhaus, E.B., Clark, B.C., Harris, J.W., Payne, K.S., Dubisher, R.D., Wurts, D.W., Hund, R.A., Kuhns, R.M., Linn, T.M., Wood, J.L., May, A.J., Dworkin, J.P., Beshore, E., Lauretta, D.S. & the OSIRIS-REx Team (2018) The OSIRIS-REx Spacecraft and the Touch-and-Go Sample Acquisition Mechanism (TAGSAM). *Space Science Reviews*, 214 (7), p.107.
- Binns, R.A. (1967) Stony Meteorites bearing Maskelynite. *Nature*, 213 (5081), pp.1111–1112.
- Biver, N., Bockelée-Morvan, D., Moreno, R., Crovisier, J., Colom, P., Lis, D.C., Sandqvist, A., Boissier, J., Despois, D. & Milam, S.N. (2015) Ethyl alcohol and sugar in comet C/2014 Q2 (Lovejoy). *Science Advances*, 1 (9), p.e1500863.
- Bland, P.A., Cressey, G. & Menzies, O.N. (2004) Modal mineralogy of carbonaceous chondrites by X-ray diffraction and Mössbauer spectroscopy. *Meteoritics & Planetary Science*, 39 (1), pp.3–16.
- Bland, P.A., Jackson, M.D., Coker, R.F., Cohen, B.A., Webber, J.B.W., Lee, M.R., Duffy, C.M., Chater, R.J., Ardakani, M.G., McPhail, D.S., McComb, D.W. & Benedix, G.K. (2009) Why aqueous alteration in asteroids was isochemical: High porosity≠high permeability. *Earth and Planetary Science Letters*, 287 (3), pp.559–568.
- Bland, P.A. & Travis, B.J. (2017) Giant convecting mud balls of the early solar system. *Science Advances*, 3 (7), p.e1602514.
- Bland, P.A., Zolensky, M.E., Benedix, G.K. & Sephton, M.A. (2006) Weathering of Chondritic Meteorites. In: *Meteorites and the Early Solar System II*. pp.853–867. Available from: <<http://adsabs.harvard.edu/abs/2006mess.book..853B>>.
- Blume, W.H. (2005) Deep Impact Mission Design. *Space Science Reviews*, 117 (1–2), pp.23–42.
- Bogard, D. (1995) Impact ages of meteorites: A synthesis. *Meteoritics*, 30, p.244.
- Bogard, D.D. & Johnson, P. (1983) Martian Gases in an Antarctic Meteorite? *Science*, 221 (4611), pp.651–654.

- Boice, D.C., Soderblom, L.A., Britt, D.T., Brown, R.H., Sandel, B.R., Yelle, R.V., Buratti, B.J., Hicks, Nelson, Rayman, Oberst, J. & Thomas, N. (2000) The Deep Space 1 Encounter with Comet 19p/Borrelly. *Earth, Moon, and Planets*, 89 (1–4), pp.301–324.
- Bonner, O.D. & Curry, J.D. (1970) Infrared spectra of liquid H₂O and D₂O. *Infrared Physics*, 10 (2), pp.91–94.
- Bouvier, A., Gattacceca, J., Agee, C., Grossman, J. & Metzler, K. (2017) The Meteoritical Bulletin, No. 104. *Meteoritics & Planetary Science*, 52 (10), pp.2284–2284.
- Bouvier, L.C., Costa, M.M., Connelly, J.N., Jensen, N.K., Wielandt, D., Storey, M., Nemchin, A.A., Whitehouse, M.J., Snape, J.F., Bellucci, J.J., Moynier, F., Agranier, A., Gueguen, B., Schönbachler, M. & Bizzarro, M. (2018) Evidence for extremely rapid magma ocean crystallization and crust formation on Mars. *Nature*, 558 (7711), pp.586–589.
- Boynton, W.V., Starzyk, P.M. & Schmitt, R.A. (1976) Chemical evidence for the genesis of the ureilites, the achondrite Chassigny and the nakhlites. *Geochimica et Cosmochimica Acta*, 40 (12), pp.1439–1447.
- Branney, M.J. & Brown, R.J. (2011) Impactoclastic Density Current Emplacement of Terrestrial Meteorite-Impact Ejecta and the Formation of Dust Pellets and Accretionary Lapilli: Evidence from Stac Fada, Scotland. *The Journal of Geology*, 119 (3), pp.275–292.
- Brearley, A.J. (2006) The action of water. In: *Meteorites and the Early Solar System II*. The University of Arizona Press, pp.587–624. Available from: <<https://uapress.arizona.edu/book/meteorites-and-the-early-solar-system-ii>> [Accessed 10 April 2018].
- Brearley, A.J. & Jones, R.H. (1998) Chondritic meteorites. In: *In Planetary materials, edited by Papike J. J., Reviews in Mineralogy*. Mineralogical Society of America, pp.3.1-3.398. Available from: <<http://ring.geoscienceworld.org/content/36/1/3.1>> [Accessed 23 September 2016].
- Bridges, J.C., Burchell, M.J., Changela, H.C., Foster, N.J., Creighton, J.A., Carpenter, J.D., Gurman, S.J., Franchi, I.A. & Busemann, H. (2010) Iron oxides in comet 81P/Wild 2. *Meteoritics & Planetary Science*, 45 (1), pp.55–72.
- Bridges, J.C., Catling, D.C., Saxton, J.M., Swindle, T.D., Lyon, I.C. & Grady, M.M. (2001) Alteration Assemblages in Martian Meteorites: Implications for Near-Surface Processes. *Space Science Reviews*, 96 (1–4), pp.365–392.
- Bridges, J.C., Changela, H.G., Nayakshin, S., Starkey, N.A. & Franchi, I.A. (2012) Chondrule fragments from Comet Wild2: Evidence for high temperature processing in the outer Solar System. *Earth and Planetary Science Letters*, 341–344, pp.186–194.

- Bridges, J.C., Franchi, I.A., Hutchison, R., Sexton, A.S. & Pillinger, C.T. (1998) Correlated mineralogy, chemical compositions, oxygen isotopic compositions and size of chondrules. *Earth and Planetary Science Letters*, 155 (3), pp.183–196.
- Bridges, J.C. & Grady, M.M. (2000) Evaporite mineral assemblages in the nakhlite (martian) meteorites. *Earth and Planetary Science Letters*, 176 (3–4), pp.267–279.
- Bridges, J.C. & Warren, P.H. (2006) The SNC meteorites: basaltic igneous processes on Mars. *Journal of the Geological Society*, 163 (2), pp.229–251.
- Brown, R.J., Branney, M.J., Maher, C. & Dávila-Harris, P. (2010) Origin of accretionary lapilli within ground-hugging density currents: Evidence from pyroclastic couplets on Tenerife. *Geological Society of America Bulletin*, 122 (1–2), pp.305–320.
- Brownlee, D., Joswiak, D. & Matrajt, G. (2012) Overview of the rocky component of Wild 2 comet samples: Insight into the early solar system, relationship with meteoritic materials and the differences between comets and asteroids. *Meteoritics & Planetary Science*, 47 (4), pp.453–470.
- Brownlee, D., Tsou, P., Aléon, J., Alexander, C.M.O., Araki, T., Bajt, S., Baratta, G.A., Bastien, R., Bland, P., Bleuët, P., Borg, J., Bradley, J.P., Brearley, A., Brenker, F., Brennan, S., Bridges, J.C., Browning, N.D., Brucato, J.R., Bullock, E., Burchell, M.J., Busemann, H., Butterworth, A., Chaussidon, M., Chevront, A., Chi, M., Cintala, M.J., Clark, B.C., Clemett, S.J., Cody, G., Colangeli, L., Cooper, G., Cordier, P., Daghlian, C., Dai, Z., D’Hendecourt, L., Djouadi, Z., Dominguez, G., Duxbury, T., Dworkin, J.P., Ebel, D.S., Economou, T.E., Fakra, S., Fairey, S.A.J., Fallon, S., Ferrini, G., Ferroir, T., Fleckenstein, H., Floss, C., Flynn, G., Franchi, I.A., Fries, M., Gainsforth, Z., Gallien, J.-P., Genge, M., Gilles, M.K., Gillet, P., Gilmour, J., Glavin, D.P., Gounelle, M., Grady, M.M., Graham, G.A., Grant, P.G., Green, S.F., Grossemy, F., Grossman, L., Grossman, J.N., Guan, Y., Hagiya, K., Harvey, R., Heck, P., Herzog, G.F., Hoppe, P., Hörz, F., Huth, J., Hutcheon, I.D., Ignatyev, K., Ishii, H., Ito, M., Jacob, D., Jacobsen, C., Jacobsen, S., Jones, S., Joswiak, D., Jurewicz, A., Kearsley, A.T., Keller, L.P., Khodja, H., Kilcoyne, A.L.D., Kissel, J., Krot, A., Langenhorst, F., Lanzirrotti, A., Le, L., Leshin, L.A., Leitner, J., Lemelle, L., Leroux, H., Liu, M.-C., Luening, K., Lyon, I., MacPherson, G., Marcus, M.A., Marhas, K., Marty, B., Matrajt, G., McKeegan, K., Meibom, A., Mennella, V., Messenger, K., Messenger, S., Mikouchi, T., Mostefaoui, S., Nakamura, T., Nakano, T., Newville, M., Nittler, L.R., Ohnishi, I., Ohsumi, K., Okudaira, K., Papanastassiou, D.A., Palma, R., Palumbo, M.E., Pepin, R.O., Perkins, D., Perronnet, M., Pianetta, P., Rao, W., Rietmeijer, F.J.M., Robert, F., Rost, D., Rotundi, A., Ryan, R., Sandford, S.A., Schwandt, C.S., See, T.H., Schlutter, D., Sheffield-Parker, J., Simionovici, A., Simon, S., Sitnitsky, I., Snead, C.J., Spencer, M.K., Stadermann, F.J., Steele, A., Stephan, T., Stroud, R., Susini, J., Sutton, S.R., Suzuki, Y., Taheri, M., Taylor, S., Teslich, N., Tomeoka, K., Tomioka, N., Toppani, A., Trigo-Rodríguez, J.M., Troadec, D., Tsuchiyama, A., Tuzzolino, A.J., Tylliszczak, T., Uesugi, K., Velbel, M., Vellenga, J., Vicenzi, E., Vincze, L., Warren, J., Weber, I., Weisberg, M., Westphal, A.J., Wirick, S., Wooden, D., Wopenka, B., Wozniakiewicz, P., Wright, I., Yabuta, H., Yano, H., Young, E.D., Zare, R.N., Zega, T., Ziegler, K., Zimmerman, L., Zinner, E. & Zolensky, M. (2006) Comet 81P/Wild 2 Under a Microscope. *Science*, 314 (5806), pp.1711–1716.

- Brownlee, D.E. (1979) Interplanetary dust. *Reviews of Geophysics*, 17 (7), pp.1735–1743.
- Brownlee, D.E., Horz, F., Newburn, R.L., Zolensky, M., Duxbury, T.C., Sandford, S., Sekanina, Z., Tsou, P., Hanner, M.S., Clark, B.C., Green, S.F. & Kissel, J. (2004) Surface of Young Jupiter Family Comet 81P/Wild 2: View from the Stardust Spacecraft. *Science*, 304 (5678), pp.1764–1769.
- Brownlee, D.E., Joswiak, D., Matrajt, G., Ramien, N., Bradley, J., Ishii, H., Westphal, A.J. & Gainforth, Z. (2010) The Nature of Moderately Fragmenting Comet Dust: Case Studies of Tracks 25 (Inti) and Track 77. In: p.2146. Available from: <<http://adsabs.harvard.edu/abs/2010LPI...41.2146B>> [Accessed 20 September 2016].
- Brownlee, D.E., Tsou, P., Anderson, J.D., Hanner, M.S., Newburn, R.L., Sekanina, Z., Clark, B.C., Hörz, F., Zolensky, M.E., Kissel, J., McDonnell, J. a. M., Sandford, S.A. & Tuzzolino, A.J. (2003) Stardust: Comet and interstellar dust sample return mission. *Journal of Geophysical Research: Planets*, 108 (E10), p.8111.
- Bruker (2011) OPUS version 7.0 Spectroscopic Software Reference Manual. Available from: <ftp://ftp.gps.caltech.edu/pub/tccon/tccon_manuals_and_documentation/IFS125/OPUS_Manual.pdf> [Accessed 14 May 2018].
- Budde, G., Burkhardt, C., Brennecka, G.A., Fischer-Gödde, M., Kruijer, T.S. & Kleine, T. (2016) Molybdenum isotopic evidence for the origin of chondrules and a distinct genetic heritage of carbonaceous and non-carbonaceous meteorites. *Earth and Planetary Science Letters*, 454, pp.293–303.
- Budde, G., Burkhardt, C. & Kleine, T. (2018) Early Solar System dynamics inferred from molybdenum isotope anomalies in meteorites. In: 2353.
- Budde, G., Kruijer, T.S. & Kleine, T. (2018) Hf-W chronology of CR chondrites: Implications for the timescales of chondrule formation and the distribution of ²⁶Al in the solar nebula. *Geochimica et Cosmochimica Acta*, 222, pp.284–304.
- Burchell, M.J., Cole, M.J., McDonnell, J.A.M. & Zarnecki, J.C. (1999) Hypervelocity impact studies using the 2 MV Van de Graaff accelerator and two-stage light gas gun of the University of Kent at Canterbury. *Measurement Science and Technology*, 10 (1), p.41.
- Burchell, M.J., Fairey, S. a. J., Wozniakiewicz, P., Brownlee, D.E., Hörz, F., Kearsley, A.T., See, T.H., Tsou, P., Westphal, A., Green, S.F., Trigo-Rodríguez, J.M. & Domínguez, G. (2008) Characteristics of cometary dust tracks in Stardust aerogel and laboratory calibrations. *Meteoritics & Planetary Science*, 43 (1–2), pp.23–40.
- Burchell, Mark J., Graham, G. & Kearsley, A. (2006) Cosmic Dust Collection in Aerogel. *Annual Review of Earth and Planetary Sciences*, 34 (1), pp.385–418.
- Burchell, M. J., Mann, J., Creighton, J.A., Kearsley, A.T., Graham, G. & Franchi, I.A. (2006) Identification of minerals and meteoritic materials via Raman techniques after

- capture in hypervelocity impacts on aerogel. *Meteoritics & Planetary Science*, 41 (2), pp.217–232.
- Burkhardt, C., Kleine, T., Oberli, F., Pack, A., Bourdon, B. & Wieler, R. (2011) Molybdenum isotope anomalies in meteorites: Constraints on solar nebula evolution and origin of the Earth. *Earth and Planetary Science Letters*, 312 (3), pp.390–400.
- Calas, G., Petiau, J. & Manceau, A. (1986) X-ray absorption spectroscopy of geological materials. *Journal de Physique Colloques*, 47 (C8), pp.C8-813-C8-818.
- Calvin, S. (2013) *XAFS for Everyone*. 1 edition. Boca Raton, CRC Press.
- Cameron, A.G.W. & Benz, W. (1991) The origin of the moon and the single impact hypothesis IV. *Icarus*, 92 (2), pp.204–216.
- Canup, R.M. & Asphaug, E. (2001) Origin of the Moon in a giant impact near the end of the Earth's formation. *Nature*, 412 (6848), pp.708–712.
- Carr, M.H. (2007) *The Surface of Mars*. Cambridge University Press.
- Cartwright, J.A., Gilmour, J.D. & Burgess, R. (2013) Martian fluid and Martian weathering signatures identified in Nakhla, NWA 998 and MIL 03346 by halogen and noble gas analysis. *Geochimica et Cosmochimica Acta*, 105, pp.255–293.
- Cartwright, J.A., Ott, U., Herrmann, S. & Agee, C.B. (2014) Modern atmospheric signatures in 4.4 Ga Martian meteorite NWA 7034. *Earth and Planetary Science Letters*, 400, pp.77–87.
- Cassata, W.S. & Borg, L.E. (2016) A new approach to cosmogenic corrections in $^{40}\text{Ar}/^{39}\text{Ar}$ chronometry: Implications for the ages of Martian meteorites. *Geochimica et Cosmochimica Acta*, 187, pp.279–293.
- Cassata, W.S., Cohen, B.E., Mark, D.F., Trappitsch, R., Crow, C.A., Wimpenny, J., Lee, M.R. & Smith, C.L. (2018) Chronology of martian breccia NWA 7034 and the formation of the martian crustal dichotomy. *Science Advances*, 4 (5), p.eaap8306.
- Cassata, W.S., Hilton, C., Borg, L. & Agee, C.B. (2016) Noble Gas Systematics of Martian Meteorite Northwest Africa 10416. In: *Goldschmidt Conference Abstracts*. Available from: <<https://goldschmidtabstracts.info/abstracts/abstractView?id=2016002689>> [Accessed 13 September 2018].
- Castaing, R. (1951) *Application des sondes électroniques à une méthode d'analyse ponctuelle chimique et cristallographique*.
- Changela, H.G. (2011) Electron and X-ray Microanalysis of Planetary Materials: from Comet 81P/Wild2 to the Surface of Mars. Thesis. University of Leicester. Available from: <<https://lra.le.ac.uk/handle/2381/9378>>.

- Changela, H.G. & Bridges, J.C. (2010) Alteration assemblages in the nakhlites: Variation with depth on Mars. *Meteoritics & Planetary Science*, 45 (12), pp.1847–1867.
- Changela, H.G., Bridges, J.C. & Gurman, S.J. (2012) Extended X-ray Absorption Fine Structure (EXAFS) in Stardust tracks: Constraining the origin of ferric iron-bearing minerals. *Geochimica et Cosmochimica Acta*, 98, pp.282–294.
- Cherniak, D.J., Lanford, W.A. & Ryerson, F.J. (1991) Lead diffusion in apatite and zircon using ion implantation and Rutherford Backscattering techniques. *Geochimica et Cosmochimica Acta*, 55 (6), pp.1663–1673.
- Christiansen, E.L. & Friesen, L. (1997) Penetration equations for thermal protection materials. *International Journal of Impact Engineering*, 20 (1), pp.153–164.
- Ciesla, F.J. (2010) The distributions and ages of refractory objects in the solar nebula. *Icarus*, 208 (1), pp.455–467.
- Cinque, G., Frogley, M.D. & Bartolini, R. (2011) Far-IR/THz spectral characterization of the coherent synchrotron radiation emission at diamond IR beamline B22. *Rendiconti Lincei*, 22 (1), pp.33–47.
- Ciucci, A., Palumbo, P., Brunetto, R., Della Corte, V., De Angelis, S., Rotundi, A., Rietmeijer, F.J.M., Zona, E., Colangeli, L., Esposito, F., Mazzotta Epifani, E., Mennella, V., Inarta, S., Peterzen, S., Masi, S. & Ibba, R. (2011) DUSTER (Dust in the Upper Stratosphere Tracking Experiment and Retrieval) . PRELIMINARY ANALYSIS. *Memorie della Societa Astronomica Italiana Supplementi*, 16, p.119.
- Clark, B.C., Mason, L.W. & Kissel, J. (1987) Systematics of the CHON and Other Light Element Particle Populations in Comet p/ Halley. *Astronomy and Astrophysics*, 187, p.779.
- Clark, B.E., Binzel, R.P., Howell, E.S., Cloutis, E.A., Ockert-Bell, M., Christensen, P., Barucci, M.A., DeMeo, F., Lauretta, D.S., Connolly, H., Soderberg, A., Hergenrother, C., Lim, L., Emery, J. & Mueller, M. (2011) Asteroid (101955) 1999 RQ36: Spectroscopy from 0.4 to 2.4 μ m and meteorite analogs. *Icarus*, 216 (2), pp.462–475.
- Cliff, G. & Lorimer, G.W. (1975) The quantitative analysis of thin specimens. *Journal of Microscopy*, 103 (2), pp.203–207.
- CLSE (2018) South Pole – Aitken Basin Landing Site Database [Internet]. Available from: https://www.lpi.usra.edu/exploration/SPA_Basin_Landing_Site_DB/ [Accessed 27 September 2018].
- Combes, M., Moroz, V.I., Crifo, J.F., Lamarre, J.M., Charra, J., Sanko, N.F., Soufflot, A., Bibring, J.P., Cazes, S., Coron, N., Crovisier, J., Emerich, C., Encrenaz, T., Gispert, R., Grigoryev, A.V., Guyot, G., Krasnopolsky, V.A., Nikolsky, Y.V. & Rocard, F. (1986) Infrared sounding of comet Halley from VEGA 1. *Nature*, 321, pp.266–268.
- Connolly, H.C. & Jones, R.H. (2016) Chondrules: The canonical and noncanonical views. *Journal of Geophysical Research: Planets*, 121 (10), pp.1885–1899.

- Cornell, R.M. & Schwertmann, U. (2003) *The Iron Oxides: Structure, Properties, Reactions, Occurrences and Uses*. John Wiley & Sons.
- De Gregorio, B.T., Stroud, R.M., Nittler, L.R. & Kilcoyne, A.L.D. (2017) Evidence for Reduced, Carbon-rich Regions in the Solar Nebula from an Unusual Cometary Dust Particle. *The Astrophysical Journal*, 848 (2), p.113.
- Deer, W.A., Howie, R.A. & Zussman, J. (1992) *An introduction to the rock-forming minerals*. Longman Scientific & Technical.
- Deer, W.A., Howie, R.A. & Zussman, J. (2001) *Rock-forming Minerals: Feldspars, Volume 4A*. Geological Society of London.
- Dehn, J. (1987) A unified theory of penetration. *International Journal of Impact Engineering*, 5 (1), pp.239–248.
- Della Corte, V., Rietmeijer, F.J.M., Rotundi, A. & Ferrari, M. (2014) Introducing a New Stratospheric Dust-Collecting System with Potential Use for Upper Atmospheric Microbiology Investigations. *Astrobiology*, 14 (8), pp.694–705.
- Desch, S.J., Kalyaan, A. & Alexander, C.M.O. (2018) The Effect of Jupiter's Formation on the Distribution of Refractory Elements and Inclusions in Meteorites. *The Astrophysical Journal*, (Accepted). Available from: <<http://arxiv.org/abs/1710.03809v3>>.
- Diamond (2018) Bird's eye view of the synchrotron [Internet]. Available from: <<https://www.diamond.ac.uk/Science/Machine/Components.html>> [Accessed 10 September 2018].
- Diaz-Moreno, S., Amboage, M., Basham, M., Boada, R., Bricknell, N.E., Cibin, G., Cobb, T.M., Filik, J., Freeman, A., Geraki, K., Gianolio, D., Hayama, S., Ignatyev, K., Keenan, L., Mikulska, I., Mosselmans, J.F.W., Mudd, J.J. & Parry, S.A. (2018) The Spectroscopy Village at Diamond Light Source. *Journal of Synchrotron Radiation*, 25 (4), pp.998–1009.
- Dobrică, E. & Brearley, A.J. (2011) Crystalline Silicates in Comet 81P/Wild 2 from the Stardust Track 81. *Meteoritics and Planetary Science Supplement*, 74, p.5413.
- Dobrică, E., Engrand C., Duprat J., Gounelle M., Leroux H., Quirico E. & Rouzaud J.-N. (2009) Connection between micrometeorites and Wild 2 particles: From Antarctic snow to cometary ices. *Meteoritics & Planetary Science*, 44 (10), pp.1643–1661.
- Downs, R.T. & Hall-Wallace, M. (2003) The *American Mineralogist* crystal structure database. *American Mineralogist*, 88 (1), pp.247–250.
- Doyle, P.M., Jogo, K., Nagashima, K., Krot, A.N., Wakita, S., Ciesla, F.J. & Hutcheon, I.D. (2015) Early aqueous activity on the ordinary and carbonaceous chondrite parent bodies recorded by fayalite. *Nature Communications*, 6, p.7444.
- Duke, M.B. (2003) Sample return from the lunar South Pole-Aitken Basin. *Advances in Space Research*, 31 (11), pp.2347–2352.

- Dunn, T.L., Gross, J., Ivanova, M.A., Runyon, S.E. & Bruck, A.M. (2016) Magnetite in the unequilibrated CK chondrites: Implications for metamorphism and new insights into the relationship between the CV and CK chondrites. *Meteoritics & Planetary Science*, 51 (9), pp.1701–1720.
- Duxbury, T.C., Newburn, R.L. & Brownlee, D.E. (2004) Comet 81P/Wild 2 size, shape, and orientation. *Journal of Geophysical Research: Planets*, 109 (E12), p.E12S02.
- Dvorak, R., Loibnegger, B. & Maindl, T.I. (2017) Possible origin of Theia, the Moon-forming impactor with Earth. *Astronomische Nachrichten*, 338 (4), pp.366–374.
- Ebel, D.S., Weisberg, M.K. & Beckett, J.R. (2012) Thermochemical stability of low-iron, manganese-enriched olivine in astrophysical environments. *Meteoritics & Planetary Science*, 47 (4), pp.585–593.
- Ehlmann, B.L., Mustard, J.F., Clark, R.N., Swayze, G.A. & Murchie, S.L. (2011) Evidence for Low-Grade Metamorphism, Hydrothermal Alteration, and Diagenesis on Mars from Phyllosilicate Mineral Assemblages. *Clays and Clay Minerals*, 59 (4), pp.359–377.
- Ehlmann, B.L., Mustard, J.F., Murchie, S.L., Bibring, J.-P., Meunier, A., Fraeman, A.A. & Langevin, Y. (2011) Subsurface water and clay mineral formation during the early history of Mars. *Nature*, 479 (7371), pp.53–60.
- Elkins-Tanton, L.T. (2018) Asteroid 16 Psyche: NASA's 14th Discovery Mission. *Elements*, 14 (1), pp.68–68.
- Emerich, C., Lamarre, J.M., Moroz, V.I., Combes, M., Sanko, N.F., Nikolsky, Y.V., Rocard, F., Gispert, R., Coron, N., Bibring, J.P., Encrenaz, T. & Crovisier, J. (1987) Temperature and Size of the Nucleus of Comet p/ Halley Deduced from IKS Infrared VEGA-1 Measurements. *Astronomy and Astrophysics*, 187, p.839.
- Emsley, J. (2011) *Nature's Building Blocks: An A-Z Guide to the Elements*. OUP Oxford.
- Espy, A., Blum, J. & Kehoe, T.J.J. (2011) Interplanetary Dust Community White Paper to the Planetary Science Decadal Survey , 2011-2020.
- Evans, J. (2018) *X-ray Absorption Spectroscopy for the Chemical and Materials Sciences*. John Wiley & Sons.
- Farley, K.A., Malespin, C., Mahaffy, P., Grotzinger, J.P., Vasconcelos, P.M., Milliken, R.E., Malin, M., Edgett, K.S., Pavlov, A.A., Hurowitz, J.A., Grant, J.A., Miller, H.B., Arvidson, R., Beegle, L., Calef, F., Conrad, P.G., Dietrich, W.E., Eigenbrode, J., Gellert, R., Gupta, S., Hamilton, V., Hassler, D.M., Lewis, K.W., McLennan, S.M., Ming, D., Navarro-González, R., Schwenzer, S.P., Steele, A., Stolper, E.M., Sumner, D.Y., Vaniman, D., Vasavada, A., Williford, K., Wimmer-Schweingruber, R.F., Blake, D.F., Bristow, T., DesMarais, D., Edwards, L., Haberle, R., Hoehler, T., Hollingsworth, J., Kahre, M., Keely, L., McKay, C., Wilhelm, M.B., Bleacher, L., Brinckerhoff, W., Choi, D., Dworkin, J.P., Floyd, M., Freissinet, C., Garvin, J., Glavin, D., Harpold, D.,

Martin, D.K., McAdam, A., Raaen, E., Smith, M.D., Stern, J., Tan, F., Trainer, M., Meyer, M., Posner, A., Voytek, M., Anderson, R.C., Aubrey, A., Behar, A., Blaney, D., Brinza, D., Christensen, L., Crisp, J.A., DeFlores, L., Feldman, J., Feldman, S., Flesch, G., Hurowitz, J., Jun, I., Keymeulen, D., Maki, J., Mischna, M., Morookian, J.M., Parker, T., Pavri, B., Schoppers, M., Sengstacken, A., Simmonds, J.J., Spanovich, N., Juarez, M. de la T., Webster, C.R., Yen, A., Archer, P.D., Cucinotta, F., Jones, J.H., Morris, R.V., Niles, P., Rampe, E., Nolan, T., Fisk, M., Radziemski, L., Barraclough, B., Bender, S., Berman, D., Dobreá, E.N., Tokar, R., Williams, R.M.E., Yingst, A., Leshin, L., Cleghorn, T., Huntress, W., Manhès, G., Hudgins, J., Olson, T., Stewart, N., Sarrazin, P., Vicenzi, E., Wilson, S.A., Bullock, M., Ehresmann, B., Peterson, J., Rafkin, S., Zeitlin, C., Fedosov, F., Golovin, D., Karpushkina, N., Kozyrev, A., Litvak, M., Malakhov, A., Mitrofanov, I., Mokrousov, M., Nikiforov, S., Prokhorov, V., Sanin, A., Tretyakov, V., Varenikov, A., Vostrukhin, A., Kuzmin, R., Clark, B., Wolff, M., Botta, O., Drake, D., Bean, K., Lemmon, M., Anderson, R.B., Herkenhoff, K., Lee, E.M., Sucharski, R., Hernández, M.Á. de P., Ávalos, J.J.B., Ramos, M., Kim, M.-H., Plante, I., Muller, J.-P., Ewing, R., Boynton, W., Downs, R., Fitzgibbon, M., Harshman, K., Morrison, S., Kortmann, O., Palucis, M., Williams, A., Lugmair, G., Wilson, M.A., Rubin, D., Jakosky, B., Balic-Zunic, T., Frydenvang, J., Jensen, J.K., Kinch, K., Koefoed, A., Madsen, M.B., Stipp, S.L.S., Boyd, N., Campbell, J.L., Perrett, G., Pradler, I., VanBommel, S., Jacob, S., Owen, T., Rowland, S., Savijärvi, H., Boehm, E., Böttcher, S., Burmeister, S., Guo, J., Köhler, J., García, C.M., Mueller-Mellin, R., Bridges, J.C., McConnochie, T., Benna, M., Franz, H., Bower, H., Brunner, A., Blau, H., Boucher, T., Carmosino, M., Atreya, S., Elliott, H., Halleaux, D., Rennó, N., Wong, M., Pepin, R., Elliott, B., Spray, J., Thompson, L., Gordon, S., Newsom, H., Ollila, A., Williams, J., Bentz, J., Nealson, K., Popa, R., Kah, L.C., Moersch, J., Tate, C., Day, M., Kocurek, G., Hallet, B., Sletten, R., Francis, R., McCullough, E., Cloutis, E., Kate, I.L. ten, Kuzmin, R., Fraeman, A., Scholes, D., Slavney, S., Stein, T., Ward, J., Berger, J. & Moores, J.E. (2014) In Situ Radiometric and Exposure Age Dating of the Martian Surface. *Science*, 343 (6169), p.1247166.

Fellers, T.J. & Davidson, M.W. (2014) Introduction to Micrometry. Available from: <<http://www.microscopyu.com/articles/formulas/measurements.html>> [Accessed 25 August 2014].

Floss, C., Stadermann, F.J., Kearsley, A.T., Burchell, M.J. & Ong, W.J. (2013) The Abundance of Presolar Grains in Comet 81P/Wild 2. *The Astrophysical Journal*, 763 (2), p.140.

Flynn, G.J., Bleuet, P., Borg, J., Bradley, J.P., Brenker, F.E., Brennan, S., Bridges, J., Brownlee, D.E., Bullock, E.S., Burghammer, M., Clark, B.C., Dai, Z.R., Daghlian, C.P., Djouadi, Z., Fakra, S., Ferroir, T., Floss, C., Franchi, I.A., Gainsforth, Z., Gallien, J.-P., Gillet, P., Grant, P.G., Graham, G.A., Green, S.F., Grossemy, F., Heck, P.R., Herzog, G.F., Hoppe, P., Hörz, F., Huth, J., Ignatyev, K., Ishii, H.A., Janssens, K., Joswiak, D., Kearsley, A.T., Khodja, H., Lanzirrotti, A., Leitner, J., Lemelle, L., Leroux, H., Luening, K., MacPherson, G.J., Marhas, K.K., Marcus, M.A., Matrajt, G., Nakamura, T., Nakamura-Messenger, K., Nakano, T., Newville, M., Papanastassiou, D.A., Pianetta, P., Rao, W., Riekel, C., Rietmeijer, F.J.M., Rost, D., Schwandt, C.S., See, T.H., Sheffield-Parker, J., Simionovici, A., Sitnitsky, I., Snead, C.J., Stadermann, F.J., Stephan, T., Stroud, R.M., Susini, J., Suzuki, Y., Sutton, S.R., Taylor, S., Teslich, N., Troadec, D., Tsou, P., Tsuchiyama, A., Uesugi, K., Vekemans, B., Vicenzi, E.P.,

- Vincze, L., Westphal, A.J., Wozniakiewicz, P., Zinner, E. & Zolensky, M.E. (2006) Elemental Compositions of Comet 81P/Wild 2 Samples Collected by Stardust. *Science*, 314 (5806), pp.1731–1735.
- Frank, D.R., Zolensky, M.E. & Le, L. (2014) Olivine in terminal particles of Stardust aerogel tracks and analogous grains in chondrite matrix. *Geochimica et Cosmochimica Acta*, 142, pp.240–259.
- Friel, J.J. (2003) *X-ray and image analysis in electron microscopy*. 2nd ed. Princeton, NJ, Princeton Gamma-Tech. Available from: <<http://www.berkeley-nucleonics.com/resources/MicroscopyBook.pdf>>.
- Fries, M., Burchell, M., Kearsley, A. & Steele, A. (2009) Capture effects in carbonaceous material: A Stardust analogue study. *Meteoritics & Planetary Science*, 44 (10), pp.1465–1474.
- Fujiwara, A., Kawaguchi, J., Yeomans, D.K., Abe, M., Mukai, T., Okada, T., Saito, J., Yano, H., Yoshikawa, M., Scheeres, D.J., Barnouin-Jha, O., Cheng, A.F., Demura, H., Gaskell, R.W., Hirata, N., Ikeda, H., Kominato, T., Miyamoto, H., Nakamura, A.M., Nakamura, R., Sasaki, S. & Uesugi, K. (2006) The Rubble-Pile Asteroid Itokawa as Observed by Hayabusa. *Science*, 312 (5778), pp.1330–1334.
- Fulle, M., Altobelli, N., Buratti, B., Choukroun, M., Fulchignoni, M., Grün, E., Taylor, M.G.G.T. & Weissman, P. (2016) Unexpected and significant findings in comet 67P/Churyumov-Gerasimenko: an interdisciplinary view. *Monthly Notices of the Royal Astronomical Society*, 462, pp.S2–S8.
- Gaffey, M.J., Burbine, T.H. & Binzel, R.P. (1993) Asteroid spectroscopy: Progress and perspectives. *Meteoritics & Planetary Science*, 28 (2), pp.161–187.
- Gainsforth, Z., Butterworth, A.L., Stodolna, J., Westphal, A.J., Huss, G.R., Nagashima, K., Oglione, R., Brownlee, D.E., Joswiak, D., Tyliszczak, T. & Simionovici, A.S. (2015) Constraints on the formation environment of two chondrule-like igneous particles from comet 81P/Wild 2. *Meteoritics & Planetary Science*, 50 (5), pp.976–1004.
- Gattacceca, J., Rochette, P., Scorzelli, R.B., Munayco, P., Agee, C., Quesnel, Y., Cournède, C. & Geissman, J. (2014) Martian meteorites and Martian magnetic anomalies: A new perspective from NWA 7034. *Geophysical Research Letters*, 41 (14), p.2014GL060464.
- Geiger, T. & Bischoff, A. (1995) Formation of opaque minerals in CK chondrites. *Planetary and Space Science*, 43 (3), pp.485–498.
- Genge, M.J., Larsen, J., Ginneken, M.V. & Suttle, M.D. (2017) An urban collection of modern-day large micrometeorites: Evidence for variations in the extraterrestrial dust flux through the Quaternary. *Geology*, 45 (2), pp.119–122.
- Germani, M.S., Bradley, J.P. & Brownlee, D.E. (1990) Automated thin-film analyses of hydrated interplanetary dust particles in the analytical electron microscope. *Earth and Planetary Science Letters*, 101 (2), pp.162–179.

- Ghosh, A. & McSween, H.Y. (1998) A Thermal Model for the Differentiation of Asteroid 4 Vesta, Based on Radiogenic Heating. *Icarus*, 134 (2), pp.187–206.
- Gilbert, J.S. & Lane, S.J. (1994) The origin of accretionary lapilli. *Bulletin of Volcanology*, 56 (5), pp.398–411.
- Glavin, D., Squyres, S. & CAESAR project team (2018) An Overview of the Comet Astrobiology Exploration Sample Return (CAESAR) New Frontiers Mission. In: *Geophysical Research Abstracts*. CO Meeting Organizer EGU2018. Available from: <<https://meetingorganizer.copernicus.org/EGU2018/sessionprogramme/PS>> [Accessed 13 September 2018].
- Golombek, M.P., Crumpler, L.S., Grant, J.A., Greeley, R., Cabrol, N.A., Parker, T.J., Rice, J.W., Ward, J.G., Arvidson, R.E., Moersch, J.E., Fergason, R.L., Christensen, P.R., Castaño, A., Castaño, R., Haldemann, A.F.C., Li, R., Bell, J.F. & Squyres, S.W. (2006) Geology of the Gusev cratered plains from the Spirit rover traverse. *Journal of Geophysical Research: Planets*, 111 (E2), p.E02S07.
- Gooding, J.L. (1992) Soil mineralogy and chemistry on Mars: Possible clues from salts and clays in SNC meteorites. *Icarus*, 99 (1), pp.28–41.
- Gooding, J.L. (1986) Weathering of stony meteorites in Antarctica. Available from: <<http://adsabs.harvard.edu/abs/1986anme.work...48G>>.
- Gooding, J.L., Zolensky, M.E. & Wentworth, S.J. (1991) Aqueous alteration of the Nakhla meteorite. *Meteoritics*, 26, pp.135–143.
- Goossens, S., Sabaka, T.J., Genova, A., Mazarico, E., Nicholas, J.B. & Neumann, G.A. (2017) Evidence for a low bulk crustal density for Mars from gravity and topography. *Geophysical Research Letters*, 44 (15), p.2017GL074172.
- Gotić, M. & Musić, S. (2007) Mössbauer, FT-IR and FE SEM investigation of iron oxides precipitated from FeSO₄ solutions. *Journal of Molecular Structure*, 834–836, pp.445–453.
- Graup, G. (1981) Terrestrial chondrules, glass spherules and accretionary lapilli from the suevite, Ries Crater, Germany. *Earth and Planetary Science Letters*, 55 (3), pp.407–418.
- Greenwood, R.C., Franchi, I.A., Kearsley, A.T. & Alard, O. (2010) The relationship between CK and CV chondrites. *Geochimica et Cosmochimica Acta*, 74 (5), pp.1684–1705.
- Gualtieri, A.F. & Venturelli, P. (1999) In situ study of the goethite-hematite phase transformation by real time synchrotron powder diffraction. *American Mineralogist*, 84 (5–6), pp.895–904.
- Gulick, S.P.S., Barton, P.J., Christeson, G.L., Morgan, J.V., McDonald, M., Mendoza-Cervantes, K., Pearson, Z.F., Surendra, A., Urrutia-Fucugauchi, J., Vermeesch, P.M. & Warner, M.R. (2008) Importance of pre-impact crustal structure for the asymmetry of the Chicxulub impact crater. *Nature Geoscience*, 1 (2), p.131.

Haggerty, S.E. & Baker, I. (1967) The alteration of olivine in basaltic and associated lavas. *Contributions to Mineralogy and Petrology*, 16 (3), pp.233–257.

Hainsworth, S. (2014) ESEM and EDX System. Available from: <<http://www.le.ac.uk/engineering/svh2/esem.htm>> [Accessed 25 August 2014].

Halliday, A.N. (2008) A young Moon-forming giant impact at 70–110 million years accompanied by late-stage mixing, core formation and degassing of the Earth. *Philosophical Transactions of the Royal Society of London A: Mathematical, Physical and Engineering Sciences*, 366 (1883), pp.4163–4181.

Hansford, G.M. (2015) *Unit Cell Fit, IDL programme*.

He, Y.T. & Traina, S.J. (2007) Transformation of magnetite to goethite under alkaline pH conditions. *Clay Minerals*, 42 (1), pp.13–19.

Herd, C.D.K., Walton, E.L., Agee, C.B., Muttik, N., Ziegler, K., Shearer, C.K., Bell, A.S., Santos, A.R., Burger, P.V., Simon, J.I., Tappa, M.J., McCubbin, F.M., Gattacceca, J., Lagroix, F., Sanborn, M.E., Yin, Q.-Z., Cassata, W.S., Borg, L.E., Lindvall, R.E., Kruijer, T.S., Brennecke, G.A., Kleine, T., Nishiizumi, K. & Caffee, M.W. (2017) The Northwest Africa 8159 martian meteorite: Expanding the martian sample suite to the early Amazonian. *Geochimica et Cosmochimica Acta*, 218, pp.1–26.

Hewins, R.H., Zanda, B., Humayun, M., Nemchin, A., Lorand, J.-P., Pont, S., Deldicque, D., Bellucci, J.J., Beck, P., Leroux, H., Marinova, M., Remusat, L., Göpel, C., Lewin, E., Grange, M., Kennedy, A. & Whitehouse, M.J. (2017) Regolith breccia Northwest Africa 7533: Mineralogy and petrology with implications for early Mars. *Meteoritics & Planetary Science*, 52 (1), pp.89–124.

Hicks, L.J. (2015) X-ray spectroscopy and electron microscopy of planetary materials. Thesis. Department of Physics and Astronomy, University of Leicester. Available from: <<https://lra.le.ac.uk/handle/2381/31986>> [Accessed 11 June 2015].

Hicks, L.J., Bridges, J.C. & Gurman, S.J. (2014) Ferric saponite and serpentine in the nakhlite martian meteorites. *Geochimica et Cosmochimica Acta*, 136, pp.194–210.

Hicks, L.J., MacArthur, J.L., Bridges, J.C., Price, M.C., Wickham-Eade, J.E., Burchell, M.J., Hansford, G.M., Butterworth, A.L., Gurman, S.J. & Baker, S.H. (2017) Magnetite in Comet Wild 2: Evidence for parent body aqueous alteration. *Meteoritics & Planetary Science*, 52 (10), pp.2075–2096.

Hillier, J. & Baker, R.F. (1944) Microanalysis by Means of Electrons. *Journal of Applied Physics*, 15 (9), pp.663–675.

Ho, T.-M., Baturkin, V., Grimm, C., Grundmann, J.T., Hobbie, C., Ksenik, E., Lange, C., Sasaki, K., Schlotterer, M., Talapina, M., Termtanasombat, N., Wejmo, E., Witte, L., Wrasmann, M., Wübbels, G., Rößler, J., Ziach, C., Findlay, R., Biele, J., Krause, C., Ulamec, S., Lange, M., Mierheim, O., Lichtenheldt, R., Maier, M., Reill, J., Sedlmayr, H.-J., Bousquet, P., Bellion, A., Bompis, O., Cenac-Morthe, C., Deleuze, M., Fredon, S., Jurado, E., Canalias, E., Jaumann, R., Bibring, J.-P., Glassmeier, K.H., Hercik, D., Grott, M., Celotti, L., Cordero, F., Hendrikse, J. & Okada, T. (2017) MASCOT—The

Mobile Asteroid Surface Scout Onboard the Hayabusa2 Mission. *Space Science Reviews*, 208 (1), pp.339–374.

Hörz, F., Bastien, R., Borg, J., Bradley, J.P., Bridges, J.C., Brownlee, D.E., Burchell, M.J., Chi, M., Cintala, M.J., Dai, Z.R., Djouadi, Z., Dominguez, G., Economou, T.E., Fairey, S.A.J., Floss, C., Franchi, I.A., Graham, G.A., Green, S.F., Heck, P., Hoppe, P., Huth, J., Ishii, H., Kearsley, A.T., Kissel, J., Leitner, J., Leroux, H., Marhas, K., Messenger, K., Schwandt, C.S., See, T.H., Snead, C., Stadermann, F.J., Stephan, T., Stroud, R., Teslich, N., Trigo-Rodríguez, J.M., Tuzzolino, A.J., Troadec, D., Tsou, P., Warren, J., Westphal, A., Wozniakiewicz, P., Wright, I. & Zinner, E. (2006) Impact Features on Stardust: Implications for Comet 81P/Wild 2 Dust. *Science*, 314 (5806), pp.1716–1719.

Howard, K.T., Alexander, C.M.O., Schrader, D.L. & Dyl, K.A. (2015) Classification of hydrous meteorites (CR, CM and C2 ungrouped) by phyllosilicate fraction: PSD-XRD modal mineralogy and planetesimal environments. *Geochimica et Cosmochimica Acta*, 149, pp.206–222.

Howard, K.T., Benedix, G.K., Bland, P.A. & Cressey, G. (2010) Modal mineralogy of CV3 chondrites by X-ray diffraction (PSD-XRD). *Geochimica et Cosmochimica Acta*, 74 (17), pp.5084–5097.

Huber, M.S. & Koeberl, C. (2017) Accretionary lapilli from the Sudbury impact event. *Meteoritics & Planetary Science*, 52 (6), pp.1257–1276.

Hughes, A.L.H. & Armitage, P.J. (2010) Particle Transport in Evolving Protoplanetary Disks: Implications for Results from Stardust. *The Astrophysical Journal*, 719 (2), p.1633.

Humayun, M. (2013) A Unique Piece of Mars. *Science*, 339 (6121), pp.771–772.

Humayun, M., Nemchin, A., Zanda, B., Hewins, R.H., Grange, M., Kennedy, A., Lorand, J.-P., Göpel, C., Fieni, C., Pont, S. & Deldicque, D. (2013) Origin and age of the earliest Martian crust from meteorite NWA 7533. *Nature*, 503, pp.513–516.

Huss, G.R., Rubin, A.E. & Grossman, J.N. (2006) Thermal Metamorphism in Chondrites. In: *Meteorites and the Early Solar System II*. pp.567–586. Available from: <<http://adsabs.harvard.edu/abs/2006mess.book..567H>>.

Hutchison, R. (2004) *Meteorites: A Petrologic, Chemical and Isotopic Synthesis*. Cambridge University Press.

ICDD (2014) PDF-4/Minerals 2014 database, Int. Centre for Diffraction Data. Available from: <<http://www.icdd.com>>.

Ireland, T.R. & Williams, I.S. (2003) Considerations in Zircon Geochronology by SIMS. *Reviews in Mineralogy and Geochemistry*, 53 (1), pp.215–241.

Irving, A.J. (2018) List of Martian Meteorites [Internet]. Available from: <<http://www.imca.cc/mars/martian-meteorites-list.htm>> [Accessed 30 July 2018].

- Ishii, H.A. (2018) Comparison of GEMS in interplanetary dust particles and GEMS-like objects in a Stardust impact track in aerogel. *Meteoritics & Planetary Science*, In press (0). Available from: <<https://onlinelibrary.wiley.com/doi/abs/10.1111/maps.13182>>.
- Ishii, H.A., Bradley, J.P., Dai, Z.R., Chi, M., Kearsley, A.T., Burchell, M.J., Browning, N.D. & Molster, F. (2008) Comparison of Comet 81P/Wild 2 Dust with Interplanetary Dust from Comets. *Science*, 319 (5862), pp.447–450.
- Ivanov, B.A. (2001) Mars/Moon Cratering Rate Ratio Estimates. *Space Science Reviews*, 96 (1–4), pp.87–104.
- Jacob, D., Stodolna Julien, Leroux Hugues, Langenhorst Falko & Houdellier F. (2010) Pyroxenes microstructure in comet 81P/Wild 2 terminal Stardust particles. *Meteoritics & Planetary Science*, 44 (10), pp.1475–1488.
- Johnson, B.C. & Melosh, H.J. (2014) Formation of melt droplets, melt fragments, and accretionary impact lapilli during a hypervelocity impact. *Icarus*, 228, pp.347–363.
- Johnson, B.C., Minton, D.A., Melosh, H.J. & Zuber, M.T. (2015) Impact jetting as the origin of chondrules. *Nature*, 517 (7534), pp.339–341.
- Johnson, M.C., Rutherford, M.J. & Hess, P.C. (1991) Chassigny petrogenesis: Melt compositions, intensive parameters and water contents of Martian (?) magmas. *Geochimica et Cosmochimica Acta*, 55 (1), pp.349–366.
- Jones, R.H., Grossman, J.N. & Rubin, A.E. (2005) Chemical, Mineralogical and Isotopic Properties of Chondrules: Clues to Their Origin. In: p.251. Available from: <<http://cdsads.u-strasbg.fr/abs/2005ASPC..341..251J>> [Accessed 22 September 2018].
- Joswiak, D.J., Brownlee D. E., Nguyen A. N. & Messenger S. (2017) Refractory materials in comet samples. *Meteoritics & Planetary Science*, 52 (8), pp.1612–1648.
- Joswiak, D.J., Brownlee, D.E., Matrajt, G., Westphal, A.J. & Snead, C.J. (2009) Kosmochloric Ca-rich pyroxenes and FeO-rich olivines (Kool grains) and associated phases in Stardust tracks and chondritic porous interplanetary dust particles: Possible precursors to FeO-rich type II chondrules in ordinary chondrites. *Meteoritics & Planetary Science*, 44 (10), pp.1561–1588.
- Joswiak, D.J., Brownlee, D.E., Matrajt, G., Westphal, A.J., Snead, C.J. & Gainsforth, Z. (2012) Comprehensive examination of large mineral and rock fragments in Stardust tracks: Mineralogy, analogous extraterrestrial materials, and source regions. *Meteoritics & Planetary Science*, 47 (4), pp.471–524.
- Joswiak, D.J., Nakashima, D., Brownlee, D.E., Matrajt, G., Ushikubo, T., Kita, N.T., Messenger, S. & Ito, M. (2014) Terminal particle from Stardust track 130: Probable Al-rich chondrule fragment from comet Wild 2. *Geochimica et Cosmochimica Acta*, 144, pp.277–298.

- Kallemeyn, G.W., Rubin, A.E. & Wasson, J.T. (1994) The compositional classification of chondrites: VI. The CR carbonaceous chondrite group. *Geochimica et Cosmochimica Acta*, 58 (13), pp.2873–2888.
- Kelley, S. (2002) K-Ar and Ar-Ar Dating. *Reviews in Mineralogy and Geochemistry*, 47 (1), pp.785–818.
- King, A.J., Schofield P. F. & Russell S. S. (2017) Type 1 aqueous alteration in CM carbonaceous chondrites: Implications for the evolution of water-rich asteroids. *Meteoritics & Planetary Science*, 52 (6), pp.1197–1215.
- King, T.V.V. & King, E.A. (1981) Accretionary dark rims in unequilibrated chondrites. *Icarus*, 48 (3), pp.460–472.
- Kissel, J., Brownlee, D.E., Büchler, K., Clark, B.C., Fechtig, H., Grün, E., Hornung, K., Igenbergs, E.B., Jessberger, E.K., Krueger, F.R., Kuczera, H., McDonnell, J. a. M., Morfill, G.M., Rahe, J., Schwehm, G.H., Sekanina, Z., Utterback, N.G., Völk, H.J. & Zook, H.A. (1986) Composition of comet Halley dust particles from Giotto observations. *Nature*, 321 (6067s), pp.336–337.
- Kissel, J., Glasmachers A., Grün E., Henkel H., Höfner H., Haerendel G., von Hoerner H., Hornung K., Jessberger E. K., Krueger F. R., Möhlmann D., Greenberg J. M., Langevin Y., Silén J., Brownlee D., Clark B. C., Hanner M. S., Hoerz F., Sandford S., Sekanina Z., Tsou P., Utterback N. G., Zolensky M. E. & Heiss C. (2003) Cometary and Interstellar Dust Analyzer for comet Wild 2. *Journal of Geophysical Research: Planets*, 108 (E10). Available from: <<https://agupubs.onlinelibrary.wiley.com/doi/full/10.1029/2003JE002091>> [Accessed 20 March 2018].
- Kissel, J., Sagdeev, R.Z., Bertaux, J.L., Angarov, V.N., Audouze, J., Blamont, J.E., Büchler, K., Evlanov, E.N., Fechtig, H., Fomenkova, M.N., Hoerner, H. von, Inogamov, N.A., Khromov, V.N., Knabe, W., Krueger, F.R., Langevin, Y., Leonas, V.B., Levasseur-Regourd, A.C., Managadze, G.G., Podkolzin, S.N., Shapiro, V.D., Tabaldyev, S.R. & Zubkov, B.V. (1986) Composition of comet Halley dust particles from Vega observations. *Nature*, 321 (6067s), pp.280–282.
- Klein, C. & Philpotts, A.R. (2012) Earth Materials by Cornelis Klein [Internet]. Available from: <<https://core/books/earth-materials/1B6CFFF928CF72EAAFEAD12C4CC359C9>> [Accessed 9 September 2018].
- Kring, D.A. & Durda, D.D. (2012) *A Global Lunar Landing Site Study to Provide the Scientific Context for Exploration of the Moon*. Lunar and Planetary Institute. Available from: <<https://www.lpi.usra.edu/exploration/CLSE-landing-site-study/>> [Accessed 27 September 2018].
- Krogh, T.E., McNutt, R.H. & Davis, G.L. (1982) Two high precision U–Pb zircon ages for the Sudbury Nickel Irruptive. *Canadian Journal of Earth Sciences*, 19 (4), pp.723–728.

- Krot, A.N., Amelin, Y., Bland, P., Ciesla, F.J., Connelly, J., Davis, A.M., Huss, G.R., Hutcheon, I.D., Makide, K., Nagashima, K., Nyquist, L.E., Russell, S.S., Scott, E.R.D., Thrane, K., Yurimoto, H. & Yin, Q.-Z. (2009) Origin and chronology of chondritic components: A review. *Geochimica et Cosmochimica Acta*, 73 (17), pp.4963–4997.
- Krot, A.N., Petaev Michael I., Scott Edward R. D., Choi Byeon-Gak, Zolensky Michael E. & Keil Klaus (1998) Progressive alteration in CV3 chondrites: More evidence for asteroidal alteration. *Meteoritics & Planetary Science*, 33 (5), pp.1065–1085.
- Kruijer, T.S., Burkhardt, C., Budde, G. & Kleine, T. (2017) Age of Jupiter inferred from the distinct genetics and formation times of meteorites. *Proceedings of the National Academy of Sciences*, 114 (26), pp.6712–6716.
- Kuebler, K.E., Jolliff, B.L., Wang, A. & Haskin, L.A. (2006) Extracting olivine (Fo–Fa) compositions from Raman spectral peak positions. *Geochimica et Cosmochimica Acta*, 70 (24), pp.6201–6222.
- Kuiper, G.P. (1951) On the Origin of the Solar System. *Proceedings of the National Academy of Sciences*, 37 (1), pp.1–14.
- Lapen, T.J., Richter, M., Andreasen, R., Irving, A.J., Satkoski, A.M., Beard, B.L., Nishiizumi, K., Jull, A.J.T. & Caffee, M.W. (2017) Two billion years of magmatism recorded from a single Mars meteorite ejection site. *Science Advances*, 3 (2), p.e1600922.
- Lauretta, D.S., Balram-Knutson, S.S., Beshore, E., Boynton, W.V., Drouet d’Aubigny, C., DellaGiustina, D.N., Enos, H.L., Golish, D.R., Hergenrother, C.W., Howell, E.S., Bennett, C.A., Morton, E.T., Nolan, M.C., Rizk, B., Roper, H.L., Bartels, A.E., Bos, B.J., Dworkin, J.P., Highsmith, D.E., Lorenz, D.A., Lim, L.F., Mink, R., Moreau, M.C., Nuth, J.A., Reuter, D.C., Simon, A.A., Bierhaus, E.B., Bryan, B.H., Ballouz, R., Barnouin, O.S., Binzel, R.P., Bottke, W.F., Hamilton, V.E., Walsh, K.J., Chesley, S.R., Christensen, P.R., Clark, B.E., Connolly, H.C., Crombie, M.K., Daly, M.G., Emery, J.P., McCoy, T.J., McMahon, J.W., Scheeres, D.J., Messenger, S., Nakamura-Messenger, K., Richter, K. & Sandford, S.A. (2017) OSIRIS-REx: Sample Return from Asteroid (101955) Bennu. *Space Science Reviews*, 212 (1), pp.925–984.
- Ledlow, M.J., Zeilik, M., Burns, J.O., Gisler, G.R., Zhao, J.-H. & Baker, D.N. (1992) Subsurface emissions from Mercury - VLA radio observations at 2 and 6 centimeters. *The Astrophysical Journal*, 384, pp.640–655.
- Leng, Y. (2010) *Materials Characterization: Introduction to Microscopic and Spectroscopic Methods*. 2nd ed. John Wiley & Sons (Asia) Pte Ltd.
- Lerotic, M., Mak, R., Wirick, S., Meirer, F. & Jacobsen, C. (2014) MANTiS: a program for the analysis of X-ray spectromicroscopy data. *Journal of Synchrotron Radiation*, 21 (Pt 5), pp.1206–1212.
- Leroux, H., Jacob, D., Marinova, M., Hewins, R.H., Zanda, B., Pont, S., Lorand, J.-P. & Humayun, M. (2016) Exsolution and shock microstructures of igneous pyroxene clasts in the Northwest Africa 7533 Martian meteorite. *Meteoritics & Planetary Science*, 51 (5), pp.932–945.

- Leroux, H., Jacob, D., Stodolna, J., Nakamura-Messenger, K. & Zolensky, M.E. (2008) Igneous Ca-rich pyroxene in comet 81P/Wild 2. *American Mineralogist*, 93 (11–12), pp.1933–1936.
- Leroux, H., Rietmeijer, F.J.M., Velbel, M.A., Brearley, A.J., Jacob, D., Langenhorst, F., Bridges, J.C., Zega, T.J., Stroud, R.M., Cordier, P., Harvey, R.P., Lee, M., Gounelle, M. & Zolensky, M.E. (2008) A TEM study of thermally modified comet 81P/Wild 2 dust particles by interactions with the aerogel matrix during the Stardust capture process. *Meteoritics & Planetary Science*, 43 (1–2), pp.97–120.
- Leroux, H., Stroud Rhonda M., Dai Zu Rong, Graham Giles A., Troadec David, Bradley John P., Teslich Nick, Borg Janet, Kearsley Anton T. & Hörz Friedrich (2008) Transmission electron microscopy of cometary residues from micron-sized craters in the Stardust Al foils. *Meteoritics & Planetary Science*, 43 (1-2), pp.143–160.
- Leshin, L.A., Epstein, S. & Stolper, E.M. (1996) Hydrogen isotope geochemistry of SNC meteorites. *Geochimica et Cosmochimica Acta*, 60 (14), pp.2635–2650.
- Levison, H., Olkin, C., Noll, K. & Marchi, S. (2017) Lucy: Surveying the diversity of Trojans. *European Planetary Science Congress*, 11, pp.EPSC2017-963.
- Levison, H.F. & Duncan, M.J. (1997) From the Kuiper Belt to Jupiter-Family Comets: The Spatial Distribution of Ecliptic Comets. *Icarus*, 127 (1), pp.13–32.
- Lindsay, F.N., Delaney, J.S., Turrin, B.D., Herzog, G.F., Park, J. & Swisher, C.C. (2016) Ar Ages of Martian Meteorite Northwest Africa 7034. In: p.3013. Available from: <<http://adsabs.harvard.edu/abs/2016LPI....47.3013L>> [Accessed 5 April 2016].
- Lindsay, F.N., Turrin, B.D., Göpel, C., Herzog, G.F., Zanda, B., Hewins, R., Park, J., Delaney, J.S. & Swisher, C.C. (2014) 40Ar/39Ar Ages of Martian Meteorite NWA 7533. In: p.5383. Available from: <<http://adsabs.harvard.edu/abs/2014LPICo1800.5383L>> [Accessed 30 October 2017].
- Lindsley, D.H. & Andersen, D.J. (1983) A two-pyroxene thermometer. *Journal of Geophysical Research: Solid Earth*, 88 (S02), pp.A887–A906.
- Liu, Y., Ma, C., Beckett, J.R., Chen, Y. & Guan, Y. (2016) Rare-earth-element minerals in martian breccia meteorites NWA 7034 and 7533: Implications for fluid–rock interaction in the martian crust. *Earth and Planetary Science Letters*, 451, pp.251–262.
- Lorand, J.-P., Hewins, R.H., Remusat, L., Zanda, B., Pont, S., Leroux, H., Marinova, M., Jacob, D., Humayun, M., Nemchin, A., Grange, M., Kennedy, A. & Göpel, C. (2015) Nickeliferous pyrite tracks pervasive hydrothermal alteration in Martian regolith breccia: A study in NWA 7533. *Meteoritics & Planetary Science*, 50 (12), pp.2099–2120.
- Lorimer, G.W., Al-Salman, S.A. & Cliff, G. (1977) The quantitative analysis of thin specimens: effects of absorption, fluorescence and beam spreading. EMAG 77. In: *Institute of Physics Conference Series*. Glasgow, pp.369–372.

- LPI (2018) The Meteoritical Bulletin Database. Available from: <<http://www.lpi.usra.edu/meteor/metbull.php>>.
- LPI Luna (2018) Luna Mission [Internet]. Available from: <<https://www.lpi.usra.edu/lunar/missions/luna/>> [Accessed 30 July 2018].
- MacArthur J.L., Bridges J.C., Hicks L.J., Burgess R., Joy K.H., Branney M.J., Hansford G.M., Baker S.H., Schwenzer S.P., Gurman S.J., Stephen N.R., Steer E.D., Piercy J.D. & Ireland T.R. (In press, 2018) Mineralogical Constraints on the Thermal History of Martian Regolith Breccia Northwest Africa 8114. *Geochimica et Cosmochimica Acta*. <https://doi.org/10.1016/j.gca.2018.11.026>
- Mahaffy, P.R., Webster, C.R., Atreya, S.K., Franz, H., Wong, M., Conrad, P.G., Harpold, D., Jones, J.J., Leshin, L.A., Manning, H., Owen, T., Pepin, R.O., Squyres, S., Trainer, M. & Team, M.S. (2013) Abundance and Isotopic Composition of Gases in the Martian Atmosphere from the Curiosity Rover. *Science*, 341 (6143), pp.263–266.
- Mangold, N., Carter, J., Poulet, F., Dehouck, E., Ansan, V. & Loizeau, D. (2012) Late Hesperian aqueous alteration at Majuro crater, Mars. *Planetary and Space Science*, 72 (1), pp.18–30.
- Mangold, N., Kite, E.S., Kleinhans, M.G., Newsom, H., Ansan, V., Hauber, E., Kraal, E., Quantin, C. & Tanaka, K. (2012) The origin and timing of fluvial activity at Eberswalde crater, Mars. *Icarus*, 220 (2), pp.530–551.
- Marty, B., Alexander, C.M.O. & Raymond, S.N. (2013) Primordial Origins of Earth's Carbon. *Reviews in Mineralogy and Geochemistry*, 75 (1), pp.149–181.
- Marzo, G.A., Davila, A.F., Tornabene, L.L., Dohm, J.M., Fairén, A.G., Gross, C., Kneissl, T., Bishop, J.L., Roush, T.L. & McKay, C.P. (2010) Evidence for Hesperian impact-induced hydrothermalism on Mars. *Icarus*, 208 (2), pp.667–683.
- Mason, B., Nelen, J.A., Muir, P. & Taylor, S.R. (1976) The composition of the Chassigny meteorite. *Meteoritics*, 11, pp.21–27.
- Matrajt, G. & Brownlee, D.E. (2006) Acrylic embedding of Stardust particles encased in aerogel. *Meteoritics & Planetary Science*, 41 (11), pp.1715–1720.
- Matrajt, G., Wirick, S., Ito, M., Messenger, S., Brownlee, D. & Joswiak, D. (2007) Carbon Investigation of Stardust Particles: A TEM, NanoSIMS and XANES Study. In: p.1201. Available from: <<http://adsabs.harvard.edu/abs/2007LPI....38.1201M>> [Accessed 26 September 2016].
- Matzel, J.E.P., Ishii, H.A., Joswiak, D., Hutcheon, I.D., Bradley, J.P., Brownlee, D., Weber, P.K., Teslich, N., Matrajt, G., McKeegan, K.D. & MacPherson, G.J. (2010) Constraints on the Formation Age of Cometary Material from the NASA Stardust Mission. *Science*, 328 (5977), pp.483–486.
- McCall, G.J.H., Bowden, A.J. & Howarth, R.J. (2006) *The History of Meteoritics and Key Meteorite Collections: Fireballs, Falls and Finds*. Geological Society of London.

- McCanta, M.C. & Dyar, M.D. (2017) Impact-related thermal effects on the redox state of Ca-pyroxene. *Meteoritics & Planetary Science*, 52 (2), pp.320–332.
- McCubbin, F.M., Boyce, J.W., Novák-Szabó, T., Santos, A.R., Tartèse, R., Muttik, N., Domokos, G., Vazquez, J., Keller, L.P., Moser, D.E., Jerolmack, D.J., Shearer, C.K., Steele, A., Elardo, S.M., Rahman, Z., Anand, M., Delhaye, T. & Agee, C.B. (2016) Geologic history of Martian regolith breccia Northwest Africa 7034: Evidence for hydrothermal activity and lithologic diversity in the Martian crust. *Journal of Geophysical Research: Planets*, p.2016JE005143.
- McDougall, I., Dougall, I.M., McDougall, P. of G.I., Harrison, T.M., Harrison, C. in E.M.M. & Harrison, P. of G.D. of E. and S.S.T.M. (1999) *Geochronology and Thermochronology by the $^{40}\text{Ar}/^{39}\text{Ar}$ Method*. Oxford University Press.
- McGetchin, T.R., Settle, M. & Head, J.W. (1973) Radial thickness variation in impact crater ejecta: implications for lunar basin deposits. *Earth and Planetary Science Letters*, 20 (2), pp.226–236.
- McKay, D.S., Jr., E.K.G., Thomas-Keprta, K.L., Vali, H., Romanek, C.S., Clemett, S.J., Chillier, X.D.F., Maechling, C.R. & Zare, R.N. (1996) Search for Past Life on Mars: Possible Relic Biogenic Activity in Martian Meteorite ALH84001. *Science*, 273 (5277), pp.924–930.
- Mckay, D.S. & Morrison, D.A. (1971) Lunar breccias. *Journal of Geophysical Research*, 76 (23), pp.5658–5669.
- McKeegan, K.D., Kallio, A.P.A., Heber, V.S., Jarzebinski, G., Mao, P.H., Coath, C.D., Kunihiro, T., Wiens, R.C., Nordholt, J.E., Moses, R.W., Reisenfeld, D.B., Jurewicz, A.J.G. & Burnett, D.S. (2011) The Oxygen Isotopic Composition of the Sun Inferred from Captured Solar Wind. *Science*, 332 (6037), pp.1528–1532.
- McMillan, E.M. (1945) The Synchrotron---A Proposed High Energy Particle Accelerator. *Physical Review*, 68 (5–6), pp.143–144.
- McSween, H.Y. (1979) Are carbonaceous chondrites primitive or processed? A review. *Reviews of Geophysics*, 17 (5), pp.1059–1078.
- McSween, H.Y. (2013) Planetary science: A chunk of ancient Mars. *Nature*, 503 (7477), pp.473–474.
- McSween, H.Y. (1985) SNC meteorites: Clues to Martian petrologic evolution? *Reviews of Geophysics*, 23 (4), pp.391–416.
- McSween, H.Y., Jr. (1994) What we have learned about Mars from SNC meteorites. *Meteoritics*, 29, pp.757–779.
- McSween, H.Y., Jr. & Stolper, E. (1980) Basaltic Meteorites. *Scientific American*, 242 (6), pp.54–63.
- McSween Jr., H.Y. & Treiman, A.H. (1998) Martian meteorites. In: *In Planetary materials, edited by Papike J. J., Reviews in Mineralogy*. Washington, D.C.,

Mineralogical Society of America. Available from: <<http://repository.si.edu/handle/10088/20542>> [Accessed 25 May 2018].

McSwiggen, P.L., Morey, G.B. & Cleland, J.M. (1994) Occurrence and genetic implications of hyalophane in manganese-rich iron-formation, Cuyuna Iron Range, Minnesota, USA. *Mineralogical Magazine*, 58 (392), pp.387–399.

Melosh, H.J. (2011) Regoliths, weathering, and surface texture. In: *Planetary Surface Processes*. Cambridge University Press, pp.276–310.

Melosh, H.J., Bland, P.A., Collins, G.S., Johnson, B.C., Minton, D.A., Caffee, M. & Bae, J. (2018) Chondrite Origins in Nebular Fiefdoms of the Early Solar System. In: p.1673. Available from: <<http://adsabs.harvard.edu/abs/2018LPI...49.1673M>> [Accessed 23 September 2018].

Merk, R., Breuer, D. & Spohn, T. (2002) Numerical Modeling of ²⁶Al-Induced Radioactive Melting of Asteroids Considering Accretion. *Icarus*, 159 (1), pp.183–191.

Michael, G., Basilevsky, A. & Neukum, G. (2018) On the history of the early meteoritic bombardment of the Moon: Was there a terminal lunar cataclysm? *Icarus*, 302, pp.80–103.

Ming, D.W., Mittlefehldt, D.W., Morris, R.V., Golden, D.C., Gellert, R., Yen, A., Clark, B.C., Squyres, S.W., Farrand, W.H., Ruff, S.W., Arvidson, R.E., Klingelhöfer, G., McSween, H.Y., Rodionov, D.S., Schröder, C., de Souza, P.A. & Wang, A. (2006) Geochemical and mineralogical indicators for aqueous processes in the Columbia Hills of Gusev crater, Mars. *Journal of Geophysical Research: Planets*, 111 (E2), p.E02S12.

Minitti, M.E., Mustard, J.F. & Rutherford, M.J. (2002) Effects of glass content and oxidation on the spectra of SNC-like basalts: Applications to Mars remote sensing. *Journal of Geophysical Research: Planets*, 107 (E5), pp.6–1.

Mittlefehldt, D.W. (1994) ALH84001, a cumulate orthopyroxenite member of the martian meteorite clan. *Meteoritics*, 29 (2), pp.214–221.

Mittlefehldt, D.W., McCoy, T.J., Goodrich, C.A. & Kracher, A. (1998) Non-chondritic meteorites from asteroidal bodies. In: *In Planetary materials, edited by Papike J. J., Reviews in Mineralogy*. Washington, D.C., Mineralogical Society of America. Available from: <<http://repository.si.edu/handle/10088/20542>> [Accessed 25 May 2018].

Monkawa, A., Mikouchi, T., Koizumi, E., Chokai, J. & Miyamoto, M. (2004) Fast Cooling History of the Chassigny Martian Meteorite. In: p.1535. Available from: <<http://adsabs.harvard.edu/abs/2004LPI...35.1535M>> [Accessed 1 April 2014].

Morris, R.V., Klingelhöfer, G., Schröder, C., Rodionov, D.S., Yen, A., Ming, D.W., de Souza, P.A., Fleischer, I., Wdowiak, T., Gellert, R., Bernhardt, B., Evlanov, E.N., Zubkov, B., Foh, J., Bonnes, U., Kankeleit, E., Gütlich, P., Renz, F., Squyres, S.W. & Arvidson, R.E. (2006) Mössbauer mineralogy of rock, soil, and dust at Gusev crater, Mars: Spirit's journey through weakly altered olivine basalt on the plains and

pervasively altered basalt in the Columbia Hills. *Journal of Geophysical Research: Planets*, 111 (E2), p.E02S13.

Mosselmans, J.F.W., Quinn, P.D., Dent, A.J., Cavill, S.A., Moreno, S.D., Peach, A., Leicester, P.J., Keylock, S.J., Gregory, S.R., Atkinson, K.D. & Rosell, J.R. (2009) I18 – the microfocuss spectroscopy beamline at the Diamond Light Source. *Journal of Synchrotron Radiation*, 16 (6), pp.818–824.

Mustard, J.F., Murchie, S.L., Pelkey, S.M., Ehlmann, B.L., Milliken, R.E., Grant, J.A., Bibring, J.-P., Poulet, F., Bishop, J., Dobrea, E.N., Roach, L., Seelos, F., Arvidson, R.E., Wiseman, S., Green, R., Hash, C., Humm, D., Malaret, E., McGovern, J.A., Seelos, K., Clancy, T., Clark, R., Marais, D.D., Izenberg, N., Knudson, A., Langevin, Y., Martin, T., McGuire, P., Morris, R., Robinson, M., Roush, T., Smith, M., Swayze, G., Taylor, H., Titus, T. & Wolff, M. (2008) Hydrated silicate minerals on Mars observed by the Mars Reconnaissance Orbiter CRISM instrument. *Nature*, 454 (7202), pp.305–309.

Muttik, N., McCubbin, F.M., Keller, L.P., Santos, A.R., McCutcheon, W.A., Provencio, P.P., Rahman, Z., Shearer, C.K., Boyce, J.W. & Agee, C.B. (2014) Inventory of H₂O in the ancient Martian regolith from Northwest Africa 7034: The important role of Fe oxides. *Geophysical Research Letters*, pp.8235–8244.

Nakamura, T., Noguchi, T., Tanaka, M., Zolensky, M.E., Kimura, M., Tsuchiyama, A., Nakato, A., Ogami, T., Ishida, H., Uesugi, M., Yada, T., Shirai, K., Fujimura, A., Okazaki, R., Sandford, S.A., Ishibashi, Y., Abe, M., Okada, T., Ueno, M., Mukai, T., Yoshikawa, M. & Kawaguchi, J. (2011) Itokawa Dust Particles: A Direct Link Between S-Type Asteroids and Ordinary Chondrites. *Science*, 333 (6046), pp.1113–1116.

Nakamura, T., Noguchi, T., Tsuchiyama, A., Ushikubo, T., Kita, N.T., Valley, J.W., Zolensky, M.E., Kakazu, Y., Sakamoto, K., Mashio, E., Uesugi, K. & Nakano, T. (2008) Chondrulelike Objects in Short-Period Comet 81P/Wild 2. *Science*, 321 (5896), pp.1664–1667.

Nakamura-Messenger, K., Keller, L.P., Clemett, S.J., Messenger, S. & Ito, M. (2011) Nanometer-scale anatomy of entire Stardust tracks. *Meteoritics & Planetary Science*, 46 (7), pp.1033–1051.

Nakashima, D., Ushikubo, T., Joswiak, D.J., Brownlee, D.E., Matrajt, G., Weisberg, M.K., Zolensky, M.E. & Kita, N.T. (2012) Oxygen isotopes in crystalline silicates of comet Wild 2: A comparison of oxygen isotope systematics between Wild 2 particles and chondritic materials. *Earth and Planetary Science Letters*, 357–358, pp.355–365.

Nakashima, D., Ushikubo, T., Kita, N.T., Weisberg, M.K., Zolensky, M.E. & Ebel, D.S. (2015) Late formation of a comet Wild 2 crystalline silicate particle, Pyxie, inferred from Al–Mg chronology of plagioclase. *Earth and Planetary Science Letters*, 410, pp.54–61.

NASA (2018) NASA JPL Small-Body Database Search Engine [Internet]. Available from: <https://ssd.jpl.nasa.gov/sbdb_query.cgi#x> [Accessed 20 June 2018].

- NASA-JSC (2018) Stardust Sample Catalog Database [Internet]. Available from: <<https://curator.jsc.nasa.gov/stardust/catalog/index.cfm#search>> [Accessed 22 September 2018].
- National Research Council (2011) *Vision and Voyages for Planetary Science in the Decade 2013-2022*. National Academies Press. Available from: <<https://www.nap.edu/catalog/13117/vision-and-voyages-for-planetary-science-in-the-decade-2013-2022>> [Accessed 20 September 2018].
- Nayakshin, S., Cha, S.-H. & Bridges, J.C. (2011) The tidal downsizing hypothesis for planet formation and the composition of Solar system comets. *Monthly Notices of the Royal Astronomical Society: Letters*, 416 (1), pp.L50–L54.
- Nelder, J.A. & Mead, R. (1965) A Simplex Method for Function Minimization. *The Computer Journal*, 7 (4), pp.308–313.
- Nemchin, A.A., Humayun, M., Whitehouse, M.J., Hewins, R.H., Lorand, J.-P., Kennedy, A., Grange, M., Zanda, B., Fieni, C. & Deldicque, D. (2014) Record of the ancient martian hydrosphere and atmosphere preserved in zircon from a martian meteorite. *Nature Geoscience*, 7 (9), pp.638–642.
- Nemchin, A.A., Pidgeon, R.T., Healy, D., Grange, M.L., Whitehouse, M.J. & Vaughan, J. (2009) The comparative behavior of apatite-zircon U-Pb systems in Apollo 14 breccias: Implications for the thermal history of the Fra Mauro Formation. *Meteoritics & Planetary Science*, 44 (11), pp.1717–1734.
- Newburn, R.L., Bhaskaran, S., Duxbury, T.C., Fraschetti, G., Radey, T. & Schwochert, M. (2003) Stardust Imaging Camera. *Journal of Geophysical Research: Planets*, 108 (E10), p.8116.
- Nier, A.O. & McElroy, M.B. (1977) Composition and structure of Mars' Upper atmosphere: Results from the neutral mass spectrometers on Viking 1 and 2. *Journal of Geophysical Research*, 82 (28), pp.4341–4349.
- Noguchi, T., Nakamura, T., Okudaira, K., Yano, H., Sugita, S. & Burchell, M.J. (2007) Thermal alteration of hydrated minerals during hypervelocity capture to silica aerogel at the flyby speed of Stardust. *Meteoritics & Planetary Science*, 42 (3), pp.357–372.
- Nyquist, L.E., Bogard, D.D., Shih, C.-Y., Greshake, A., Stöffler, D. & Eugster, O. (2001) Ages and Geologic Histories of Martian Meteorites. *Space Science Reviews*, 96 (1–4), pp.105–164.
- Nyquist, L.E., Shih, C.-Y., McCubbin, F.M., Santos, A.R., Shearer, C.K., Peng, Z.X., Burger, P.V. & Agee, C.B. (2016) Rb-Sr and Sm-Nd isotopic and REE studies of igneous components in the bulk matrix domain of Martian breccia Northwest Africa 7034. *Meteoritics & Planetary Science*, 51 (3), pp.483–498.
- Ogliore, R.C. (2010) Comparison of the oxidation state of Fe in comet 81P/Wild 2 and chondritic-porous interplanetary dust particles. *Lawrence Berkeley National Laboratory*. Available from: <<http://escholarship.org/uc/item/6989n4hc>> [Accessed 26 September 2016].

Ogliore, R.C., Huss, G.R., Nagashima, K., Butterworth, A.L., Gainsforth, Z., Stodolna, J., Westphal, A.J., D. Joswiak & Tyliczszak, T. (2012) Incorporation of a Late-forming Chondrule into Comet Wild 2. *The Astrophysical Journal Letters*, 745 (2), p.L19.

Okada, T., Fukuhara, T., Tanaka, S., Taguchi, M., Imamura, T., Arai, T., Senshu, H., Ogawa, Y., Demura, H., Kitazato, K., Nakamura, R., Kouyama, T., Sekiguchi, T., Hasegawa, S., Matsunaga, T., Wada, T., Takita, J., Sakatani, N., Horikawa, Y., Endo, K., Helbert, J., Müller, T.G. & Hagermann, A. (2017) Thermal Infrared Imaging Experiments of C-Type Asteroid 162173 Ryugu on Hayabusa2. *Space Science Reviews*, 208 (1–4), pp.255–286.

Oort, J.H. (1950) The structure of the cloud of comets surrounding the Solar System and a hypothesis concerning its origin. *Bulletin of the Astronomical Institutes of the Netherlands*, 11, pp.91–110.

Pace, L.F., Richter, K., Nakamura-Messenger, K. & McQuillan, J. (2018) OSIRIS-REx and Hayabusa2 Sample Cleanroom Design and Construction Planning at NASA-JSC. *Lunar and Planetary Science Conference*, (2018), p.2507.

Palguta, J., Schubert, G. & Travis, B.J. (2010) Fluid flow and chemical alteration in carbonaceous chondrite parent bodies. *Earth and Planetary Science Letters*, 296 (3), pp.235–243.

Pan, Y. & Fleet, M.E. (1991) Barian feldspar and barian-chromian muscovite from the Hemlo area, Ontario. *The Canadian Mineralogist*, 29 (3), pp.481–498.

Poulet, F., Bibring, J.-P., Mustard, J.F., Gendrin, A., Mangold, N., Langevin, Y., Arvidson, R.E., Gondet, B., Gomez, C., Berthé, M., Erard, S., Forni, O., Manaud, N., Poulleau, G., Soufflot, A., Combes, M., Drossart, P., Encrenaz, T., Fouchet, T., Melchiorri, R., Bellucci, G., Altieri, F., Formisano, V., Fonti, S., Capaccioni, F., Cerroni, P., Coradini, A., Korablev, O., Kottsov, V., Ignatiev, N., Titov, D., Zasova, L., Pinet, P., Schmitt, B., Sotin, C., Hauber, E., Hoffmann, H., Jaumann, R., Keller, U., Arvidson, R., Mustard, J. & Forget, F. (2005) Phyllosilicates on Mars and implications for early martian climate. *Nature*, 438 (7068), pp.623–627.

Prinz, M., Hlava, P.H. & Keil, K. (1974) The Chassigny meteorite: a relatively iron-rich cumulate dunite. *Meteoritics*, 9, p.393.

Quirico, E., Moroz, L.V., Schmitt, B., Arnold, G., Faure, M., Beck, P., Bonal, L., Ciarniello, M., Capaccioni, F., Filacchione, G., Erard, S., Leyrat, C., Bockelée-Morvan, D., Zinzi, A., Palomba, E., Drossart, P., Tosi, F., Capria, M.T., De Sanctis, M.C., Raponi, A., Fonti, S., Mancarella, F., Orofino, V., Barucci, A., Blecka, M.I., Carlson, R., Despan, D., Faure, A., Fornasier, S., Gudipati, M.S., Longobardo, A., Markus, K., Mennella, V., Merlin, F., Piccioni, G., Rousseau, B. & Taylor, F. (2016) Refractory and semi-volatile organics at the surface of comet 67P/Churyumov-Gerasimenko: Insights from the VIRTIS/Rosetta imaging spectrometer. *Icarus*, 272, pp.32–47.

Ravel, B. & Newville, M. (2005) ATHENA, ARTEMIS, HEPHAESTUS: data analysis for X-ray absorption spectroscopy using IFEFFIT. *Journal of Synchrotron Radiation*, 12, pp.537–541.

- Reed, S.J.B. (2005) *Electron Microprobe Analysis and Scanning Electron Microscopy in Geology*. Cambridge, Cambridge University Press. Available from: <<http://ebooks.cambridge.org/ebook.jsf?bid=CBO9780511610561>> [Accessed 13 August 2014].
- Remusat, L., Zanda, B., Beck, P., Lorand, J.-P., Pont, S., Leroux, H. & Hewins, R. (2015) New Constraints on the Water Budget in the Martian Breccia Meteorite NWA 7533. In: *Meteoritics and Planetary Science*. p.5125. Available from: <<http://adsabs.harvard.edu/abs/2015LPICo1856.5125R>> [Accessed 6 April 2016].
- Renne, P.R., Balco, G., Ludwig, K.R., Mundil, R. & Min, K. (2011) Response to the comment by W.H. Schwarz et al. on “Joint determination of ^{40}K decay constants and $^{40}\text{Ar}^*/^{40}\text{K}$ for the Fish Canyon sanidine standard, and improved accuracy for $^{40}\text{Ar}/^{39}\text{Ar}$ geochronology” by P.R. Renne et al. (2010). *Geochimica et Cosmochimica Acta*, 75 (17), pp.5097–5100.
- Rietmeijer, F.J.M. (1998) Interplanetary Dust Particles. In: *In Planetary materials, edited by Papike J. J., Reviews in Mineralogy*. Mineralogical Society of America, pp.2.1-2.87. Available from: <<http://ring.geoscienceworld.org/content/36/1/3.1>> [Accessed 23 September 2016].
- Robertson, E.C. (1988) *Thermal properties of rocks*. U.S. Geological Survey,. Available from: <<http://pubs.er.usgs.gov/publication/ofr88441>>.
- RRUFF Database (2006) Goethite R050142 - RRUFF Database: Raman, X-ray, Infrared, and Chemistry [Internet]. Available from: <<http://rruff.info/Goethite/R050142>> [Accessed 15 June 2016].
- Rubin, A.E. (2018) Carbonaceous and noncarbonaceous iron meteorites: Differences in chemical, physical, and collective properties. *Meteoritics & Planetary Science*, 0 (0). Available from: <<https://onlinelibrary.wiley.com/doi/abs/10.1111/maps.13128>>.
- Russell, S.S., Hartmann, L., Cuzzi, J., Krot, A.N., Gounelle, M. & Weidenschilling, S. (2006) Timescales of the Solar Protoplanetary Disk. In: *Meteorites and the Early Solar System II*. University of Arizona Press, Tucson, pp.233–251. Available from: <<http://adsabs.harvard.edu/abs/2006mess.book..233R>>.
- Ruzicka, A., Grossman, J., Bouvier, A., Herd, C.D.K. & Agee, C.B. (2015) The Meteoritical Bulletin, No. 101. *Meteoritics & Planetary Science*, 50 (9), pp.1661–1661.
- Saiki, T., Sawada, H., Okamoto, C., Yano, H., Takagi, Y., Akahoshi, Y. & Yoshikawa, M. (2013) Small carry-on impactor of Hayabusa2 mission. *Acta Astronautica*, 84, pp.227–236.
- Sanderson, D.D. (1974) Spatial Distribution and Origin of Magnetite in an Intrusive Igneous Mass. *GSA Bulletin*, 85 (7), pp.1183–1188.
- Santos, A.R., Agee, C.B., McCubbin, F.M., Shearer, C.K., Burger, P.V., Tartèse, R. & Anand, M. (2015) Petrology of igneous clasts in Northwest Africa 7034: Implications for the petrologic diversity of the martian crust. *Geochimica et Cosmochimica Acta*, 157, pp.56–85.

- Schmieder, M., Kennedy, T., Jourdan, F., Buchner, E. & Reimold, W.U. (2018) A high-precision $^{40}\text{Ar}/^{39}\text{Ar}$ age for the Nördlinger Ries impact crater, Germany, and implications for the accurate dating of terrestrial impact events. *Geochimica et Cosmochimica Acta*, 220, pp.146–157.
- Schnohr, C.S. & Ridgway, M. eds. (2015) *X-Ray Absorption Spectroscopy of Semiconductors*. Berlin Heidelberg, Springer-Verlag. Available from: <<http://www.springer.com/gb/book/9783662443613>> [Accessed 23 May 2018].
- Schumacher, R. & Schmincke, H.-U. (1995) Models for the origin of accretionary lapilli. *Bulletin of Volcanology*, 56 (8), pp.626–639.
- Schwenzer, S.P. & Kring, D.A. (2009) Impact-generated hydrothermal systems capable of forming phyllosilicates on Noachian Mars. *Geology*, 37 (12), pp.1091–1094.
- Scott, E.R.D. & Krot, A.N. (2007) Chondrites and Their Components. In: H. D. Holland & K. K. Turekian eds. *Treatise on Geochemistry*. Oxford, Pergamon, pp.1–72. Available from: <<http://www.sciencedirect.com/science/article/pii/B0080437516011452>> [Accessed 22 September 2018].
- Scott, E.R.D., Krot, A.N. & Sanders, I.S. (2018) Isotopic Dichotomy among Meteorites and Its Bearing on the Protoplanetary Disk. *The Astrophysical Journal*, 854 (2), p.164.
- Sekanina, Z., Brownlee, D.E., Economou, T.E., Tuzzolino, A.J. & Green, S.F. (2004) Modeling the Nucleus and Jets of Comet 81P/Wild 2 Based on the Stardust Encounter Data. *Science*, 304 (5678), pp.1769–1774.
- Shearer, C.K., Papike, J.J. & Rietmeijer, F.J.M. (1998) The Planetary Sample Suite and Environments of Origin. In: *In Planetary materials, edited by Papike J. J., Reviews in Mineralogy*. Mineralogical Society of America, pp.1.01-1.28. Available from: <<http://ring.geoscienceworld.org/content/36/1/3.1>> [Accessed 23 September 2016].
- Shinno, I. (1980) Relations between (130) spacing, chemical composition, and cation site preference of olivine. *Journal of the Japanese Association of Mineralogists, Petrologists and Economic Geologists*, 75 (10), pp.343–352.
- Siegert, S., Branney, M.J. & Hecht, L. (2017) Density current origin of a melt-bearing impact ejecta blanket (Ries suevite, Germany). *Geology*, 45 (9), pp.855–858.
- Simon, S.B., Joswiak, D.J., Ishii, H.A., Bradley, J.P., Chi, M., Grossman, L., Aléon, J., Brownlee, D.E., Fallon, S., Hutcheon, I.D., Matrajt, G. & McKeegan, K.D. (2008) A refractory inclusion returned by Stardust from comet 81P/Wild 2. *Meteoritics & Planetary Science*, 43 (11), pp.1861–1877.
- Smith, M.R., Laul, J.C., Ma, M.S., Huston, T., Verkouteren, R.M., Lipschutz, M.E. & Schmitt, R.A. (1984) Petrogenesis of the SNC (shergottites, nakhlites, chassignites) meteorites: Implications for their origin from a large dynamic planet, possibly Mars. *Journal of Geophysical Research: Solid Earth*, 89 (S02), pp.B612–B630.

- Snead, C.J., McCubbin, F.M., Nakamura-Messenger, K. & Righter, K. (2018) Advances in Small Particle Handling of Astromaterials in Preparation for OSIRIS-REx and Hayabusa2: Initial Developments. *Lunar and Planetary Science Conference*, (2083), p.2426.
- Snodgrass, C., Jones, G.H., Boehnhardt, H., Gibbings, A., Homeister, M., Andre, N., Beck, P., Bentley, M.S., Bertini, I., Bowles, N., Capria, M.T., Carr, C., Ceriotti, M., Coates, A.J., Della Corte, V., Donaldson Hanna, K.L., Fitzsimmons, A., Gutiérrez, P.J., Hainaut, O.R., Herique, A., Hilchenbach, M., Hsieh, H.H., Jehin, E., Karatekin, O., Kofman, W., Lara, L.M., Laudan, K., Licandro, J., Lowry, S.C., Marzari, F., Masters, A., Meech, K.J., Moreno, F., Morse, A., Orosei, R., Pack, A., Plettemeier, D., Prialnik, D., Rotundi, A., Rubin, M., Sánchez, J.P., Sheridan, S., Tieloff, M. & Winterboer, A. (2017) The Castalia mission to Main Belt Comet 133P/Elst-Pizarro. *Advances in Space Research*. Available from: <<http://www.sciencedirect.com/science/article/pii/S0273117717306622>> [Accessed 13 September 2018].
- Solano, E., Frontera, C., Puig, T., Obradors, X., Ricart, S. & Ros, J. (2014) Neutron and X-ray diffraction study of ferrite nanocrystals obtained by microwave-assisted growth. A structural comparison with the thermal synthetic route. *Journal of Applied Crystallography*, 47 (1), pp.414–420.
- Stephan, T. (2009) TOF-SIMS Analysis of Cometary Fragments Extracted from a Stardust Aerogel Track. *Lunar and Planetary Science Conference*, p.1698.
- Stodolna, J., Gainsforth, Z., Butterworth, A.L. & Westphal, A.J. (2014) Characterization of preserved primitive fine-grained material from the Jupiter family comet 81P/Wild 2 – A new link between comets and CP-IDPs. *Earth and Planetary Science Letters*, 388, pp.367–373.
- Stodolna, J., Jacob, D. & Leroux, H. (2012) Mineralogy and petrology of Stardust particles encased in the bulb of track 80: TEM investigation of the Wild 2 fine-grained material. *Geochimica et Cosmochimica Acta*, 87, pp.35–50.
- Stöffler, D. & Grieve, R.A.F. (2007) *Impactites. In: Metamorphic Rocks: A Classification and Glossary of Terms - Cambridge University Press*. edited by Fettes D. and Desmons J. Cambridge, UK. Cambridge University Press. Available from: <<http://www.cambridge.org/catalogue/catalogue.asp?isbn=9780521336185&ss=toc>> [Accessed 29 June 2017].
- Straub, D.W., Burns, R.G. & Pratt, S.F. (1991) Spectral signature of oxidized pyroxenes: implications to remote sensing of terrestrial planets. *Journal of Geophysical Research: Planets*, 96 (E3), pp.18819–18830.
- Sugiura, N. & Fujiya, W. (2014) Correlated accretion ages and $\epsilon^{54}\text{Cr}$ of meteorite parent bodies and the evolution of the solar nebula. *Meteoritics & Planetary Science*, 49 (5), pp.772–787.
- Swindle, T.D., Treiman, A.H., Lindstrom, D.J., Burkland, M.K., Cohen, B.A., Grier, J.A., Li, B. & Olson, E.K. (2000) Noble gases in iddingsite from the Lafayette

meteorite: Evidence for liquid water on Mars in the last few hundred million years. *Meteoritics & Planetary Science*, 35 (1), pp.107–115.

Tachibana, S., Abe, M., Arakawa, M., Fujimoto, M., Iijima, Y., Ishiguro, M., Kitazato, K., Kobayashi, N., Namiki, N., Okada, T., Okazaki, R., Sawada, H., Sugita, S., Takano, Y., Tanaka, S., Watanabe, S., Yoshikawa, M., Kunitake, H. & Team, T.H.P. (2014) Hayabusa2: Scientific importance of samples returned from C-type near-Earth asteroid (162173) 1999 JU3. *Geochemical Journal*, 48 (6), pp.571–587.

Takenouchi, A., Mikouchi, T. & Kogure, T. (2017) Mineralogical study of brown olivine in Northwest Africa 1950 shergottite and implications for the formation mechanism of iron nanoparticles. *Meteoritics & Planetary Science*, 52 (12), pp.2491–2504.

Taylor, M.G.G.T., Altobelli, N., Buratti, B.J. & Choukroun, M. (2017) The Rosetta mission orbiter science overview: the comet phase. *Philosophical Transactions of the Royal Society of London. Series A, Mathematical, Physical and Engineering Sciences*, 375 (2017), p.20160262.

Tedesco, E.F. & Desert, F.-X. (2002) The Infrared Space Observatory Deep Asteroid Search. *The Astronomical Journal*, 123 (4), p.2070.

Tomeoka, K., Tomioka, N. & Ohnishi, I. (2008) Silicate minerals and Si-O glass in comet Wild 2 samples: Transmission electron microscopy. *Meteoritics & Planetary Science*, 43 (1–2), pp.273–284.

Treiman, A.H. (2003) Traces of Ancient Martian Life in Meteorite ALH84001: An Outline of Status in late 2003. *NASA Planetary Protection Office References Web Site*. Available from: <http://www.lpi.usra.edu/lpi/annual_report_2004.pdf> [Accessed 26 March 2014].

Tschermak, G. (1872) Die Meteoriten von Shergotty und Gopalpur. *Sitzber. Math.-Naturw. Klasse Akad. Wiss. Wien*, 65 (122).

Tsou, P., Brownlee, D.E., Sandford, S.A., Hörz, F. & Zolensky, M.E. (2003) Wild 2 and interstellar sample collection and Earth return. *Journal of Geophysical Research: Planets*, 108 (E10), p.8113.

Tsuchiyama, A., Uesugi, M., Matsushima, T., Michikami, T., Kadono, T., Nakamura, T., Uesugi, K., Nakano, T., Sandford, S.A., Noguchi, R., Matsumoto, T., Matsuno, J., Nagano, T., Imai, Y., Takeuchi, A., Suzuki, Y., Ogami, T., Katagiri, J., Ebihara, M., Ireland, T.R., Kitajima, F., Nagao, K., Naraoka, H., Noguchi, T., Okazaki, R., Yurimoto, H., Zolensky, M.E., Mukai, T., Abe, M., Yada, T., Fujimura, A., Yoshikawa, M. & Kawaguchi, J. (2011) Three-Dimensional Structure of Hayabusa Samples: Origin and Evolution of Itokawa Regolith. *Science*, 333 (6046), pp.1125–1128.

Tsuda, Y., Yoshikawa, M., Abe, M., Minamino, H. & Nakazawa, S. (2013) System design of the Hayabusa 2—Asteroid sample return mission to 1999 JU3. *Acta Astronautica*, 91, pp.356–362.

- TU Wien, A. (2018) X-ray absorption spectroscopy (XAS). Available from: <<http://www.ati.ac.at/index.php?id=247>>.
- Tubus, B. (2017) *Schematic view of STEM mode*. Available from: <<https://commons.wikimedia.org/w/index.php?curid=64503919>>.
- Turner, S.M.R., Bridges, J.C., Grebby, S. & Ehlmann, B.L. (2016) Hydrothermal activity recorded in post Noachian-aged impact craters on Mars. *Journal of Geophysical Research: Planets*, 121 (4), p.2015JE004989.
- Tuzzolino, A.J., Economou T. E., McKibben R. B., Simpson J. A., McDonnell J. A. M., Burchell M. J., Vaughan B. A. M., Tsou P., Hanner M. S., Clark B. C. & Brownlee D. E. (2003) Dust Flux Monitor Instrument for the Stardust mission to comet Wild 2. *Journal of Geophysical Research: Planets*, 108 (E10). Available from: <<https://agupubs.onlinelibrary.wiley.com/doi/full/10.1029/2003JE002086>> [Accessed 20 March 2018].
- Tuzzolino, A.J., Economou, T.E., Clark, B.C., Tsou, P., Brownlee, D.E., Green, S.F., McDonnell, J. a. M., McBride, N. & Colwell, M.T.S.H. (2004) Dust Measurements in the Coma of Comet 81P/Wild 2 by the Dust Flux Monitor Instrument. *Science*, 304 (5678), pp.1776–1780.
- UCR (2018) Introduction to Energy Dispersive X-ray Spectrometry (EDS). Available from: <<http://cfamm.ucr.edu/documents/eds-intro.pdf>> [Accessed 9 December 2018].
- Udry, A., Lunning, N.G., McSween Jr., H.Y. & Bodnar, R.J. (2014) Petrogenesis of a vitrophyre in the martian meteorite breccia NWA 7034. *Geochimica et Cosmochimica Acta*, 141, pp.281–293.
- Urey, H.C. & Craig, H. (1953) The composition of the stone meteorites and the origin of the meteorites. *Geochimica et Cosmochimica Acta*, 4 (1–2), pp.36–82.
- Van Schmus, W.R. & Wood, J.A. (1967) A chemical-petrologic classification for the chondritic meteorites. *Geochimica et Cosmochimica Acta*, 31 (5), pp.747–765.
- Veksler, V.I. (1944) A new method of accelerating relativistic particles. In: *Comptes Rendus (Doklady) de L'Académie Des Sciences de L'URSS*. 8. Édition de l'Académie des sciences de l'URSS, pp.329–331. Available from: <https://books.google.co.uk/books/about/Comptes_Rendus_Doklady_de_L_Acad%C3%A9mie_De.html?id=665HAQAIAAJ&redir_esc=y>.
- VG (2017) *VG Studio Max*. Volume Graphics. Available from: <<https://www.volumegraphics.com/en/products/vgstudio-max.html>> [Accessed 26 January 2018].
- Villeneuve, J., Libourel, G. & Soulié, C. (2015) Relationships between type I and type II chondrules: Implications on chondrule formation processes. *Geochimica et Cosmochimica Acta*, 160, pp.277–305.
- Volk, K. & Malhotra, R. (2008) The Scattered Disk as the Source of the Jupiter Family Comets. *The Astrophysical Journal*, 687 (1), p.714.

- Walsh, K.J., Morbidelli, A., Raymond, S.N., O'Brien, D.P. & Mandell, A.M. (2011) A low mass for Mars from Jupiter's early gas-driven migration. *Nature*, 475 (7355), pp.206–209.
- Warren, P.H. (2011) Stable-isotopic anomalies and the accretionary assemblage of the Earth and Mars: A subordinate role for carbonaceous chondrites. *Earth and Planetary Science Letters*, 311 (1), pp.93–100.
- Warren, P.H. & Rubin, A.E. (2010) Pyroxene-selective impact smelting in ureilites. *Geochimica et Cosmochimica Acta*, 74 (17), pp.5109–5133.
- Wasson, J.T., Isa, J. & Rubin, A.E. (2013) Compositional and petrographic similarities of CV and CK chondrites: A single group with variations in textures and volatile concentrations attributable to impact heating, crushing and oxidation. *Geochimica et Cosmochimica Acta*, 108, pp.45–62.
- Wechsler, B.A., Lindsley, D.H. & Prewitt, C.T. (1984) Crystal structure and cation distribution in titanomagnetites (Fe (sub 3-x) Ti_x O₄). *American Mineralogist*, 69 (7–8), pp.754–770.
- Weisberg, M.K., McCoy, T.J. & Krot, A.N. (2006) Systematics and Evaluation of Meteorite Classification. In: *Meteorites and the Early Solar System II*. pp.19–52. Available from: <<http://adsabs.harvard.edu/abs/2006mess.book...19W>> [Accessed 21 April 2017].
- Weiss, D.K. & Head, J.W. (2016) Impact ejecta-induced melting of surface ice deposits on Mars. *Icarus*, 280, pp.205–233.
- Westphal, A.J., Anderson, D., Butterworth, A.L., Frank, D.R., Lettieri, R., Marchant, W., Von Korff, J., Zevin, D., Ardizzone, A., Campanile, A., Capraro, M., Courtney, K., Criswell, M.N., Crumpler, D., Cwik, R., Gray, F.J., Hudson, B., Imada, G., Karr, J., Wah, L.L.W., Mazzucato, M., Motta, P.G., Rigamonti, C., Spencer, R.C., Woodrough, S.B., Santoni, I.C., Sperry, G., Terry, J.-N., Wordsworth, N., Yahnke, T., Allen, C., Ansari, A., Bajt, S., Bastien, R.K., Bassim, N., Bechtel, H.A., Borg, J., Brenker, F.E., Bridges, J., Brownlee, D.E., Burchell, M., Burghammer, M., Changela, H., Cloetens, P., Davis, A.M., Doll, R., Floss, C., Flynn, G., Gainsforth, Z., Grün, E., Heck, P.R., Hillier, J.K., Hoppe, P., Huth, J., Hvide, B., Kearsley, A., King, A.J., Lai, B., Leitner, J., Lemelle, L., Leroux, H., Leonard, A., Nittler, L.R., Oglione, R., Ong, W.J., Postberg, F., Price, M.C., Sandford, S.A., Tresseras, J.-A.S., Schmitz, S., Schoonjans, T., Silversmit, G., Simionovici, A.S., Solé, V.A., Srama, R., Stephan, T., Sterken, V.J., Stodolna, J., Stroud, R.M., Sutton, S., Tieloff, M., Tsou, P., Tsuchiyama, A., Tyliszczak, T., Vekemans, B., Vincze, L. & Zolensky, M.E. (2014) Stardust Interstellar Preliminary Examination I: Identification of tracks in aerogel. *Meteoritics & Planetary Science*, 49 (9), pp.1509–1521.
- Westphal, A.J., Bridges, J.C., Brownlee, D.E., Butterworth, A.L., De Gregorio, B.T., Dominguez, G., Flynn, G.J., Gainsforth, Z., Ishii, H.A., Joswiak, D., Nittler, L.R., Oglione, R.C., Palma, R., Pepin, R.O., Stephan, T. & Zolensky, M.E. (2017) The future of Stardust science. *Meteoritics & Planetary Science*, 52 (9), pp.1859–1898.

- Westphal, A.J., Snead, C., Borg, J., Quirico, E., Raynal, P.-I., Zolensky, M.E., Ferrini, G., Colangeli, L. & Palumbo, P. (2002) Small hypervelocity particles captured in aerogel collectors: Location, extraction, handling and storage. *Meteoritics & Planetary Science*, 37 (6), pp.855–865.
- Westphal, A.J., Snead, C., Butterworth, A., Graham, G.A., Bradley, J.P., Bajt, S., Grant, P.G., Bench, G., Brennan, S. & Pianetta, P. (2004) Aerogel keystones: Extraction of complete hypervelocity impact events from aerogel collectors. *Meteoritics & Planetary Science*, 39 (8), pp.1375–1386.
- Whipple, F.L. (1950) A comet model. I. The acceleration of Comet Encke. *The Astrophysical Journal*, 111, pp.375–394.
- Wickham-Eade, J.E., Burchell, M.J., Price, M.C., Hicks, L.J., MacArthur, J.L. & Bridges, J.C. (2017) Raman identification of olivine grains in fine grained mineral assemblages fired into aerogel. *Procedia Engineering*, 204, pp.413–420.
- Wiechert, U., Halliday, A.N., Lee, D.-C., Snyder, G.A., Taylor, L.A. & Rumble, D. (2001) Oxygen Isotopes and the Moon-Forming Giant Impact. *Science*, 294 (5541), pp.345–348.
- Williams, D.B. & Carter, C.B. (2009a) Quantitative X-ray Analysis. In: *Transmission Electron Microscopy*. Springer, Boston, MA, pp.639–662. Available from: <https://link.springer.com/chapter/10.1007/978-0-387-76501-3_35>.
- Williams, D.B. & Carter, C.B. (2009b) The Transmission Electron Microscope. In: D. B. Williams & C. B. Carter eds. *Transmission Electron Microscopy: A Textbook for Materials Science*. Boston, MA, Springer US, pp.639–662. Available from: <https://doi.org/10.1007/978-0-387-76501-3_35>.
- Wilson, E.J.N. (1996) Fifty years of synchrotrons [Internet]. Available from: <<https://cds.cern.ch/record/339572>> [Accessed 8 September 2018].
- Wilson, R. (2014) Scanning Electron Microscopy. Available from: <<http://www2.le.ac.uk/departments/geology/analytical/semnew2>> [Accessed 25 August 2014].
- Wittmann, A., Korotev, R.L., Jolliff, B.L., Irving, A.J., Moser, D.E., Barker, I. & Rumble, D. (2015) Petrography and composition of Martian regolith breccia meteorite Northwest Africa 7475. *Meteoritics & Planetary Science*, 50 (2), pp.326–352.
- Wood, J.E., Williams, D.B. & Goldstein, J.I. (1984) Experimental and theoretical determination of kAFe factors for quantitative X-ray microanalysis in the analytical electron microscope. *Journal of Microscopy*, 133 (3), pp.255–274.
- Wooden, D.H. (2008) Cometary Refractory Grains: Interstellar and Nebular Sources. In: *Origin and Early Evolution of Comet Nuclei*. Space Sciences Series of ISSI. Springer, New York, NY, pp.75–108. Available from: <https://link.springer.com/chapter/10.1007/978-0-387-85455-7_6> [Accessed 29 May 2018].

- Wozniakiewicz, P.J., Ishii, H.A., Kearsley, A.T., Bradley, J.P., Price, M.C., Burchell, M.J., Teslich, N. & Cole, M.J. (2015) The survivability of phyllosilicates and carbonates impacting Stardust Al foils: Facilitating the search for cometary water. *Meteoritics & Planetary Science*, 50 (12), pp.2003–2023.
- Wozniakiewicz, P.J., Kearsley, A.T., Burchell, M.J., Price, M.C., Ishii, H.A. & Cole, M.J. (2018) Preparation of large Stardust aluminum foil craters for analysis. *Meteoritics & Planetary Science*, 53 (5), pp.1066–1080.
- Xu, W., Van der Voo, R., Peacor, D.R. & Beaubouef, R.T. (1997) Alteration and dissolution of fine-grained magnetite and its effects on magnetization of the ocean floor. *Earth and Planetary Science Letters*, 151 (3), pp.279–288.
- Yada, T., Sakamoto, K., Yoshitake, M., Kumagai, K., Nishimura, M., Nakano, Y., Furuya, S., Abe, M., Okada, T., Tachibana, S., Yurimoto, H. & Fujimoto, M. (2018) From Hayabusa to Hayabusa2: Present Status and Plans for Sample Curations of Asteroidal Sample Return Missions by JAXA. *LPI Contributions*, 2067, p.6117.
- Yancey, T.E. & Guillemette, R.N. (2008) Carbonate accretionary lapilli in distal deposits of the Chicxulub impact event Chicxulub carbonate lapilli. *GSA Bulletin*, 120 (9–10), pp.1105–1118.
- Yin, Q.Z., McCubbin, F.M., Zhou, Q., Santos, A.R., Tartèse, R., Li, X., Li, Q., Liu, Y., Tang, G., Boyce, J.W., Lin, Y., Yang, W., Zhang, J., Hao, J., Elardo, S.M., Shearer, C.K., Rowland, D.J., Lerche, M. & Agee, C.B. (2014) An Earth-like beginning for ancient Mars indicated by alkali-rich volcanism at 4.4 Ga. *LPSC XLV*, Abstract #1320. Available from: <<http://www.hou.usra.edu/meetings/lpsc2014/pdf/1320.pdf>>.
- Zak, L. (1991) Hyalophane-zoisite veins from the pyrite- rhodochrosite deposits near Litosice in eastern Bohemia (Czechoslovakia). *Casopis Mineral. Geol.*, 36, pp.67–75.
- Zhu, D., Cui, Y., Hapugoda, S., Vining, K. & Pan, J. (2012) Mineralogy and crystal chemistry of a low grade nickel laterite ore. *Transactions of Nonferrous Metals Society of China*, 22 (4), pp.907–916.
- Zobov, N.F., Polyansky, O.L., Le Sueur, C.R. & Tennyson, J. (1996) Vibration-rotation levels of water beyond the Born-Oppenheimer approximation. *Chemical Physics Letters*, 260 (3), pp.381–387.
- Zolensky, M., Nakamura-Messenger, K., Rietmeijer, F., Leroux, H., Mikouchi, T., Ohsumi, K., Simon, S., Grossman, L., Stephan, T., Weisberg, M., Velbel, M., Zega, T., Stroud, R., Tomeoka, K., Ohnishi, I., Tomioka, N., Nakamura, T., Matrajt, G., Joswiak, D., Brownlee, D., Langenhorst, F., Krot, A., Kearsley, A., Ishii, H., Graham, G., Dai, Z.R., Chi, M., Bradley, J., Hagiya, K., Gounelle, M., Keller, L. & Bridges, J. (2008) Comparing Wild 2 particles to chondrites and IDPs. *Meteoritics & Planetary Science*, 43 (1–2), pp.261–272.
- Zolensky, M.E. & Thomas, K.L. (1995) Iron and iron-nickel sulfides in chondritic interplanetary dust particles. *Geochimica et Cosmochimica Acta*, 59 (22), pp.4707–4712.

Bibliography

Zolensky, M.E., Zega, T.J., Yano, H., Wirick, S., Westphal, A.J., Weisberg, M.K., Weber, I., Warren, J.L., Velbel, M.A., Tsuchiyama, A., Tsou, P., Toppani, A., Tomioka, N., Tomeoka, K., Teslich, N., Taheri, M., Susini, J., Stroud, R., Stephan, T., Stadermann, F.J., Snead, C.J., Simon, S.B., Simionovici, A., See, T.H., Robert, F., Rietmeijer, F.J.M., Rao, W., Perronnet, M.C., Papanastassiou, D.A., Okudaira, K., Ohsumi, K., Ohnishi, I., Nakamura-Messenger, K., Nakamura, T., Mostefaoui, S., Mikouchi, T., Meibom, A., Matrajt, G., Marcus, M.A., Leroux, H., Lemelle, L., Le, L., Lanzirotti, A., Langenhorst, F., Krot, A.N., Keller, L.P., Kearsley, A.T., Joswiak, D., Jacob, D., Ishii, H., Harvey, R., Hagiya, K., Grossman, L., Grossman, J.N., Graham, G.A., Gounelle, M., Gillet, P., Genge, M.J., Flynn, G., Ferroir, T., Fallon, S., Ebel, D.S., Dai, Z.R., Cordier, P., Clark, B., Chi, M., Butterworth, A.L., Brownlee, D.E., Bridges, J.C., Brennan, S., Brearley, A., Bradley, J.P., Bleuet, P., Bland, P.A. & Bastien, R. (2006) Mineralogy and Petrology of Comet 81P/Wild 2 Nucleus Samples. *Science*, 314 (5806), pp.1735–1739.